

DESIGN, FABRICATION, AND VALIDATION OF A MICROCONTROLLER  
BASED SUPERCOOLING CONTROL UNIT FOR USE IN FOOD  
PRESERVATION.

A THESIS SUBMITTED TO THE GRADUATE DIVISION OF THE  
UNIVERSITY OF HAWAI'I AT MĀNOA IN PARTIAL FULFILLMENT  
OF THE REQUIREMENTS FOR THE DEGREE OF

MASTER OF SCIENCE

IN

BIOLOGICAL ENGINEERING

Nov 2017

By

Raymond A. Hoptowit

Thesis Committee:

Soojin Jun, Chairperson

Samir Khanal

Yong Li

Keywords: Supercooling, food preservation, data logging, MCU, freezing

© 2017  
Raymond A. Hoptowit

## **ACKNOWLEDGEMENTS**

I would like to express my sincere gratitude to those who have helped me complete this thesis:

To my advisor Dr. Soojin Jun for his support and guidance throughout my research. And for his patience and welcomed tendency to place the concerns of his students first, I am grateful.

To Dr. Yong Li for his advice and suggestions regarding statistical analysis and experimental procedures.

To Dr. Samir Khanal for his review and suggestion of the project and thesis.

To Roberto Rodriguez III for his immense assistance, advice, and the conversation we shared regarding the project and its development.

To my lab-mates who have helped me tremendously throughout my studies and research.

This research was supported by the U.S. Department of Agriculture (USDA), National Institute of Food and Agriculture, Project number: 2016-33610-25447 and 2014-67017-21650.

To my family, for their continued support and encouragement throughout my life.

## ABSTRACT

Freezing is the most widely used food preservation technique in the commercial and domestic market, however the freezing process causes irreversible damages to foods as ice nucleation occurs. New emerging technologies attempt to prevent these damages from occurring by delaying ice formation within foods while maintaining internal sub-zero temperatures (i.e., Supercooling). Investigations into the simultaneous application of pulsating electric fields (PEF) and oscillating magnetic fields (OMF) during the freezing process for extension of the supercooled state within foods have been conducted. In such studies it is common to use numerous electrical equipment and instruments to precisely measure and regulate the power applied to the test food during the supercooling process. As a result, these studies have proven to be quite expensive.

In an effort to reduce costs, improve portability, and simplify the data collection process a supercooling control unit was developed to replace all major equipment related to supercooling research conducted at the University of Hawai'i at Mānoa (Hawaii, USA). The control unit regulates and monitors all power within the magnetic and electric field generation systems. A separate thermocouple based temperature measurement system allows for monitoring of any temperatures associated with the test food sample or ambient environments. Data logging is accomplished either through on-board SD™ card or through USB port to external PC.

The supercooling control unit offers a total uncertainty of  $\pm 0.7^{\circ}\text{C}$  for temperature measurements,  $\pm 1.71\%$  of measurements for the PEF current,  $\pm 1.67\%$  of measurements for PEF voltage,  $\pm 2.88\%$  of measurements for OMF current, and  $\pm 1.91\%$  of measurements for OMF voltage. Supercooling experiments conducted with the newly developed control unit have shown agreeable measurements with lab grade electrical equipment. 180g top round beef steak (London broil) was successfully supercooled at  $-4^{\circ}\text{C}$  for a validation period of 7 days, various food quality assessments conducted on the beef showed comparable results with data from previous supercooling studies.

The control unit provides a seamless data collection process, while maintaining an adequate level of precision and accuracy within collected data. The newly developed device cuts costs, improved portability, and offers a scale-able platform upon which additional functionality can be implemented.

## TABLE OF CONTENTS

ACKNOWLEDGEMENTS .....	iii
ABSTRACT .....	iv
LIST OF TABLES .....	viii
LIST OF FIGURES .....	ix
LIST OF ABBREVIATION AND SYMBOLS .....	xii
CHAPTER 1. INTRODUCTION .....	1
1.1 Freezing .....	1
1.1.1 Freezing in the Food Industry .....	2
1.1.2 Current Freezing Technologies in the Food Industry .....	4
1.1.3 Emerging Freezing Technologies in the Food Industry .....	5
1.2 Supercooling in Foods .....	8
1.2.1 Technology and Theory of Supercooling Research .....	8
1.3 Problem Statement and Project Scope .....	10
CHAPTER 2. HARDWARE AND DESIGN .....	13
2.1 Design Overview .....	13
2.2 Oscillating Magnetic Field Generation System (OMF) .....	17
2.2.1 H-Bridge .....	17
2.2.2 OMF H-Bridge Power Module Selection and Operation .....	20
2.2.3 OMF Bias Voltage System .....	22
2.3 Pulsating Electric Field Generation System (PEF) .....	22
2.3.1 PEF H-Bridge Power Module Selection and Operation .....	22
2.3.2 PEF Bias Voltage System .....	23
2.4 Current Sensing System .....	23
2.4.1 Shunt Resistor Based Current Measurement Model .....	23
2.4.2 OMF Current Sensing System Component Selection and Design .....	26
2.4.3 PEF Current Sensing System Component Selection and Design .....	28
2.5 Voltage Sensing System .....	29
2.6 Temperature Measurement System .....	30
2.6.1 Thermocouple Based Temperature Measurement Model .....	30
2.6.2 Resistance Temperature Detector (RTD) Measurement Model .....	32
2.6.3 Thermocouple Temperature Measurement System Component Selection and Design .....	33
2.7 Added Functionality .....	37

2.7.1 Data logging .....	37
2.7.2 User Interface.....	38
2.8 Custom Circuit Board Layout .....	38
2.9 Enclosure.....	39
2.10 Cost Estimate .....	41
2.11 Size and Weight.....	41
CHAPTER 3. SOFTWARE .....	42
3.1 PEF and OMF Waveform Generation.....	42
3.2 Determination of Thermocouple Measurements.....	42
3.3 Determination of Current Measurement .....	44
3.3.1 PEF Current Measurement.....	44
3.3.2 OMF current Measurement.....	46
3.4 Backend System Control .....	47
CHAPTER 4. PRELIMINARY VALIDATIONS .....	50
4.1 Thermocouple Calibration Technique.....	50
4.1.1 Emf Measurement System, Methods and Materials .....	51
4.1.2 Emf measurement System, Results and Discussion.....	53
4.1.3 RTD CJC System, Methods and Materials .....	57
4.1.4 RTD CJC System, Results and Discussion.....	58
4.1.5 Total Uncertainty of the Thermocouple System.....	61
4.2 Current measurement .....	66
4.2.1 Materials and Methods.....	66
4.2.2 Results and Discussion .....	66
4.2.3 Total Uncertainty of OMF and PEF Current Measurement Systems .....	74
4.3 Voltage Measurement .....	78
4.3.1 Materials and Methods.....	78
4.3.2 Results and Discussion .....	78
4.3.3 Total Uncertainty of the PEF and OMF Voltage Measurement System.....	81
CHAPTER 5. OPERATIONAL VALIDATION .....	84
5.1 Methods and Materials.....	84
5.1.1 Supercooling Equipment and Protocol .....	84
5.1.2 Sample Preparation.....	86
5.1.3 Drip Loss.....	86

5.1.4 pH Measurements.....	87
5.1.5 Warner-Bratzler Shear .....	87
5.1.6 Digital Color Analysis.....	87
5.2 Results and Discussion .....	88
CHAPTER 6. CONCLUSIONS, POTENTIAL IMPACT, AND RECOMMENDATIONS .....	96
6.1 Conclusions .....	96
6.2 Potential Impacts .....	96
6.3 Recommendations .....	97
APPENDICES .....	98
Appendix A: MCU code .....	98
Appendix B. MatLab Code.....	118
Appendix C. Bill of Material, Electronic Components .....	120
Appendix D. Costs of Goods Sold Analysis.....	128
Appendix E. Summary of Thermocouple emf Measurement System Calibration Data .....	129
Appendix F. Summary of Thermocouple system RTD CJC data .....	132
REFERENCES.....	133

## LIST OF TABLES

Table 1. Costs associated with a typical supercooling experimental equipment.....	11
Table 2. Key components found on the control unit.....	14
Table 3. Key Design Specification for OMF and PEF systems.....	14
Table 4. Common high side MOSFET gate driving circuits. Reprinted from HV Floating MOS-Gate Driver ICs, Application Note AN-978 RevD, 2007. International Rectifiers, p. 29. ....	19
Table 5. Standard thermocouple wires, their material composition, Seebeck coefficients [113], and their typical associated limits of uncertainty. ....	30
Table 6. Common RTD material, and their associated resistivity. ....	32
Table 7. Most Common RTD standards and their classified RTD grade. The defining equations express uncertainty associated with RTD grade, where t is absolute temperature in degrees Celsius. ....	32
Table 8. Emf bias mean and standard deviation of multiplexing stage and filtering stage of CU. ....	55
Table 9. Resistive load current measurement summary. ....	67
Table 10. Sample chamber load current measurement summary. ....	68
Table 11. PEF current measurement summary with 100Ohms resistive load.....	72
Table 12. Electrical current measurement summary between CU and DAQ. All values are units of Amperes.....	89
Table 13. Electrical Voltage measurement summary between DAQ and CU data.....	90
Table 14. Temperature measurement summary between DAQ and CU. Units are °C.....	90
Table 15. Pre-calibrated data, Temperature measurements summary. Bias error is the difference between Fluid bath temperatures and CU measured temperatures. ....	129
Table 16. Pre-calibrated data, emf measurement summary. Bias error is the difference between DAQ emf and CU measured emf. ....	130
Table 17. Pre-calibrated data with calibration correction applied, temperature measurement summary. ....	131
Table 18. Pre-calibrated data, DAQ measured data points.....	132
Table 19. Pre-Calibrated data, CU measured data points. Bias error is taken as the difference between CU measured temp and DAQ measured Ice bath temp. ....	132
Table 20. Post-Calibrated data, CU measured data points. Bias error is taken as the difference between CU measured temp and DAQ measured Ice bath temp. ....	132

## LIST OF FIGURES

Figure 1. A typical temperature time curve of food placed within a freezer. ....	3
Figure 2. Typical experimental Setup of a supercooling experiment as described by Mok et al. [56], [54]. .....	11
Figure 3. Simplified block diagram of the control unit’s overall system design. PC/Laptop and LCD display are interfaced with MCU serial UART, communication between the two is toggled between a digital switch. The external sample chamber houses the OMF and PEF field generating electrodes and electromagnets. ....	14
Figure 4. A populated control unit PCB, with key components labeled. ....	15
Figure 5. Electrical schematic of control unit. ....	16
Figure 6. Typical H-bridge schematic. Switches are labeled Q1 through Q4, clamping diodes are D1 through D4. ....	17
Figure 7. The logic gate signal conditioning stage. JK flip-flop, NAND gate, and NOT gates. Signals fed into the IRAMX20UP60A are labeled NAND_2, NAND_3, NOT_2, and NOT_3.....	20
Figure 8. OMF logic gate stage visualized. A) The OMF H-bridge with the NAND and NOT outputs connections. B) The pulse waveforms at NAND and NOT outputs, green indicates off state, blue indicates on state. C) The switching action due to NAND and NOT gate pulses visualized, the resulting current path is indicated in orange, green circles indicate on switches, and red x-marks indicate off switches. ....	21
Figure 9. Circuit schematic of bias voltage selection used for OMF H-bridge positive power rail. ....	22
Figure 10. Waveform across shunt resistor induced by current flow through a London broil beef sample placed within the supercooling sample chamber. ....	25
Figure 11. Voltage drop waveform across shunt resistor induced by current flow through OMF electromagnets. ....	26
Figure 12. Current measurement points within OMF system. ....	27
Figure 13. Simplified Schematic of the current measurement system for OMF and PEF systems. PEF is on the bottom with a single LT1999, and OMF on top. ....	29
Figure 14. Thermocouple basic circuit. ....	31
Figure 15. Thermocouple system stages. The three main stages are contained within an isothermal block to maintain thermal uniformity. ....	34
Figure 16. Filtering circuit schematic. Tags DA and DB denote entry of thermocouple signal from the switching stage. AIN0/REFP1 and AIN1 is the filter circuit’s connection to analog to digital conversion stage. ....	35
Figure 17. Selected UI interface pages created within the 4d-Workshop-4 IDE using the built in ViSi-Genie tool. ....	38
Figure 18. Control unit PCB, Green boxes indicate analog signal planes and the orange region the digital signal planes, pink circles point out the signal bridges across the thermocouple ground planes and bulk ground plane of PCB. Blue box is the OMF system designed to meet safety clearance standards as recommended by IEC/UL 61010. ....	39
Figure 19. 3D rendering of control unit in exploded view. ....	40
Figure 20. Control unit fully assembled. In the image above the unit is operating in USB data logging mode. ....	41
Figure 21. Pseudo code of thermocouple measurement system. ....	44

Figure 22. Pseudo code of PEF current measurement protocol. Determining $V_{rms}$ and $I_{rms}$ is done externally to CU with MatLab 2015a with raw data stored on SD card. ....	46
Figure 23. SRdata Global control variable displayed and initialized to zero, the corresponding bits and their associated relevance to IC packages can be seen. Each IC package controlled by SRdata has their corresponding truth tables which characterize their bit switching functionality. ....	48
Figure 24. Simplified control unit board program routine. When under the LabView option the control unit board will operate based on commands from LabView. ....	49
Figure 25. Thermocouple comparison calibration technique, experimental diagram .....	52
Figure 26. Error of CU, when compared with ITS-90 T-type thermocouple reference data .....	53
Figure 27. Residual plot of 2 <sup>nd</sup> order polynomial used to convert measured emf into degree Celsius. ....	54
Figure 28. Box plots of emf bias across multiplexer and filtering stages of thermocouple circuit. ....	55
Figure 29. CU Thermocouple linear fit calibration model. Red dotted lines indicated 95% confidence interval. ....	56
Figure 30. Error measured by CU over temperature ranges. Blue line indicates error in measurements prior to calibration. Red line is error with calibration applied to the pre-calibration data. ....	57
Figure 31. RTD preliminary verification, experimental setup. ....	58
Figure 32. Infrared image of CU board under operation with OMF at 60V and PEF at 6V. ....	59
Figure 33. Error of CJC system. The curve shown represents the difference magnitude of error in degree Celsius between DAQ measured ice bath temperature vs. CU measured ice bath temperature. ....	59
Figure 34. RTD CJC offset/bias data fitted with a 4 <sup>th</sup> order polynomial. ....	60
Figure 35. Error magnitude of CU measurement vs. Ice bath temperature measurements after calibration Equation (4.4) is applied to pre-calibrated data. The orange spline visually shows the error associated with pre-calibrated data, and the purple spline the error after correction. ....	61
Figure 36. Total uncertainty associated with reference probe measurement. ....	62
Figure 37. $V_{pp}$ noise ADS1220 input terminal. ....	63
Figure 38. Uncertainties accounted for in emf measurement system. ....	64
Figure 39. Uncertainties associated with the RTD CJC system. ....	65
Figure 40. OMF waveform reconstructed from CU raw data at 10Hz, 70V sample chamber load. ....	67
Figure 41. OMF current measurement system LT1999 noise spread. ....	68
Figure 42. OMF current measurement summary. Difference magnitude of current measurements between DAQ and CU. ....	69
Figure 43. OMF offset correction curve. ....	70
Figure 44. PEF current measurements across 100Hz to 20kHz. ....	71
Figure 45. PEF waveform reconstructed from CU data at 20kHz, 10.4V with resistive dummy load .....	71
Figure 46. Difference magnitude of PEF measurements between DAQ and CU. ....	72
Figure 47. PEF current measurement system LT1999 noise spread. ....	73
Figure 48. PEF offset correction curve. ....	74
Figure 49. Total uncertainties associated with current measurement reference data collection equipment. ....	75
Figure 50. Uncertainties accounted for within the OMF current measurement system. ....	76
Figure 51. Uncertainties accounted for within the PEF current measurement system. ....	77
Figure 52. OMF voltage validation data, x-axis is the reference data collected from DAQ and y-axis the OMF voltage collected and logged by CU. ....	78

Figure 53. Measurement difference between DAQ measured OMF voltage and CU measured OMF voltage.....	79
Figure 54. PEF voltage validation data, x-axis is the reference data collected from DAQ and y-axis the PEF voltage collected and logged by CU .....	80
Figure 55. Measurement difference between DAQ measured PEF voltage and CU measured PEF voltage. ....	80
Figure 56. Total uncertainty associated with reference equipment and data of the voltage system.....	81
Figure 57. OMF and PEF uncertainties accounted for with voltage measurement system. ....	82
Figure 58. The complete Supercooling system, with 1. Power supply, 2. Control unit, and 3. The Sample chamber. ....	86
Figure 59. Temperature profile of seven-day supercooled London broil beef with OMF and PEF treatment. ....	89
Figure 60. Drip loss across three trials. ....	91
Figure 61. Texture Analysis summary across three trials .....	92
Figure 62. Digital color analysis summary. ....	93
Figure 63. Sample digital images used during color analysis, taken from trial 3 of color analysis.....	94
Figure 64. pH measurements across three trials. ....	95

## LIST OF ABBREVIATION AND SYMBOLS

### Standard Agencies

ASTM	American Society for Testing and Materials
IEC	International Electrotechnical Commission
ANSI	American National Standards Institute
NCSL	National Conference of Standards Laboratories
ISO	International Organization for Standardization
NIST	National Institute of Standards and Technology

### Abbreviations

Listed in order of appearance.

CNT	Classical Nucleation Theory
HNT	Homogenous Nucleation Temperature
HFT	Heterogeneous Nucleation Temperature
ATLA	Automatic Lag Time Apparatus
ISP	Ice Structuring Proteins
CA	Cryoprotectant Agents
INP	Ice Nucleation Proteins
HPF	High Pressure assisted Freezing
PSF	High pressure Shift assisted Freezing
RF	Radio Frequency
MF	Magnetic Field
EF	Electric Field
OMF	Oscillating Magnetic Field
PEF	Pulsating Electric Field
DAQ	Data Acquisition
CU	Control Unit
UI	User Interface
IDE	Integrated Development Environment
MOSFET	Metal Oxide Field Effect Transistor
BJT	Bipolar Junction Transistor
IGBT	Insulated Gate Bipolar Transistor
TTL	Transistor-Transistor Logic
MCU	Microcontroller Unit
WSON	Very Very Thin Small Outline No Lead Package
RMS	Root Mean Square
ADC	Analog to Digital Converter
I <sup>2</sup> C	Inter-integrated Circuit
SPI	Serial Peripheral Interface Bus
FSR	Full Scale Range
emf	electro-motive force
CJC	Cold Junction Compensation
RTD	Resistance Temperature Detector
SLE	Special Limits of Error

TSV	Transient-voltage Suppression diode
IDAC	Current Digital to Analog Converter
UART	Universal Asynchronous Receiver-transmitter
PCB	Printed Circuit Board
CAD	Computer Aided Design
CTI	Comparative Tracking Index
LSB	Least Significant Bit
SRAM	Static Random-Access Memory
CS	Chip Select
NMR	Normal Mode Rejection
CMRR	Common Mode Rejection Ratio
CIE-L*a*b	Commission Internationale de l'éclairage color space

## Symbols

Listed in order of appearance.

$V_{gs}$	Gate to source voltage
$J$	Current density
$\sigma$	Conductivity
$E$	Electric field
$v$	Velocity of charge
$B$	Magnetic flux density
$I$	Current
$V$	Voltage
$R_i$	Resistance
$P$	Power
$T$	Time
$t_0$	Initial time
$V_{RMS}$	Root mean squared voltage
$V_{pk}$	Peak voltage
$D$	Duty cycle
$f_s$	Sampling frequency
$f_c$	Signal frequency
$R_i$	Resistor resistance, subscript $i$ denotes resistor identification
$V_{in}$	Input voltage
$V_{out}$	Output voltage
$S_{AB}, S_A, S_B$	Average Seebeck coefficient of material A and B, and individual Seebeck coefficient of material A and B
$T_1, T_2$	Temperature at point 1 and point 2
$E_{emf}$	Thermocouple emf
$t_{90}$	Reference temperature derived from ITS-90 data
$C_i$	Empirical coefficients derived from ITS-90 data
$A, B, C$ $\alpha, \delta, \beta$	Callendar-VanDusen coefficients
$R_{100}, R_0, R_T$	RTD resistances at 100°C and 0°C and temperature $T$
$C_{Diff}, C_{CM}$	Differential-mode capacitor capacitance, common-mode capacitor capacitance

$V_n$	Thermal resistor noise rms
$\Delta f$	Spectral noise density
$T$	Absolute temperature
$\omega$	Angular frequency
$\ddot{A}$	Transformation function, cut off frequency
$k$	Boltzmann constant
AVSS	Power supply voltage
AVDD	Power supply ground
G	Gain
$V_{ref}$	Reference voltage
$T_{RTD}$	Temperature transduced by RTD sensor
$R_{RTD}$	RTD resistance at $T_{RTD}$
$emf_{CJC}$	emf induced by $T_{RTD}$ into thermocouple measurements at junction 2 Figure 14
$T_{thermo}$	Thermocouple measured temperature
$x$	CU measured CJC voltage, CU measured temperature, CU measured PEF/OMF current
$OMF_{freq}$	OMF frequency
$PEF_{freq}$	PEF frequency
$N_{df}$	Degrees of freedom
$E_i, E_{fit}$	thermocouple emf and emf fitted to ITS-90 data
$U_A, U_B, U$	Total Uncertainty of type-A errors, type-B errors, and overall total uncertainty
K	Convergence factor
$emf_c$	Thermocouple bias correction emf
$T_c$	CJC temperature correction
$y$	OMF/PEF offset correction
CF	Crest Factor
$\Delta E$	Color change
$L_i, a_i, b_i$	CIE-L*a*b values, subscripts denote before and after

## CHAPTER 1. INTRODUCTION

### 1.1 Freezing

A phase transition in a sample occurs due to the development of a supersaturated state which develops through changes in chemistry, pressure, temperature, and other physical conditions such as electromagnetic fields or acoustic waves [1], [2], [3]. Freezing is an example of a phase transition from liquid to solid due to changes in temperature. The transition associated with the mother phase during freezing can occur in two ways, heterogeneously in which impurities, seeds, ions, dust or other solutes in the mother phase provide regions of stability for cluster formation and growth. Or homogeneously in which clusters of a new phase form spontaneously and grow evenly throughout the mother phase [4].

Cluster formation and its study can be categorized as nucleation theory which first began when Fahrenheit studied freezing of water to develop his temperature scale [5]. Advances in the field have led to the widely used classical nucleation theory (CNT) developed by Becker and Döring, Band, and Frenkel [6], [7], [8]. The theory attempts to describe the freezing process in terms of a freezing rate [ $\text{m}^{-3}\text{s}^{-1}$ ] via thermodynamic and kinematic components of a sample (e.g., water). The freezing rate given by CNT can be better understood as the rate of cluster formation in a known volume of sample leading to complete phase change. The use of CNT has been limited to simple systems with well-defined thermodynamic and kinematic components, uncertainties associated with these parameters can lead to large uncertainties in freezing rate estimated by CNT. For example Ickes et al. has shown a minor difference of 0.5% within thermodynamic parameter led to a 94% uncertainty in freezing rate given by CNT [9]. In addition, CNT fails to account for other factors which influences freezing such as interaction potentials, solvent/impurities influences, and mechanisms of nucleation. Thus, to better understand the freezing process, alternative nucleation theories such as dynamical nucleation theory, diffuse interface theory, and density functional theory have been developed, however CNT remains the most popular model used in nucleation related research despite its limitation.

Most fundamental research associated with freezing has focused upon homogenous nucleation, in practice achieving homogenous nucleation is very difficult. Often this type of cluster formation requires a highly-supersaturated state within the test sample. For example liquid water's homogenous nucleation temperature (the temperature required to induce homogenous nucleation, HNT) for freezing is roughly  $-39^{\circ}\text{C}$  [4], with tendency to be slightly volume dependent. Under laboratory conditions homogenous nucleation can be observed with ultra-pure samples of water within the micro-liter to pico-

liter range. Hence its widely believed most if not all types of nucleation encountered in the laboratory or elsewhere is non-homogenous.

Heterogeneous freezing or practical freezing, has been hypothesized to occur in four separate ways: contact freezing [10], deposition freezing [11], condensation freezing [12] and immersion freezing [13]. Any four of these nucleation mechanisms in tandem with several environmental factors can promote or suppress cluster formation within a sample. This can be observed by studying the heterogeneous freezing temperature (the temperature required to induce heterogeneous freezing, HFT) which has been shown to be highly dependent upon the mechanism of freezing. Pruppacher and Klett have determined that the HFT associated with contact freezing to be higher than that of immersion freezing [14]. Furthermore, HFT has also been shown to be dependent upon volume size, sample purity, and vessel type [15], [16], [17]. Barlow and Haymet [18] explored HFT further with an automatic lag time apparatus (ATLA) with which repeated measurements of a single sample were taken to gauge changes in HFT. From 200 individual freezing cycles, they found a variance of 0.7°C in HFT. In addition, CNT prediction in comparison with ATLA samples spiked with freezing catalysts showed orders of magnitude difference in results. Nucleation remains an enigmatic phenomenon due to the stochastic nature of cluster formation, predicting such events is perhaps impossible, however there is evidence some influence can be exhibited onto the freezing process.

### **1.1.1 Freezing in the Food Industry**

Freezing is one of the most widely used food preservation techniques in the commercial and domestic markets thanks to its simplicity and ability to preserve a wide variety of foods. The freezing process involves the lowering of food temperatures to or below -18°C [19], during which foods will experience a change in their physical state when ice nucleation occurs. Within these cold conditions biological and chemical reactions attributed to food spoilage are reduced allowing for an upwards of a 12-month preservation period depending on food item [20]. However, unavoidable degradation in food quality will occur during the freezing process. This degradation is attributed to ice formation within foods as liquid water undergoes a phase change to solid ice [21], [22]. The degree of damage associated with the phase change process is often attributed to the rate of freezing, it has been demonstrated faster freezing rates produce smaller and more evenly distributed ice crystals [23].

The global frozen food market in the year 2015 has exceeded 250 billion USD, within the USA the market is estimated to be 51.97 billion USD, with the bulk of its value concentrated in the ready-to-eat frozen foods sector, followed by frozen meats and frozen fruits and vegetables [24], [25]. Growth

within the American market is estimated to reach 72.98 billion USD by 2024. Various social and economic factors have been attributed to this future trend, and as a result much of the advancement in freezing technology has focused on improvements to freezing rate and cost reduction to meet the changing global landscape [20]. In today's world, freezing is the only large scale food preservation technique capable of dampening variations in seasonal foods, consumer demand, supply, and provide a means of safe mass transport of bulk foods across large distances [26], [27], [28].

The freezing process associated with foods follows five basic steps (Figure 1), first an initial cooling period occurs, followed by a supercooled stage, which can potentially be sustained under certain circumstance. During this meta-stable period prior to ice nucleation, free water within the food matrix exists in a supersaturated state. However, inadvertently ice nucleation occurs, resulting in a release of latent heat which raises the internal food temperature to its freezing temperature [26]. Ice crystal growth and its associated size will mainly be determined in this stage, as the rate of latent heat removal becomes the critical factor in achieving small and uniform ice crystal sizes [29]. Pure water undergoing the freezing process seen in Figure 1 would reveal a freezing point of 0°C: in comparison foods can exist as a solid or liquid with mixtures of various solutes which can result in slightly different freezing temperatures amongst the same food types. Furthermore, within foods slight temperature gradients have been observed due to the differences in solute concentration, and free water throughout their matrix [28]. However, no matter the type of food or the methods/technology used to achieve freezing, all food products follow a similar freezing process of Figure 1. The quality of the end food product will be dependent upon the efficiency of freezing process and physical factors of the food being frozen (i.e.,

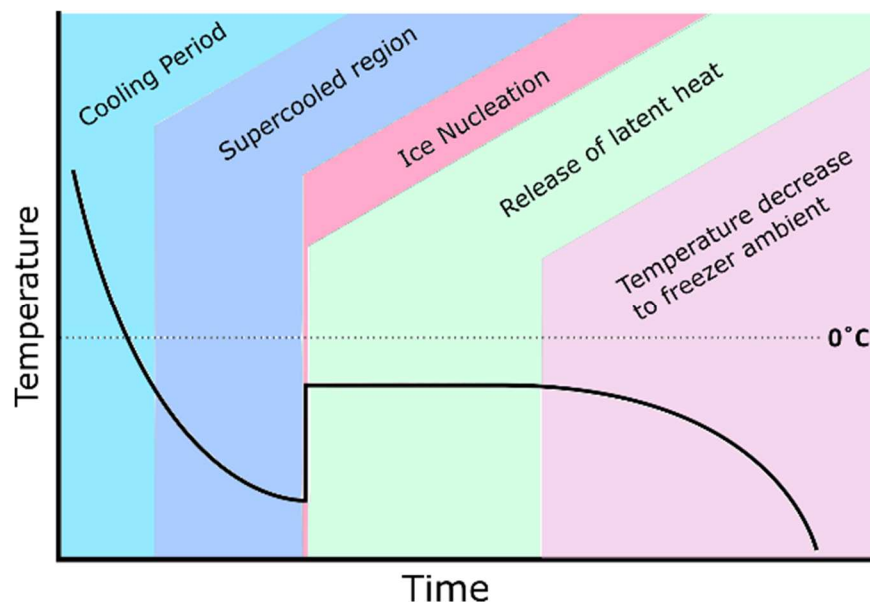


Figure 1. A typical temperature time curve of food placed within a freezer.

thermal conductivity, dimension/shape of food, surface heat transfer coefficient, etc.). Thus, selection of the proper freezing technology for foods becomes critical in minimizing ice damage and maintaining quality.

### **1.1.2 Current Freezing Technologies in the Food Industry**

The most commonly used freezing technology in the food industry today are air blast, contact plate, immersion, and cryogenic methods [26]. Air Blast is by far the oldest and most widely used technology, it is simple and cost-effective however the time to freeze and freezing rate are the worst when in comparison with other conventional technologies. The principles behind its operation are based upon force air convection making it suitable for freezing irregularly shaped foods such as fruits and vegetables. But its major drawback comes from the limitations associated with cold air distribution, convection rate, and air velocity [30]. Several variants of air blast technology exist such as belt freezers and fluidized bed freezers which are more specialized for certain food type or continuous inline production.

Contact plate technologies use cold metallic contact plates containing refrigerant to increase freezing rates of foods. During this process, pressure is applied to the food by the contact plates from opposing ends. The high thermal conductivity of the metal plates allow for a higher freezing rate and shorter freezing times, but the technology is only suitable for foods which exhibit regular shapes such as hamburger patties or fish fillet [31].

Immersion freezing technology uses a liquid medium, usually glycerol, glycol, sodium chloride, calcium chloride, or some derivative of a salt or sugar mixture in which the foods to be frozen are immersed. The higher heat conducting properties of liquids vs. air makes this an effective method in decreasing freezing time, but the major drawback to immersion is the possibility of transferring solutes of the immersion fluid to the food. Often flexible membranes are used to shield the food products from direct contact with the fluid medium and if full immersion is not desired the fluid can be applied in aerosolized form [26].

Cryogenic freezing technology applies cooling refrigerant directly onto the food, this is done in three major ways: (i) vaporization of the refrigerant to be blown over foods, (ii) foods are immersed into the refrigerant, (iii) or the refrigerant is sprayed directly onto the food. Method (iii) is the most commonly used technique, the refrigerants used within food applications are liquid nitrogen or carbon dioxide. Due to the high heat transfer rates and very low freezing temperature associated with

refrigerants the process is very efficient. But high costs of refrigerants has limited the application of this technology to premium products [26].

### **1.1.3 Emerging Freezing Technologies in the Food Industry**

Emerging food freezing technologies can be broken down into three major categories: (i) improving existing food technologies to further increase freezing rates, (ii) alteration of food properties before freezing, and (iii) attempting direct control over ice formation and suppression [32]. A recent example of an improvement made upon an existing technology is impingement freezing, this new technique has shown freezing time reductions of up to 79% over traditional blast freezers [33]. As a result, impingement has seen quick adoption by industry.

Food additives for the purpose of altering freezing characteristics first became popular with the discovery of ice structuring proteins (ISP), which can be found in many cold environment organisms [32], [34], [35]. Studies have shown ISP proteins act to restructure the shape, size and aggregation of ice crystals during the freezing process. In addition to ISPs other classes of proteins known as cryoprotectant agents (CA) and ice nucleation proteins (INP) act to protect cell structures from ice damage or induce ice nucleation. INPs have not been commercially adopted but CAs have been used widely throughout history and come in many forms such as amino acids, sugars, inorganic salts and carbohydrates [36].

An interesting development in freezing technology research has been a shift from optimizing the freezing process to attempting direct control over ice nucleation. Several methods are currently under investigation which all aim to either inhibit, induce or control ice formation within foods. And perhaps the most widely researched technology in this new field is pressure assisted freezing, which can be broken down into two categories high pressure assisted freezing (HPF), and high-pressure shift assisted freezing (PSF). The working principle behind HPF is to increase density of ice by the application of high pressures (up to 300MPa) during the entirety of a freezing process [37]. By doing so different forms of ice with densities higher than that of liquid water can be created, in such states ice exists in a non-crystalline structure which has been theorized to reduce tissue damage in foods. PSF on the other hand is a more economical alternative to HPF as the high-pressure conditions only exist partially during the freezing process. When the food samples have reached a desired sub-zero temperature a sudden release in pressure induces homogenous-like ice nucleation throughout the food resulting in evenly distributed small ice crystal [32]. PSF in particular has been demonstrated to inactivate various microorganisms at 207MPa in smoked salmon mince [38], but even with added benefits, pressure assisted

freezing remains within the realm of research due to the high capital costs associated with high pressure treatments.

Ultrasound technologies have been used in the food industry for sterilization and enzyme inactivation, but more recently its application into freezing has been investigated [39], [32]. Power ultrasound or low frequency ultrasound has been found to induce freezing by creating cavitation bubbles within food samples [40]. Most investigations into ultrasound technology have been in application with immersion type freezers as the liquid medium involved with such systems allows for more effective ultrasound treatment of food samples. In addition, ultrasound has also been theorized to break apart large ice crystals and enhance mass and heat transfer due to micro-streaming effects [39]. But many factors have been shown to affect the application of ultrasound assisted freezing, making it difficult to optimize the process for a wide variety of foods. Kiani et al. [41] has shown flow rates, sample position, cooling medium, ultrasound frequency and power have direct relations with cavitation bubble population and streaming.

Electromagnetic assisted freezing encompasses a field of research which has investigated the possible influences electric fields, magnetic fields, radio frequency and microwave frequencies impart onto the freezing process. In particular, the interaction between water and electromagnetic forces have been the primary focus in such investigations. Microwaves operating at frequencies of 2.45GHz are used within the food industry and domestically to heat foods, it is well known that interactions between microwaves and water molecules induce a dipole rotation at the atomic level, which in turn generates heat by collisions with other water molecules. This same concept has been applied during the freezing process to investigate its effects upon ice cluster formation at sub-zero temperatures. Early studies have shown a 92% reduction in the degree of supercooling with a 62% reduction in ice crystal size. A rather counter-intuitive outcome considering a reduced degree of supercooling is often associated with larger ice crystals [42], [43].

Microwave frequencies are small portion of the radio frequency spectrum, and any application of such radiation outside of the strictly defined microwave frequency range can be considered radio frequencies application (RF). Radio frequencies work in the same theorized manner as microwave frequencies in that interaction with water molecules at the atomic level can influence ice nucleation. The freezing of pork loin with RF treatment has shown reduced ice crystal size [42], the authors of the study postulate the heating effects of RF application are responsible for prolonging the rapid surface freezing of their foods during cryogenic treatment, which prevented large fracturing in their samples.

Both microwave and radio frequency assisted freezing are new fields of research and little published data is available for examination.

Magnetic fields (MF) and electric field (EF) application during the food freezing process has seen growing interest in recent years. Static and time varying applications have been studied with various food types, giving mixed results. For example the application of an oscillating magnetic field (OMF) at intensities of 0.5 to 0.7mT at 50Hz during the freezing process of various foods has reportedly shown advantageous results over traditional freezing [44]. A separate study showcasing OMF application of 200 to 300mT at 60 to 100Hz in combination with a dehumidifying device maintained fresh like qualities in test food samples [45]. However, these studies were funded with commercial interests and are in sharp contrast with results presented in peer-reviewed research papers. When comparing food quality factors between MF treated foods with non-MF treated foods, Suzuki [46] and Watanabe [47] found no difference in results between treatments with and without the application of 0.5mT MF at 50Hz. James et al. [32], [48] has also shown no measurable differences between treated and un-treated MF samples using a commercial freezing systems with built-in MF technology. Static MF applications with foods have not been widely investigated and only a single study with carp has been published, in which no significant effect of static MF treatment was observed [49].

EF treatment studies have shown more measurable effects on food during freezing when in comparison to MF studies. A static EF treatment on pork samples during the freezing process has shown smaller ice crystal formations [50], indicating a desirable positive effect for EF treatment during freezing. Pulsed electric field (PEF) treatments have been theorized to increase membrane permeability within foods, leading to an increased accessibility to intracellular materials, cutting down on freezing times [51], [52]. This reduction in freezing was observed during PEF treatment of potatoes, however a significant degradation in structural texture was also observed. PEF treatments prior to and during the freezing process have also been used to enhance the uptake of ISP, CA and INP agents as a combination technology [53].

The simultaneous application of MF and EF technology during the food freezing process has also been proposed, but investigations into the combination technology have been sparse. One study tied to a commercial enterprise has claimed the combined effects of MF and EF technology reduced freezing times within chicken and tuna by more than 50% [44], unfortunately these results have not been verified independently. Recent publications exploring the potential of the combined EF and MF technology has claimed in its ability to totally inhibit ice crystal nucleation by maintaining a supercooled state within food samples [54], [55], [56]. The authors of the study postulated a vibrational effect

produced by the combined MF and EF technology act upon free and bound water found within a food matrix, which ultimately prevented structured ice from propagating. The investigation into the exact mechanism and theory behind the prevention of ice nucleation has collectively been referenced as the study of supercooling.

## **1.2 Supercooling in Foods**

Supercooling when in relation to the study of foods is defined as the lowering of a food product temperature below its usual freezing point with no phase change event occurring (i.e., ice nucleation). Within food science the term supercooling has been interchangeably referred to as undercooled, subcooled, and freezing point depression [57]. A few examples of food products which have undergone supercooling studies include vegetables [48], [58], [59], [60], fish [61], [62], [63], fruits [59], and meat [64], [65]. These studies have shown the degree of supercooling is highly food specific, for example when varying the concentration of orange juice across 46° and 66° Brix, the degree of supercooling shifted 90% [65]. Foods which have achieved and maintained supercooled conditions have exhibited longer shelf life due to lower storage temperatures over traditional chilled storage temperature ranges [66]. In contrast, some studies have shown negative impacts on food samples during supercooled storage, Ando et al. [61], experienced decreased firmness of yellow tail mackerel when stored at a supercooled temperature of -1.5°C. Supercooling technology in its current state has not shown reliable operation, however as a mature technology, supercooling has the potential to improve the shelf life of various highly perishable foods. Stonehouse et al [57] is recommended for a more thorough review of supercooling within food applications.

### **1.2.1 Technology and Theory of Supercooling Research**

The direct prevention of ice nucleation within food items is a new field of research and as such topics on the matter detailing the technologies and methods involved are scarce. Most studies have focused on observing the natural supercooling phenomenon present within foods and determining which factors impact the degree and stability of supercooling the most. As a result, the most common approach to inducing and maintaining a supercooled state within foods has been strict temperature control, often achieved with commercial freezing equipment. Charoenrein et al. [67] used a cryogenic cabinet freezer (Minibatch 1000 L, Bangkok Industrial Gas Co., Bangkok, Thailand) with adjustable liquid nitrogen flow rate for strict control of internal freezer temperatures in the range of -80° to -20°C. The same researches also used a commercial chest freezer (SF-C1497, Sanyo, Osaka, Japan) to compare the

impact of slower cooling rates to supercooling stability of a starch gel food model. James et al. [60] used an unspecified commercial freezer with whole garlic bulbs placed within an insulated polystyrene vessel to prolong freezing rate and observe its impact upon supercooling. Later he varied the static air temperature using an experimental wind tunnel with whole garlic bulbs placed within polystyrene vessel. Fukuma et al. [63] achieved static temperature control with a lab incubator (NH-60S, Ninomiya Sangyo, Chiba, Japan), of which the temperature setting was gradually reduced over a course of several days to prevent ice nucleation from thermally induced shock. These studies focused on temperature control with a special emphasis on cooling rate as being the most important factors in supercooling of foods. Indicating no special technology is required in achieving and maintaining a supercooled state with the prior mentioned food items.

Studies focusing on a more fundamental approach to the supercooling enigma have attempted to address how static and time-varying uniform/non-uniform EF and MF interact with water. The basic conclusions of which indicate EF in the excess of  $10^9$  V/M is required to re-orient crystalline water to achieve inhibition of ice [1], with lower EF of  $10^5$  V/M inducing ice nucleation [68]. The former study used computer methods to derive its conclusion, and the latter used an unspecified high DC voltage generator with two parallel plate non-contact electrodes for EF experimentation. The proposed mechanism upon which EF influences water within these studies is to either weaken or strengthen hydrogen bonds depending on orientation, strength and frequency of the applied EF [1], [69], [70], [71]. Other studies involving water in direct contact with EF electrodes often resulted in electrolysis, where  $O_2$  is produced at the anode and  $H_2$  at the cathode [72]. However interestingly when using direct contact metallic electrodes, the positioning of water molecules and ions can be greatly affected at much smaller voltage levels when compared to non-contact EF. For example, a  $-0.23V_{DC}$  applied to electrode resulted on average, a reorientation of water molecules away from electrode with a structured interfacial water layer extending out  $15\text{\AA}$  [73]. Ions found within water during contact EF application are attracted or repelled depending on electrode polarity, and furthermore localized water orientation and structuring seen at the electrode surfaces has been reported to occur on surfaces of polar minerals. Within these studies electrode material were often specified and chosen to achieve the desired effect of rapid nucleation or prevention, electrode type ordered from highest probability of nucleation to least is  $Al = Cu > Ag > Au > Pt > C$  [74].

MF application for food freezing processes has been met with larger criticism vs EF application due to a contradicting data and low repeatability of the studies. Again, the predominant mechanism postulated by various authors for MF effects on water is the strengthening or weakening of hydrogen

bonds. Wang et al. [75] and Zhou et al. [76] theorize MF acts to weaken hydrogen bonds which ultimately affect water properties governing the freezing mechanism to prevent increased supercooling. Chang et al. [77] believes the opposite to be the case and MF fields act to strengthen hydrogen bonds within water to promote supercooling. Inaba et al. [78] demonstrated exposure of water to a 6T MF increased the freezing point of water by 0.0056°C, giving evidence to MF strengthening hydrogen bonding. Zhou [79] reported supercooling within water increased with a 5.95mT MF exposure. In contrast Aleksandrov et al. [80], Zhao et al. [81], and Otero et al. [82], [83] reported negative or no effects of MF on water supercooling with various MF strengths between 0mT to 505mT. The studies which focused on static MF application mainly used permanent neodymium magnets in various configurations and sizes to achieve a desired field strength and shape. In non-static MF studies, MF generation was most likely achieved with electromagnets, unfortunately information regarding coil characteristics are unspecified (i.e., coil turns, coil geometry, wire diameter, wire composition, voltage/current applied, core material).

### **1.3 Problem Statement and Project Scope**

Due to the nature of supercooling research significant time and resources are required to confirm a sample's supercooled stability, which can tie up valuable resources. Portability and size of such equipment also can be an issue as funding and industry interest drives the transition of the technology from the research realm to commercial. To accomplish this several engineering hurdles must be overcome to realize supercooling as a viable technology, thus development of a new platform is needed.

Current lab equipment used for supercooling studies consists of DAQ (34970A, Keysight, Santa Rosa, CA), used in tandem with lab grade function generators (33210A, Keysight, Santa Rosa, CA) and custom-built power supplies. Peripherals required for DAQ functionality include 16-channel switching module (34902A, Keysight, Santa Rosa, CA), differential voltage probes (PR-60, B&K Precision, Yorba Linda, CA), and current monitor transformer (Model 411/150, Pearson Electronics, Palo Alto, CA). Additional equipment needed include, a variac (SC-5M, PHC Enterprise Torrance, CA), oscilloscope (HMO1202, Rohde&Schwarz, Munich, Germany), isolation transformer (GRP-1200, Mean Well, New Taipei City, Taiwan), chest freezer (HF71CM33NM, Haier, Qingdao, China), and PC/Laptop capable of running MatLab (MathWorks, Natick, MA) and/or LabView (National Instruments Corporation, Austin, TX) [54], [56].

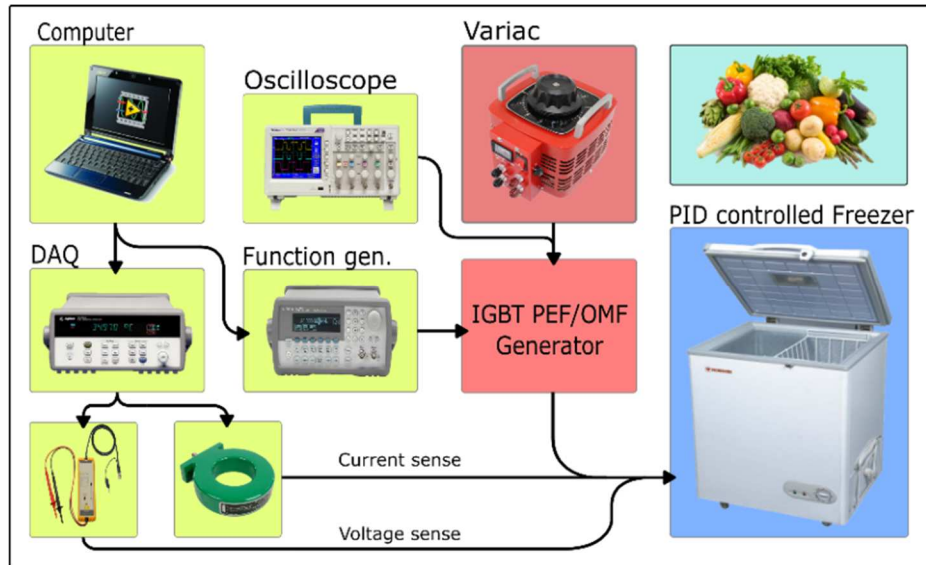


Figure 2. Typical experimental Setup of a supercooling experiment as described by Mok et al. [56], [54].

Table 1. Costs associated with a typical supercooling experimental equipment.

Equipment	Price	Quantity
KeySight 34970A	\$2,341.00*	1
KeySight 33210A	\$2,284.00*	1
KeySight 34902A	\$991.00*	1
Custom PSU	\$600.00	1
Pearson Current Monitor 411/150	\$625.00	2 <sup>‡</sup>
BK Precision PR-60	\$389.00	2 <sup>‡</sup>
PHC Enterprise SC-5M	\$52.27	2 <sup>‡</sup>
Rohde&Schwarz HMO1202	\$1,756.00	1
Mean Well GRP-1200	\$99.95	1
Haier HF71CM33NW	\$224.07	1
MathWorks <u>Matlab</u>	\$500.00	1
National Instruments LabView	\$399.00**	1
<b>Total</b>	<b>\$11,327.56</b>	<b>15</b>

\*Calibration and Uncertainty package included in price

\*\*Yearly subscription based pricing

<sup>‡</sup> two required for OMF and PEF system

The initial investment on equipment for a single supercooling experiment roughly totals \$11,327 USD, to observe data generation and progress at a reasonable rate a minimum of three complete sets are recommended. However even with this number, progress will be limited, and equipment costs will continue to be a major bottleneck.

The overall goal of this project is to create a cheap, portable, and easily reproducible custom control unit (CU) for use in supercooling experimentation related to food preservation. Specific objectives to meet this goal include:

1. Integration of data logging capabilities to track current/voltage of OMF and PEF systems, and temperatures of ambient conditions/samples during supercooling experiments.
2. Incorporate simple regulations and controls based upon logged data and sensor readings for adjustments of power delivered to OMF/PEF systems during experimentation.
3. Characterize operational conditions to ensure reliable operation of the control unit.

The successful execution of a newly designed control unit would allow for reduced costs, increased portability, productivity and quicker generation of data.

## CHAPTER 2. HARDWARE AND DESIGN

### 2.1 Design Overview

A custom prototype CU was developed for use in supercooling experimentation, modularity of the design allows for use of various power supplies at inputs of OMF and PEF power. Output power delivered to an external sample chamber housing OMF and PEF generation components is accomplished with H-bridge circuitry. The OMF system is based upon a smart power module (IRAMX20UP60A, Infineon Technologies, Neubibery, Germany) with active H-bridge protection, PEF systems utilizes a small package motor drive (DRV8839, Texas Instruments, Dallas, TX) with built in over current, and H-bridge protection. The H-bridge architectures used within the custom circuitry design allows for easy biphasic waveform generation to accomplish electric/magnetic field reversal at various desired frequencies and duties.

Data captured within on CU includes current/voltages for both OMF/ PEF system, and temperature measurements based upon thermocouples technology. Current/voltage measurement data is used to monitor and control power delivery to the external sample chamber. The data collected can either be logged onto an onboard miniSD™ card or transferred through USB serial interface to PC/Laptop. A user chooses the mode of operation through touch screen UI (ULCD-32PTU-AR, 4DSystems, Michinbury, Australia). When miniSD™ logging is enabled the CU is capable of self-contained operation, under USB logging a third-party serial monitoring program is required to capture data at USB port. All data logging, sensor interfacing, and OMF/PEF control is accomplished with a simple 8-bit microcontroller (ATMEGA328P-MUR, Atmel Corp., San Jose, CA), programmed using the Arduino IDE Version 1.8.1 (Arduino, Torino, Italy). All power entries into the custom circuit are over voltage and reverse polarity protected, the thermocouple system was designed to meet IEC61000-4 standards for voltage transients, surges, and discharge.

Major components found on the control unit design are identified in Table 2. A simplified block diagram of the overall control unit design is in Figure 3. All design and component selection are based upon key design specifications identified through electrical measurements taken during supercooling experimentation, the key design specifications are summarized in Table 3. Electrical schematic and populated custom printed circuit board are shown in Figure 4 and 5.

Table 2. Key components found on the control unit

Component	Part Number	Purpose
OMF H-bridge	IRAMX20UP60A	OMF field generation
PEF H-bridge	DRV8839	PEF field generation
OMF bias voltage	TL783	OMF voltage level adjustment
PEF bias voltage	MC33269D	PEF voltage level adjustment
Small signal ADC	ADS1220	Temperature measurement
OMF current monitor	INA200	Over current protection
PEF current monitor	LT1999	OMF/PEF current measurement

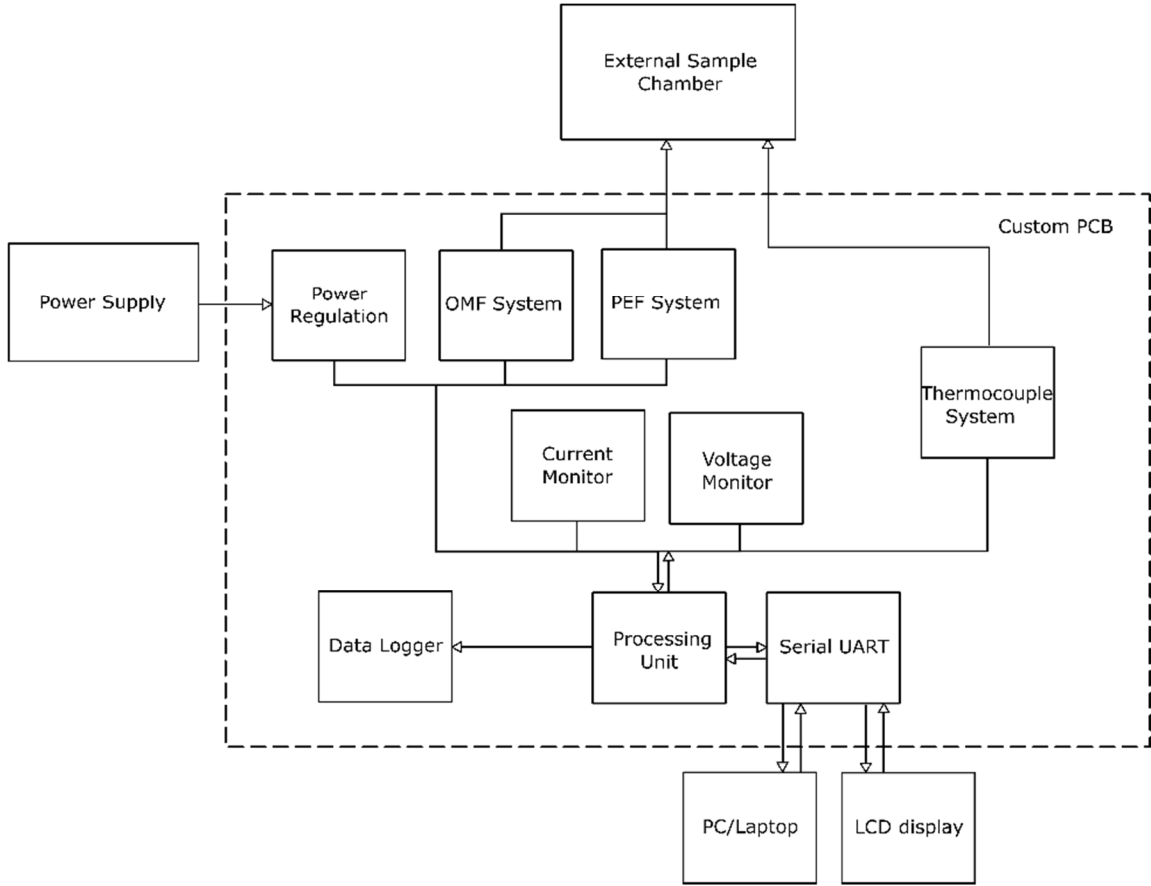


Figure 3. Simplified block diagram of the control unit's overall system design. PC/Laptop and LCD display are interfaced with MCU serial UART, communication between the two is toggled between a digital switch. The external sample chamber houses the OMF and PEF field generating electrodes and electromagnets.

Table 3. Key Design Specification for OMF and PEF systems

Key Design Specification	
OMF	PEF
Current range: 300mA – 4A	Current range: 10mA – 80mA
Voltage range: 5V – 70V	Voltage range: 0V – 10V
Signal Frequency: 1Hz – 10Hz	Signal Frequency: 50Hz – 12kHz
Duty range: 0 – 100%	Duty range: 0 – 100%

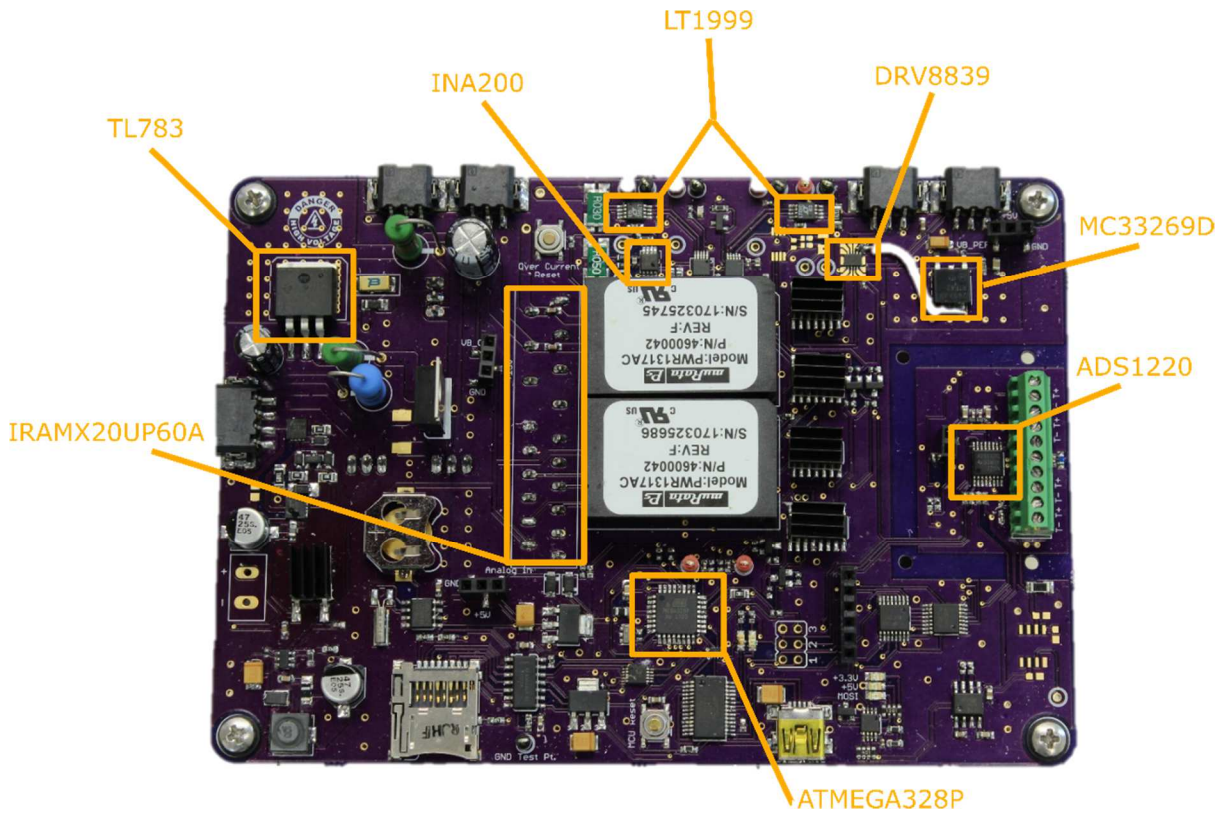


Figure 4. A populated control unit PCB, with key components labeled.

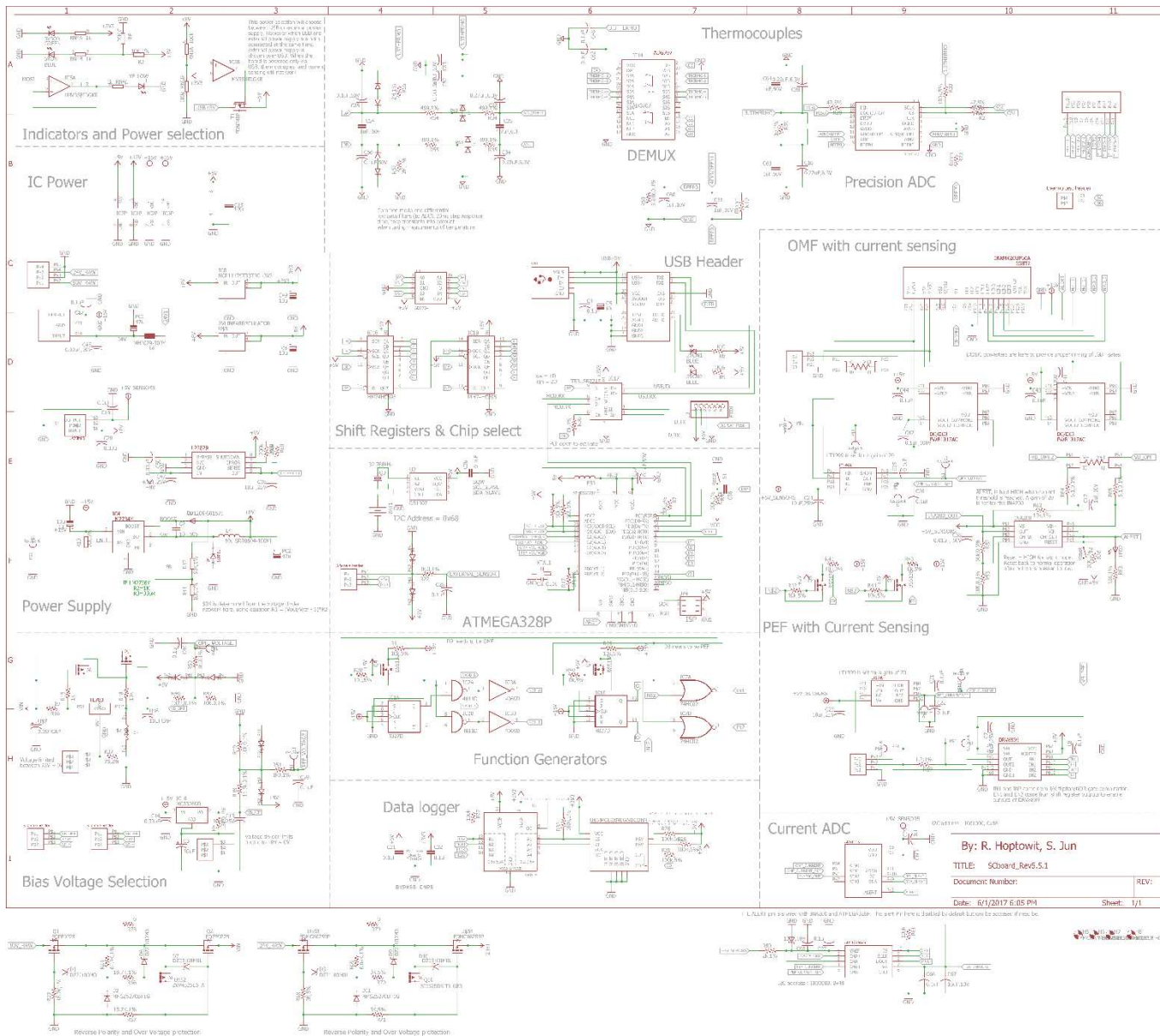


Figure 5. Electrical schematic of control unit.

## 2.2 Oscillating Magnetic Field Generation System (OMF)

### 2.2.1 H-Bridge

An H-bridge circuit consists of four switches, which are typically bipolar transistors or MOSFETs (metal-oxide-semiconductor field-effect transistor). The circuit's name is derived from the typical H like configuration of the switches when shown graphically in Figure 6, this type of circuit is often used to drive inductive loads such as motors and can be found ubiquitously throughout power electronic applications [84]. By opening and closing the four switches, flow of current can be controlled through a load depicted at the center of Figure 6, in a DC motor application this can result in a forward/reverse motion or with the use of PWM (pulse width modulation), speed control.

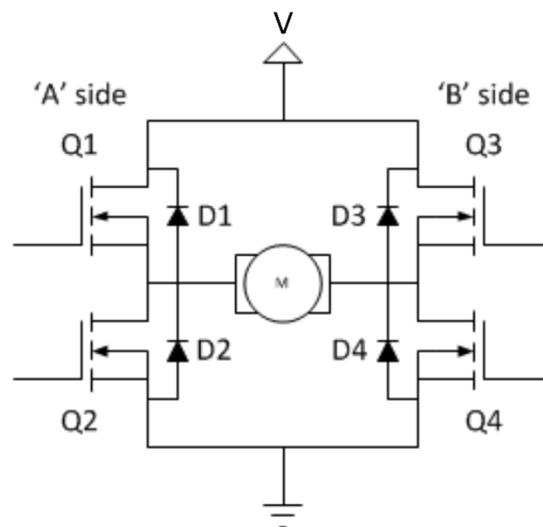


Figure 6. Typical H-bridge schematic. Switches are labeled Q1 through Q4, clamping diodes are D1 through D4.

During switching actions, the H-bridge can experience short-circuit conditions when both switches on the A or B side (Figure 6) of the H-bridge are on at the same time. Modern H-bridge IC (integrated circuits) packages often include built in fault detection to avoid such conditions and carefully designed H-bridge systems include periods between switching in which all switches are momentarily off. This extra measure is implemented as a safe guard against short circuit conditions, however during this momentary off state, an inductive load such as motors or electromagnets can develop large voltage spikes during a phenomenon known as inductive kick-back. Protection against these high voltage conditions are often provided by catch diodes placed across each individual switch. The diodes provide a path of current flow during the momentary off conditions in the switching process.

The core components within an H-bridge are the switches, which can be either mechanical in nature or a solid-state device, with prevalence more to the latter. Solid-state switches known broadly as transistors work by either limiting or promoting current flow through semi-conductor material. Older H-

bridge designs implemented P-channel MOSFETs or PNP BJTs (bipolar junction transistors) on the high side of the bridge with N-channel MOSFETs or NPN BJTs on the low side. The primary semiconductor material found within BJTs and MOSFETs known as N-type and P-type are created using silicon or germanium crystal lattice structures doped with impurities [85], [86], [87]. These impurities dictate characteristics regarding their electrical conductivity. Specific arrangement and doping concentrations of impurities allows for unique characteristics in specific types of transistors, choosing one type of transistor over the other will greatly affects H-bridge design. Most modern low voltage H-bridge designs use N-channel MOSFETs on both high and low side of the bridge to achieve higher efficiencies, as BJTs and P-channel MOSFETs typically have larger on resistances. However, when using N-channel MOSFETs exclusively, proper gate driving circuitry is required to ensure reliable switching of the N-channel MOSFETs during operation. The main complexity in a N-channel MOSFETs composed H-bridge design comes from the high side switches [88], [89]. N-channel MOSFETs have a minimum turn on voltage denoted as  $V_{GS}$  (voltage from the gate to source pins). In typical application, the N-channel MOSFET is often situated at the low side of a load with its source pin referenced to ground. Within a H-bridge the high side N-channel MOSFET's source pin will be referenced to the load, a small voltage drop may occur as current flows through the MOSFET, but the voltage experienced on the source pin will be very close to the voltage experienced on the drain pin. To properly turn on the high side MOSFET a voltage higher than the voltage on the drain pin by a magnitude of  $V_{GS}$  must be applied to the gate pin. Typical  $V_{GS}$  values of N-channel MOSFETs can range from 0.4V-15V, this makes the use of a floating voltage source a requirement to drive the high side N-channel MOSFETs.

Several methods exist which can be implemented to drive the high side MOSFETs as summarized in Table 4. Many IC packages exist which can drive single MOSFETs, half-bridge, full-bridge or even 3 phase systems. Whatever circuit design used for the floating voltage source the end requirement remains the same, to provide a floating voltage level capable of maintaining  $V_{GS}$  for the high side MOSFETs [90].

Table 4. Common high side MOSFET gate driving circuits. Reprinted from HV Floating MOS-Gate Driver ICs, Application Note AN-978 RevD, 2007. International Rectifiers, p. 29.

Method	Basic Circuit	Key Features
Floating Gate Drive Supply		<ul style="list-style-type: none"> <li>• Full gate control for indefinite periods of time</li> <li>• Cost impact of isolated supply is significant (one required for each high side MOSFET)</li> <li>• Level shifting a ground referenced signal can be tricky. Level shifter must sustain full voltage, switch first with minimal propagation delays and lower power consumption</li> <li>• Opto isolators tend to be relatively expensive, limited in bandwidth and noise sensitive</li> </ul>
Pulse Transformer		<ul style="list-style-type: none"> <li>• Simple and cost effective but limited in many respects</li> <li>• Operation over wide duty cycles requires complex techniques</li> <li>• Transformer size increases significantly as frequency decreases</li> <li>• Significant parasitics create less than ideal operation with fast switching waveforms</li> </ul>
Charge Pump		<ul style="list-style-type: none"> <li>• Can be used to generate an "over-rail" voltage controlled by a level shifter or to "pump" the gate when MOSFET is turned on</li> <li>• In the first case the problems of a level shifter have to be tackled</li> <li>• In the second case turn on times tend to be too long for switching applications</li> <li>• In either case, gate can be kept on for an indefinite period of time</li> <li>• In efficiencies in the voltage multiplication circuit may require more than two stages of pumping</li> </ul>
Bootstrap		<ul style="list-style-type: none"> <li>• Simple and inexpensive with some of the limitations of the pulse transformer: duty cycle and on-time are both constrained by the need to refresh the bootstrap capacitor</li> <li>• If the capacitor is charged from a high voltage rail, power dissipation can be significant</li> <li>• Requires level shifter with its associated difficulties</li> </ul>
Carrier Drive		<ul style="list-style-type: none"> <li>• Gives full gate control for an indefinite period of time but is somewhat limited in switching performance. This can be improved with added complexity</li> </ul>

In high voltage/current with low frequency applications, IGBTs (insulated gate bipolar transistor) are recommended over MOSFET within H-bridge designs. IGBTs combine the high current carrying capabilities of BJTs with the ease of implementation of MOSFETs at the cost of slower switching speeds [91], [92]. Selection between MOSFETs or IGBTs in a H-bridge design will be determined by the intended application of the H-bridge.

### 2.2.2 OMF H-Bridge Power Module Selection and Operation

H-bridge design, gate driving, and transient voltage protection are implemented within a single smart power module package chosen for the OMF system (IRAMX20UP60A). This hybrid IC allows for an overall simplified design with built in protection against fault conditions, transient voltages, internal thermal monitoring, and over-current protection capabilities. The manufacturer stated SiP2 package allows for heat isolation from sensitive components and minimizes overall IC footprint, saving valuable circuit board space.

The IRAMX20UP60A package implements a three-phase IGBT based bridge circuit controlled by internal driver IC. The three-phase bridge is configured to operate in an H-bridge configuration by inactivating one of the phase leg switches via driver IC input controls. The built in IGBT switches are rated to 20Amperes, 450V (catch diode rated 650V), at PWM carrier frequencies of up to 20kHz, these features ensure scalability for future applications of the control unit. Each IGBT switch can be controlled via input using common TTL (transistor-transistor logic) signals making MCU (microcontroller unit) based implementation simple. In addition, an  $I_{TRIP}$  pin is provided for high speed shutdown of the IRAMX20UP60A in the event of an over-current condition. A custom external high speed current monitoring circuit was designed to take advantage of this feature.

The IRAMX20UP60A provides internal boot-strap circuitry to drive the high side IGBTs, however an external boot-strap capacitor is required for proper operation. The capacitor chosen will be frequency dependent, as a result operation of the IC package will be limited to a certain bandwidth. To overcome this limitation an external DC-DC converter (PWR1317AC, muRata, Nahaokakyo, Japan) was used to act as a floating voltage source. In this manner, a +15V bias is provided to the high side IGBT gates at all times.

Biphasic wave form generation at H-bridge output is required during supercooling experimentation [54], to accomplish this a PWM signal generated by the MCU is fed into a logic gate signal conditioning circuit shown in Figure 7.

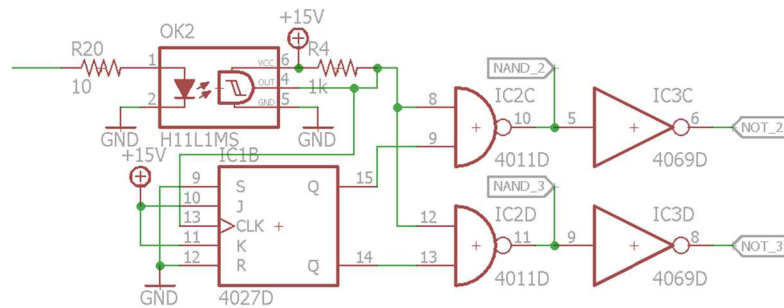


Figure 7. The logic gate signal conditioning stage. JK flip-flop, NAND gate, and NOT gates. Signals fed into the IRAMX20UP60A are labeled NAND\_2, NAND\_3, NOT\_2, and NOT\_3.

The conditioned signal is broken down into pulses which are then fed into their appropriate IGBT gate control pinouts on the IRAMX20UP60A. The logic gates involved within the OMF system include a JK flip-flop set to a toggle state under synchronous operation, in this mode the JK flip-flop driven by the PWM signal can respond instantaneously to changes in duty or frequency of the PWM signal. The toggling JK flip-flop's outputs are fed into a NAND gate then to NOT gates. The outputs of the NAND and NOT gates are used to control IGBT switching times, Figure 8 A) and B) shows the output pulses of the NAND and NOT logic gates and their associated connections the IRAMX20UP60A's H-bridge IGBT gates. Each stage numbered 1 through 7 in Figure 8 B) and C) indicate a H-bridge switching action, the opening and closing of each gate and how the action corresponds to the flow of current through the load is seen in C).

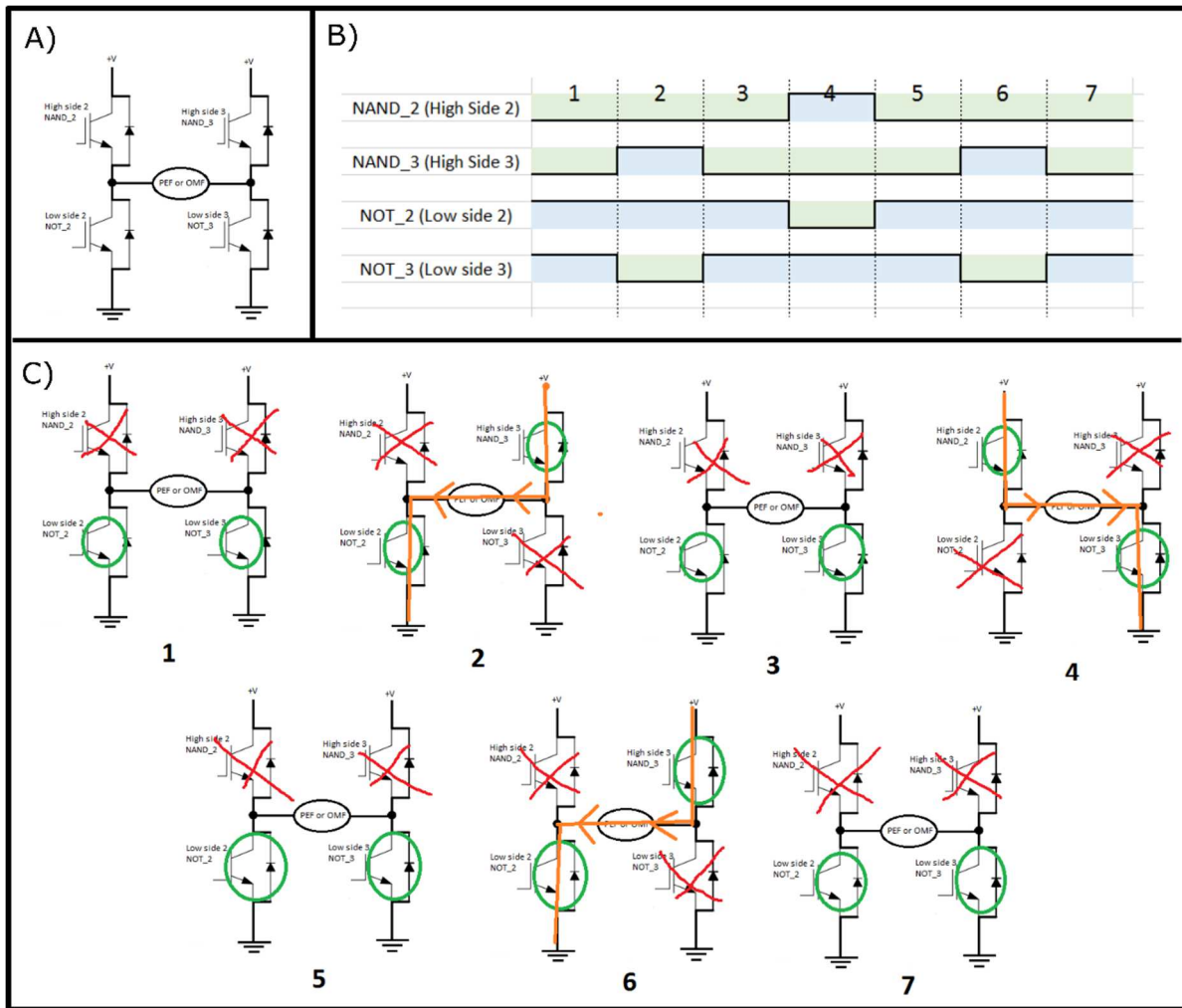


Figure 8. OMF logic gate stage visualized. A) The OMF H-bridge with the NAND and NOT outputs connections. B) The pulse waveforms at NAND and NOT outputs, green indicates off state, blue indicates on state. C) The switching action due to NAND and NOT gate pulses visualized, the resulting current path is indicated in orange, green circles indicate on switches, and red x-marks indicate off switches.

### 2.2.3 OMF Bias Voltage System

Bias voltage selection applied to the positive rail of the OMF H-bridge is accomplished with an adjustable linear voltage regulator (TL783, Texas Instruments, Dallas, TX). A reference voltage applied to the ADJ pin on the device allows for adjustment of voltage levels, this is accomplished with the use of a resistor and external rheostat configured as a simple voltage divider. The rheostat allows for adjustment in the range of 1.25V to 73V, current sourcing capabilities of the TL783 has been boosted with a current boost circuit. An NPN BJT (BUJ403A, WeEn Semiconductors, Shanghai, China) with gate driving via PNP BJT (TIP30C, Fairchild Semiconductors, Sunnyvale, CA) allows for a sustained current draw of 6Amperes.

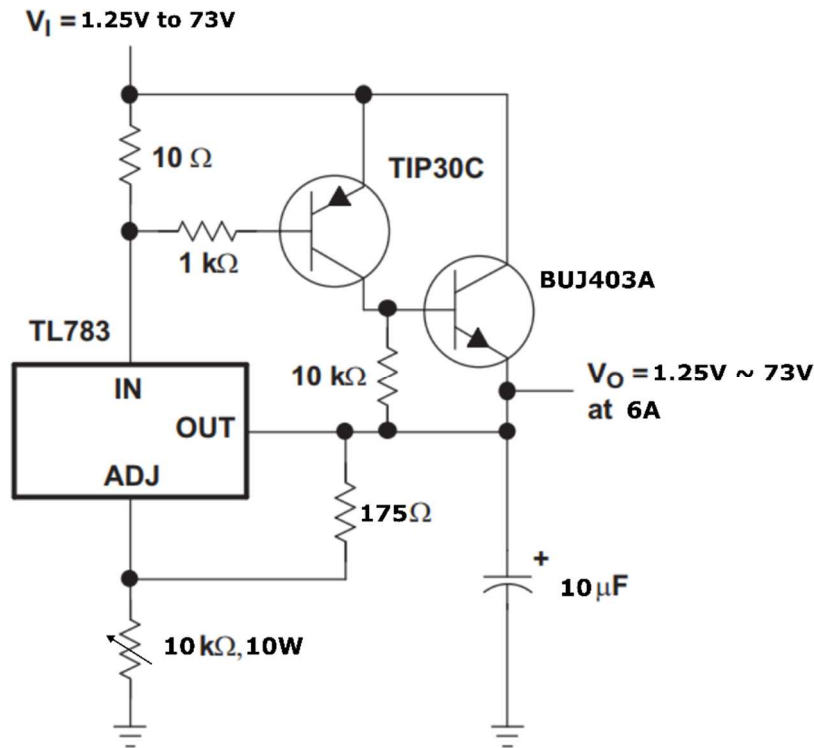


Figure 9. Circuit schematic of bias voltage selection used for OMF H-bridge positive power rail.

## 2.3 Pulsating Electric Field Generation System (PEF)

### 2.3.1 PEF H-Bridge Power Module Selection and Operation

The PEF system is based upon the same H-bridge circuit design however, the PEF system has considerably lower power requirements. Due to this factor, the topology of the design can be reduced, and a smaller smart power module H-bridge package was selected (DRV8839). Capable of driving a load up to 1.8Amps at 11V, the module can provide double the power required in current experimental protocols, allowing for headway in scalability. The 12 pin WSON package reduces the system footprint to an absolute minimum, all the while maintaining an impressive list of features built within. Internally built

functions protect against short-circuit, overcurrent and undervoltage lockout, and over temperature conditions. The difficulties associated with proper gate driving of H-bridges switches are handled internally with built-in charge pump circuitry. H-bridge switch control is accomplished through two user accessible inputs controlled by PWM. The two inputs control either side of the H-bridge allowing for full reversal of current based upon switching sequences seen at the inputs. The timing of the switching inputs is handled from a single PWM signal generated from the MCU and fed into a logic gate based signal conditioning stage. This signal conditioning stage splits the single PWM input via JK flip-flop in a synchronous toggle state, the split signal is then fed into a dual NOR gates. The outputs from the NOR gates act as the input signals used to drive the H-bridge switching within the DVR8839, in this manner the PEF system responds in real time to changes in PWM signal frequency and duty.

### 2.3.2 PEF Bias Voltage System

PEF bias voltage selection is provided by an adjustable linear voltage regulator (MC33269D, On semiconductor, Phoenix, AZ), the voltage is adjusted via rheostat placed on the load side of a voltage divider configuration. The attenuated output signal of the MC33269D is used as a feedback to regulate the voltage output of the device from 0V to 10.5V, at an 800mA total continuous current draw.

## 2.4 Current Sensing System

### 2.4.1 Shunt Resistor Based Current Measurement Model

Current measurements provide two essential purposes, to measure the amount of current passing through the system and to detect fault conditions when an excess of current is present. Shunt resistor based current measurements is the most versatile and widely used method in monitoring current. This is due to its simplicity, low cost, and its versatile applications involving DC and AC signals [93]. The relationship between voltage, current and resistance used with shunt based current measurements can be described with Lorentz law:

$$J = \sigma(E + v \times B) \quad (2.1)$$

Where J is the current density,  $\sigma$  is material conductivity, E is the electric field, v is the velocity of charge and B the magnetic flux density acting onto the charge. In most practical cases in which the compound object of interest is said to be in a rest frame, or if there is no magnetic field present [94], then the last term in Equation (2.1) is dropped and reduces to

$$J = \sigma E \quad (2.2)$$

Equation (2.2) is Ohm's law, which describes the proportionality of current and voltage across a resistance, Equation (2.2) can be reformulated to the more recognizable form

$$I = \frac{V}{R} \quad (2.3)$$

where V is the voltage drop across a resistor, I the current in Amperes and R the resistance in ohms. By placing a shunt resistor in series with a current flow a voltage drop will develop as according to Equation (2.3), the magnitude of the voltage drop will be the product of current and shunt resistance [94], [95], [96], [97].

However, due to nature of shunt resistors placement power losses associated with heat can play a major role in shunt resistor selection. Power losses associated with a shunt in a DC system is given by

$$P = RI^2 \quad (2.4)$$

where P is power in watts, R resistance in ohms and I current in amps. Examining equation (2.4) it becomes apparent that the reducing the ohms value of R is beneficial in minimizing heat losses. Within AC signal application, shunt resistors simplify voltage to current transduction because no phase shift is present between current and voltage [98], [99]. Thus, voltage drop measured across a shunt resistor are always proportional to the current no matter the load in series with the resistor. An AC signal's root mean squared (RMS) voltage across a shunt resistor is given by

$$V_{RMS} = \sqrt{\frac{1}{T} \int_{t_0}^{t_0+T} v^2(t) dt} \quad (2.5)$$

where  $1/T$  is the frequency of measured signal,  $t_0$  the initial measurement point, and  $v$  the instantaneous voltage. Given a complex waveform calculating  $V_{RMS}$  can be quite difficult, however if a waveform is known, Equation (2.5) can be simplified greatly. For example, within supercooling experimentation a biphasic square wave is applied to the PEF and OMF systems [54]. The RMS calculations within Equation (2.5) inverts all negative cycles in the biphasic wave form, which results in a square wave at a defined frequency and duty. Thus, the biphasic waveform of PEF and OMF systems can be treated as a square wave and Equation (2.5) simplifies to

$$V_{RMS} = V_{pk}\sqrt{D} \quad (2.6)$$

where  $V_p$  is the peak voltage of the square wave, and  $D$  the duty cycle [100]. However, the use of Equation (2.6) is limited, and can only be used to calculate  $V_{rms}$  when either the PEF or OMF system is driving a purely resistive load (i.e., capacitive and inductive loads will affect the shape and phase of the current wave form which is reflected in the waveform measured across a shunt resistor). Within the PEF system, foods tested prior by Mok et al. have all shown purely resistive behavior across the operational PEF frequency ranges (Figure 10).

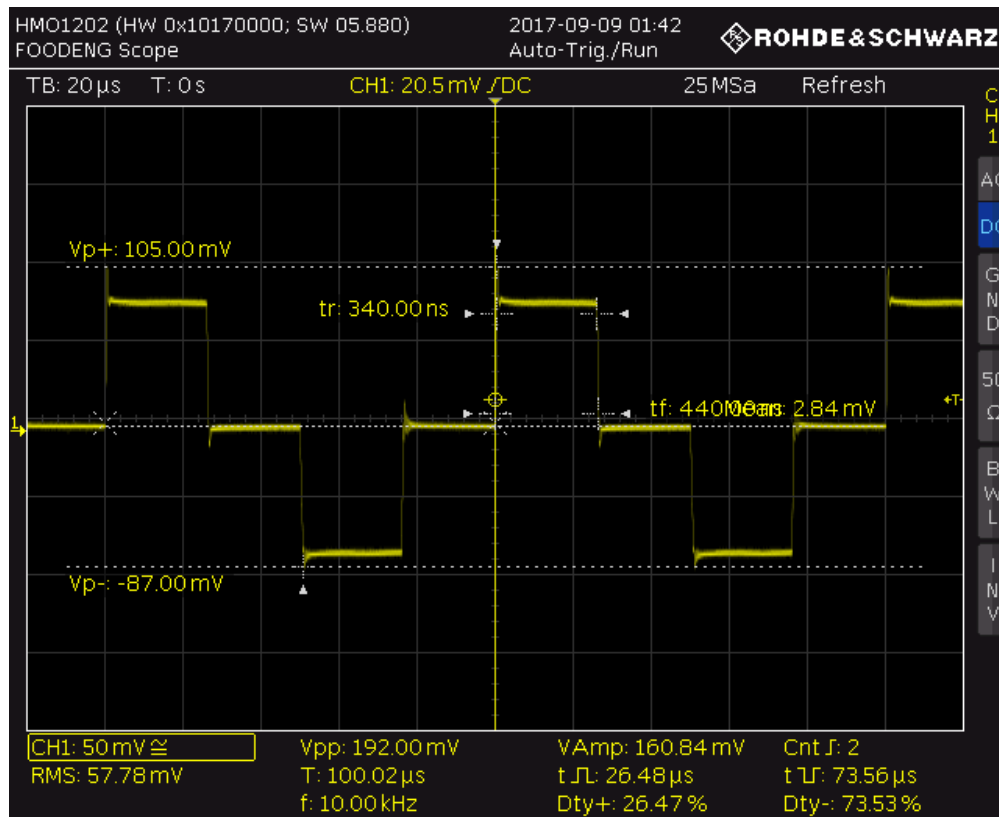


Figure 10. Waveform across shunt resistor induced by current flow through a London broil beef sample placed within the supercooling sample chamber.

The OMF system has shown inductive behaviors when driving the electromagnets used within the sample chamber. Thus, the use of Equation (2.6) is not valid with the OMF system and Equation (2.5) is required for OMF  $V_{rms}$  derivation. A typical OMF waveform across a shunt resistor when powering the supercooling chamber at 10Hz is shown in Figure 11.

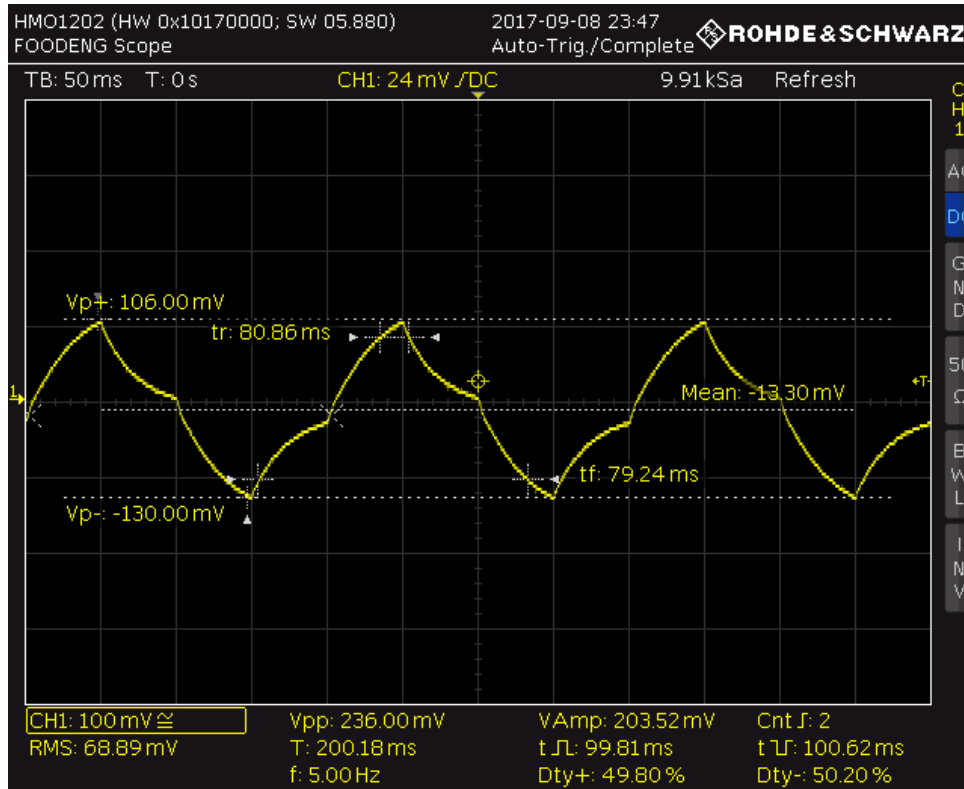


Figure 11. Voltage drop waveform across shunt resistor induced by current flow through OMF electromagnets.

Knowing the  $V_{rms}$  across a shunt resistor then becomes useful in determining power dissipation in AC conditions, and is given by

$$P = \frac{V_{RMS}^2}{R} \quad (2.7)$$

#### 2.4.2 OMF Current Sensing System Component Selection and Design

The OMF current measurement system was designed around the following specifications, in addition to those stated in Table 3.

1. Power dissipation: below 1 watt maximum
2. Operational Temp range: -20°C ~ 85°C
3. Power Supply of current system: 5V
4. Over current protection

The signal ranges involved within a typical shunt resistor based current monitoring system tend to be milli-Volts or lower. Amplification of the signal becomes necessary in such cases, for our purpose current monitor IC packages were chosen to monitor the DC H-bridge positive rail current (INA200AIDGKR, Texas Instruments, Dallas, TX) and AC load current (LT1999CMS8-20#PBF, Linear Technologies, Milpitas, CA). Measurement points of the INA200 and LT1999 can be seen in Figure 12. The INA200 is paired with

a 0.05Ohms shunt resistor (LVK24R050DER, Ohmite, Warrenville, IL), at the maximum expected current draw the power loss is less than 1 watt. The topology of a current monitoring systems becomes an important consideration when attempting to design a system for fault conditions detection. The INA200 was designed as a high side current monitor with built in 20V/V gain and high-speed comparator used to trigger the  $I_{TRIP}$  pin found on the IRAMX20UP60A. The threshold of the comparator is selected using two external precision resistors attenuating the output signal produced by the INA200, when the attenuated signal crosses the internal 0.6V reference signal a fault condition is reached. The INA200 will quickly shut-down the IRAMX20UP60A in a latched mode until a user resets the fault condition through UI input or a complete power cycling procedure of the CU.

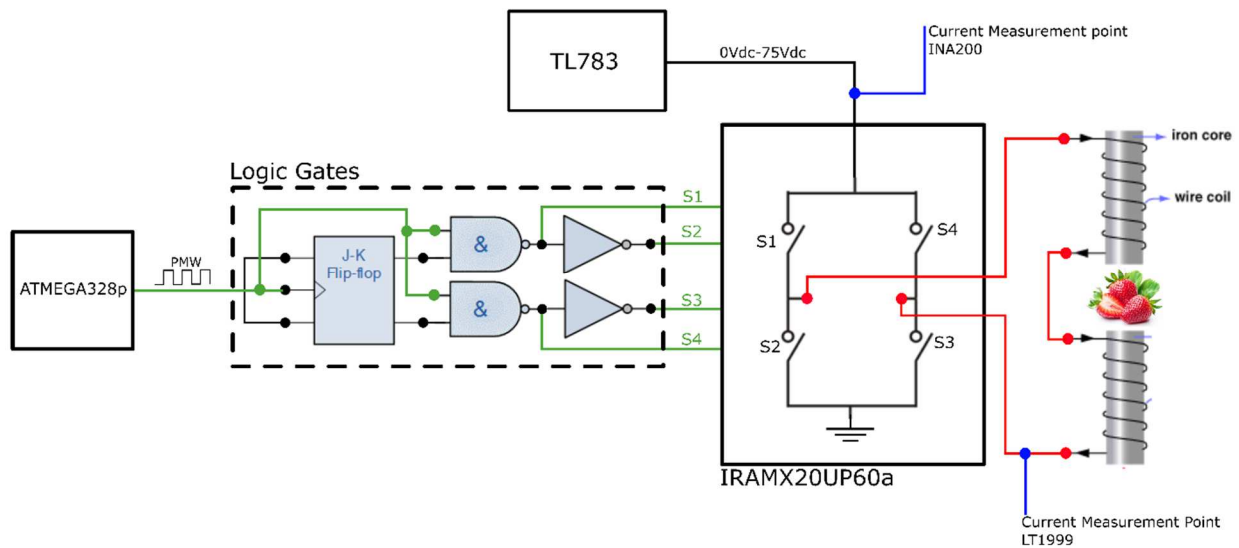


Figure 12. Current measurement points within OMF system.

The LT1999 is a current monitor specifically designed for use in AC signal environments of an H-bridge circuit. As such the LT1999 is a bi-directional current monitor with a 20V/V gain, the output signal of the device is biased at half of its power supply voltage. This is done to indicate the positive and negative cycles of an AC signal with the biased voltage level acting as a virtual ground. Paired with the LT1999 is a 0.03Ohm shunt resistor (LVK24R030DER, Ohmite, Warrenville, IL) in the kelvin sense style connection, the maximum output signal of the LT1999 is restricted to a 0.1V-4.9V swing with a 2.5V bias voltage reference point. The signals from the LT1999 and INA200 are digitized via 16-bit ADC (ADS1115IDGSR, Texas Instruments, Dallas, TX), and communicated to MCU by I<sup>2</sup>C communication protocol. The ADS1115 is set to operate at 860SPS, measuring an OMF maximum frequency of 10Hz.

### 2.4.3 PEF Current Sensing System Component Selection and Design

The PEF current measurement system was designed around the following specification, in addition to those found in Table 3.

1. Power dissipation: below 1watt maximum
2. Operational Temp range: -20°C ~ 85°C
3. Power Supply of current system: 5V
4. Minimum Sampling of 40kHz

The PEF current monitoring system only measures the AC signal because the DVR8839 H-bridge power module has built in over-current protection. The same LT1999 variant seen within the OMF system is recycled within the PEF design, and is paired with a 1.20hm shunt resistor (RC1206FR-071R2L, Yageo, Taiwan) in the kelvin sense style connection. However, unlike the OMF system the PEF system operates at considerably higher frequencies, thus requiring an ADC with a much higher sampling frequency. The minimum sampling frequency required is given by the Nyquist sampling theorem which states: *The sampling frequency should be at least twice the highest frequency contained in the signal or*

$$f_s \geq 2f_c \quad (2.8)$$

where  $f_s$  is the sampling frequency and  $f_c$  the frequency of signal being measured [101]. The PEF system operates at a maximum of 20kHz, limited by the IGBT switches found within the IRAMX20UP60A. To ensure high sampling speeds a high-speed ADC (ADC122S625C1MM/NOPB, Texas Instruments, Dallas, TX) was chosen to convert the PEF shunt resistor analog signal to digital data. The ADC122 communicates to MCU with SPI communication protocol, the SPI bus frequency is used to determine the sampling rate of the ADC122. The SPI bus frequency is dictated by the ATMEGA328P MCU and is set at 125kSPS, resulting in 6.25 samples per period with a 20kHz PEF signal. A summary of the OMF and PEF current measurement system can be seen in Figure 13.

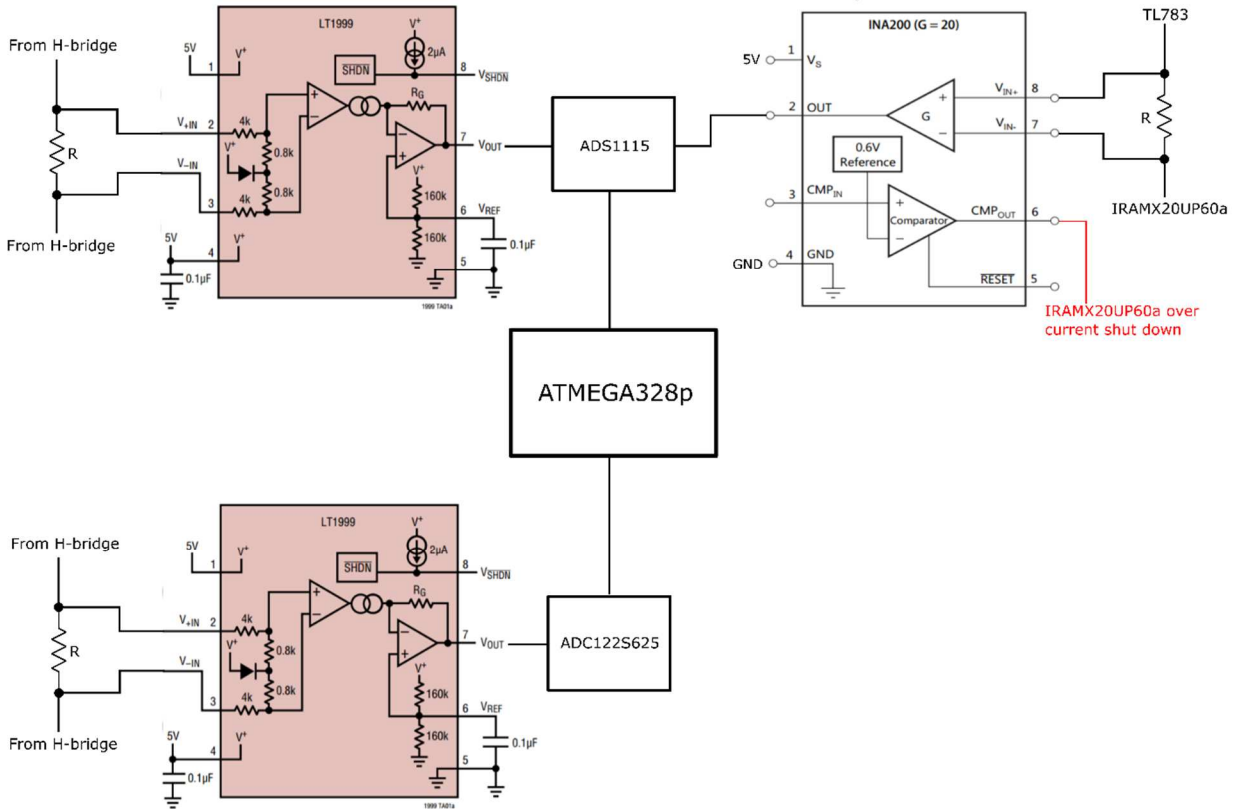


Figure 13. Simplified Schematic of the current measurement system for OMF and PEF systems. PEF is on the bottom with a single LT1999, and OMF on top.

## 2.5 Voltage Sensing System

The measurement point of the voltage sensing system is taken from the positive H-Bridge supply rail of both PEF and OMF system. The voltages here represent the peak voltages seen at the PEF and OMF H-Bridge outputs. The voltage signals are attenuated with a simple voltage divider resistor network, the level of attenuation is based upon the full-scale range (FSR) of the built in ATMEGA328P 10-bit ADC. The resistor values are chosen based upon the following

$$V_{OUT} = V_{IN} \frac{R_2}{R_1 + R_2} \quad (2.9)$$

where  $V_{OUT}$  is the attenuated voltage signal,  $V_{IN}$  the input voltage,  $R_2$  the resistor referenced to GND, and  $R_1$  the resistor in series prior to  $R_2$ . Also included in the design are basic protection from the ATMEGA329P ADC inputs with current limiting resistor and clamping diodes to prevent any possible harmful voltage and current conditions.

## 2.6 Temperature Measurement System

### 2.6.1 Thermocouple Based Temperature Measurement Model

When two dissimilar types of conductive wire are joined together to create a closed loop, and one end is heated, a continuous current develops due to an induced electro-motive-force (emf) [102], [103]. This phenomenon known as the Seebeck effect is the basis for thermocouple operation. The Seebeck effect results in measurable currents/voltages as given by

$$E_{\text{emf}} = -S_{AB}(T_2 - T_1) \quad (2.10)$$

where  $S_{AB}$  is the average Seebeck coefficient of material A and B, and T the difference in temperature of the conductive loop at point  $T_1$  and  $T_2$ , as depicted in Figure 14. This emf develops due to the thermal rearrangement of free electrons found in a conductive material [104]. The average Seebeck coefficient within equation (2.7) is defined as a measure in magnitude of the induced emf in response to temperature difference across a thermocouple wire, and is mathematically represented as

$$S_{AB} = S_A - S_B = \left( \frac{(E_{A2} - E_{A1})}{(T_2 - T_1)} \right) - \left( \frac{(E_{B2} - E_{B1})}{(T_2 - T_1)} \right) \quad (2.11)$$

where E and T are the gradients of emf and temperature within their respective material [104], [105].

Many factors will affect the value of a Seebeck coefficient including material composition, purity, defects, and phase transformations within material [106]. The average Seebeck coefficients of standard thermocouple wires as established by ASTM E230 [107] and IEC 60584 [108], are given in Table 5.

Table 5. Standard thermocouple wires, their material composition, Seebeck coefficients [113], and their typical associated limits of uncertainty.

Type	Wire Material	Seebeck Coefficient ( $\mu\text{V/K}$ )	Standard Limits (greater of)	Special Limits (greater of)
E	Chromel-Constantan	60	$\pm 1.7^\circ\text{C}$ or $\pm 0.5\%$	$\pm 1.0^\circ\text{C}$ or $\pm 0.4\%$
J	Iron-Constantan	51	$\pm 2.2^\circ\text{C}$ or $\pm 0.75\%$	$\pm 1.1^\circ\text{C}$ or $\pm 0.4\%$
T	Copper-Constantan	40	$\pm 1^\circ\text{C}$ or $\pm 0.75\%$	$\pm 0.5^\circ\text{C}$ or $\pm 0.4\%$
K	Chromel-Alumel	40	$\pm 2.2^\circ\text{C}$ or $\pm 0.75\%$	-
N	Nicrosil-Nisil	38	$\pm 2.2^\circ\text{C}$ or $\pm 0.75\%$	$\pm 1.1^\circ\text{C}$ or $\pm 0.4\%$
S	Pt(10% Rh)-Pt	11	$\pm 1.5^\circ\text{C}$ or $\pm 0.25\%$	$\pm 0.6^\circ\text{C}$ or $\pm 0.1\%$
B	Pt(30% Rh)-Pt(6% Rh)	8	$\pm 0.5\%$	$\pm 0.25\%$
R	Pt(13% Rh)-Pt	12	$\pm 1.5^\circ\text{C}$ or $\pm 0.25\%$	$\pm 1.1^\circ\text{C}$ or $\pm 0.4\%$

Practical thermocouple measurements are taken with an open loop thermocouple wire, the loop is closed by the measurement instrument as shown in Figure 14, Junction 2. This configuration

inadvertently creates additional junction points at Junction 2, the resulting measured voltage by the voltmeter will be the difference of induced emf at Junction 1 and Junction 2. Reliable measurements within the circuit of Figure 14 will depend upon Junction 2's thermal uniformity.

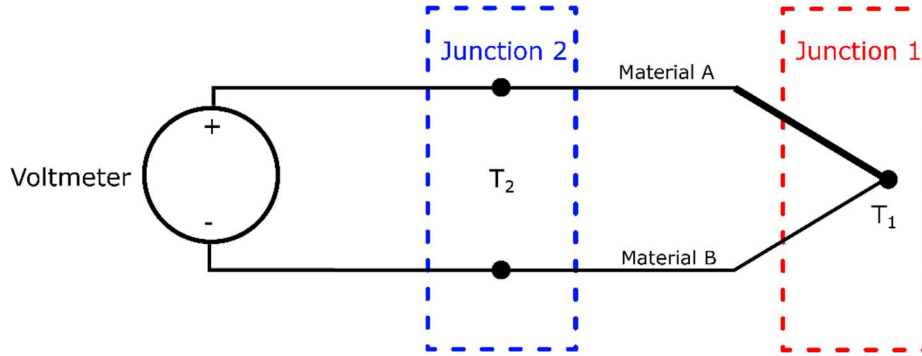


Figure 14. Thermocouple basic circuit.

To account for the newly created junction points and the unwanted emf, cold junction compensation (CJC) is used to cancel out the Junction 2 emf. To accomplish CJC, Junction 2 is either held at a known temperature or Junction 2's temperature is actively measured and converted to an equivalent emf value with the help of standard calibration curves developed and compiled within ASTM E230 or IEC 60584. The CJC procedure is carried out in three basic steps.

1. First the reference temperature at Junction 2 is measured using an accurate thermometer. The measured temperature is then converted to an equivalent emf using the standard calibration curves for a particular type of thermocouple wire in use (Type J, K, T...etc). For example, to convert a reference temperature to equivalent emf of a J-type thermocouple, the following equation is used [109]

$$E = \sum_{i=0}^n c_i (t_{90})^i \quad (2.12)$$

where  $c_i$  are coefficients derived empirically from the calibration curve, and  $t_{90}$  is the reference temperature (Junction 2) in degrees Celsius.

2. This emf is then referenced out of the end measurement and you are left with the emf induced solely by Junction 1.

$$V_m = V_{J1} - V_{J2} \rightarrow V_{J1} = V_m + V_{J2} \quad (2.13)$$

where  $V_m$  is the voltmeter voltage,  $V_{J1}$  is the emf as a result of Junction 1, and  $V_{J2}$  is the emf as a result of Junction 2.

3. Conversion of the final emf value to temperature is accomplished with the use the standard calibration curves once again. For a J-type thermocouple the following equation is used [109]

$$t_{90} = c_0 + c_1E + c_2E^2 + \dots c_iE^i \quad (2.14)$$

where  $c_i$  are the coefficients from the calibration curves, and  $E$  the final measured emf and  $t_{90}$  the final temperature.

### 2.6.2 Resistance Temperature Detector (RTD) Measurement Model

RTD or resistance temperature detectors are accurate, mostly linear, and stable over time. Due to these factors, RTDs have seen wide adaptation into applications which require high accuracy and reliability [110]. As seen in Table 6, RTDs can be constructed from an assortment of metals which exhibit changes in resistance with change in temperature. Of these metals, platinum has been the most widely used due to its wide operational range, stability, and low probability of contamination [111].

Table 6. Common RTD material, and their associated resistivity.

Metal	Resistivity ( $\Omega$ /cmf, cmf = circular mil foot)
Gold	13.00
Silver	8.8
Copper	9.26
Platinum	59.00
Tungsten	30.00
Nickel	36.00

RTDs originally suffered from poor response times due to the nature of their fabrication which required carefully insulated platinum wires [111]. However, advances in metal film RTDs fabrication have cut response times significantly while maintaining high accuracy. Standardization of RTD construction, performance, and classification has led to the development of RTD tolerance grades which specify their interchangeability (i.e., their overall accuracy) [112], [113]. The most common standards defining and governing RTD grades and classification are listed in Table 7

Table 7. Most Common RTD standards and their classified RTD grade. The defining equations express uncertainty associated with RTD grade, where  $t$  is absolute temperature in degrees Celsius.

RTD Grade/Class Classification Standards		
Standard	Tolerance	Defining Equation
ASTM E1137	Grade A	$\pm[0.13+0.00017 t ]$
ASTM E1137	Grade B	$\pm[0.25+0.00042 t ]$
IEC 607512	Class AA	$\pm[0.1+0.00017 t ]$
IEC 60751	Class A	$\pm[0.15+0.002 t ]$
IEC 60751	Class B	$\pm[0.3+0.005 t ]$
IEC 607512	Class C	$\pm[0.6+0.01 t ]$

Calibration procedures of RTD sensors are given in ISO/IEC 17025 and ANSI/NCSL Z540-1, based upon the ITS-90 temperature scales. RTDs are specified by their resistance at 0°C, common values of resistance are 50, 100, 200, 500, 1000, and 2000Ω with 100Ω platinum RTDs being the most common variant [110]. In addition to specifying various grades and types of RTDs, the standards provide measurement models based upon the Callendar-VanDusen equation presented here in their simplified form [114], [115], [116]

$$R_T = R_o(1 + AT + BT^2), \quad T > 0 \quad (2.15)$$

$$R_T = R_o(1 + AT + BT^2 + C(T - 100)T^3), \quad T < 0 \quad (2.16)$$

where  $R_T$  is the resistance of RTD at temperature  $T$  in degree Celsius,  $R_o$  the resistance of RTD at 0°C, and  $A$ ,  $B$ , and  $C$  are Callendar-VanDusen coefficients. The Callendar-VanDusen coefficients differ for RTDs categorized by their 0°C resistance and can be derived by the following

$$A = \alpha \left\{ 1 + \frac{\delta}{100} \right\}, \quad B = \frac{-\alpha\delta}{10^4}, \quad C = \frac{-\alpha\beta}{10^8} \quad (2.17)$$

where,

$$\alpha = \frac{R_{100} - R_o}{100 + R_o}, \quad \beta = \frac{-10^8 C}{\alpha}, \quad \delta = \frac{-10^4 B}{\alpha} \quad (2.18)$$

where  $R_{100}$  and  $R_o$  are the RTD resistances at 100°C and 0°C. Typical RTDs are designed to have a nominal alpha value of  $\alpha = 0.00385$  per °C [114]. Equation (2.15) allows us to determine the absolute temperature  $T$  when the resistance  $R_T$  is known

$$T = \frac{-A + \sqrt{A^2 - 4B \left( 1 - \frac{R_T}{R_o} \right)}}{2B} \quad (2.19)$$

Equation (2.19) only accounts for conditions in which  $T > 0$  (i.e.,  $R > 100$ ), solving for negative conditions of  $T$  from Equation (2.16) becomes considerably more difficult, as a result  $R$  vs.  $T$  curves are often supplied by RTD manufactures to construct a least square fit model form the data.

### 2.6.3 Thermocouple Temperature Measurement System Component Selection and Design

In addition to the key design specification stated in Table 3, the thermocouple temperature measurement system was designed around the following.



signal sensing. Communication between MCU and ADS1220 is accomplished with SPI communication protocol, configuration of the ADS1220 is accomplished with bit registry commands via SPI.

The filter design begins with understanding the ADS1220 input signal requirements, as detailed within its datasheet [117]. Differential noise caused by common-mode capacitor (Figure 12, C35 and C34) mismatches is minimized following industry standard stated rule: *the differential capacitors (Figure 12, C35) should be at least ten times greater in value than common-mode capacitors* [118].

$$C_{Diff} > 10C_{CM} \quad (2.20)$$

Where  $C_{Diff}$  and  $C_{CM}$  denote the differential capacitor and common-mode capacitor values.

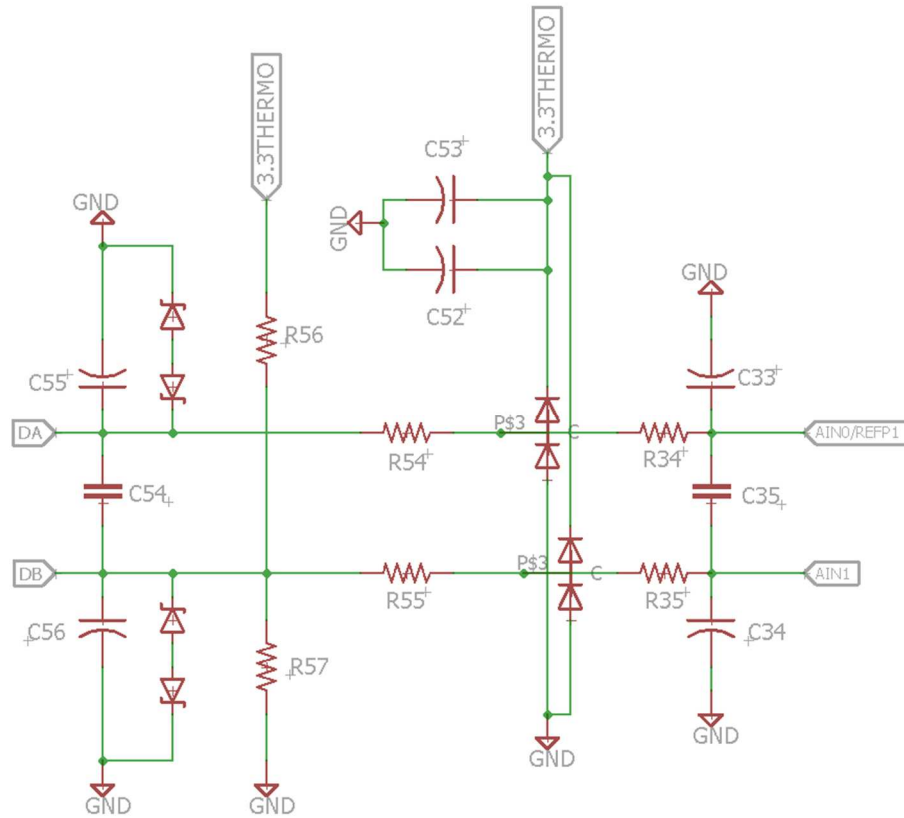


Figure 16. Filtering circuit schematic. Tags DA and DB denote entry of thermocouple signal from the switching stage. AIN0/REFP1 and AIN1 is the filter circuit's connection to analog to digital conversion stage.

The errors associated with filter resistor (Figure 16, R54, R55, R34, R35) mismatches and thermal noise are minimized by selecting high accuracy components with minimal thermal drift. Using the Johnson-Nyquist equation for resistor noise

$$V_n = \sqrt{4kTR\Delta f} \quad (2.21)$$

where  $V_n$  is resistor noise in rms,  $k = 1.38 \cdot 10^{-23}$  J/K,  $T = 298$ K,  $R$  the resistor values, and  $\Delta f$  the spectral noise density. Determining proper values for differential capacitors, common-mode capacitors and filter resistors starts by integrating the spectral noise density in Equation (2.21) over our expected frequency range [118], [119], [120]

$$\Delta f = \frac{1}{2\pi} \int_0^{\infty} \frac{d\omega}{1 + (\omega C_1 R_{Diff})^2} = \frac{1}{4C_1 R_{Diff}} \quad (2.22)$$

and substituting Equation (2.22) into (2.21).

$$V_n = \sqrt{3kTR_{Diff} \frac{1}{4C_1 R_{Diff}}} = \sqrt{\frac{kT}{C_1}}, \quad \text{where } C_1 = \left( C_{Diff} + \frac{C_{CM}}{2} \right) \quad (2.23)$$

The transfer function of filter circuit in Figure 12 is [118], [119]

$$\ddot{A} = \frac{1}{1 + j\omega R_{Diff} \left( C_{Diff} + \frac{1}{2} C_{CM} \right)} \quad (2.24)$$

where cut off frequency  $\ddot{A}$ , is chosen to be 10000 time smaller than the modulation frequency of the Delta-sigma ADC architecture found within the ADS1220 ( $\omega = 2\pi \cdot 256$ kHz). Setting  $\ddot{A} = 0.001$  [117] capacitor and resistor values were determined with Equations (2.20), (2.23), and (2.24).

In addition to the filter's resistors and capacitors in Figure 16, several other protective components are present in the design to meet IEC61000-4 standard for protection against voltage transients, surges, and discharge. These components are C55, C54, C56 with their accompanying TVS diodes, along with catch diodes labeled P\$3, and their bypass capacitors C53, and C52. Resistors R56 and R57 play a critical role in conditioning the thermocouple input signals by biasing them to the proper common mode voltage range required by the ADS1220, and is given by [117]

$$AVSS + 0.2 + \frac{V_{ING}}{2}, \quad AVDD - 0.2 - \frac{V_{ING}}{2} \quad (2.25)$$

where  $AVSS$  is the reference voltage signal applied to the ADS1220 GND pin,  $AVDD$  the power voltage level applied to the ADS1220 PWR pin,  $V_{in}$  the maximum expected signal magnitude at ADC1220 measurement pins and  $G$  the gain set within the built in PGA of the ADS1220. The biasing resistors are typically in the range of Mega-ohms to prevent loading onto the thermocouple sensing lines, and the

resistor ratio is set to the mid-point voltage level of the values given by Equation (2.25). Complete part numbers and their values of the filter circuit can be found in Appendix A.

Cold junction compensation is accomplished with the built in IDAC of the ADS1220, a 500 $\mu$ A excitation current creates the required voltage drop through an RTD (PTS060301B100RP100, Vishay Beyschlag, Malvern, PA). Using Equation (2.3) resistance can be calculated and temperature of the reference point deduced. An external shunt resistor (ERA-8ARB3241V, Panasonic Electronic Components, Newark, NJ) is used to generate a reference voltage, the same 500 $\mu$ A IDAC current used for the RTD is passed through the shunt resistor. The ratiometric nature of this measurement negates any possible noise generated within the ADS1220's IDAC during RTD measurement. The same reference voltage is used during thermocouple measurements.

## **2.7 Added Functionality**

### **2.7.1 Data logging**

Data logging is achieved in two primary methods, storage of data on an SD™ card or through data transmission via USB to a data capturing device such as a laptop/PC. A user chooses which method to operate in through input command on the UI touch screen (ULCD-32PUT-AR), the MCU receives the input command via serial UART (universal asynchronous receiver-transmitter) and selects appropriate communication channel by digital switch (TS3USB221RSER, Texas Instruments, Dallas, TX). When data is logged to the SD™ card, an IC voltage level translator (TXB0104DR, Texas Instruments, Dallas, TX) safely shifts logics levels between the 5V MCU SPI lines to 3.3V SD™ card SPI lines. The Micro SD™ form factor is accepted onto the control unit card slot. For reliable communication between PC/Laptop during USB data logging mode an intermediary IC package (FT232RL-REEL, FTDI, Glasgow, UK) is used to convert the MCU UART signals to USB serial transmission format.

The data logging system includes a real-time clock for time-stamping recorded data. The clock IC (DS1307Z+T&R, Maxim Integrated, San Jose, CA), communicates through I<sup>2</sup>C communication protocol to MCU, the MCU pools the clock data with any sensor readings selected for logging and transmits the data out to either SD™ card or USB. Paired with the clock IC is a precision 32.7680kHz crystal oscillator (ECS-.327-12.5-13FLX-C, ECS Inc, Olathe, KS) for timing pulse generation, the crystal oscillator and clock IC are both capable of being powered from a single 3V CR1225 coin cell battery to maintain time and date during low power conditions.

## 2.7.2 User Interface

User inputs and interface is accomplished with the uLCD-32PTU intelligent display module. This compact and cost-effective display incorporates a stream-lined development work flow suited for a front-end graphics interface. The display module communicates to the control unit ATMEGA328P MCU through serial UART, simple serial data is exchanged between the two devices. All graphical processing is handled by the onboard display module MCU, a micro SD™ slot is provided for storage of multimedia resource files used by display module MCU to construct the user graphical interface. ATMEGA328P compatibility and development within the Arduino IDE was greatly simplified with manufacturer provided library code.

Generation of multimedia resources and machine code of the display module MCU was accomplished within 4d-Workshop-4 IDE Version 4.3.0.10 (4DSystems, Minchinbury, AS). All graphical resources were created using 4D-Workshop-4 ViSi-Genie tool (Figure 17), the tool allows for placement and customization of graphical display layout and functionality, in this manner UI implementation was greatly simplified.



Figure 17. Selected UI interface pages created within the 4d-Workshop-4 IDE using the built in ViSi-Genie tool.

## 2.8 Custom Circuit Board Layout

The control unit PCB (printed circuit board) was designed within Eagle CAD (Autodesk, Mill Valley, CA), and sent to a fabrication (Oshpark, Portland, Oregon). A 4-layer board using a single unbroken ground plane was used to reduce large current loops of the numerous traces to and from various IC packages [121], [122]. The mixed signals involved on the control unit board along with the gridded

analog and digital portion of PCB as seen in Figure 18. The small analog signals involved within the thermocouple system makes surface topology of component, trace, and ground plane placement important in maintaining signal integrity. The ground planes involved within the thermocouple system was physically separated from the bulk ground planes of PCB to create an isothermal block. All traces to and from the thermocouple ground planes employ the ground bridging technique to provide a return path for trace signals [123], [124], [125]. High voltage components associated with the OMF system found on the PCB board were designed to meet IEC/UL 61010 standard for lab equipment safety [126]. Topology of the OMF system meets the proper isolation distances required to prevent creepage currents, and flashovers between traces and components.

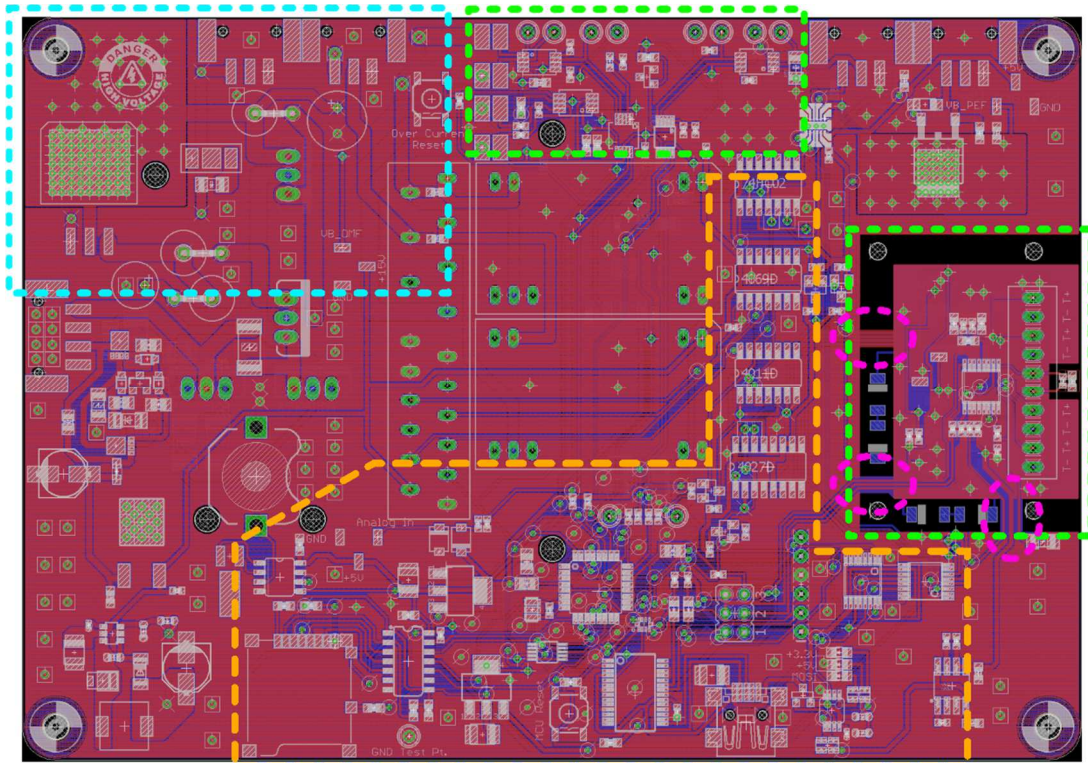


Figure 18. Control unit PCB, Green boxes indicate analog signal planes and the orange region the digital signal planes, pink circles point out the signal bridges across the thermocouple ground planes and bulk ground plane of PCB. Blue box is the OMF system designed to meet safety clearance standards as recommended by IEC/UL 61010.

## 2.9 Enclosure

The IEC/UL 61010 standard provides guidelines on device classification against electrical shock or failure. These classifications are based upon creepage distance, clearance distance, insulation type/material, CTI (comparative tracking index) of insulation, pollution degree, and level of insulation redundancy. Covered in section 2.8 was PCB spacing requirement as stated within IEC/UL 61010 for





Figure 20. Control unit fully assembled. In the image above the unit is operating in USB data logging mode.

## 2.10 Cost Estimate

Appendix C contains the bill of materials (BoM) associated with the costs of custom PCB, and electronic components. Total electronic component cost is \$300.32, a single prototype board is \$81.18. Appendix D contains the cost of goods sold analysis. Manufacturer cost total \$941.63, the gross margin based off an average sales prices (ASP) of \$1500 is 22% or \$322.97.

Average power consumption was measured as 0.047kWh over a 7-day continuous operational period. At the average 2016 Oahu, Hawaii residential electrical rate of \$0.26, the total cost incurred over a single year for 24hr continuous operation would be \$106.18.

## 2.11 Size and Weight

The control unit PCB board measures 5.61" by 3.94" (142.74mm by 100.00mm). Fully assembled within the custom enclosure, the unit measures 10" by 6" by 3" (Length, width, height). The total weight of the control unit system is 61oz (1.73kg).

## CHAPTER 3. SOFTWARE

### 3.1 PEF and OMF Waveform Generation

The PEF and OMF system take advantage of the ATMEGA328P's built in Timers. The ATMEGA328P has three Timers labelled Timer0, Timer1, and Timer2. All time keeping functionality used within the Arduino IDE relies on Timer0. Timer1 and Timer2 are used to generate OMF and PEF waveforms, Timer1 is a 16-bit timer used for OMF waveform generation, PEF waveforms are generated via the 8-bit Timer2. The 16-bit timer used within the OMF system is required for a 1Hz minimum signal oscillation. PWM signals are generated from Timer1 and Timer2, the frequency and duty of the generated signals is controlled by direct manipulation the ATMEGA328P's timer registries [127].

OMF and PEF waveform protocols are based upon timing sequences developed by Mok et al. [56], [54], [55]. The sequences are executed in a looping fashion, the duration, of each timing sequence can be set individually. The timing sequences operate in two major phases, phase 1 is associated with above freezing temperature or the cooling period within Figure 1. During this time PEF waveform generation is turned off until a critical temperature is reached. The critical temperature is measured by the thermocouple system and its set point is dependent upon food type as detailed by Mok et al. and can be assigned accordingly via user input.

### 3.2 Determination of Thermocouple Measurements

Near tandem measurements of RTD and thermocouple sensors are made to minimize time lag for CJC. The RTD measurement is translated from analog to digital by the ADS1220 ADC. The digital data first received by the ATMEGA328P MCU is the ADC code, the ADC code represents the bin in which the measurement falls within the ADC's FSR. This code is translated to measured voltage by multiplication with the least significant bit (LSB). The LSB represents the smallest possible voltage signal able to be represented by the ADC, for the ADS1220 the LSB is given by

$$\text{LSB} = \left( \frac{(2V_{\text{ref}}/G)}{2^{24}} \right) \text{SF} \quad (3.1)$$

where  $V_{\text{ref}}$  is the reference voltage of the ADS1220,  $G$  the gain of the built in PGA, and  $\text{SF}$  a desired scaling factor. Once the measurement voltage has been determined via Equation (3.1), resistance can be determined using Equation (2.3). The resistance value is used to determine the RTD measured temperature from a least squares 2<sup>nd</sup> order polynomial model derived from manufacturer supplied data [128]

$$T_{RTD} = 0.00009876R_{RTD}^2 + 2.361R_{RTD} - 246 \quad (3.2)$$

where  $T_{RTD}$  is the physical temperature measured by RTD, and  $R_{RTD}$  is the resistance from Equation (2.3).  $T_{RTD}$  is used for CJC of thermocouple measurements via

$$emf_{CJC} = 0.00004T_{RTD}^2 + 0.0386T_{RTD} - 0.0004 \quad (3.3)$$

where  $emf_{CJC}$  is the equivalent emf induced by  $T_{RTD}$  for T-type thermocouple. Equation (3.3) was derived from the ITS-90 T-type thermocouple standard curve using a second order polynomial model [109].

Thermocouple ADC code translation follows Equation (3.1), the ADC measured thermocouple voltage undergoes CJC via Equation (2.13). The voltage derived from Equation (2.13) is translated to the physical temperature by the following

$$T_{thermo} = -0.7385x^2 + 25.95x + 0.007606 \quad (3.4)$$

where  $T_{thermo}$  is the thermocouple measured temperature, and  $x$  the voltage given by ADS1220 after CJC. Equation (3.4) was derived from ITS-90 T-type thermocouple standard curve using a second order polynomial model [109]. Figure 21 diagrams the thermocouple pseudo code measurement process used within the control unit.

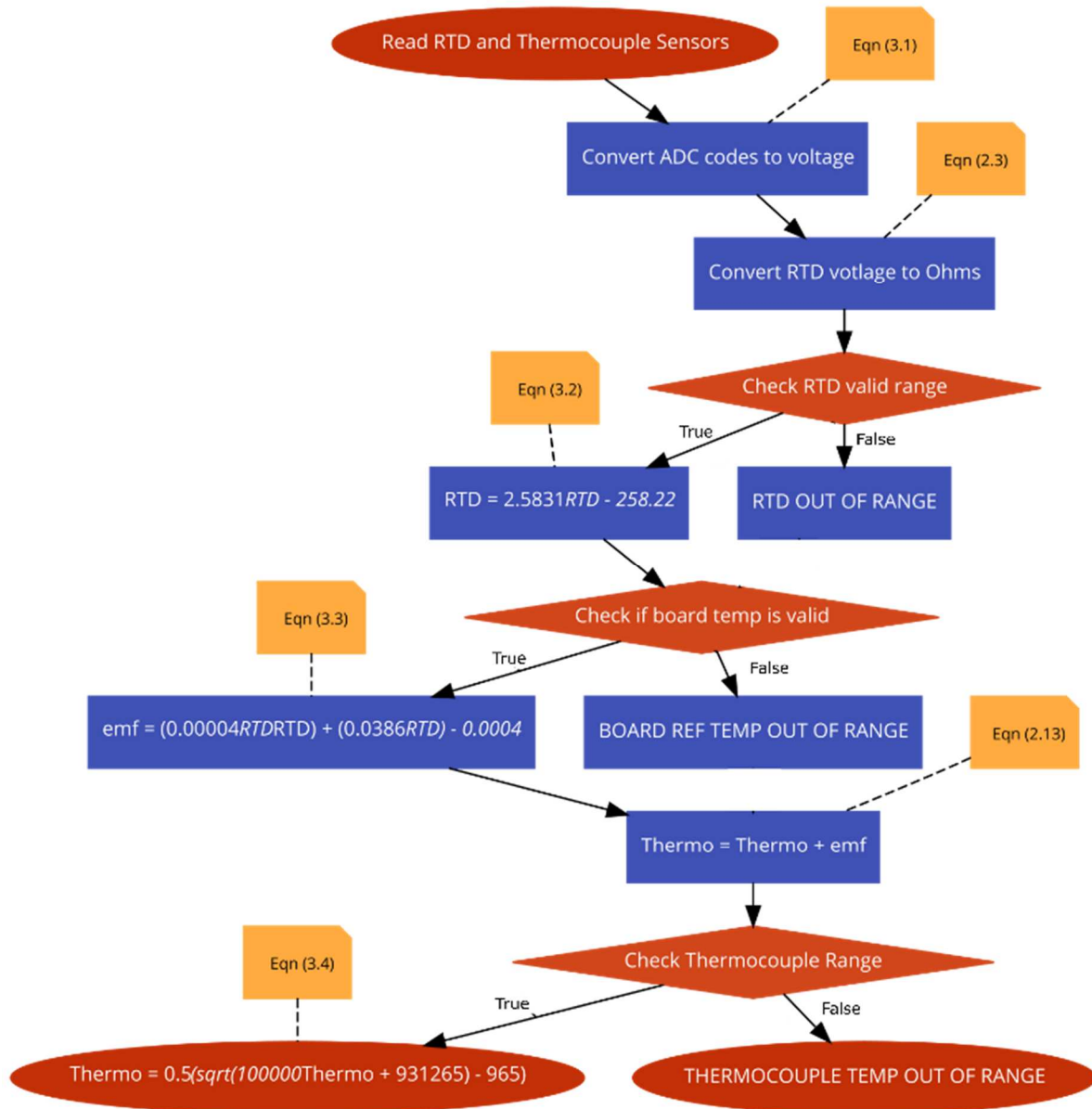


Figure 21. Pseudo code of thermocouple measurement system.

### 3.3 Determination of Current Measurement

#### 3.3.1 PEF Current Measurement

PEF based current measurement require moderately high sampling speeds due to the PEF operational frequency range. Determining reliable current measurements requires a reconstruction of the waveform through several instantaneous measurements above the PEF frequency. The ATMEGA328P has 2KB of SRAM available for all computations, global variables and local variables storage. To minimize the possibility of SRAM shortage the current measurement system uses a scaling

method to control sampling rates. This is accomplished by implementing delays between instantaneous current measurements which scale with PEF frequency. The scaling factor follows a basic rule, twelve evenly distributed instantaneous measurements are made for every two periods of PEF waveform. This can be mathematically represented as,

$$SF = \left( \frac{\left( \frac{1}{(PEF_{freq}/2)} \right)}{12} \right) 1000000 \quad (3.5)$$

where SF is the scaling factor in units of micro-seconds, and  $PEF_{freq}$  the user set PEF frequency. Twelve samples per 2 periods of PEF waveform was chosen due to the operational limit of the ADC122 ADC used within the PEF system. Paired with the ATMEGA328P at an SPI bus speed of 4MHz, the ADC122 is limited to 120kSPS. Conversion of the instantaneous measurements begins with LSB of the ADC122 is given by,

$$LSB = \frac{2V_{ref}}{4096} \quad (3.6)$$

where  $V_{ref}$  is the reference voltage applied to the ADC122 which is hardware set at 2.5V. The translated ADC code given by the ADC122 is multiplied by Equation (3.6), resulting in the instantaneous voltage drop across the shunt resistor. In this manner 12 consecutive measurements are taken and stored within an array and logged to SD™ card. The logged data is analyzed externally to the CU within MatLab 2015a (MathWorks, Natick, MA), Equation (2.5) or (2.6) is used depending on waveform shape, which is dependent upon load characteristics. When Equation (2.6) is used, a sorting algorithm is required to determine peaks of the biphasic waveform, to accomplish this a density based clustering algorithm was employed to group similar measurements together based upon an  $\epsilon$  value and `minPts` value.  $\epsilon$  within the clustering algorithm, sets the minimum distance between data points before they can be grouped together, and `minPts` sets the minimum number of data points required to form a group. For PEF measurements  $\epsilon$  was set to 70 by analysis of raw data collected during experimentation, `minPts` was set to 2 because of the low data volume being analyzed. Once data points were grouped, each group's means were calculated, and the maximum and minimum values were taken as the biphasic wave form's averaged peak values. These peak values were taken in absolute form and averaged to be used within Equation (2.6) to find  $V_{rms}$  which is then plugged into Equation (2.3) to determine  $I_{rms}$ . Figure 22 diagrams the PEF current measurement process within the control unit.

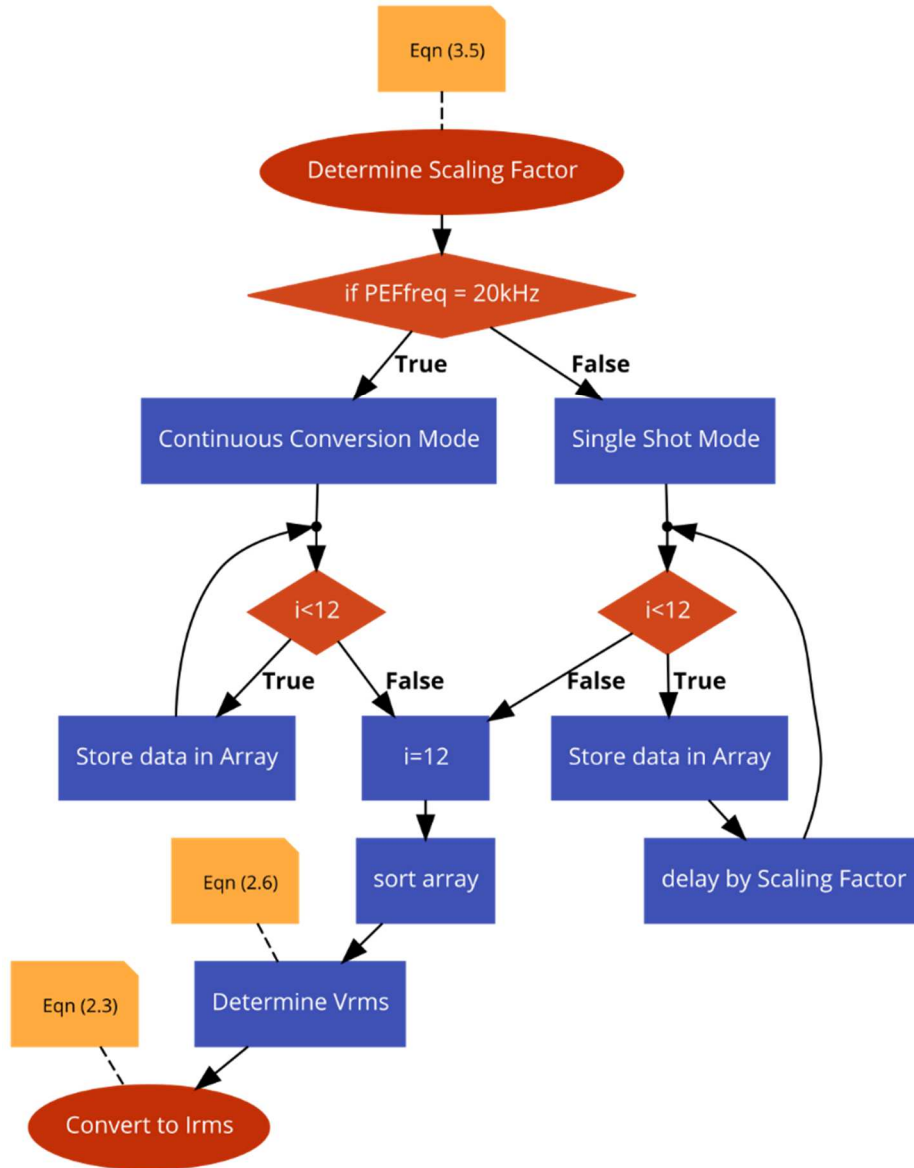


Figure 22. Pseudo code of PEF current measurement protocol. Determining  $V_{rms}$  and  $I_{rms}$  is done externally to CU with MatLab 2015a with raw data stored on SD card.

### 3.3.2 OMF current Measurement

The OMF based current measurement is like the PEF system with a few minor adjustments. 24 instantaneous voltage samples are taken over a single waveform period, opposed to 12 over 2 periods of the PEF system. The OMF system's SF factor is given by

$$SF = \left( \frac{\left( \frac{1}{(OMF_{freq}/2)} \right)}{12} \right) 1000 \quad (3.6)$$

where  $OMF_{freq}$  is the user define frequency. And the LSB of the ADS1115 within the OMF system is given by,

$$LSB = \frac{FSR}{2^{16}} \quad (3.7)$$

where FSR is the full-scale range of the ADS1115, set by the internal PGA gain. In the CU design, the FSR is set to  $\pm 4.092V$  for a gain of 1. Equation (2.5) for the OMF system is used to determine  $V_{rms}$ . The same pseudo code process seen in Figure 21 can be applied to the OMF current measurement operation.

### 3.4 Backend System Control

The CU PCB has various IC packages with SPI communication protocols for data transmission to and from MCU. In addition, several components on the board require periodic switching via input pins for functionality. For example, the digital switch (TS3USB221E, Texas Instruments, Dallas, TX) used to toggle between SD and USB data logging requires two permanent connections to toggle between channels. Each SPI device on board also requires a single permanent connection for proper chip selection (CS) during SPI communication. The ATMEGA328P does not have enough physical pins to accommodate all devices so an expansion of output pins was added using shift registers. The shift registers outputs toggles between LOW and HIGH logic levels via four control inputs from MCU. Two parallel shift registers expand the digital output capabilities of the MCU by 16 pins. Each individual pin is controlled through the manipulation of a 16-bit global variable named `SRdata` within code (Figure 20). The 16 pins of the shift registers correspond to the 16-bit `SRdata` variable where the most significant bit of `SRdata` corresponds to the first output pin on the leading shift register. In this manner `SRdata` is manipulated digitally in which a zero corresponds to a LOW logic level, and a 1 a HIGH logic level. `SRdata` can be referenced to examine which IC package are active or communicating with MCU. Switching of shift registers outputs is executed with a bit-banging operation, where the `SRdata` variable is fed to shift register via 4 control inputs.

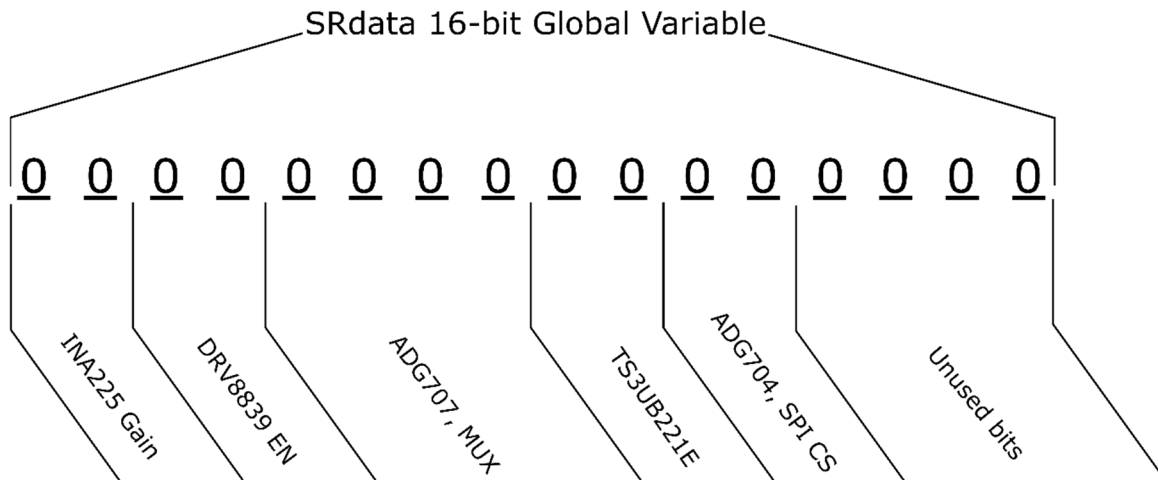


Figure 23. SRdata Global control variable displayed and initialized to zero, the corresponding bits and their associated relevance to IC packages can be seen. Each IC package controlled by SRdata has their corresponding truth tables which characterize their bit switching functionality.

The LCD UI interface functionality operates based upon an interrupt routine. All inputs taken from the LCD UI are sent to control unit board MCU, the specific input actions (button push, slider adjustment, etc) are identified by the information header structure as defined by 4Dsystems. The structure is interpreted by control unit board MCU and the specific actions associated with input carried out. Backend manipulation of SRdata through LCD UI input is carried out during these routines. The overall code controlling the CU board is summarized in Figure 24, the MCU test code used in this study can be examined in Appendix A.

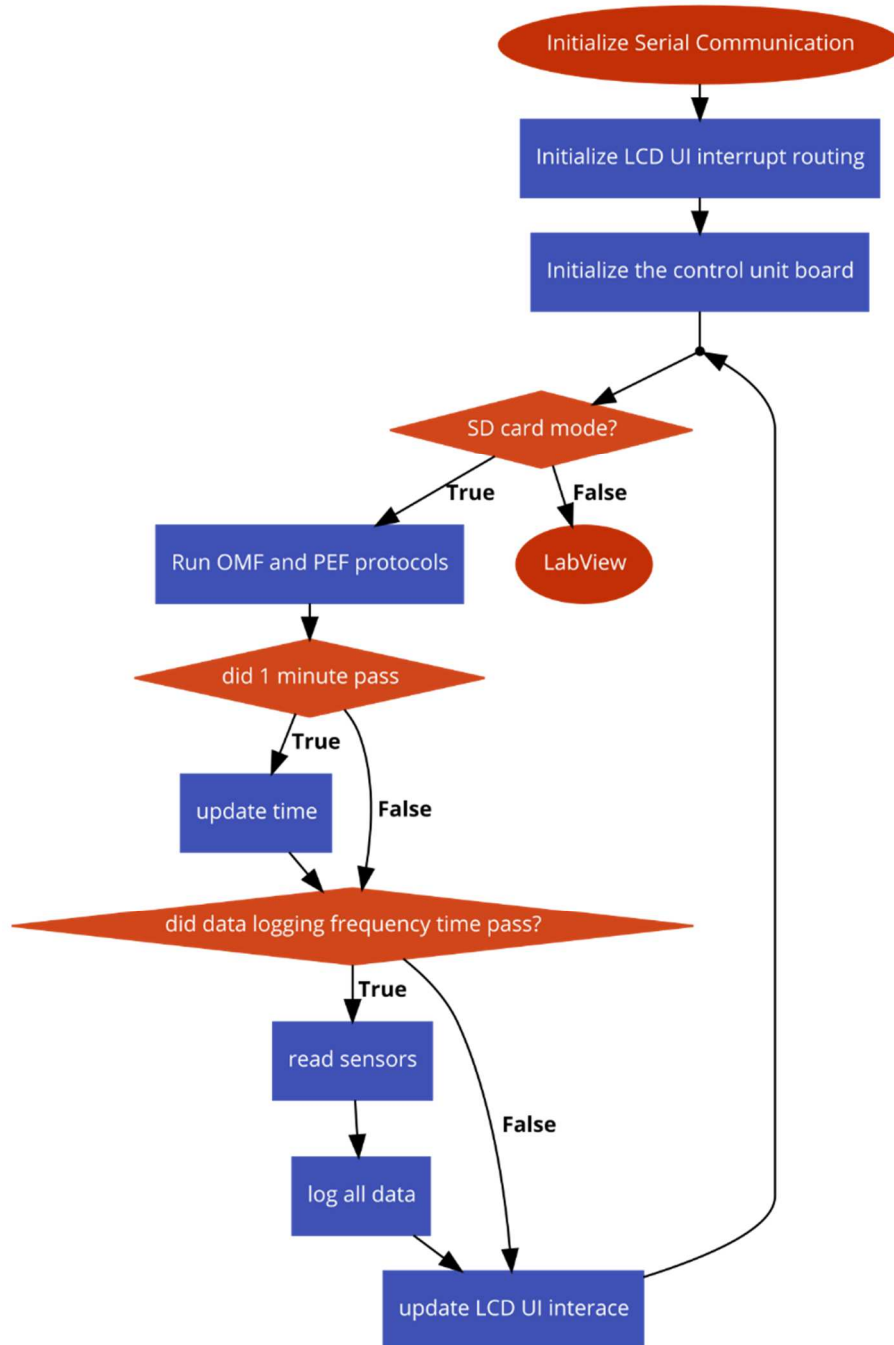


Figure 24. Simplified control unit board program routine. When under the LabView option the control unit board will operate based on commands from LabView.

## CHAPTER 4. PRELIMINARY VALIDATIONS

Upon completion of CU fabrication, testing and verification of proper functionality is needed to ensure reliable operation. This is done with a systematic approach of preliminary verifications: the goal of this step is to isolate key systems and test their limitations to acquire a range in which operation is guaranteed. In addition, improvements upon the system through offset correction and/or calibration is achieved by characterizing each system through the preliminary verifications procedures.

### 4.1 Thermocouple Calibration Technique

Comparison calibration technique consists of measuring the emf of a thermocouple under test within an isothermal medium while simultaneously measuring the temperature of the medium with a reference thermometer. The reference thermometer itself needs to be of high enough precision and accuracy to achieve a desired overall result. Success of this test method will largely depend upon the ability to maintain the measuring junction of the test thermocouple and the reference thermometer at the same temperatures. Errors involved in comparison calibration techniques can arise from two types of errors as defined under ISO/ANSI uncertainty budget analysis [129], [130]. First is Type-A error defined as standard uncertainty based upon valid statistical methods in treating data (e.g., standard deviation, least squares fitting, etc). And second are Type-B errors derived from scientific data, manufacturer stated specifications, or any other uncertainties derived from relevant information based upon scientific judgment.

Within comparison calibration of thermocouples, Type-B errors will come from manufacturer stated tolerances of equipment, materials, and reference data. Type-A errors will be derived from data collected during the comparison calibration at various calibration points, these will include standard deviations (as a measure of precision), offsets/bias, and interpolation errors when relating reference data to measured data. Interpolation errors for conversion of thermocouple emf to physical temperatures according to ASTM E563-11 and ASTM E2730-10 can be expressed as the root-mean-square deviations.

$$u = \sqrt{\frac{1}{N_{df}} \sum_i (E_i - E_{fit})^2} \quad (4.1)$$

Where  $u$  is the root-mean-squared deviation,  $N_{df}$  degrees of freedom, and  $E_i$  is the emf value of the test thermocouple.  $E_{fit}$  is an emf derived from the difference polynomial fitted to data points  $\Delta E = E_r - E_t$ .

Where  $E_r$  is the ITS-90 reference data emf and  $E_t$  the emf value of thermocouple system under test. The  $\Delta E$  polynomial serves as a calibration equation correcting offsets/biases across the tested temperature ranges.

The summation of Type-A errors and Type-B errors is achieved with a root-sum-squares method,

$$U = \pm K[(U_A)^2 + (U_B)^2]^{\frac{1}{2}} \quad (4.2)$$

Where  $U$  is the overall total uncertainty,  $U_A$  is the total Type-A uncertainty, and  $U_B$  total Type-B uncertainty computed via the root sum of squares.  $K$  within Equation (4.2) is a convergence factor analogous to  $2\sigma$  for 95% coverage or  $3\sigma$  for 99% coverage, where  $\sigma$  = standard deviation. All uncertainties within  $U_A$  are calculated as single standard deviations,  $U_B$  errors when dealing with manufacturer stated specification are often stated in  $2\sigma$  or  $3\sigma$  uncertainties. Careful judgement is required when dealing with  $U_B$  errors to avoid overstating or understating uncertainties.

The thermocouple system on the CU board will undergo comparison calibration of the emf measurement system and an end-to-end calibration for RTD CJC system separately. In this manner errors derived from each system can be assessed separately in a more effective and simple manner.

#### 4.1.1 Emf Measurement System, Methods and Materials

Figure 25 details the overall experimental setup related to emf comparison calibration. A variable temperature recirculating liquid bath (MX07R-20, PolyScience, Niles, Illinois) with silicone based fluid medium (Polycool H-50 silicone fluid, PolyScience, Niles, IL), and bypass kit (510-495, PolyScience, Niles, IL) was used to maintain calibration temperature point of  $-20^\circ\text{C}$  to  $40^\circ\text{C}$  in  $10^\circ\text{C}$  increments, when setting temperature points, a minimum of 20minutes was given to reach thermal stability before testing began. A polystyrene lid for the liquid bath was fashioned to act as a port for RTD fluid bath reference probe (PR-20-2-100-1/8-2-E-T, Omega, Norwalk, CT) and thermocouple assembly which consisted of probe (BLMI-304-T-18U-6, Omega, Norwalk, CT), connector (OSTW-T-M/F, Omega, Norwalk, CT) and T-type thermocouple wire (TT-T-24-TWSH-SLE-50, Omega, Norwalk, CT). The probes placed through the polystyrene lid were spaced 3cm apart. The thermocouples under test achieved CJC with a cold junction reference probe (TRP-T, Omega, Norwalk, CT) placed within an ice bath prepared following ASTM E563-11. The ice bath temperature was monitored with RTD probe (PR-10-2-100-1/8-6-E, Omega, Norwalk, CT), a new ice bath was made every 2-hours during experimentation. All probes were immersed a minimum of 3" into their respective medium to avoid heat flow along metal sheaths. All thermocouples involved were ungrounded to their shielding to avoid cross talk between probes and environment. All

RTD probes were of 4-wire configuration. Ambient temperature during experimentation was monitored using RTD probe (RTD-1-F3102-36-T, Omega, Norwalk, CT) placed near the CU. Thermocouples under test were directly connected to CU thermocouple input screw terminals, each terminal was tested at all calibration temperature points. The fluid bath reference probe, ice bath probe and ambient temperature probe were connected to DAQ (34970A, Agilent, Santa Clara, CA) through 16-channel multiplexer (34902A, Agilent, Santa Clara, CA). In addition, the DAQ measured DC voltages of the thermocouples at 6.5digit resolution in the 100mV range. The DC voltage measurements occurred at points emf#1 and emf#2 as depicted in Figure 22, emf#1 is the raw thermocouple emf, and emf#2 is the emf signal after passing through the CU thermocouple system’s multiplexer and filtering stage.

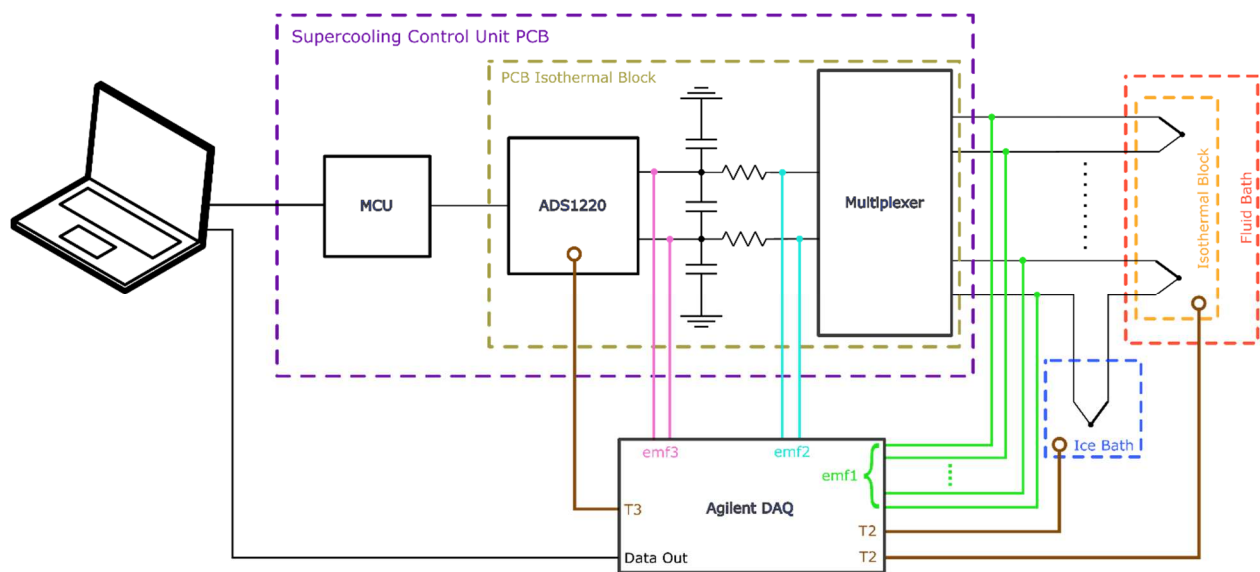


Figure 25. Thermocouple comparison calibration technique, experimental diagram

Data was collected at 3 second intervals for 10mins for each run, a total of three runs were conducted for each thermocouple channel at each temperature calibration point. To ensure data collected by the CU and DAQ were comparable, a TTL signal from CU was used as an external trigger for DAQ data collection timing. Both CU and DAQ data was captured on laptop computer, CU data was captured with Arduino IDE serial monitoring (Arduino, Torino, Italy), and DAQ data was collected with Benchlink Data logger software (Keysight, Santa Rosa, CA). All statistical analysis of collected data was carried out in MatLab R2015a (MathWorks, Natick, MA), and Excel 2016 (Microsoft Corp, Redmond, WA). The CU was powered with custom power supply with PEF and OMF functionality initialized at 20kHz PEF, 50% duty at 6V for PEF, and 1Hz, 50% duty at 60V for OMF.

#### 4.1.2 Emf measurement System, Results and Discussion

The CU's thermocouple system exhibited a non-linear relationship (Figure 26) with error over the temperature test range between -20°C and 40°C. Pre-calibration measurements showed a maximum deviation of 0.346°C from RTD reference probe at -20°C. A summation of variance showed an average 0.0152°C standard deviation across all trials, channels and temperature test measurement points. A complete summary of the pre-calibration trials for temperature readings can be seen in Appendix E.

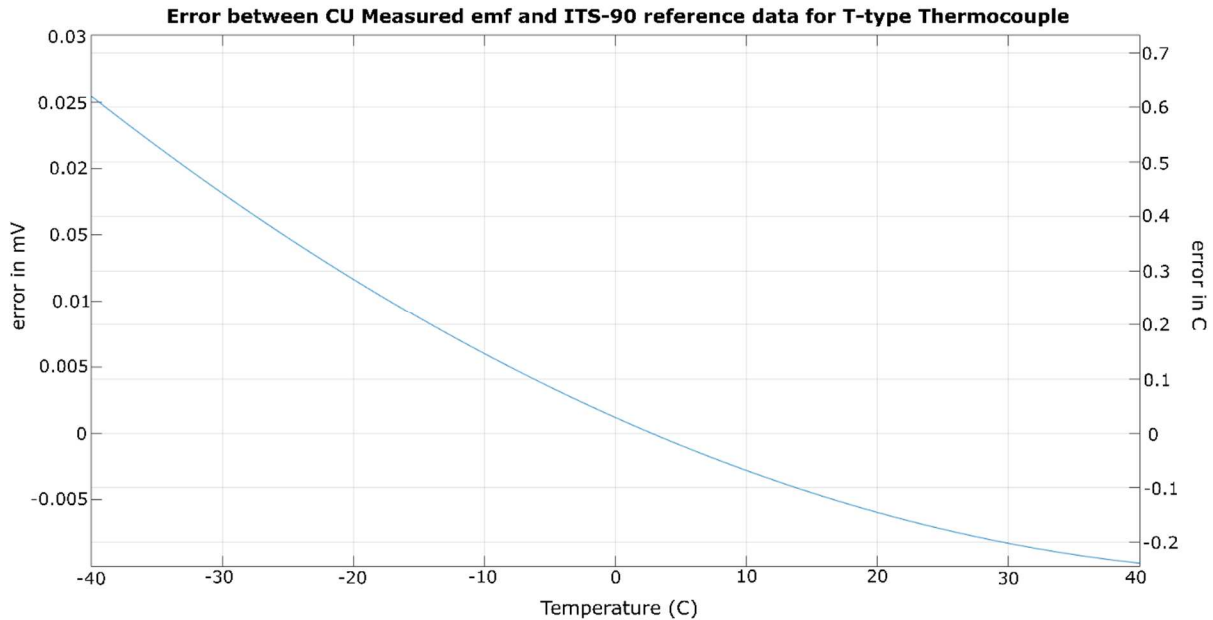


Figure 26. Error of CU, when compared with ITS-90 T-type thermocouple reference data

The non-linearity seen in Figure 23 is a direct result of deviation from ITS-90 reference data, where the deviation gradually grows when measuring temperatures below 0°C. This trend appears to be a common phenomenon among ADS1220 small signal IC packages when examining data sheets, and application notes [118], [117]. Other sources contributing to the large errors in the lower temperature range comes directly from the transfer function used to convert measured emf signals to degree Celsius. A 2<sup>nd</sup> order polynomial derived from ITS-90 T-type thermocouple reference data in the range of -40°C to 40°C was used within the CU code during testing. The errors in using this transfer function is given in a residual plot (Figure 24). The errors between 0mV and -1mV contribute directly to increasing errors when measuring temperatures below -0°C.

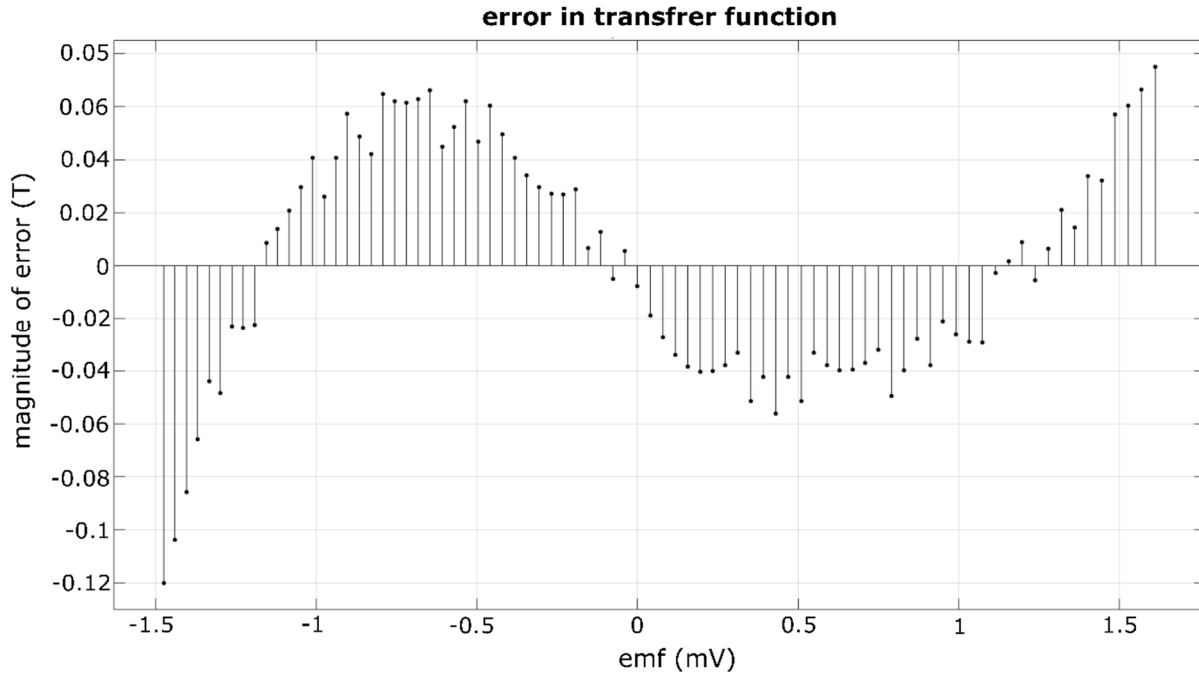


Figure 27. Residual plot of 2<sup>nd</sup> order polynomial used to convert measured emf into degree Celsius.

Offset/bias introduced by the initial multiplexer and filtering stage of the thermocouple circuit was corrected. Taking the difference between emf measured at emf#1 and emf#2 for all trials (Figure 28), a relatively constant offset was shown present in the signal (Table 8). Prior to taking the difference between emf#1 and emf#2, a paired F-test was conducted to determine if any changes in variance occurred to the signal as it traveled from emf#1 to emf#2 (i.e., if any new noise was introduced between the two measurement points). All paired F-tests showed an acceptance of the tested null hypothesis, with no statistically significant changes in variance detected.

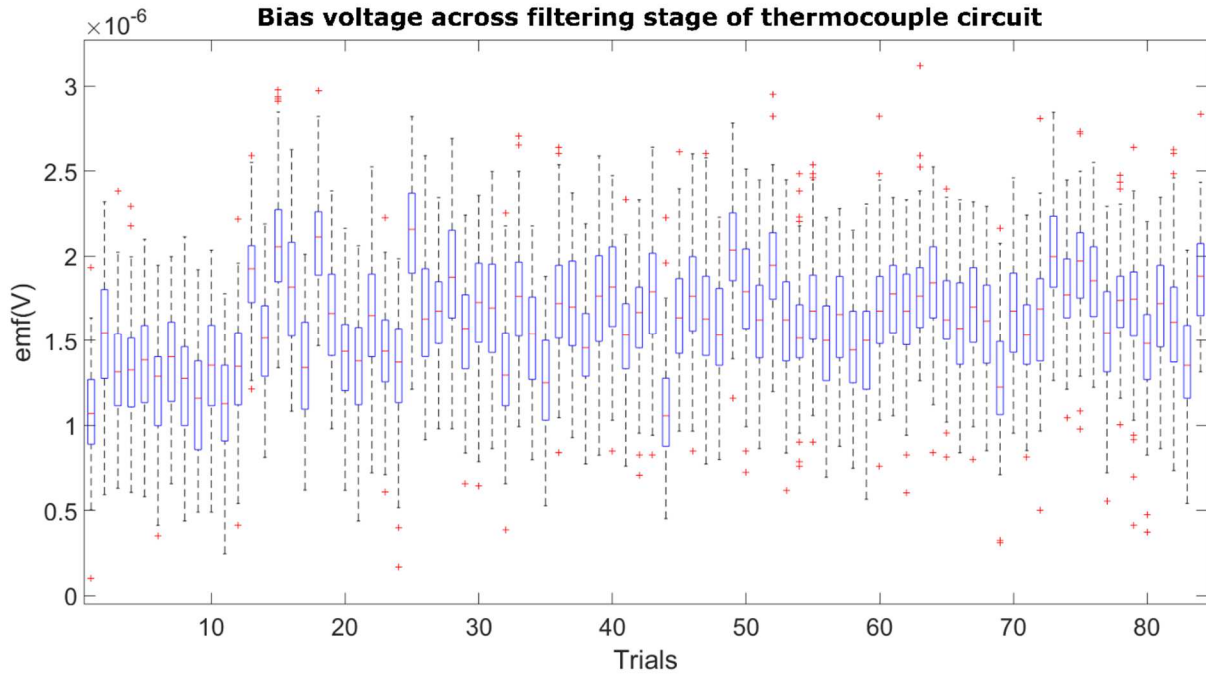


Figure 28. Box plots of emf bias across multiplexer and filtering stages of thermocouple circuit.

Table 8. Emf bias mean and standard deviation of multiplexing stage and filtering stage of CU.

	Offset Mean	Standard Deviation
emf(V)	1.6025E-06	3.2471E-07
°C	0.039	0.0079

Emf#2 is the emf signal prior to entering the ADS1220, by taking the difference between emf#2 and the emf reported by CU, a calibration function was developed. The emf difference was plotted over measured CU emf as shown in Figure 29, the data was fitted with a linear model, resulting in the equation,

$$emf_c = 0.005781emf_m - 0.000002619 \quad (4.3)$$

where  $emf_c$  is the correction value in V to be added to the measured  $emf_m$ . The linear model has an R-squared value of 0.9794, with RMSE of 6.536e-07V. A complete summary of the emf measurement during pre-calibration can be seen in Appendix E.

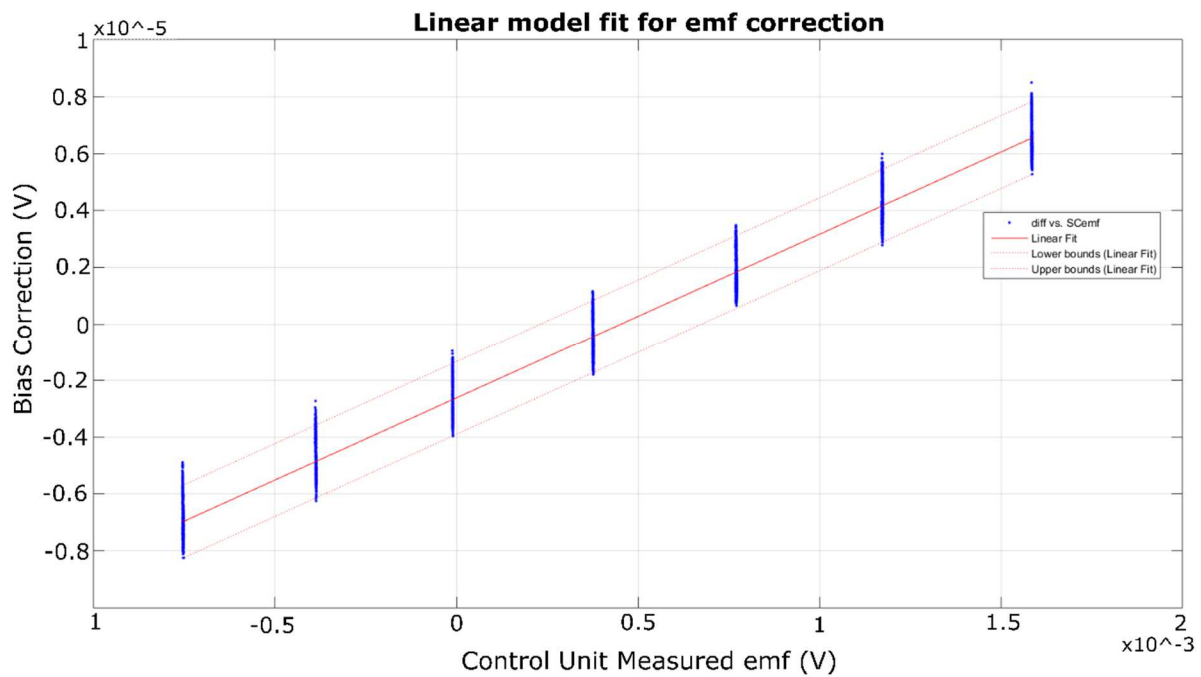


Figure 29. CU Thermocouple linear fit calibration model. Red dotted lines indicated 95% confidence interval.

Applying the offset/bias correction and calibration Equation (4.3) to the pre-calibrated data allowed for a 55.4% reduction in average temperature measurement error. Validity of measurements is shown to improve across  $-20^{\circ}\text{C}$  to  $40^{\circ}\text{C}$ , the average standard deviation of temperature error (taken as the precision of measurements) remains the same at  $0.006^{\circ}\text{C} - 0.0058^{\circ}\text{C}$ . A complete summary of the calibration correction applied to pre-calibrated data can be seen in Appendix E.

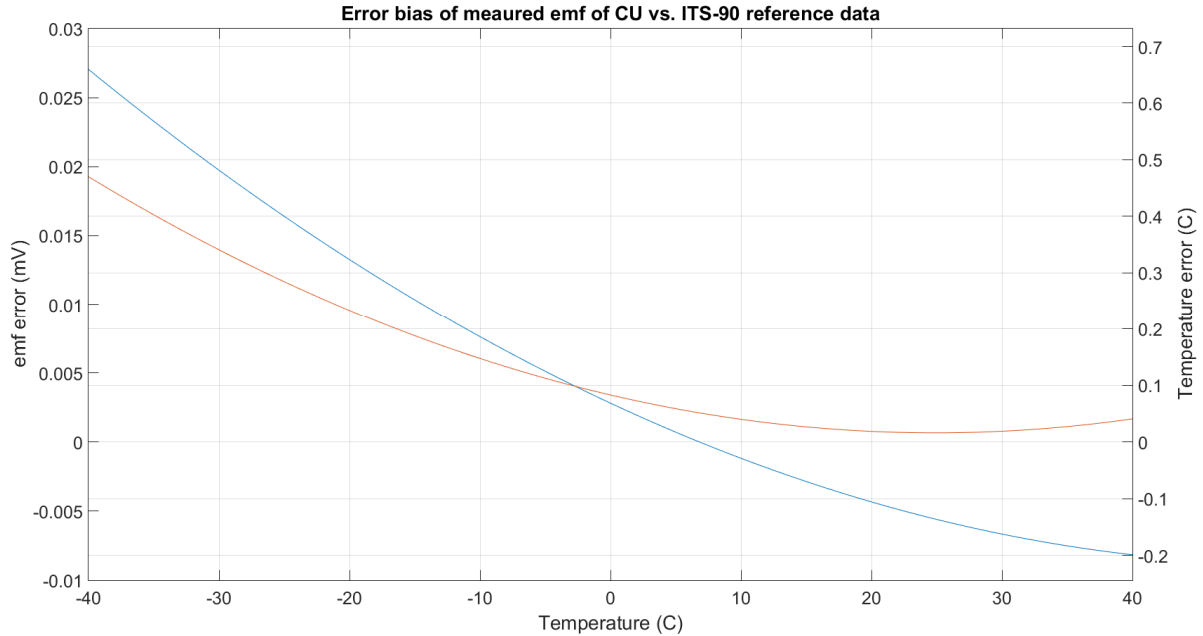


Figure 30. Error measured by CU over temperature ranges. Blue line indicates error in measurements prior to calibration. Red line is error with calibration applied to the pre-calibration data.

#### 4.1.3 RTD CJC System, Methods and Materials

Figure 31 summarizes the RTD preliminary verification setup. A thermal oven (LO-90-E, TPS, New Columbia, PA) was used to test temperatures between 45°C to 85°C in 10°C increments. A programmable digital freezer (FR-K13PXES, Daewoo, Seoul, South Korea) was used to test temperatures between -20°C to 10°C in 10°C increments. A final test point at room temperature (22°C) was included. Between temperature adjustments with the thermal oven, a minimum of 20mins was given to ensure thermal stability before data collection occurred. With the digital freezer, a minimum of 24 hours was given between temperature adjustment to ensure thermal stability. A fully assembled CU with dummy load attached was placed within the thermal oven and programmable freezer. The CU's temperature was monitored with T-type thermocouples (TT-40-SLE-50, Omega, Norwalk, CT) at two locations, one at the thermocouple screw terminal and the second at the CU board surface next to surface mounted RTD used for CJC. Internal temperature of the thermal chamber was monitored with RTD probe (PR-20-2-100-1/8-2-E-T, Omega, Norwalk, CT). The CU itself actively measured the temperature of an external ice bath (prepared following ASTM E563-11) via thermocouple assembly consisting of probe (BLMI-304-T-18U-6, Omega, Norwalk, CT), connector (OSTW-T-M/F, Omega, Norwalk, CT) and T-type thermocouple wire (TT-T-24-TWSH-SLE-50). The thermocouple assembly was attached to channel 1 of the screw terminal. The ice bath was also monitored externally with RTD probe (PR-10-2-100-1/8-6-E, Omega,

Norwalk, CT), all probes and thermocouples not associated with CU were monitored by DAQ (34970A, Agilent, Santa Clara, CA) with 16-channel multiplexer (34902A, Agilent, Santa Clara, CA).

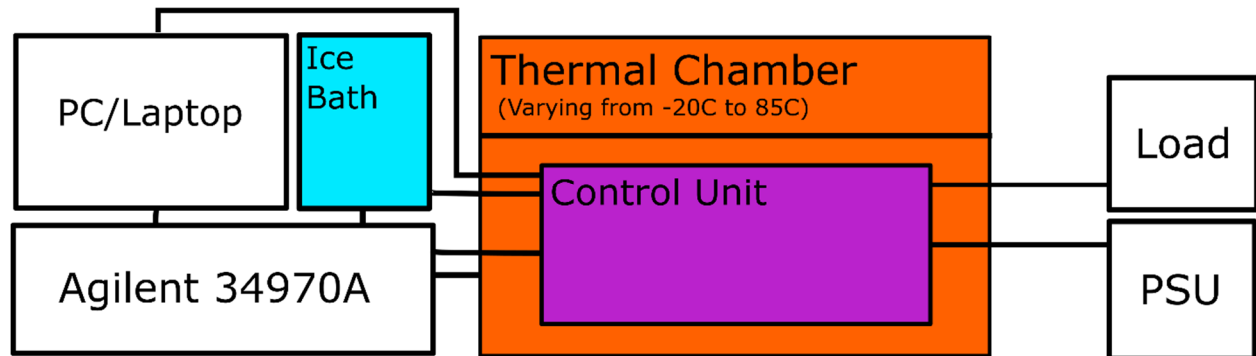


Figure 31. RTD preliminary verification, experimental setup.

Data was collected at 3 second intervals over a 10 minutes testing period after thermal stability was verified. A total of three trials for each temperature set point was conducted. Data collected by external DAQ and data spooled by CU was synced via TTL trigger signal provided by CU to DAQ. Both CU and DAQ data was collected onto a laptop computer with Arduino IDE serial monitoring (Arduino, Torino, Italy) and Benchlink data logging software (Keysight, Santa Rosa, CA). All statistical analysis of collected data was carried out in MatLab R2015a (MathWorks, Natick, MA), and Excel 2016 (Microsoft Corp, Redmond, WA). The CU was powered with custom power supply with PEF and OMF functionality initialized at 20kHz PEF, 50% duty at 6V for PEF, and 1Hz, 50% duty at 60V for OMF.

#### 4.1.4 RTD CJC System, Results and Discussion

The CJC system's preliminary verification protocol employs an ice bath as a known point of reference, the ice bath's temperature was monitored simultaneously by the CU and DAQ. Difficulty in relating the thermal chamber's ambient temperature to the CU's true board temperature made ambient temperatures around CU an unreliable reference source. This was because the CU board experiences self-heating from various power electronics ICs contained on the PCB as shown in Figure 32.

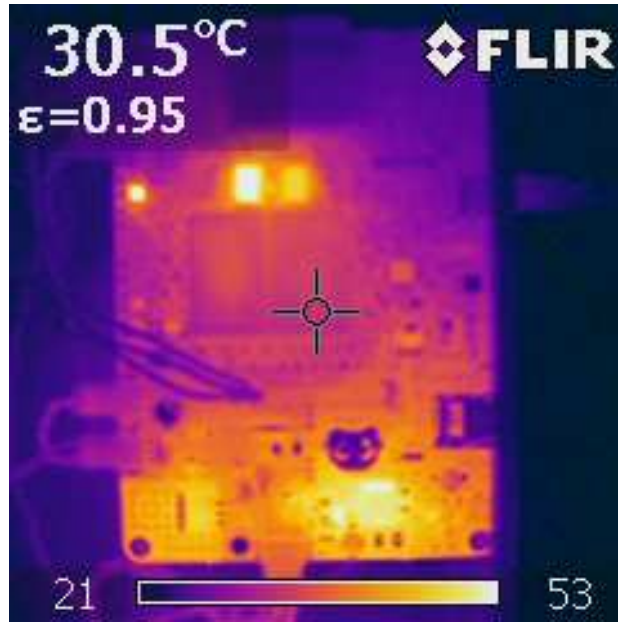


Figure 32. Infrared image of CU board under operation with OMF at 60V and PEF at 6V.

The isothermal block designed into the thermocouple system acts to promote thermal uniformity within the thermocouple system, however the screw terminal experiences a temperature gradient, which introduces large offset errors into the CJC routine.

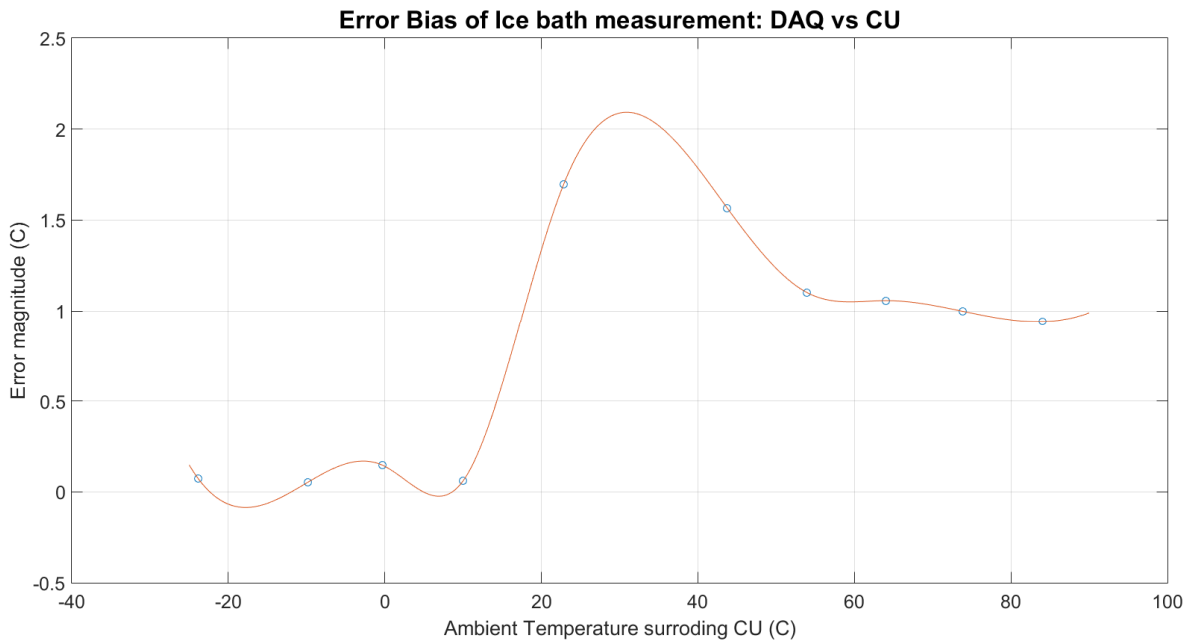


Figure 33. Error of CJC system. The curve shown represents the difference magnitude of error in degree Celsius between DAQ measured ice bath temperature vs. CU measured ice bath temperature.

The difference in ice bath temperature as measured by the DAQ and CU is used to indicate the magnitude of error as seen in Figure 33. The non-linear nature of the offset is heavily dependent upon

the ambient temperature around the CU. In the sub 10°C regions of ambient temperature, the difference in measurements between DAQ and CU are minimal, indicating CU board temperatures closely reflect the temperatures seen at the screw terminals. Above 10°C errors grow dramatically and levels off at 1°C in error magnitude. To correct this offset/bias a calibration curve was developed by taking the difference between the CU's measured board temperature and screw terminal measured temperature.

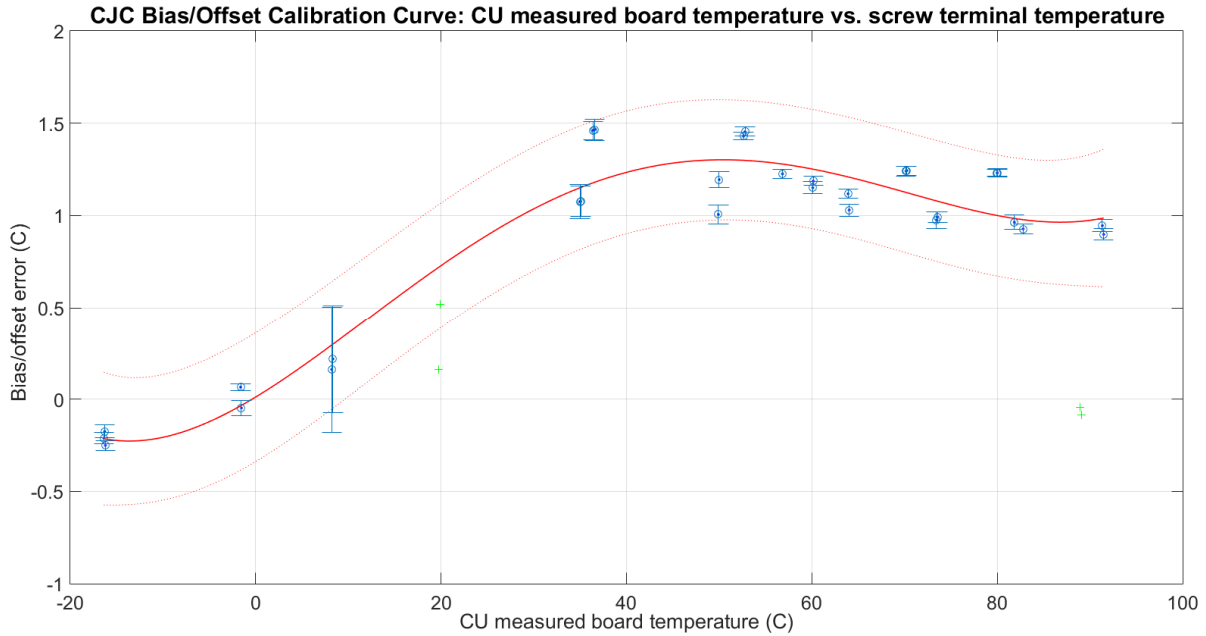


Figure 34. RTD CJC offset/bias data fitted with a 4<sup>th</sup> order polynomial.

Figure 34 summarizes the 4<sup>th</sup> order polynomial fitted on averaged data points across the temperature range of -20°C to 85°C ambient.

$$T_c = 0.0000001277x^4 - 0.00002104x^3 + 0.0006398x^2 + 0.03045x + 0.01146 \quad (4.4)$$

Where  $T_c$  is the correction temperature in degree Celsius to be subtracted from measured CU temperature  $x$ . Equation (4.4) has an R-squared value of 0.9325 with an RMSE of 0.1513°C. The green crosses within Figure 34 indicate data points which have been omitted from the model due to large variances seen across trials at their corresponding temperature set point. The omitted data points above the 20°C x-axis tick for example, exhibited large variance among trials due to the digital freezer's difficulty in maintaining a steady 10°C ambient.

When Equation (4.4) was applied to the pre-calibrated data of RTD measurement, a 73.5% reduction in total average bias error was seen while the total average standard deviation remained

roughly 0.1°C. Figure 35 shows the errors seen within measurements to pre-calibrated data prior to correction and post corrections. A complete summary of RTD CJC system’s data can be seen in Appendix F.

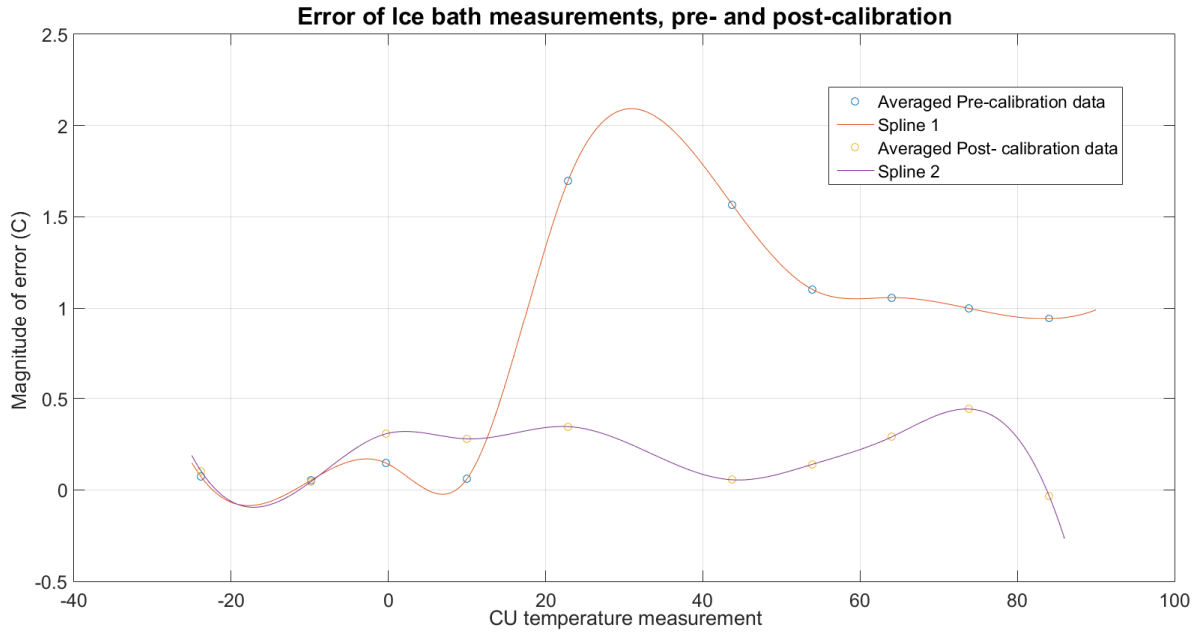


Figure 35. Error magnitude of CU measurement vs. Ice bath temperature measurements after calibration Equation (4.4) is applied to pre-calibrated data. The orange spline visually shows the error associated with pre-calibrated data, and the purple spline the error after correction.

#### 4.1.5 Total Uncertainty of the Thermocouple System

Maximum attainable accuracy of comparison calibration depends upon the reference probe and equipment used with the said probe. The RTD used within preliminary validation is of class A as defined by IEC 60715, the fluid bath used within emf measurements has a manufacturer stated  $\pm 0.07^\circ\text{C}$  (99%, or  $3\sigma$ ) uncertainty, and the Agilent 34970A DAQ has a  $\pm 0.06^\circ\text{C}$  (99%, or  $3\sigma$ ) maximum uncertainty for RTD measurements at up to 1-year after calibration. Noise rejection of the 34970A is given as a NMR (normal mode rejection) and CMRR (common mode rejection ratio) specifications of DAQ. Common mode voltages are assumed to be near ground during experimentation and thus CMRR related noise is not analyzed. NMR is stated as 60dB given an integration time of 20ms (1plc/16.7ms), this equates to maximum random uncertainty in measurement of 0.10%.

### Total Uncertainty of Reference Probe and Measurement Equipment

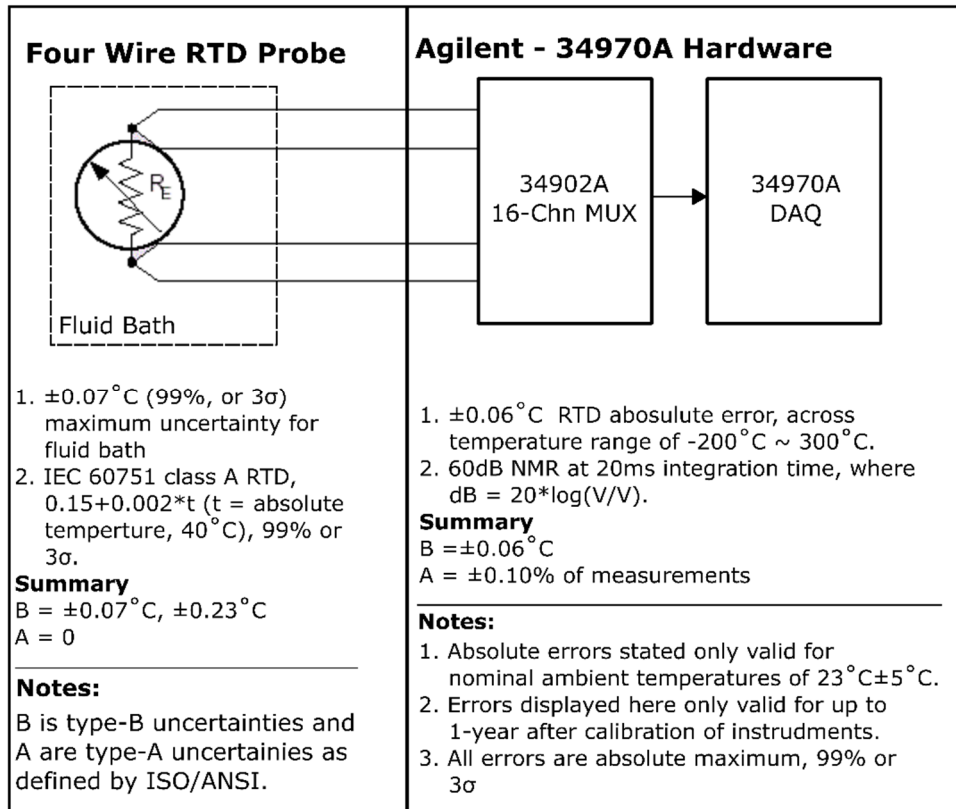


Figure 36. Total uncertainty associated with reference probe measurement.

Summary data in Figure 36 allows us to compute the total uncertainty of the reference probe measurements, type-A and type-B errors where computed with root sum of squares, and then used to compute  $U$  within Equation (4.2). Total type-B errors are  $\pm 0.0826^{\circ}\text{C}$ , total type-A uncertainties are  $\pm 0.013^{\circ}\text{C}$ , and the total uncertainty of the reference probe measurements was determined to be  $\pm 0.167^{\circ}\text{C}$  with a  $k = 2$  (95% coverage,  $2\sigma$ ).

Total uncertainty of thermocouple measurements will be a combination of the uncertainties associated with the emf measurement system, RTD CJC system, and the maximum attainable uncertainty calculated of reference probe measurements. The comparison calibration carried out for the emf measurement system, and the end-to-end calibration conducted for the RTD CJC system attempts to address the systematic errors which propagate due to design and hardware imperfections. Noise and drift errors associated with hardware remain within the measured signals however. Thermal noise associated with filter resistor, bias resistor, common mode and differential mode capacitor in the emf measurement system's filtering stage was computed analytically with Equations (2.21) – (2.23). Noise at the ADS1220 input was assessed by shorting the inputs terminals and collecting measurements. The

resulting span of the ADC code distribution is a direct measurement of the  $V_{pp}$  noise seen by the ADS1220 (Figure 37).

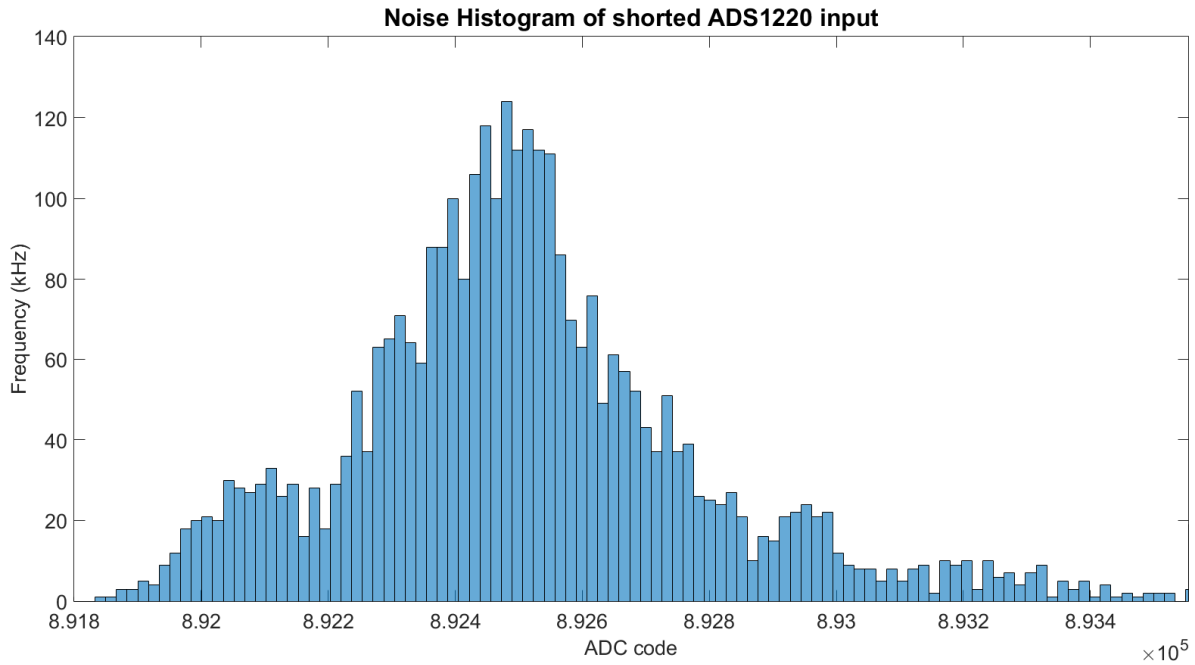


Figure 37.  $V_{pp}$  noise ADS1220 input terminal.

The noise distribution spans 1600 ADC codes, code distribution multiplied by the ADS1220 LSB given by Equation (3.1) results in a  $V_{pp}$  of  $2.414\mu\text{V}$  or a  $0.059^\circ\text{C}$  uncertainty due to noise experienced by the ADS1220 inputs. A complete summary of noise sources accounted for in uncertainty analysis of the emf measurement system can be seen in Figure 38.

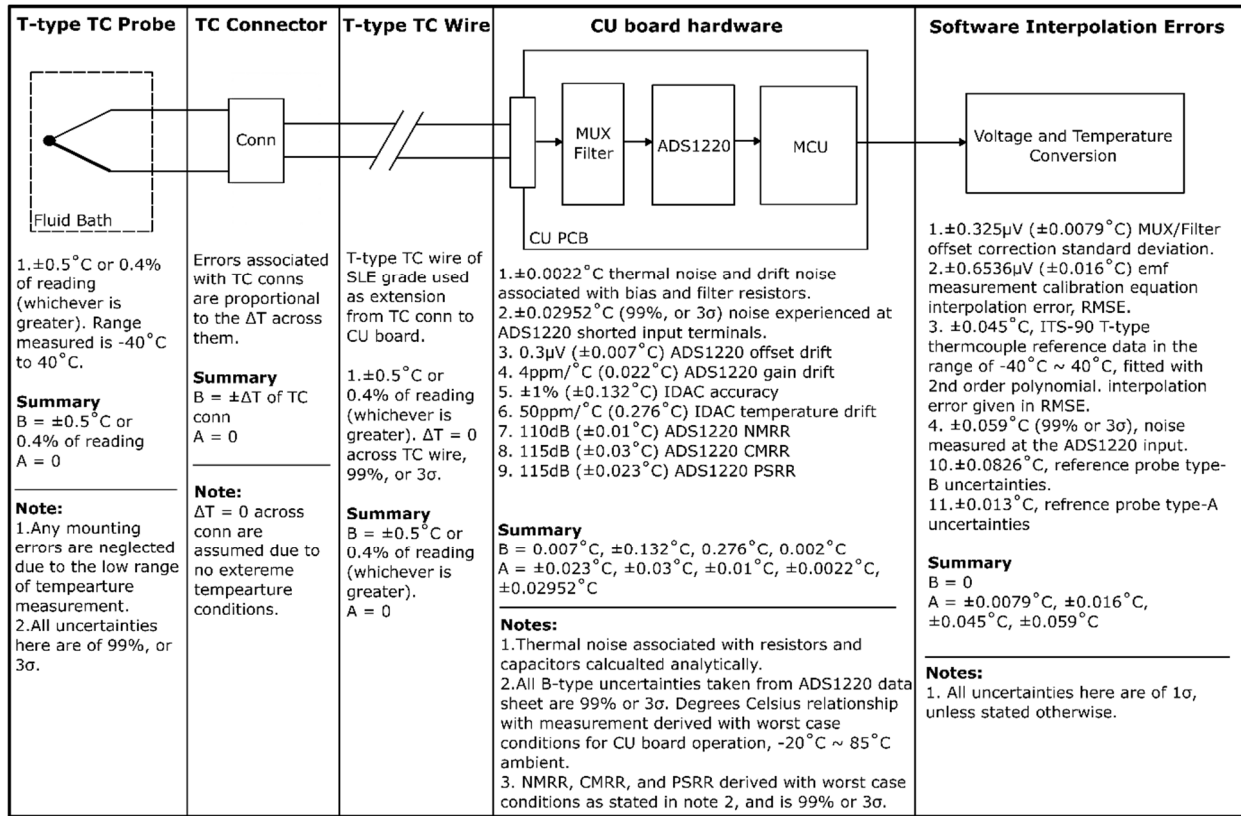


Figure 38. Uncertainties accounted for in emf measurement system.

The root sum of squares of all type-B and type-A uncertainties for the emf measurement system was calculated with the reference probe uncertainties included. Careful attention was given in identifying differences among uncertainties ( $3\sigma$  vs.  $1\sigma$ ) to not over or under-state uncertainties. Type-B uncertainty totaled  $\pm 0.257^{\circ}\text{C}$ , type-A uncertainty was determined to be  $\pm 0.0311^{\circ}\text{C}$ . The emf measurement system has a total uncertainty of  $\pm 0.518^{\circ}\text{C}$  with a  $k = 2$  (95% coverage,  $2\sigma$ ).

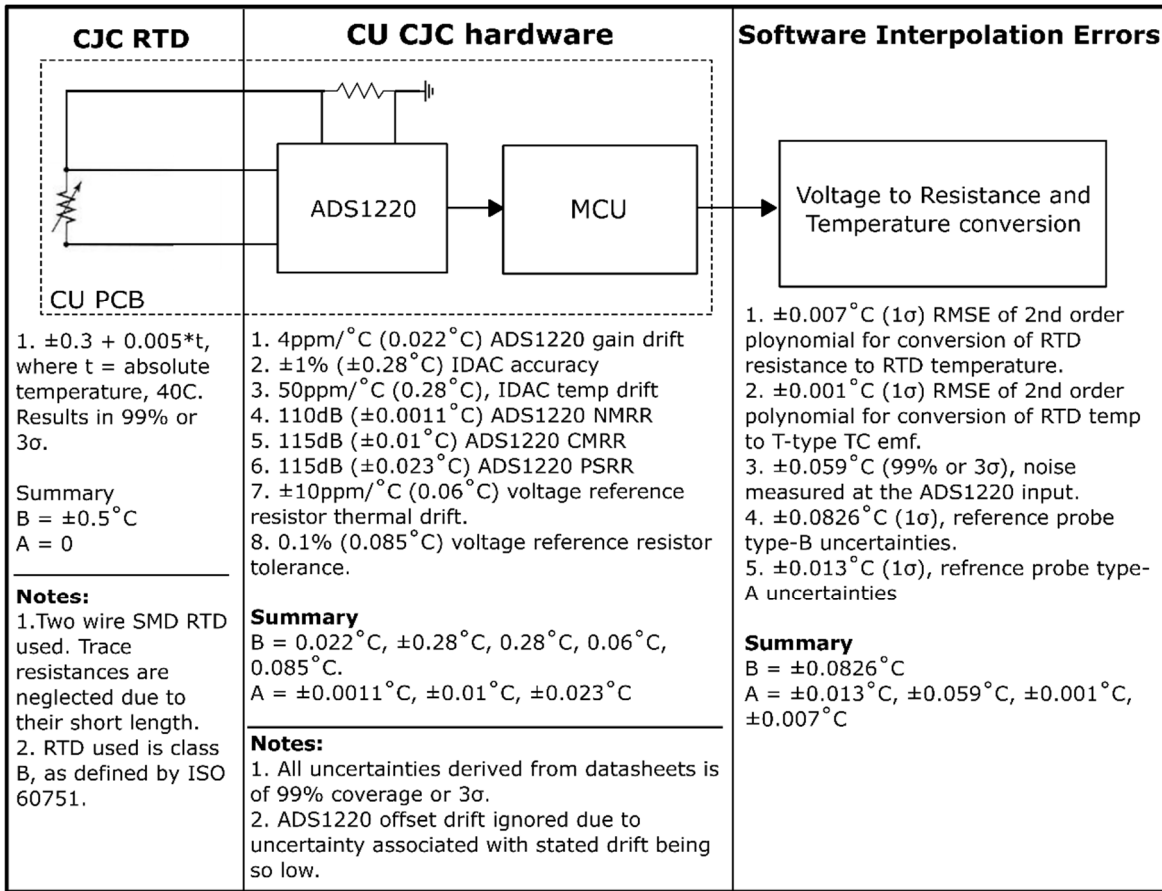


Figure 39. Uncertainties associated with the RTD CJC system.

Figure 39 shows the uncertainties associated with the RTD CJC system. Summed type-B uncertainties were calculated to be  $\pm 0.217^\circ\text{C}$ , type-A uncertainties are  $\pm 0.026^\circ\text{C}$ . The total uncertainties for the RTD CJC system as defined by Equation (4.2) is  $\pm 0.437^\circ\text{C}$  with  $k = 2$  for 95% coverage or  $2\sigma$ .

Combining all type-A and type-B uncertainties from the reference RTD measurements, emf measurement system, and the RTD CJC system allows us to compute the overall uncertainty in the thermocouple measurements used on the CU board. Combined total type-B uncertainties is  $\pm 0.346^\circ\text{C}$ , total type-A uncertainties are  $\pm 0.0426^\circ\text{C}$ , the total uncertainty of the overall thermocouple measurement system is  $\pm 0.7^\circ\text{C}$ , this stated uncertainty is valid for the measurement ranges of  $-20^\circ\text{C}$  to  $40^\circ\text{C}$ , with CU ambient temperature range of  $-20^\circ\text{C}$  to  $85^\circ\text{C}$  with the use of SLE grade T-type thermocouple wire.

## 4.2 Current measurement

### 4.2.1 Materials and Methods

Current measurements were taken every 10 seconds for a total of 44 measurements. Sampling rates of associated ADC within the PEF and OMF systems were set via software at 12 samples per 1 periods of PEF waveform for all frequency ranges, and 24 samples per 1 periods of OMF waveform for all frequency ranges. The PEF system was tested with a dummy resistive load (FMP200FRF52-100R, Yageo, Taiwan) at various voltages between 1V to 10.5V. The OMF system was tested with two separate loads, a resistive load (SQP10AJB-820R, Yageo, Taiwan) for low end current measurements, and the sample chamber electromagnets for higher current measurements. OMF voltage test settings were 6V, 22V, 38V, 55V, and 70V. Validation of current measurements was compared with data collected by Agilent DAQ (34970A, Agilent, Santa Clara, CA) using 16-channel multiplexer (34902A, Agilent, Santa Clara, CA). The Agilent DAQ measured the  $V_{AC}$  voltage drop across an external shunt resistor in series with its respective PEF or OMF load. The external shunt used for PEF validation was sized at  $1\Omega$  (WSC25151R000FEA, Vishay Dale, Shelton, CT), and the OMF external shunt was sized at  $0.02\Omega$  (WSR5R0200FEA, Vishay Dale, Shelton, CT). In addition, the Agilent DAQ also measured the applied  $V_{DC}$  of the PEF and OMF H-bridge supply rail, and the  $V_{AC}$  of CU board shunt resistor before and after the LT1999s used in the OMF and PEF system. Measurements between Agilent DAQ and CU were synced using a TTL trigger signal from CU to Agilent DAQ. Data was collected onto laptop computer with Arduino IDE serial monitoring (Arduino, Torino, Italy) for CU data and DAQ data was collected with Benchlink Data logger software (Keysight, Santa Rosa, CA). The CU was powered with custom power supply which provided  $80V_{DC}$  for OMF systems and  $24V_{DC}$  for PEF systems. All statistical analysis of collected data was carried out in MatLab R2015a (MathWorks, Natick, MA), and Excel 2016 (Microsoft Corp, Redmond, WA).

### 4.2.2 Results and Discussion

The OMF system's testing did not include a frequency sweep of OMF operational frequency range as the range of operation changes very little (1Hz to 10Hz). In addition the Agilent DAQ has a minimum 3Hz  $V_{AC}$  measurement limit, and higher accuracy at 10Hz or above [131], thus 10Hz was chosen as the testing frequency for all OMF current measurements. Captured CU data was composed of 24 instantaneous  $V_{DC}$  measurements, the OMF current waveform reconstructed from CU data is shown in Figure 40.

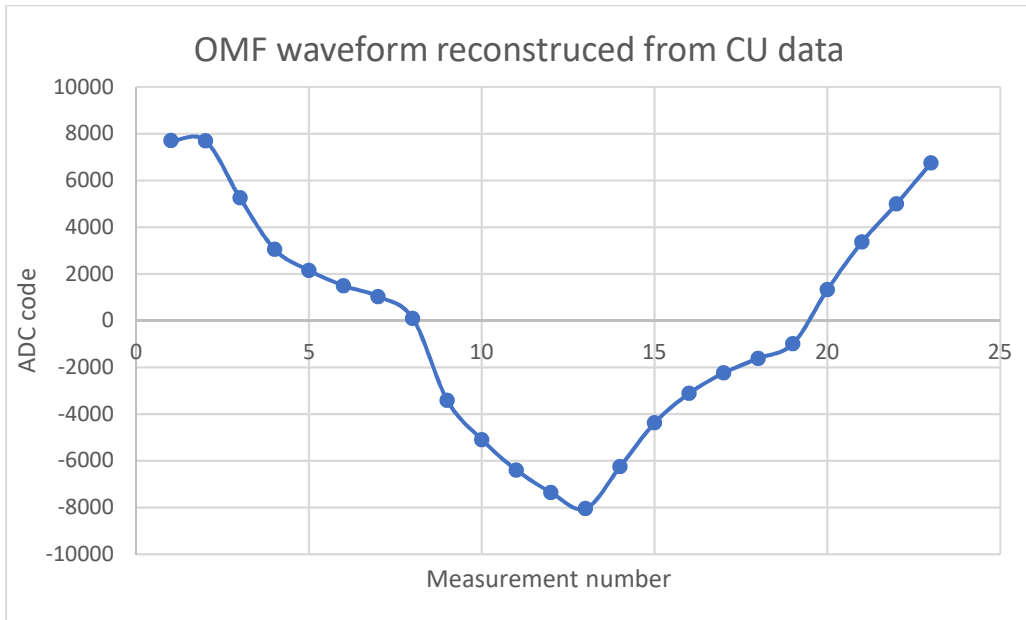


Figure 40. OMF waveform reconstructed from CU raw data at 10Hz, 70V sample chamber load.

The waveform as observed in Figure 11, closely resembles that of Figure 40, given a single period of the Figure 10’s waveform is considered. The first type of load tested on the OMF system was the resistive 820Ω load, this Ω value was selected to gauge the OMF systems’ current measurement capabilities in low current settings. A summary of the results is given in Table 9.

Table 9. Resistive load current measurement summary.

	OMF system at 10Hz, with 820Ω resistive dummy load				
	6V	22V	38V	54V	70V
Gain (V/V)	5.1612 ± 0.00005	11.913 ± 0.000147	14.811 ± 0.000223	16.235 ± 0.000283	16.768 ± 0.000351
Applied Voltage (V)	6.633 ± 0.0297	22.264 ± 0.00416	38.399 ± 0.00869	54.610 ± 0.0158	70.716 ± 0.0123
CU current (A)	0.0190 ± 0.000183	0.0288 ± 0.000696	0.0412 ± 0.00102	0.0545 ± 0.001416	0.0685 ± 0.00169
DAQ current (A)	0.000457 ± 0.000023	0.0162 ± 0.000291	0.0326 ± 0.000129	0.0468 ± 0.000190	0.0613 ± 0.000223
% diff (CU vs DAQ)	190.60%	55.88%	23.24%	15.20%	11.21%

DAQ current measurements and CU current measurements have a large %difference as indicated within Table 9, raising the test voltage resulted in lower %difference as the current flowing through the resistive load resulted in a larger measurable voltage drop across the OMF system’s on-board shunt resistor. This is expected behavior given our FSR for the ADS1115 results in a 0.125mV LSB, at 6V the expected current through an 820Ω resistive load is 5.7mA, this current through the on-board OMF shunt resistor (0.03Ω) will results in a voltage drop of 0.172mV. At this range, the theoretical limit of our ADS1115’s performance is reached. The large %differences in Table 8 also reflect the noise present within our measurement signal, which can be visualized by shorting the input terminals of the ADC and recording measurements, the result of which is shown in Figure 41.

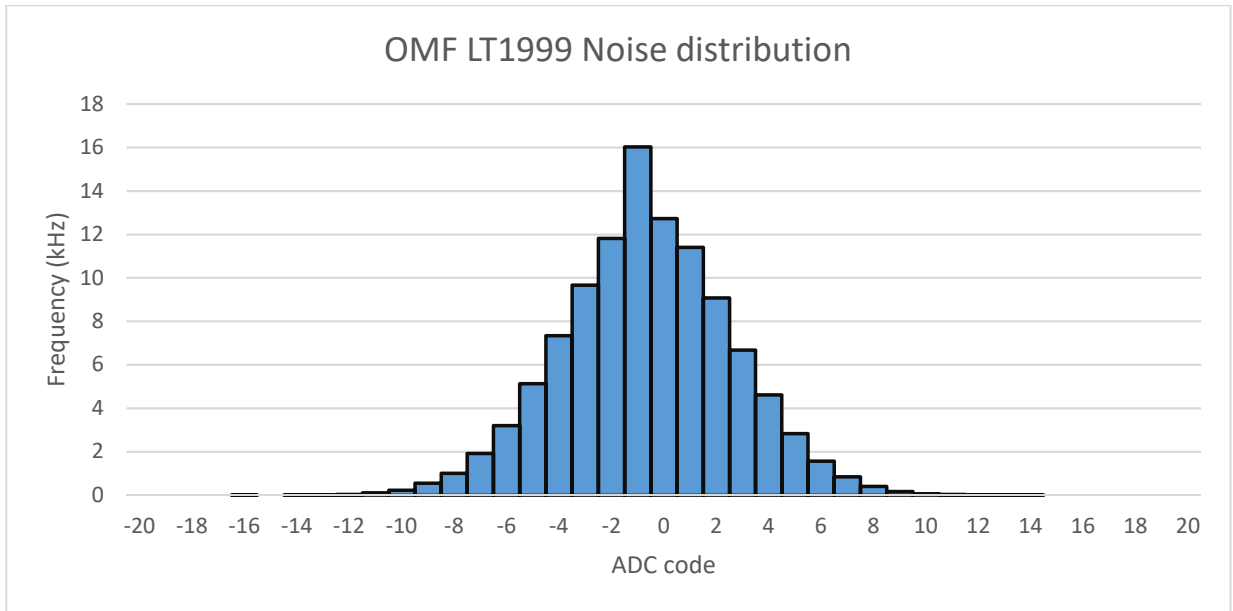


Figure 41. OMF current measurement system LT1999 noise spread.

The spread of the ADC code reflects the inherent noise within the OMF current measurement system due to internal IC imperfections and environmental factors. The 32-code spread equates to 4mV<sub>pk-pk</sub> noise, and the high measurement concentration on ADC code -1 indicates little to no internal offset within the OMF current measurement system. The low signal to noise ratio in the low current settings drowns out any reliable measurements sub 0.1 Amperes. Table 10. Contains the summary of the OMF system’s current data with the sample chamber electromagnets used as the test load.

Table 10. Sample chamber load current measurement summary.

OMF system at 10Hz, with sample chamber electromagnet load						
	6V	22V	38V	54V	70V	
<b>Gain (V/V)</b>	19.080 ± 0.000204	20.081 ± 0.000992	20.0612 ± 0.00236	20.0567 ± 0.00354	20.0542 ± 0.00454	
<b>Applied Voltage (V)</b>	6.684 ± 0.0345	23.014 ± 0.111	38.649 ± 0.4632	54.762 ± 0.624	71.877 ± 0.679	
<b>CU current (A)</b>	0.0875 ± 0.00083	0.3253 ± 0.00371	0.5495 ± 0.0073	0.779 ± 0.009104	01.023 ± 0.0129	
<b>DAQ current (A)</b>	0.0.08426 ± 0.000386	0.0318 ± 0.00173	0.537 ± 0.00388	0.763 ± 0.00595	1.0034 ± 0.00902	
<b>% diff (CU vs DAQ)</b>	3.78%	2.36%	2.21%	2.11%	1.95%	

%difference improved significantly with increasing signal strength across the OMF system’s shunt resistor. Gain leveled off to roughly 20V/V as expected with the LT1999’s built in gain set at 20V/V. Table 8’s gain values showed erroneous results due to the small voltage signal across the OMF shunt resistor making it difficult for the Agilent DAQ to measure. Combined results for Table 8 and 9 can be seen visually in Figure 42.

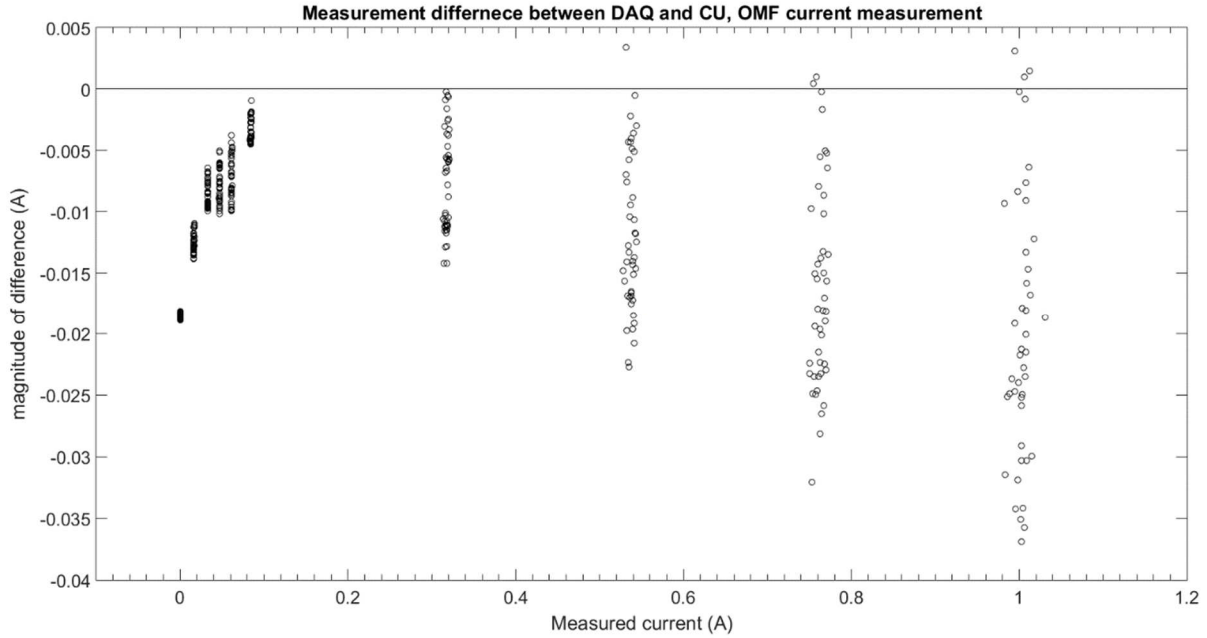


Figure 42. OMF current measurement summary. Difference magnitude of current measurements between DAQ and CU.

Below 0.1 Amperes current measurements are unreliable and are largely dictated by noise, however above 0.1 Amperes, there is a clear trend of current measurement uncertainty. As the measured current increases, the distribution of CU measurements remains at a constant 4% uncertainty of measured current with respect to DAQ measured values. The central concentration (i.e, mean) of the distributions within Figure 42 can also be seen to decrease with growing current measured by the CU. Correction of this measurement drift can be applied with a curve fitting model of the total averaged OMF data (Figure 43)

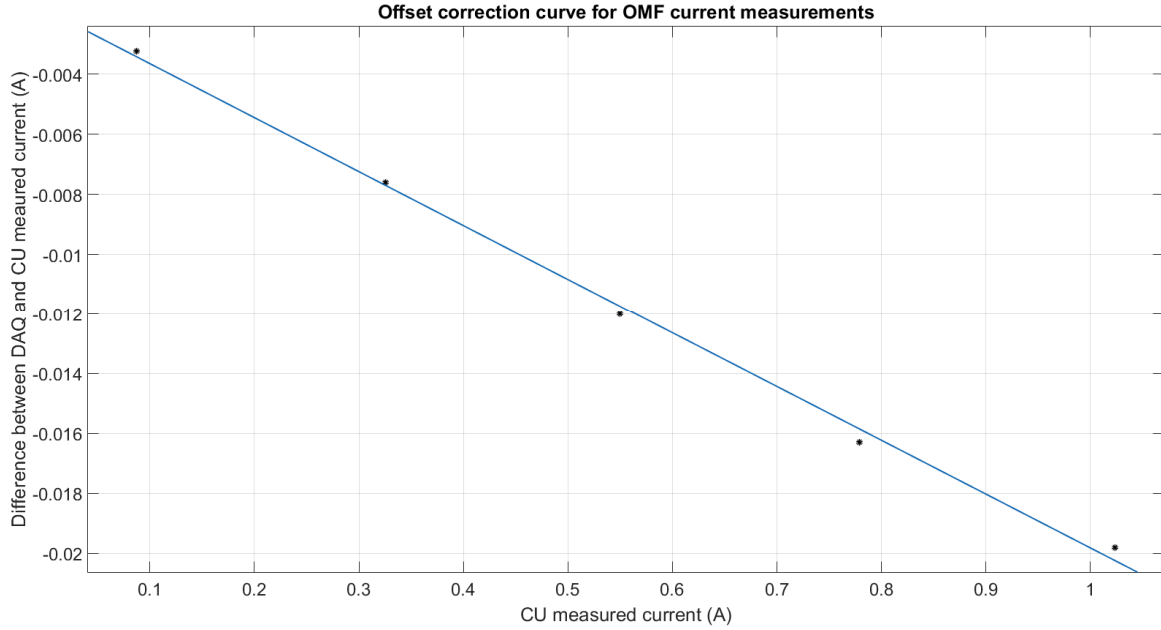


Figure 43. OMF offset correction curve.

The fitted linear model has an R-squared value of 0.9971 with RMSE of 0.0004112A. The equation overall equation is,

$$y = -0.01798x - 0.00185 \quad (4.5)$$

where  $y$  is the OMF offset correction to be summed with OMF CU current measurement  $x$ .

The PEF current measurement system spans a large frequency range which can affect current measurements due to loop inductances at the shunt resistors. A frequency sweep from 100Hz to 20kHz at a constant voltage was conducted to observe any potential changes in current measurements.

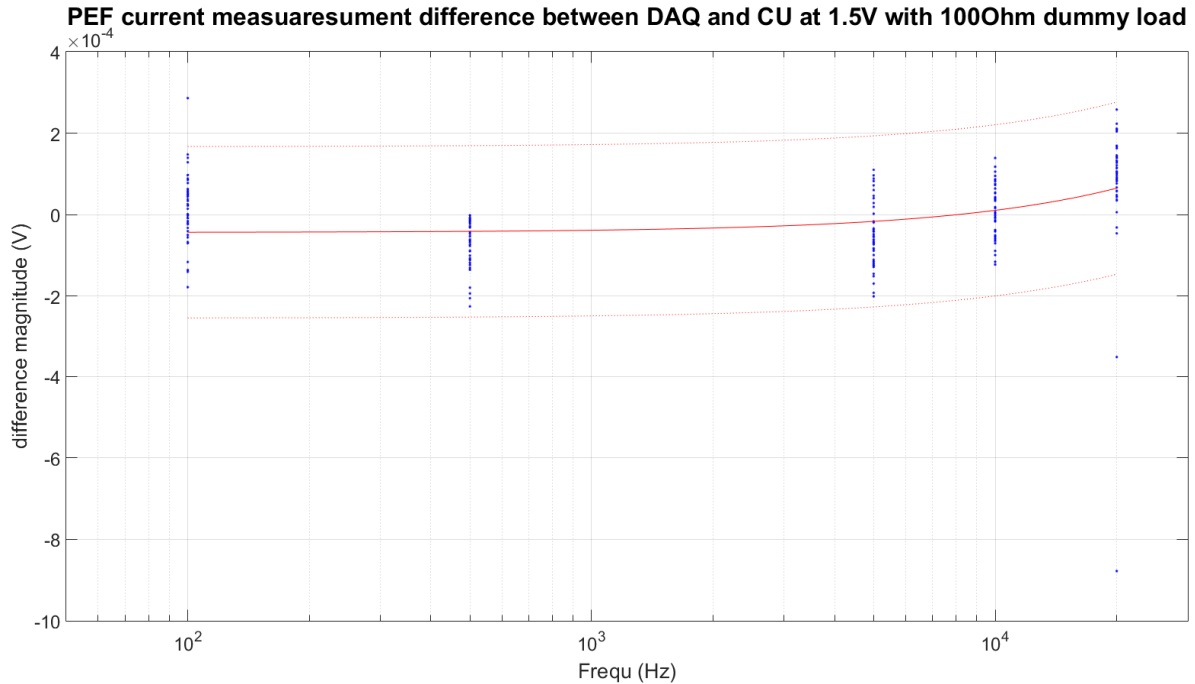


Figure 44. PEF current measurements across 100Hz to 20kHz.

As seen in Figure 44 there is very little measurable differences between current measurements across the intended operational frequency range for PEF application. Excluding outliers, the total span of measurements covers  $\pm 2\mu\text{V}$  across all frequency ranges, a much smaller value than the LSB of the ADS122 ADC (1.22mV) used within the PEF system.

The reconstructed waveform from data captured by the PEF current measurement system can be seen in Figure 45.

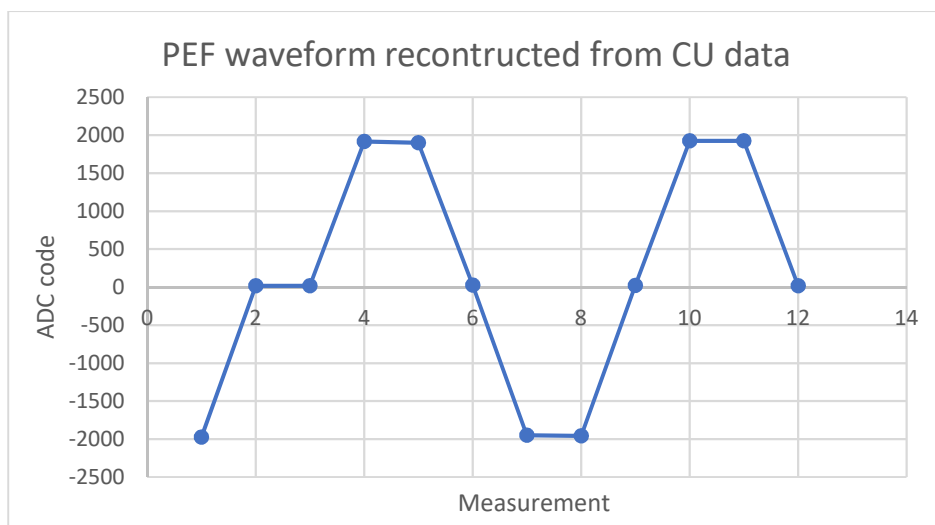


Figure 45. PEF waveform reconstructed from CU data at 20kHz, 10.4V with resistive dummy load

Comparing Figure 45 with that of Figure 10, we can see some resemblance in waveform shape. But due to hardware limitation at 20kHz PEF, the waveform seen in Figure 43 is not quite an exact representation with that of Figure 9. This can introduce large errors into  $V_{rms}$  calculations using Equation (2.5), however because we know the expected waveform's shape to be of a biphasic wave from (due to foods exhibiting resistive load behaviors) we are able to use Equation (2.6) in lieu of (2.5) for  $V_{rms}$  calculations. Table 10. Summarizes the results of PEF current measurements.

Table 11. PEF current measurement summary with 100Ohms resistive load.

PEF system at 20kHz, with 100Ω resistive load						
	1.4V	2.4V	4.4V	6.4V	8.4V	10.4V
Gain (V/V)	20.042 ± 0.00127	20.018 ± 0.00062	20.0022 ± 0.0031	19.979 ± 0.00209	19.939 ± 0.00454	19.755 ± 0.008322
Applied Voltage (V)	1.281 ± 0.000105	2.307 ± 0.000331	4.304 ± 0.00128	6.398 ± 0.00213	8.363 ± 0.00153	10.192 ± 0.00364
CU current (A)	0.0088932 ± 0.0001353	0.01601 ± 0.0001192	0.02990 ± 0.0000185	0.0445 ± 0.000269	0.05787 ± 0.0002502	0.06948 ± 0.003642
DAQ current (A)	0.009016 ± 0.00000042	0.01621 ± 0.00000083	0.0303 ± 0.00000431	0.04502 ± 0.00000697	0.0588 ± 0.0000108	0.0714 ± 0.0004902
% diff (CU vs DAQ)	1.37%	1.23%	1.26%	1.20%	1.57%	2.70%

%difference between calculated means of DAQ and CU measurements remains within 1.5% to 3%. The overall results taken as the difference between DAQ and CU measurements are plotted with respect to measured current in Figure 46.

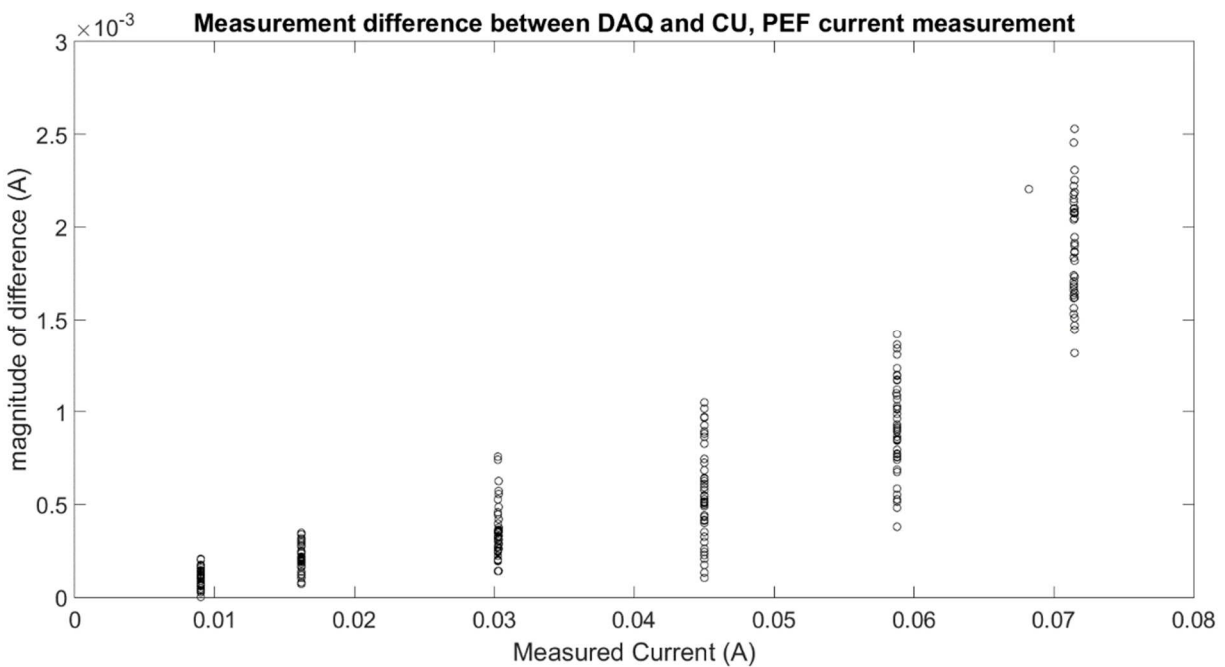


Figure 46. Difference magnitude of PEF measurements between DAQ and CU.

As measured current increases so does the spread of data points, the spread however remains constant at 2% of the measured current value, indicating uncertainty of CU measurements with respect to DAQ measurements are within 2%.

Noise within the PEF system was assessed with the histogram method as seen in Figure 47, where the input terminals of PEF current measurement system were shorted, and data collected.

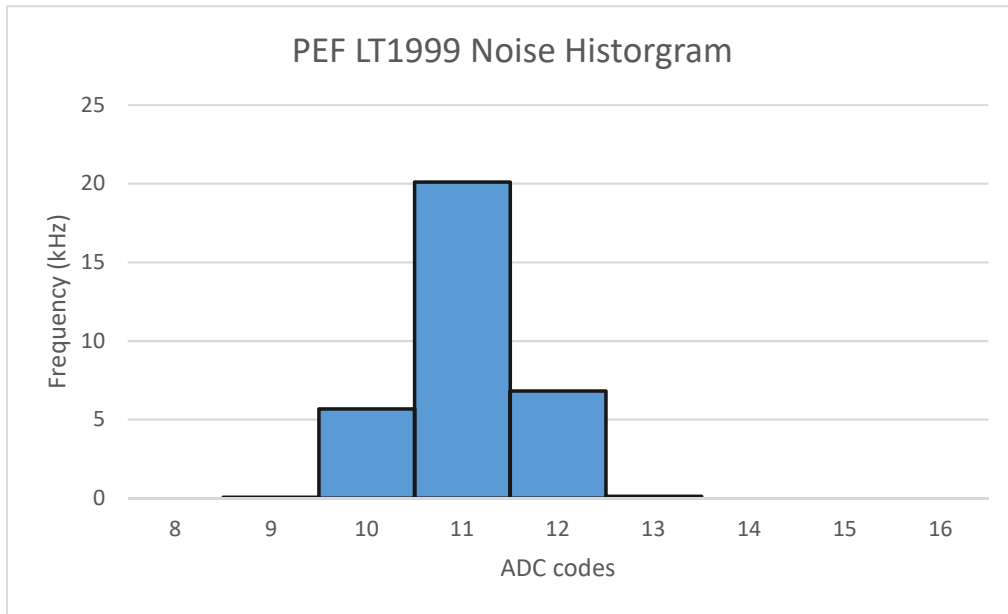


Figure 47. PEF current measurement system LT1999 noise spread.

The span of the noise present within the PEF current measurement system covers 5 ADC codes or  $6.11\text{mV}_{\text{pk-pk}}$ , which translates to a  $0.00509$  Ampere minimum measurement limit. The heavy concentration on code 11 within Figure 47 indicates an offset of  $13.431\text{mV}$  present within measurements, which can be corrected within software. The corrections are applied through an equation derived from a 3<sup>rd</sup> order polynomial curve fit of total averaged PEF data (Figure 48).

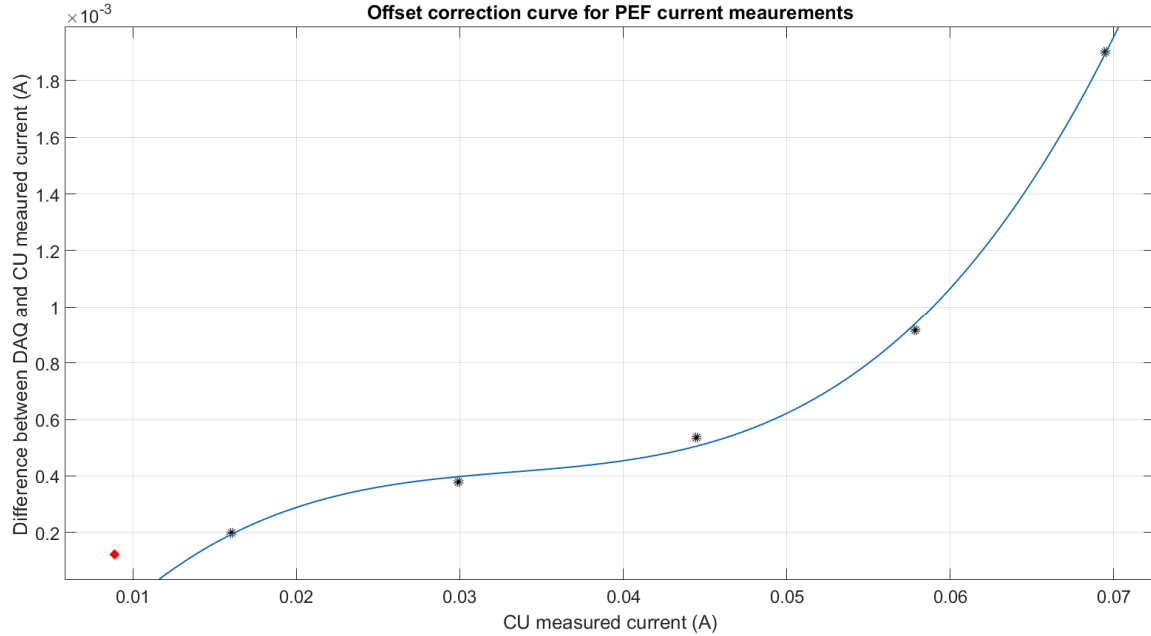


Figure 48. PEF offset correction curve.

PEF offset did not follow a linear trend as with the OMF system, also a single data point which fell below the PEF measurement threshold was excluded from the model. The R-squared value of the fitted curve is 0.999 with an RMSE of 0.00004344A. The applied equation derived from the curve fitting model is

$$y = 27.53x^3 - 2.745x^2 + 0.0959x - 0.0007516 \quad (4.6)$$

Where  $y$  is the PEF offset correction value to be summed with CU measurements  $x$ .

#### 4.2.3 Total Uncertainty of OMF and PEF Current Measurement Systems

The minimum attainable uncertainty associated with the current measurement systems will be dependent upon the uncertainty associated with the reference equipment used to compare CU collected data. In this case the Agilent DAQ and external shunt resistor used within the reference data equipment will determine the minimum attainable uncertainties. Agilent DAQ uncertainties for RMS AC voltage measurements at the shunt resistor will depend upon voltage measurement range, frequency and waveform crest factor. The DAQ technical overview provides methods in determining uncertainties of measurement with respect to the previously stated factors [131]. Worst case conditions occur when PEF and OMF systems are measuring their lowest possible current limits, 0.1 Amperes for OMF and 0.01 Amperes for PEF. In testing conditions PEF and OMF frequencies were set at 20kHz for PEF and 10Hz for OMF, crest factors were calculated with the following

$$CF = \frac{|V|_{pk}}{V_{rms}} \quad (4.7)$$

Where  $|V|_{pk}$  and  $V_{rms}$  were measured using an Oscilloscope (HMO1232, Rohde&Schwarz, Columbia, MD) across the external shunt resistor for every test voltage point. OMF crest factors remained near 1.45, and PEF at 3.32. The same NMR and CMRR from calculations from the thermocouple system total uncertainties can apply here.

The external shunt resistor used for the OMF system was sized at  $0.03\Omega$  with a  $\pm 1\%$  (99%,  $3\sigma$ ) uncertainty  $\pm 75\text{ppm}/^\circ\text{C}$  drift. The PEF shunt resistor sized at  $1\Omega$  had a  $\pm 1\%$  (99%,  $3\sigma$ ) uncertainty with  $\pm 50\text{ppm}/^\circ\text{C}$  drift. A summary of all uncertainties associated with the current measurement reference data collection equipment can be seen in Figure 49.

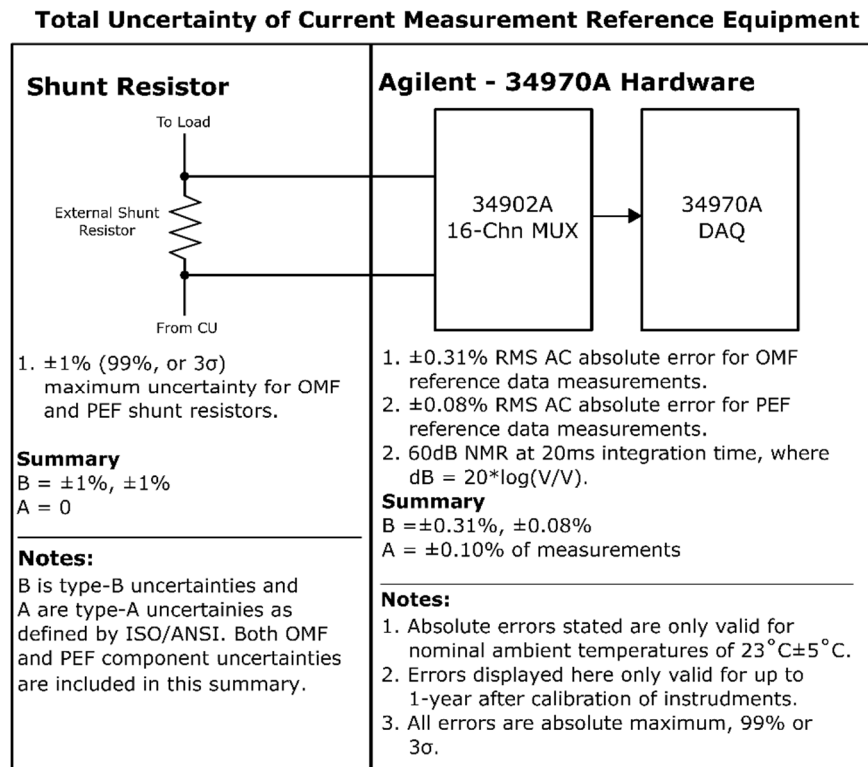


Figure 49. Total uncertainties associated with current measurement reference data collection equipment.

The total type-A uncertainties for OMF and PEF system is  $\pm 0.03\%$  and the total type-B uncertainties for OMF was determined to be  $\pm 0.35\%$ . The total type-B uncertainty for the PEF system was calculated as  $\pm 0.33\%$ . Total uncertainties associated with the current measurement reference equipment was calculated following Equation (4.2). For OMF this was determined to be  $\pm 0.7\%$  with  $k = 2$  (95%,  $2\sigma$ ), and for PEF  $\pm 0.66\%$  with  $k = 2$  (95%,  $2\sigma$ ).

The experimentally derived uncertainties in section 4.2.2 for the OMF current measurement system was 4%, and for the PEF system it was 2%. These values are the result of an end-to-end measurement calibration with all combined uncertainties associated with the current measurement hardware (on board shunt resistor, current monitor, and ADC). Ambient temperature effects upon measurements are considered through manufacturer supplied information contained within component data sheets and is summarized in Figure 50 and 51.

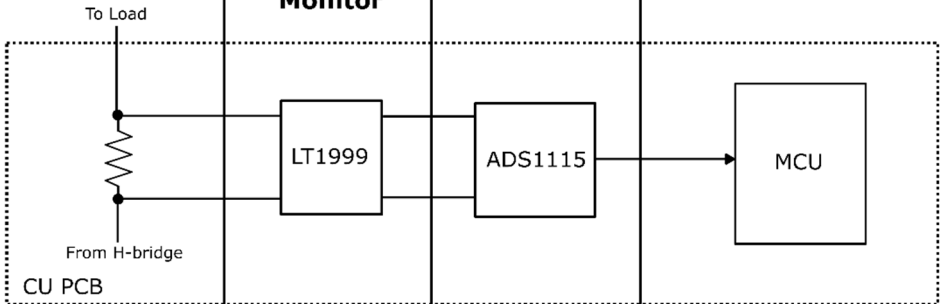
Shunt Resistor	Current Monitor	ADC	End-to-End data
 <p>1. <math>\pm 50\text{ppm}/^{\circ}\text{C}</math> drift or <math>\pm 0.325\%</math>, for <math>\Delta T</math> of <math>65^{\circ}\text{C}</math>.</p> <p><b>Summary</b>  <math>B = \pm 0.325\%</math>  <math>A = 0</math></p> <p><b>Note:</b>            1. <math>\Delta T</math> is the maximum temperature change CU board can experience given nominal operating temperature of <math>25^{\circ}\text{C}</math>, in operational range of <math>-20^{\circ}\text{C}</math> to <math>85^{\circ}\text{C}</math> ambient.            2. All uncertainties here are of 99%, or <math>3\sigma</math>.</p>	<p>1. <math>0.125\%</math> gain drift.            2. <math>8\mu\text{V}/^{\circ}\text{C}</math> offset drift or <math>0.87\%</math> measurement offset for <math>\Delta T</math> of <math>65^{\circ}\text{C}</math>.</p> <p><b>Summary</b>  <math>B = 0.125\%</math>,  <math>0.87\%</math>  <math>A = 0</math></p> <p><b>Note:</b>            1. Translation of drifts to % value was done by taking worst case condition of OMF system when measuring <math>0.1\text{A}</math> at shunt resistor.            2. All uncertainties here are of 99%, or <math>3\sigma</math>.</p>	<p>1. <math>0.005\text{LSB}/^{\circ}\text{C}</math> offset drift or <math>0.068\%</math>, for <math>\Delta T</math> of <math>65^{\circ}\text{C}</math>.            2. <math>40\text{ppm}/^{\circ}\text{C}</math> gain drift or <math>0.26\%</math>, for <math>\Delta T</math> of <math>65^{\circ}\text{C}</math>.</p> <p><b>Summary</b>  <math>B = 0.068\%</math>,  <math>0.26\%</math>  <math>A = 0</math></p> <p><b>Note:</b>            1. Translation of drifts to % value was done by taking worst case condition of OMF system when measuring <math>0.1\text{A}</math> at shunt resistor.            2. All uncertainties here are of 99%, or <math>3\sigma</math>.</p>	<p>1. <math>\pm 1.71\%</math> of measured value as derived from end-to-end experimental validation.</p> <p><b>Summary</b>  <math>B = 0</math>  <math>A = \pm 1.71\%</math></p> <p><b>Notes:</b>            1. All uncertainties here are <math>1\sigma</math>.</p>

Figure 50. Uncertainties accounted for within the OMF current measurement system.

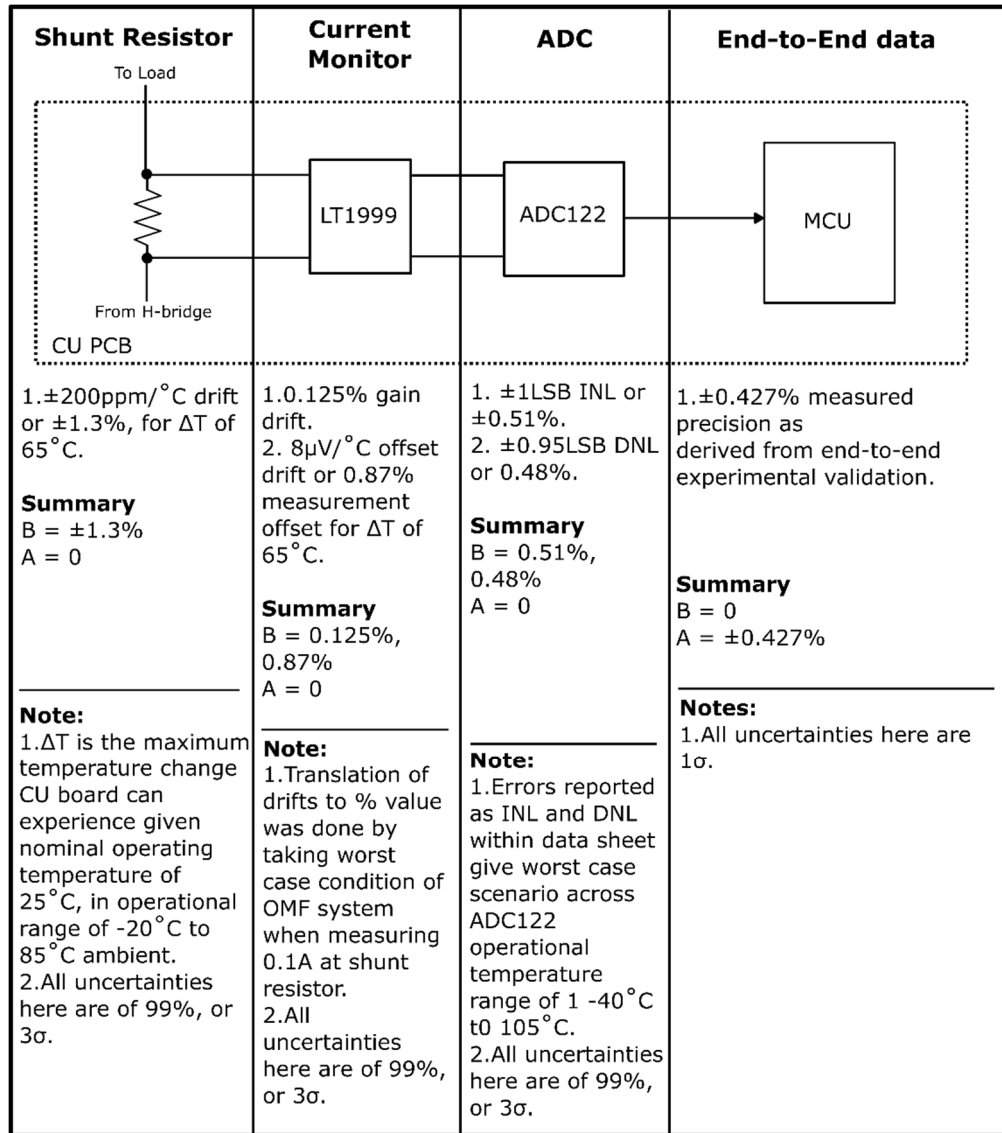


Figure 51. Uncertainties accounted for within the PEF current measurement system.

The type-A uncertainties associated with the OMF system totals to  $\pm 1.3576\%$ , type-B totals to  $0.477\%$ . The overall total uncertainty of the OMF system with reference data collection equipment uncertainties included in Equation (4.2) results in a  $U = \pm 2.88\%$  of measurement with  $k = 2$  (95%,  $2\sigma$ ). The PEF system has a total type-A uncertainty of  $\pm 0.543\%$ , and a total type-B uncertainty of  $\pm 0.66\%$ . The overall total uncertainty of the PEF system with reference data collection equipment uncertainties included in Equation (4.2) results in a  $U = \pm 1.71\%$  of measurement with  $k = 2$  (95%,  $2\sigma$ ).

### 4.3 Voltage Measurement

#### 4.3.1 Materials and Methods

Voltage on the CU board for both PEF and OMF systems were varied from maximum to minimum settings. For OMF this was between 70V and 5V, for PEF this was 10.5V and 1V. A minimum of ten measurement points between each testing range was taken for validation. An Agilent DAQ (34970A, Agilent, Santa Clara, CA) with 16-channel multiplexer (34902A, Agilent, Santa Clara, CA) was used to measure the attenuated voltage signal from the voltage measurement system. The same signal was measured by the CU's MCU and data logged onto SD™ card. The Agilent DAQ data served as reference data upon which MCU collected data was compared.

#### 4.3.2 Results and Discussion

Figure 52 is a summary of OMF voltage preliminary verification. There is a highly linear relationship between CU data and DAQ data as indicated by the linear fit model. The R-squared value of which is 1 with an RMSE of 0.07554V. Taking the difference between DAQ measured voltage and CU reported voltage results in Figure 53, the average magnitude of difference between DAQ and CU measurements was calculated as 0.14V with a standard error of 0.0807V.

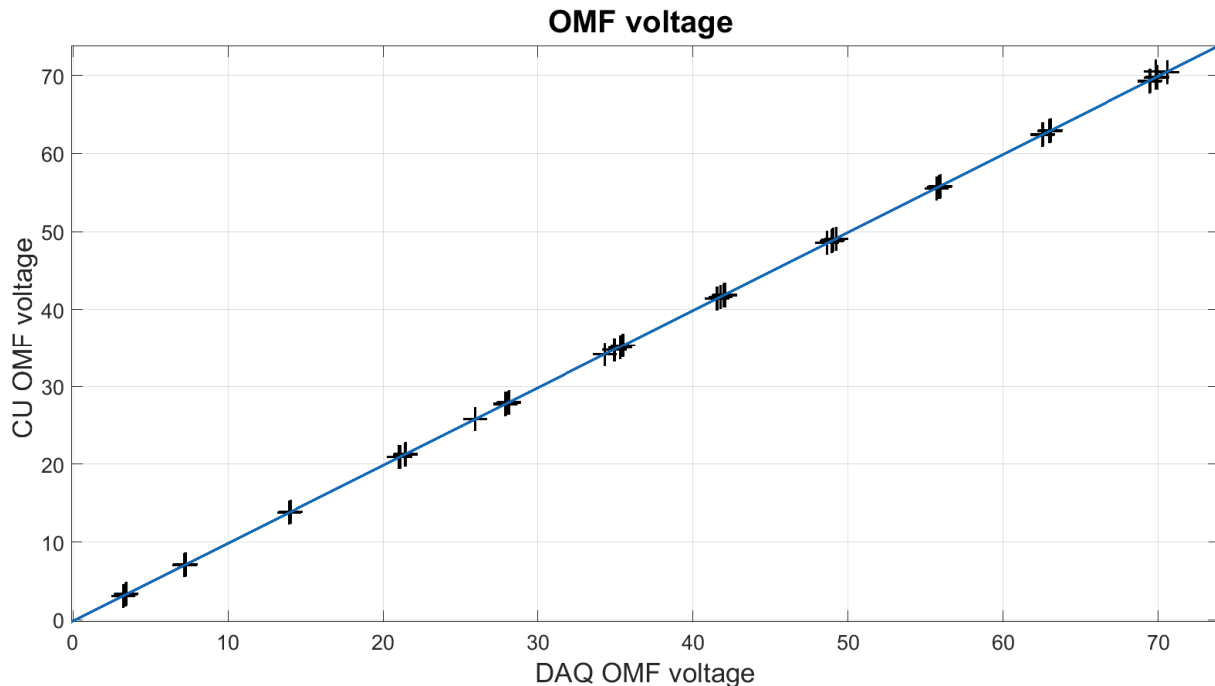


Figure 52. OMF voltage validation data, x-axis is the reference data collected from DAQ and y-axis the OMF voltage collected and logged by CU.

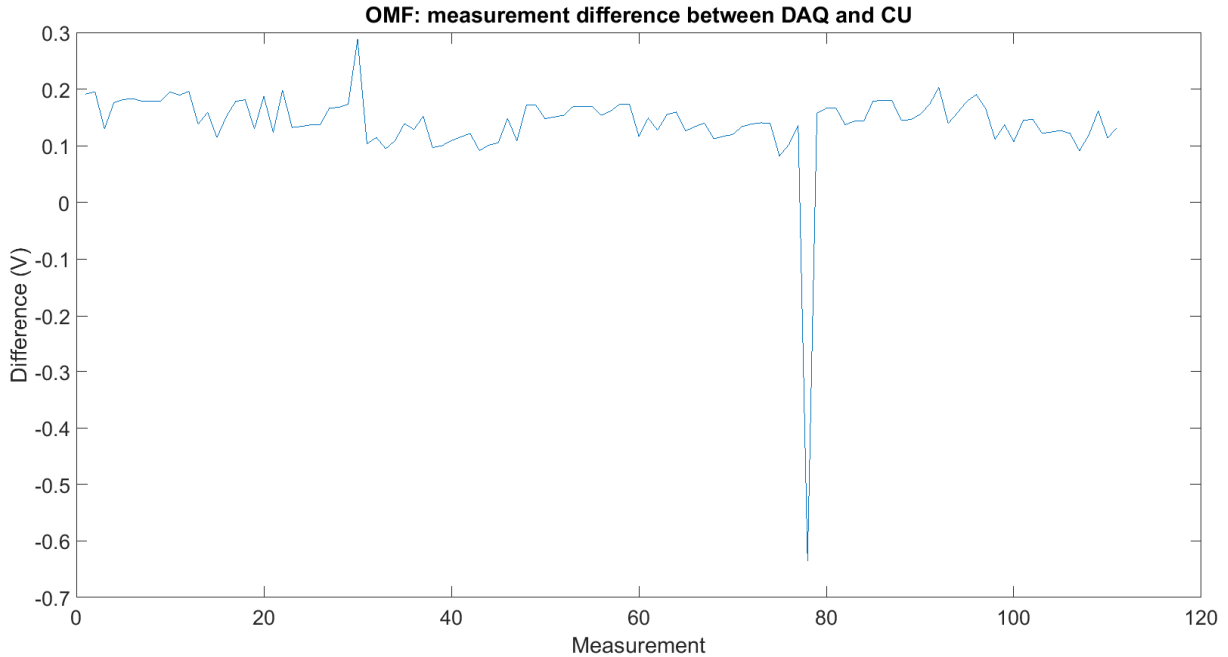


Figure 53. Measurement difference between DAQ measured OMF voltage and CU measured OMF voltage.

PEF voltage preliminary verification is summarized in Figure 54. Again, there is a highly linear relationship between CU data and DAQ collected data. The linear model fitting resulted in an R-squared value of 1 with an RMSE of 0.004424V. The difference taken between DAQ measured PEF voltage and CU measured PEF voltage can be seen in Figure 55. The average difference was calculated as 0.0298V with a standard deviation of 0.0044V.

Both PEF and OMF voltage data showed minor offsets present within their measurements, with the DAQ measurements reporting slightly higher values over the CU system. As expected the PEF voltage measurement system was able to achieve higher precision due to the smaller voltage range involved in the PEF H-bridge system and the 10-bit ADC used for voltage measurements.

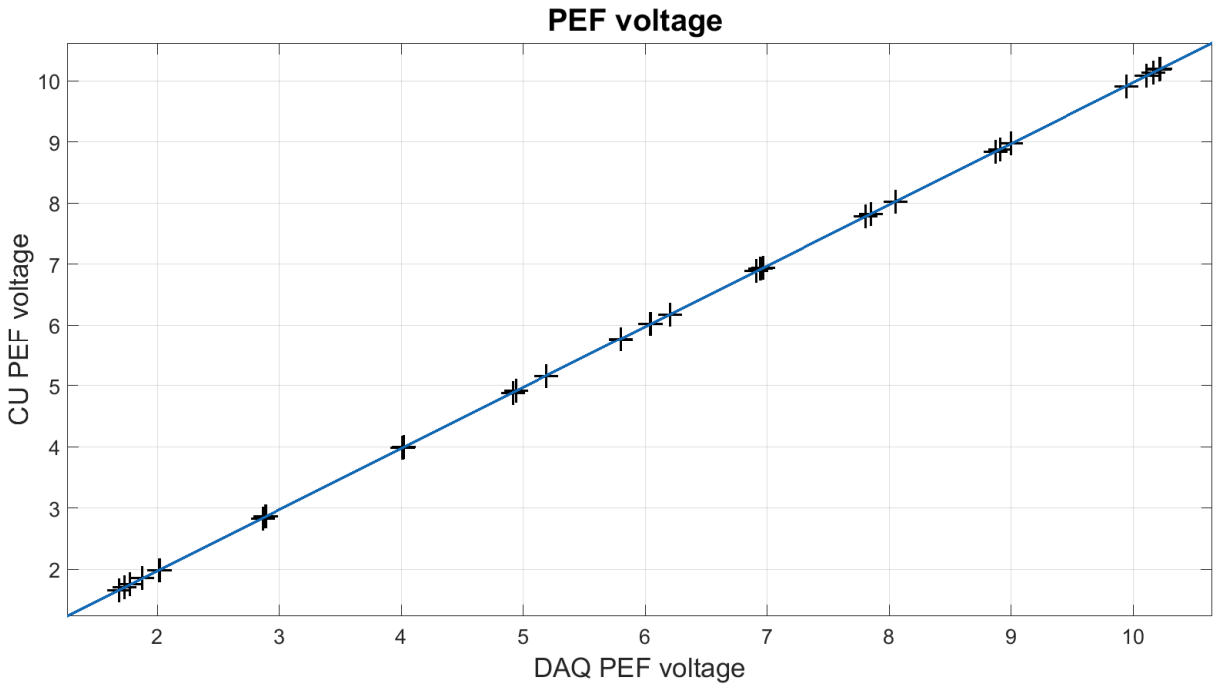


Figure 54. PEF voltage validation data, x-axis is the reference data collected from DAQ and y-axis the PEF voltage collected and logged by CU

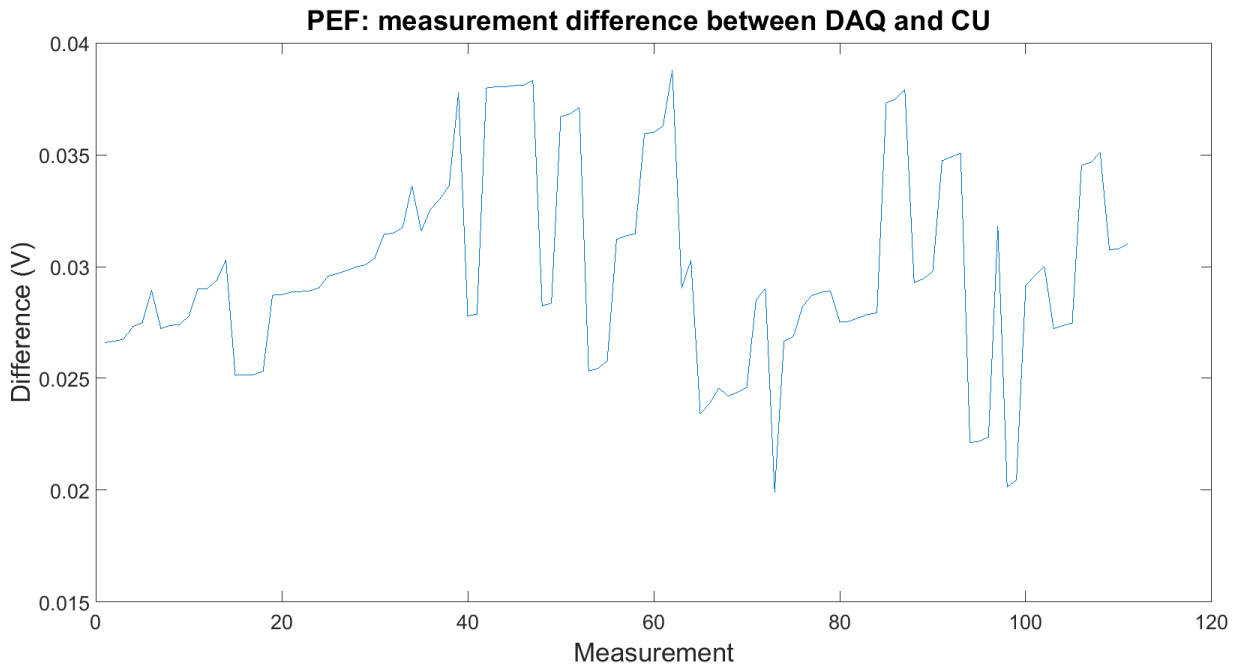


Figure 55. Measurement difference between DAQ measured PEF voltage and CU measured PEF voltage.

### 4.3.3 Total Uncertainty of the PEF and OMF Voltage Measurement System

The minimum attainable uncertainty for the voltage measurement system is dependent upon the reference equipment used for comparison. For this purpose, the Agilent DAQ was operated in 5.5-digit precision with measurement points placed prior to the ATMEGA328P. As a result, the measured voltage by the DAQ varied from 0-5V for both the PEF and OMF system. The errors involved within the reference data will be a combination of the resistor accuracy of the voltage divider network, filter resistor/capacitors, and the reference equipment itself as seen in Figure 56.

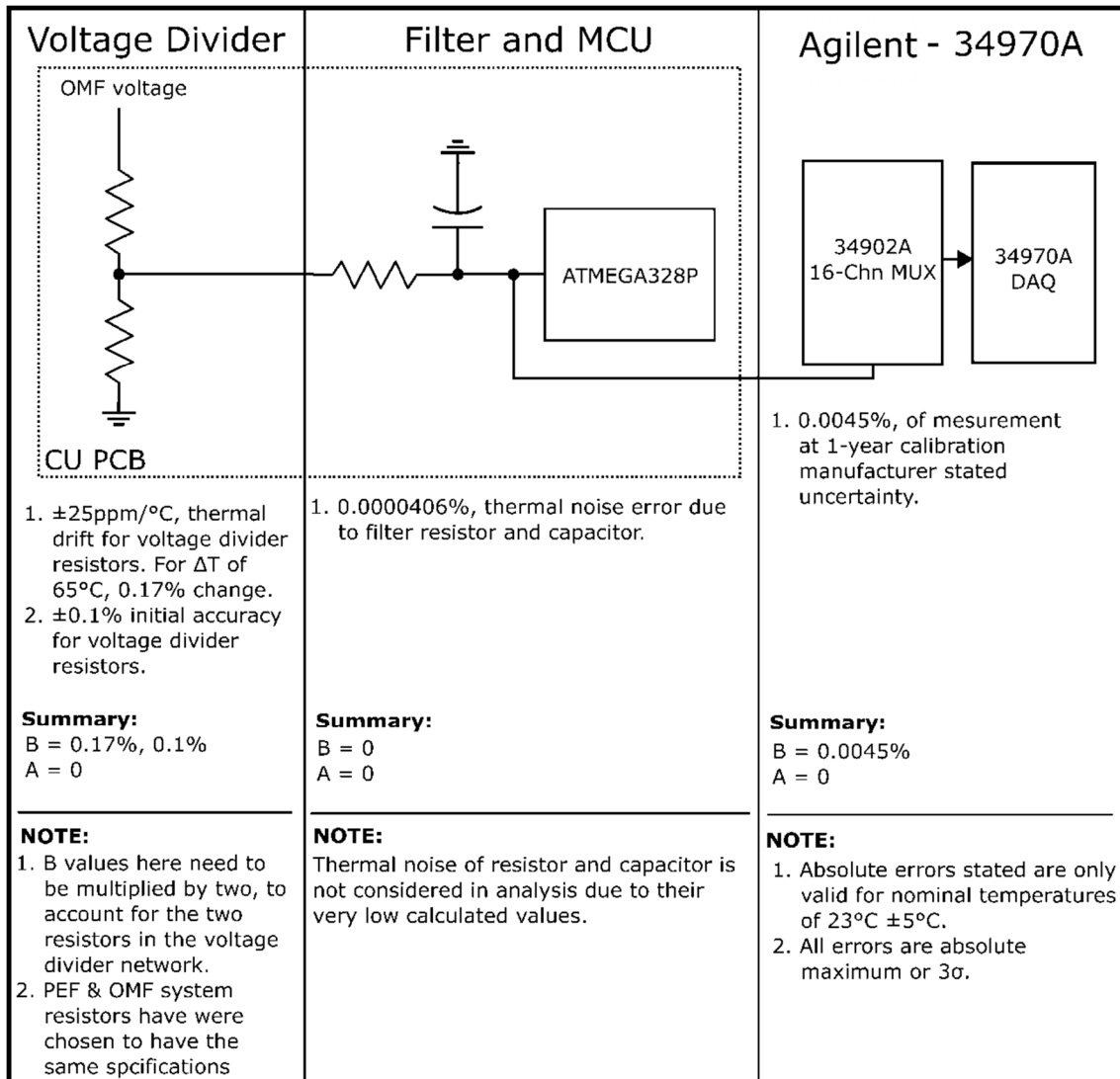


Figure 56. Total uncertainty associated with reference equipment and data of the voltage system.

The total type-A uncertainties associated with the voltage reference data was calculated as  $\pm 0.0923\%$ , and the total type-B uncertainties are zero. Total uncertainties associated with the voltage measurement reference data was calculated following Equation (4.2), and was determined to be  $U = \pm 0.1846\%$  with a  $k = 2$  (95%,  $2\sigma$ ). This value represents the minimum attainable uncertainty with the reference data comparisons.

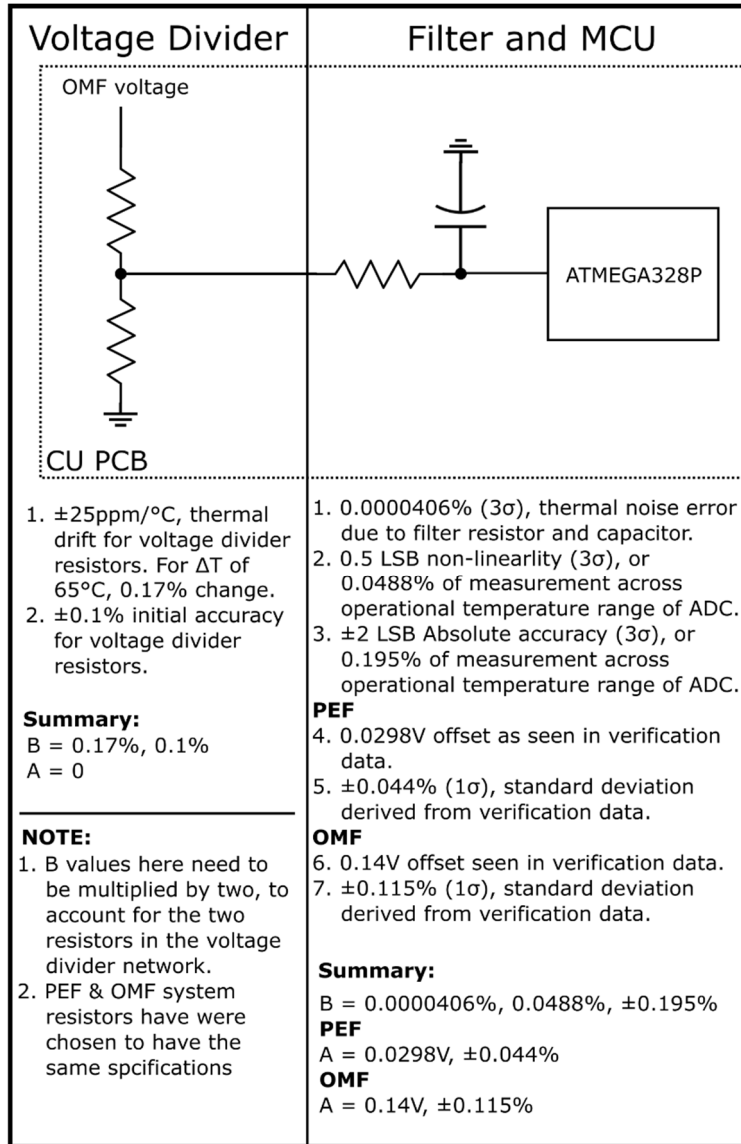


Figure 57. OMF and PEF uncertainties accounted for with voltage measurement system.

The uncertainties associated with the OMF and PEF voltage measurement system are summarized in Figure 57. The resistors chosen for the OMF and PEF system voltage divider network and filtering circuit have the same initial and thermal drift manufacturer stated uncertainties. And both

signals are fed into a single ended ADC measurement on the ATMEGA328P. Thus, the uncertainties for the OMF and PEF system will follow the same calculations except for the experimentally derived type-A uncertainties. The total type-B uncertainties for both the OMF and PEF system is  $\pm 0.175\%$ . The total type-A uncertainty for PEF is  $\pm 0.817\%$ , and for OMF is  $\pm 0.940\%$ . The overall uncertainty for PEF voltage measurements was determined to be  $U = \pm 1.67\%$  with  $k = 2$  (95%,  $2\sigma$ ), and the overall uncertainty for the OMF voltage measurements is  $U = \pm 1.91\%$  with  $k = 2$  (95%,  $2\sigma$ ). These uncertainties are mostly dictated by the offsets within PEF and OMF measurements when in comparison with reference data and can be corrected for within software.

## CHAPTER 5. OPERATIONAL VALIDATION

After confirmation of basic CU functionality with preliminary verification/calibration, the overall dynamic performance of the CU unit was tested with operational validations. This was done by gauging the CU's performance with reference to external high precision lab equipment while supercooling a chosen food sample. The chosen food sample will undergo various food quality assessments to determine if it has achieved and maintained a supercooled state. Food quality assessments conducted in this study were drip loss, pH, texture and color analysis. These food quality assessments were conducted on fresh test samples pre-experimentation and once more post experimentation. Test samples were stored in their respective conditions for a minimum of 7days, this included a test sample in a supercooled state, one in refrigeration temperatures (4°C), and another at freezer temperatures (-20°C). Past studies have shown supercooled foods exhibited quality assessments most similar to that of fresh samples [56],[54], [55], the conclusion drawn from those studies was supercooled foods suffered less ice damage while also minimizing food spoilage. Data collected by the reference lab equipment will serve to confirm CU operational reliability, while the food quality assessments will serve to confirm if a successful supercooled state was achieved.

### 5.1 Methods and Materials

#### 5.1.1 Supercooling Equipment and Protocol

The CU was placed within its custom-built enclosure and used to provide all PEF and OMF power during experimentation. Electrical power supplied to the CU was provided by a custom unregulated power supply (PS-5N80N24, AnTek, North Arlington, NJ) with 80Vdc and 24Vdc output. A custom-built chamber housing PEF electrodes and electromagnets for OMF was used for sample testing area. Data collected by the CU during experimentation consisted of OMF current raw data, PEF current raw data, PEF voltage, OMF voltage, sample temperature, and the date and time of collected data. All data collected by the CU was stored onto SD™ card in three separate files for OMF current raw data, PEF current raw data, and all other data. The sample temperature was measured by the CU using SLE grade T-type thermocouple wire (TT-40-SLE-50, Omega, Norwalk, CT) placed underneath the test sample. Electrical insulation between the thermocouple wire and test sample was provided with 1mil thickness Kapton tape (KaptonTape, Torrance, CA). The complete supercooling system was tested under conditions which simulated the intended operational environment (Lab room at 20°C ambient, pollution level 1). To gauge dynamic performance and reliability, an external Agilent DAQ (34970A, Agilent, Santa Clara, CA) with 16-channel multiplexer (34902A, Agilent, Santa Clara, CA) was used to collect the same

data collected by CU. A TTL trigger signal provided by the CU was used to sync data collection between Agilent DAQ and CU. The Agilent DAQ accomplished current measurements by monitoring the  $V_{AC}$  voltage drop across external shunt resistors placed in series between CU and the sample chamber. The external shunt used to monitor the PEF system was sized at  $1\Omega$  (WSC25151R000FEA, Vishay Dale, Shelton, CT), and the OMF system's external monitoring shunt was sized at  $0.02\Omega$  (WSR5R0200FEA, Vishay Dale, Shelton, CT).  $V_{DC}$  voltage of the OMF and PEF system was monitored through test points on the CU board at a 5.5digit resolution. Internal sample temperature and bottom sample temperature were monitored with SLE grade T-type thermocouple wires (TT-40-SLE-50, Omega, Norwalk, CT). The custom-built chamber housing PEF and OMF generation components was placed within a chest freezer (HF50CM23NW, Haier, Qingdao, China), the freezer's temperature was maintained at  $-3.5^{\circ}\text{C}$  with PID controller (D1S-2R-220, SESTOS Electronics H.K., Hong Kong) set to bang-bang control mode. The Agilent DAQ was also used to monitor the internal freezer temperature with a four-wire RTD sensor (PR-10-2-100-1/8-6-E, Omega, Norwalk, CT). Data was logged in 20 second intervals to ensure the Agilent DAQ had adequate time to scan all needed channels. All data from Agilent DAQ was monitored and collected onto PC/laptop with BenchLink software (Keysight, Santa Rosa, CA). During experimentation power consumption by the CU was monitored with a kill-a-watt meter (P3 International, New York, NY). The supercooling protocol used during experimentation is a modification of the protocols used by Mok et al. [56], [54], and Shafel [55] to achieve supercooling within meat based test samples. OMF protocol during the initial phase of sample cooling had a repeated on/off cycle of 4minutes off and 2minutes on at  $60V_{DC}$ , 1hz and 50% duty. When the critical temperature of sample set at  $-2.0^{\circ}\text{C}$  was detected by the CU thermocouple, phase 2 of supercooling protocol was initiated. PEF systems were enabled and set at 50% duty, 20kHz and 7V. OMF on/off cycles after the critical temperature event continued at 4minutes off 2minutes on with the same aforementioned settings.

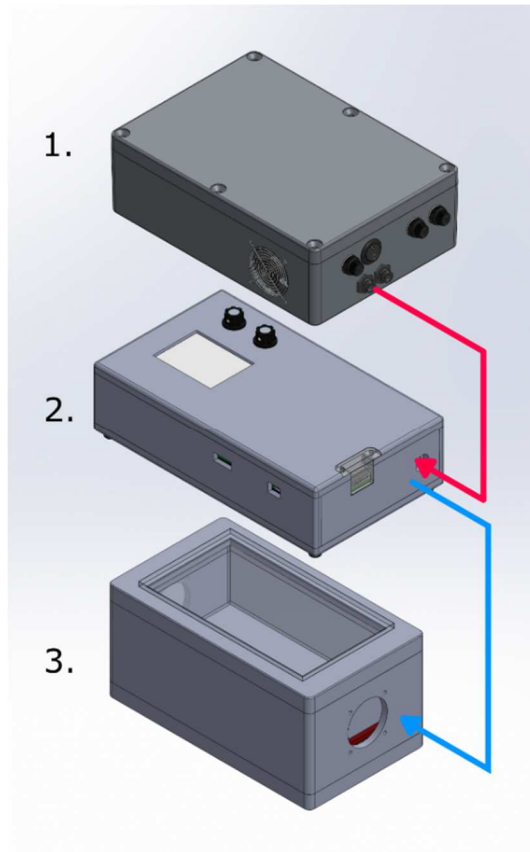


Figure 58. The complete Supercooling system, with 1. Power supply, 2. Control unit, and 3. The Sample chamber.

### 5.1.2 Sample Preparation

The test sample used during operational validation was lean beef steak (London broil) purchased at various grocery stores in the Honolulu, Hawaii region. The day of purchase is considered day 0 of this study, sample loading into the test chamber occurred on the same day. Each test sample was weighed (VWR-6000P, VWR, Radnor, PA) and cut to be within  $180\text{g} \pm 10\text{g}$ , the cut samples were wrapped in polyethylene film to avoid dehydration during experimentation. A total of three samples were prepared for each trial and placed in refrigeration ( $4^{\circ}\text{C}$ ), freezer ( $-20^{\circ}\text{C}$ ), and test chamber between the two contract PEF electrodes. Quality factor assessments were conducted on day 0 and day 7, the study was conducted in triplicates.

### 5.1.3 Drip Loss

Sample drip loss was conducted following the Thyholt & Isaksson method [132]. After initial sample preparation, each sample's weight was recorded (VWR-6000P, VWR, Radnor, PA), post experimentation the samples were weighed again after a 24-thawing period at  $4^{\circ}\text{C}$ . Any excess drip was

removed from sample before weighing with paper cloth. The overall drip loss was calculated with the following:

$$\text{Drip loss (\%)} = \frac{\text{initial weight} - \text{final weight}}{\text{initial weight}} \times 100 \quad (5.1)$$

#### 5.1.4 pH Measurements

The pH of beef samples was measured by homogenizing 10g of beef sample with 20ml of deionized water at room temperatures. Three separate measurements (S20-K SevenEasy, Mettler Toledo, Columbus, OH) were made on each sample and the average was taken. Prior to each trial's measurements, the pH probe equipment underwent a 3-point calibration at 4, 7 and 10pH.

#### 5.1.5 Warner-Bratzler Shear

Beef samples pre- and post-treatment were tested for shear strength following the Warner-Bratzler shear test methods as described within [55], [133]. Each beef sample was placed within plastic bags (Ziploc, SC Johnson, Racine, WI) and cooked within a heated fluid bath (WB20, PolyScience, Niles, IL) held at 90°C. The internal temperature of the beef samples was monitored with K-type thermocouple (PP-K-24S, Omega, Stamford, CT) attached to a portable digital thermometer (HH92, Omega, Stamford, CT), cooking was stopped when an internal temperature of 75°C was reached. Beef samples were then cooled in an ice bath (while still in their plastic bags), until their internal temperatures reached 20°C. The samples were cut into 1x1x4 cm strips, these strips were then placed onto a texture analyzer (TA.XT plus, Stable Micro Systems, Godalming, UK) with blade set probe accessory used with the Warner-Bratzler shear test (HDP/BS, Stable Micro Systems, Godalming, UK). The muscle fibers of beef samples were placed perpendicular to the complete shear of the sample, firmness (g) and toughness (g/s) of shear was measured with a probe plunging speed of 5mm/s (Firmness is peak force, toughness is work of shear). A minimum of ten measurements were made for each beef sample.

#### 5.1.6 Digital Color Analysis

Color analysis was carried out following computer vision measurements methods as described in [134], [135]. A simple light box was constructed from a cardboard box to shield the image capturing environment from stray light sources. A circular 12" diameter 32watt T9 bulb (FC12T9, Phillips, Amsterdam, Netherlands) rated at a color temperature of 6400K was mounted within the light box to achieve uniform lighting intensity. The light source was powered by an appropriately rated ballast (RLCS-

140-TP-W, Phillips, Amsterdam, Netherlands). The camera used for image capturing was an 18 Mega-Pixel SLR digital camera (EOS Rebel T3i, Canon, Tokyo, Japan) mounted with 18-55mm lens (EF-S 18-55mm f/3.5-5.6 IS II, Canon, Tokyo, Japan). When capturing images, the camera was shot in manual mode with auto white balance, 1/60 second exposure, ISO 100, and an aperture setting of F5. Focusing of image was set to automatic with image stabilization enabled. Sample positioning was adjusted to center frame before images were taken, the sample positioning relative to the light source and camera lens was positioned so that the angle between camera lens axis and light source equaled 45°. This was to ensure the diffusion reflection of color from incident light was maximized [106]. Three pictures for each sample were taken, the image data was saved in JPEG format and transferred to a computer/laptop with MatLab 2015a (MathWorks, Natick, MA). MatLab code was written to convert the RGB data of the captured JPEG images to CIE-L\*a\*b format pixel by pixel. The code allows a user to indicate a rectangular area to analyze based upon user selection, upon which MatLab's built in `rgb2lab()` function converts the image data and computes the mean and standard deviation of L, a, and b values of the CIE-L\*a\*b format. The `rgb2lab()` function is set to process image data with a reference white point of 6774K. To compare difference between samples, the net color difference was calculated using the following:

$$\Delta E = \sqrt{(L_1 - L_2)^2 + (a_1 - a_2)^2 + (b_1 - b_2)^2} \quad (5.2)$$

Where subscripts 1 and 2 indicate before and after values of the sample's respective treatments. The MatLab script used to determine CIE-L\*a\*b can be examined in Appendix B.

## 5.2 Results and Discussion

A typical time temperature profile of a supercooled London broil beef can be seen in Figure 53. All trials conducted exhibited similar time-temperature characteristics shown. Occurrence of ice nucleation during the freezing process can be determined by monitoring the sample temperature, a release of latent heat resulting from the ice nucleation within London broil beef would reveal a freezing temperature near -0.5 °C to -1.8°C [56]. No release of latent heat was detected during experimentation with measurement points placed in and around of the beef sample. In addition to temperature measurements, PEF current can be used as an indicator of ice formation within a beef sample. As ice propagates throughout water, conductivity drops dramatically due to a decrease of free ions capable of carrying electrical current [137]. After the initial activation of the PEF protocol (Figure 53, PEF current sub-graph, critical temperature of -2°C reached at roughly 2 hours), current flow through the beef

sample remained steadily at 14mA for trial 1, indicating no ice nucleation occurred (Current values are dictated by sample size and shape, during experimentation PEF current varied from 14mA to 20mA for the triplicate trials). The initial OMF protocol was maintained prior and after the critical temperature event. During the on cycles, OMF current was measured to be roughly 1.23A throughout all trials.

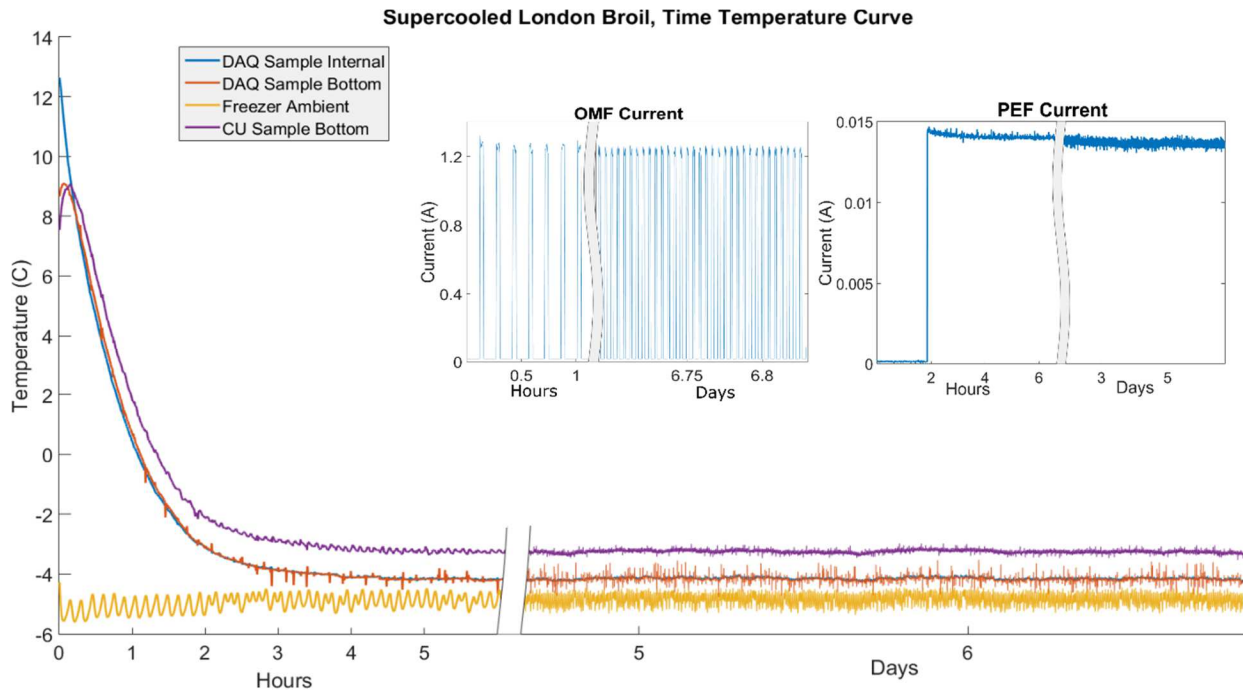


Figure 59. Temperature profile of seven-day supercooled London broil beef with OMF and PEF treatment.

During each trial two points of measurements by the DAQ was taken to monitor current within the PEF and OMF system. These points are at the external shunt resistor and another at the on-board LT1999 current shunt monitor. The CU electrical current data collected for OMF and PEF systems was compared to DAQ collected data and is summarized in the Table 12. Note in Table 12, the OMF current data for the DAQ is not included, this is because the Agilent 34970A DAQ cannot capture measurements reliably below 3Hz.

Table 12. Electrical current measurement summary between CU and DAQ. All values are units of Amperes.

		Control Unit		DAQ		%diff
		Current Mean	Current std	Current Mean	Current std	
Trial 1	OMF	1.2301	0.0223	n/a	n/a	n/a
	PEF	0.019	0.0001591	0.0193	0.0001353	1.56658
Trial 2	OMF	1.23	0.0224	n/a	n/a	n/a
	PEF	0.0138	0.00018922	0.014	0.0001549	1.438849
Trial 3	OMF	1.229	0.0222	n/a	n/a	n/a
	PEF	0.0192	0.0001238	0.0194	0.0000917	1.036269

The percent difference within Table 12 was calculated using the means between DAQ and CU collected data. The estimated, maximum uncertainty determined from preliminary validation of the PEF current system was calculated as 1.71% of measurements. All trials fall into the calculated uncertainty limit, however trial 1 comes very near to the limit even with the CU operating in ideal conditions.

Voltage measurements for both PEF and OMF systems across the three trials are summarized in Table 13. The low percent difference between CU and DAQ means indicate the voltage system are performing as intended. Table 14 summarizes the average temperatures of the beef sample after they achieved a stable supercooled temperature. The percent difference between the temperature measurements of CU and DAQ show large differences in the average reported temperature. The total uncertainty determined for the thermocouple system within section 4.2.3 was  $\pm 0.7^{\circ}\text{C}$ . Unfortunately, only trial 3 falls within this uncertainty margin. Several factors as determined by uncertainty analysis can affect the overall thermocouple measurement accuracy and precision, however a major uncertainty source overlooked was mounting errors, or errors which arise due to improper thermocouple installation. During preliminary validation, the measurement environment had no PEF or OMF applied, as such their influences during operational validation was overlooked. Proper grounding and insulation for a thermocouple becomes paramount in such environments and the test thermocouple used during operational validation offered no protection against mounting errors (bare SLE grade T-type 40-gauge thermocouple wire). During experimentation Kapton tape was used as an insulator between thermocouple and the measurement environment however, static charge build-up remained an issue as proper grounding was more difficult to achieve.

Table 13. Electrical Voltage measurement summary between DAQ and CU data.

		Control Unit		DAQ		%diff
		Voltage Mean	Voltage std	Voltage Mean	Voltage std	
Trial 1	OMF	60.0029	0.0409	60.1453	0.0382	0.237
	PEF	6.9538	0.0561	6.983	0.0568	0.419
Trial 2	OMF	60.0261	0.0518	60.1646	0.0432	0.230
	PEF	6.9982	0.0203	7.0226	0.0198	0.348
Trial 3	OMF	59.821	0.0599	59.9641	0.0511	0.239
	PEF	6.9263	0.015	6.95	0.014	0.342

Table 14. Temperature measurement summary between DAQ and CU. Units are  $^{\circ}\text{C}$ .

		Control Unit		DAQ		%diff
		Temp Mean	Temp std	Temp Mean	Temp std	
Trial 1		-3.011	0.0338	-4.090	0.2006	-30.390
Trial 2		-3.288	0.0695	-4.214	0.1058	-24.687
Trial 3		-3.287	0.0695	-3.630	0.0576	-9.918

To further validate if a supercooled state within beef samples was maintained, various food quality assessments were conducted to assess the presence of ice damage. Figure 60 summarizes drip loss across all three trials. Frozen samples experienced the greatest amount of drip loss within trials 2 and 3, however during trial 1 drip loss was minimal. Frozen food items typically experience greater drip loss due to ice damage. And as such, beef samples stored within sub-zero temperatures without OMF or PEF treatment were expected to experience the greatest drip loss, as was demonstrated with prior supercooling experiments [55], [56], [54]. Trial 1's frozen beef samples were thawed within polyethylene film wrap at 4°C for 24 hours. Trial 2 and 3 implemented a different method which involved removing all beef sample from their protective polyethylene film wrap and placing the beef samples on top of a strainer in a plastic container. This adjustment allowed for drip to fall freely from the beef samples during the thawing period.

Also of note, when comparing procedures from prior supercooling studies [55], [56], [54], the beef samples size/weight used within this study is considerably larger. For example, Shafel [55] used 40g London broil samples, and Mok et al. [56] used 100g Chicken breast. As a result, unexpected challenges with sample dehydration, sample uniformity and sample shapes consistency arose when partitioning London broil streaks by weight. Within drip loss analysis, dehydration played a major role in skewing final results especially within supercooled samples due to moisture loss towards the contact electrode interface.

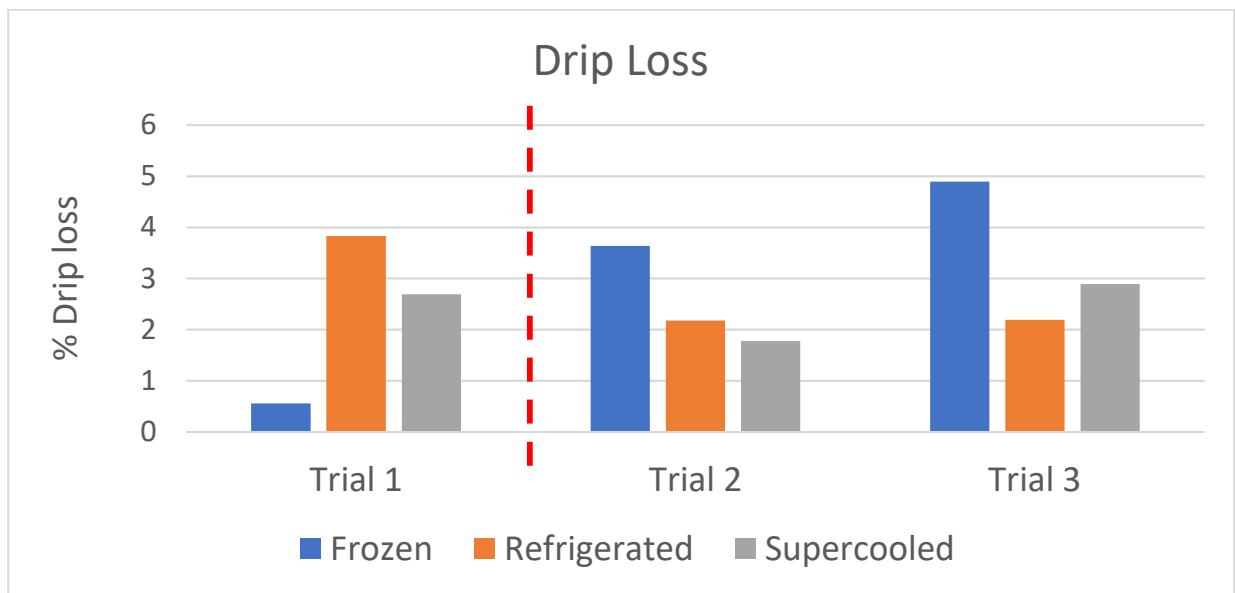


Figure 60. Drip loss across three trials. Note, Trial 2 and 3's methods were modified from Trial 1. No direct comparisons can be made between the trials separated by the red dotted line.

Sample shape and uniformity inconsistency played a major role in texture analysis error due to the natural inconsistency of tenderness present within the London broil steak cut. The name London broil actually pertains to the preparation method with tough lean beef, the cut also goes by the name top round and is taken from the semimembranosus muscle of a bovine. Prior studies have shown the tenderness of this cut has a large natural variance in shear forces measured [138], this natural variance was observed within this study as seen in Figure 61, trials 1 and 2.

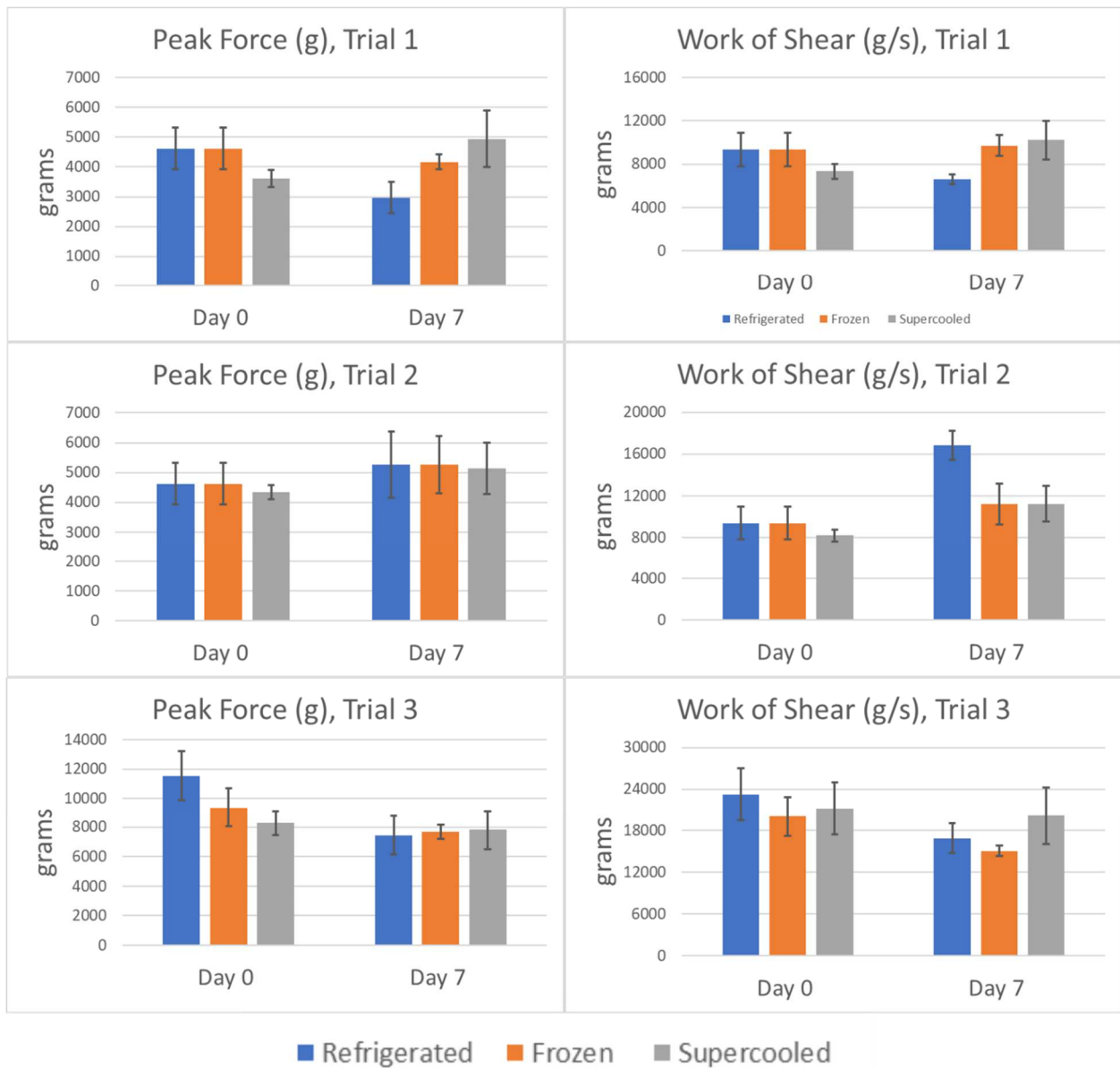


Figure 61. Texture Analysis summary across three trials

Within trial 1 and 2 of Figure 61, the textures measurements of beef samples after treatment showed higher peak forces and higher work of shear despite sample preparation of beef texture analysis (i.e., cooking time, cut size, weight) being identical. The only factor within the texture analysis procedure which varied greatly was the locations in which Day 0 and Day 7 samples were taken from in the London broil steak. Trial 3 aimed to address the issue of sample inconsistency by ensuring beef samples for each treatment was taken from its own individual London broil steak of adequate size. A minimum thickness of 1.5" was prepared by the local grocery butcher, this ensured texture samples for fresh and 7-day analysis originated from the same general vicinity of the London broil beef cut. As a result of the extra pre-cautions, Trial 3 of Figure 61 shows a similar trend to that reported by Shafel [55]. The supercooled sample remained the closest to the original fresh like texture, while both refrigerated samples and frozen samples became more tender due to ice damage or spoilage.

Figure 62 summarizes the digital color analysis across all three trials, trial 3 showed the most dramatic change in color within refrigerated and frozen samples. This may be due to the freshness of the London broil sample, as trial 3's samples were package on the day of purchase as a special order from local grocery. Trial 1 and 2's London broil sample may have been packaged a number of days prior to purchase, this data was not noted. Figure 63 contains a sample of the images used for digital color analysis for trial 3.

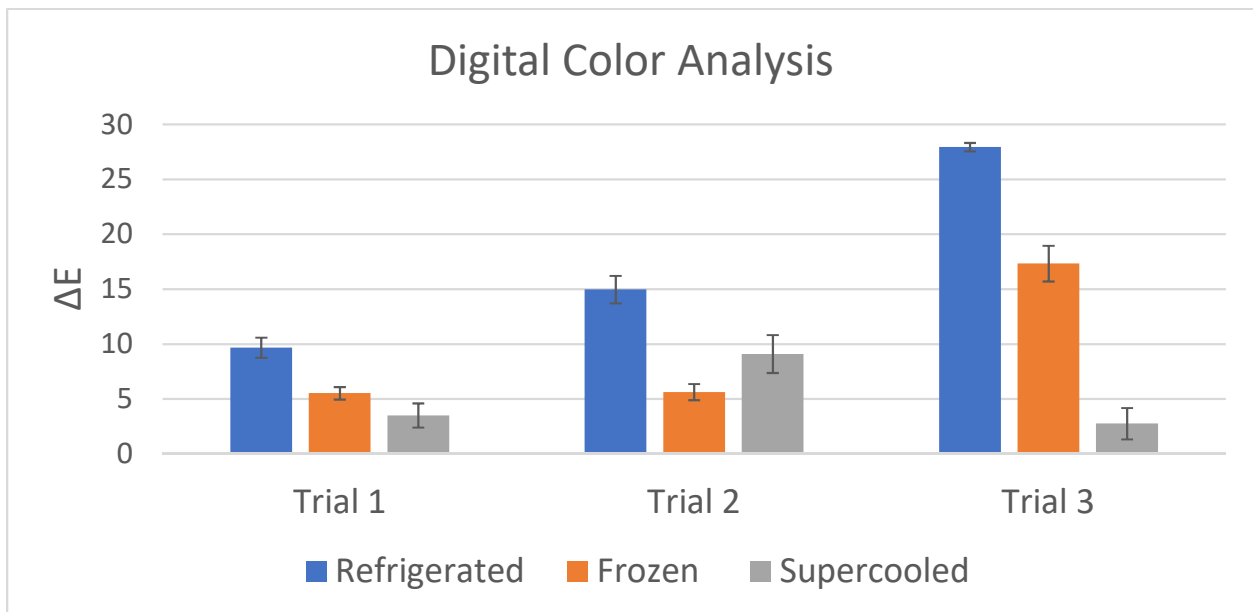


Figure 62. Digital color analysis summary.

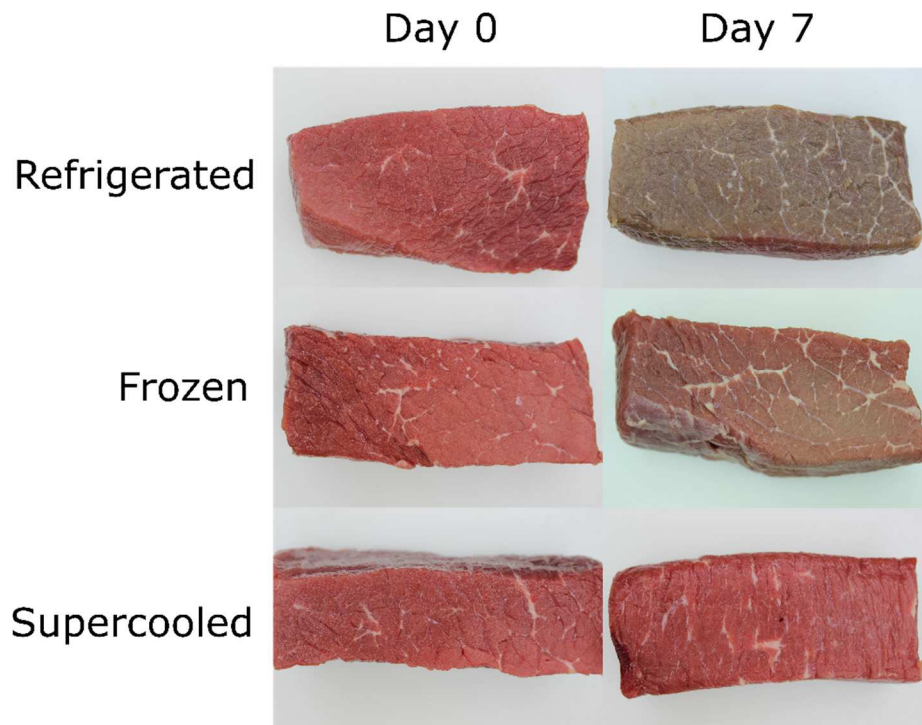


Figure 63. Sample digital images used during color analysis, taken from trial 3 of color analysis.

pH of the beef samples across all trials showed no discernable trend or pattern, Figure 64 summarizes the results across the study. Trial 1 seems to indicate an overall increase in pH is expected across all treatment types, however trial 2 indicated the opposite and we see an observed lowering of pH across all treatments. Trial 3's results shows an increase in pH within refrigerated and supercooled beef samples but a lowering of pH in the frozen sample. Shafel [55] observed a general lowering of pH of 0.2 in refrigerated, frozen, and supercooled beef samples. He contributed the phenomenon to bacterial by-products accumulation due to natural fouling or spoilage. Others have noted a raise in pH to be the norm within cold storage of beef products, again contributing the phenomenon to accumulation of bacterial byproducts and proteolysis degradation [139], [140]. Shafel used a two-week storage period for London broil beef, a storage period extending beyond 14 days may be necessary to draw a more meaningful conclusion from pH observations within supercooling experiments.

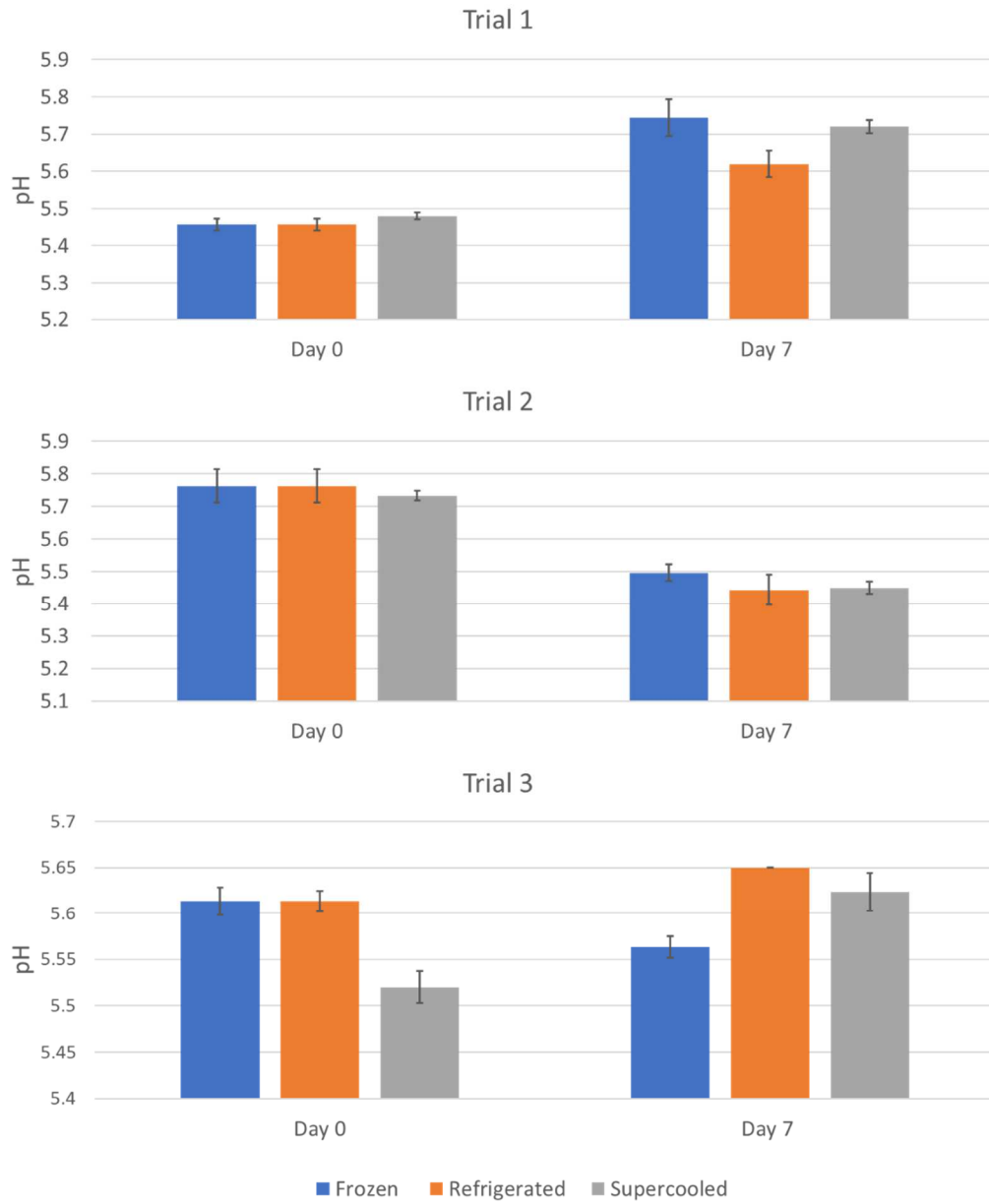


Figure 64. pH measurements across three trials.

## **CHAPTER 6. CONCLUSIONS, POTENTIAL IMPACT, AND RECOMMENDATIONS**

### **6.1 Conclusions**

The microcontroller based CU provided an overall satisfactory performance when in comparison with previous equipment and procedures used for supercooling experimentation. Current and voltage measurements fell within expected uncertainties ranges as established within preliminary validation procedures. However, thermocouple based temperature measurements remained problematic as a failure to account for mounting errors introduced an un-systematic bias error into the signal chain hampering the overall accuracy and precision achievable. Overall system weight, complexity and equipment count was reduced, and cost was minimized as expensive third-party equipment were eliminated as a requirement. In addition, third-party software is no longer required for data logging, control, and monitoring.

### **6.2 Potential Impacts**

Supercooling technology and its further development has the potential to greatly impact the way we store food and deal with food waste. The work presented here serves as the foundation for taking supercooling tech from the research realm to the commercial realm. Once mature and commercialized, the entire food chain pertaining to cold storage can be improved upon by the supercooling process. In particular shelf life extensions of foods formerly deemed unsuitable for the conventional freezing process can be achieved. Freshness of delicate fruits, vegetables, and meats can be maintained longer and as a result food waste at the industry level can be reduced. On a domestic level, home appliance equipped with supercooling technology can reduce food waste even further as it has been estimated up to 40%-50% of all food waste within the USA occurs on the consumer level [141].

Beyond food applications, supercooling research and its technology has wide reaching implications in a number of fields and industry. Freezing has always been an enigma to scientist and understanding its mechanics and nature has been a priority for many years. Several disciplines ranging from meteorology, chemical engineering, bio-preservation, and medicine can potentially benefit from the prevention of ice nucleation. In particular, bio-preservation research and its industry can see a great improvement in their storage methods, as often times their main concerns associated with sub-zero preservations of bio-materials are related to ice damage as well.

### 6.3 Recommendations

There exist several potential areas for improvement, the most obvious is the thermocouple based temperature measurement system. A bulk of the difficulty in its operation is a result of its close proximity to components on the CU PCB which produces unwanted heat. A recommended solution would be to separate the delectate analog circuitry associated with the thermocouple system onto a dedicated PCB board with SPI communication isolation. In addition, improved thermal uniformity of the separated thermocouple system can be achieved with additional thermal and electrical shielding within the CU enclosure.

Users of the CU have reported fine adjustments to the OMF and PEF bias voltage systems to be overly sensitive. A migration away from the rheostat solution currently implemented, to a complete digital solution would be a considerable improvement upon the system. This can open the potential for active voltage control during supercooling experimentation, something impossible with the current CU design.

The OMF system remains the most expensive system on the CU, reduction in its cost will greatly bring down the overall CU cost. In its current design, the OMF system uses an IGBT power module which can be swapped for a cheaper MOSFET based power module, or an even cheaper relay based system. If replacing the IGBT power module is not an option an alternative would be to consider replacing the DC-DC converters used for high side gate driving on the OMF H-bridge. The DC-DC converter currently in use can provide dual negative and positive 15V output. Only the positive 15V output is in use, significantly cheaper single output alternatives are available for consideration.

A more deeper investigation into food quality analysis and the impacts PEF and OMF fields impart onto microbes during cold storage is also recommended. To the best of my knowledge no study has been conducted on how the electromagnetic radiation based supercooling treatments interacts with the natural microbial flora present within food systems. With no ice nucleation occurring, water activity will remain high within supercooled foods and as a result it is unknown if pathogenic microbes or spoilage bacteria will remain viable at supercooling temperatures.

## APPENDICES

### Appendix A: MCU code

```
/* *****
 * NOTE: Testing code used within preliminary validation and operation validation is
 * shown below. LCD UI functionality is not included for basic testing purposes.
 * *****/

#include <PWM.h>
#include <SPI.h>
#include <Wire.h>
#include <Adafruit_ADS1015.h>
#include <RTCLib.h>
#include "SdFat.h"
#include <stdint.h>
#include "Arduino.h"

RTC_DS1307 RTC;
Adafruit_ADS1115 ads1(0x48); // ADS1115 for OMF
SdFat sd;
SdFile myFile;
uint16_t SRdata = 0x3F20; //for USB communication, DRV8839 outputs enabled, and INA225 gain
//set at 25v/v, SD card selected, ADG707 thermocouple channel 1
//selected (0000 0000 0011 1111 0010 0000)

/* *****
 * All timing variables are in units of seconds. All temp variables are in units of C
 * Duty cycle settings can be set with integer values between 0 and 255,
 * 0 setting means 100% duty cycle, and 255 means 0% duty. For examples
 *     51 = 80% duty
 *    127 = 50% duty
 *    204 = 20% duty
 * !!NOTE!! the duty cycle settings here are only true for the SCboard,
 * due to logic stage reversing duty settings. Normally duty setting of
 * 255 = 100% and 0 = 0%.
 * *****/

/* *****
 * change these variables to change OMF PEF application settings
 * *****/
float PEFfrequency = 20000; // PEF frequency
float OMFfrequency = 1; // OMF frequency
static int CriticalTemp = -2.5; // Critical Temperature to turn on PEF
static int OMFoffduration = 120; // OMF off time
static int OMFonduration = 420; // OMF on time
static int OMFduty = 127; // OMF duty setting, 50%
static int PEFphase0 = 120; // PEF phase 0 time
static int PEFphase1 = 120; // PEF phase 1 time
static int PEFphase2 = 120; // PEF phase 2 time, OMF will be on in this phase
static int PEFduty0 = 127; // PEF phase 0 duty setting, 50%
static int PEFduty1 = 127; // PEF phase 1 duty setting, 50%
static int PEFduty2 = 127; // PEF phase 2 duty setting, 50%
static int MeasurementFreq = 20; // sampling freq of data logging, units in seconds
static int SerialUpdate = 60; // serial update time, units in seconds

/* *****
 * dont change any of these variables
 * *****/
static int OMF = 9; // OMF pin
static int PEF = 3; // PEF pin
static int pin = 2; // OMF de-activate pin
bool mode = 0; // mode variable to turn PEF on when critical temperature
bool OMFstate = 0; // keeps track of OMF on/off cycle
int PEFstate = 0; // keeps track of PEF phase cycles
```

```

String PEFprint = "PEF off";           // Serial print for PEF status
String OMFprint = "OMF off";           // Serial print for OMF status
char Str0[17];                          // character string for time
float OMFvoltage = 0;                   // variable for OMF voltage
float PEFvoltage = 0;                   // variable for PEF voltage
float Temp = 0;                          // Sample Temperature value
unsigned long previousMinute = 0;        // counter for timing PEF cycles
unsigned long previousMinute2 = 0;       // counter for timing OMF cycles
unsigned long previousMinute3 = 0;       // counter for timing current and voltage measurements
unsigned long previousMinute4 = 0;       // counter for serial monitor update
char fileName1[13] = "data00.csv";       // data file name initialized
char fileName2[13] = "PEFe00.csv";      // data file name initialized
char fileName3[13] = "OMFe00.csv";      // data file name initialized
uint16_t RawconversionArray[48];        // RAW PEF ADC data conversion data array
int16_t PEFconversionArrayB[12];        // PEF ADC data conversion data array
int16_t OMFconversionArrayB[24];        // OMF ADC data conversion data array
byte SPI_Junk_Received;                 // just a dummy variable to receive simultaneous SPI data
int PEFfactor = 0;                       // PEF delay factor for even sampling across frequencies
int OMFfactor = 0;                       // OMF delay factor for even sampling across frequencies
int32_t RefTemp;
double RefTemp1;                         // used for conversion of captured ADS1220 two comp data to
int32_t Value;                            // thermocouple voltage reading from ADS1220, raw
float Value1;                             // used for conversion of captured ADS1220two comp data to
float variable

//Variables for time
uint8_t HOUR = 0;
uint8_t MINUTE = 0;
uint8_t MONTH = 0;
uint8_t DAY = 0;
uint16_t YEAR = 0;

//Pins
#define DATA 4 // PD4
#define ERASE 7 // PD7
#define LATCH 8 // PB0
#define CLOCK 6 // PD6
#define SS 10 // chip select for SPI comm.
#define FILE_BASE_NAME "Data"

//ADS1220 configuration register addresses
#define CONFIG_REG0_ADDRESS 0x00
#define CONFIG_REG1_ADDRESS 0x01
#define CONFIG_REG2_ADDRESS 0x02
#define CONFIG_REG3_ADDRESS 0x03

//ADS1220 command codes
#define SPI_MASTER_DUMMY 0xFF
#define RESET 0x06
#define START 0x08
#define WREG 0x40 //Write to registers
#define RREG 0x20 //read registers

union { // Union makes conversion from 2 bytes to an unsigned 16-bit int easy
    uint8_t bytesA[2];
    uint16_t word16A;
} dataA;

union { // Union makes conversion from 2 bytes to an unsigned 16-bit int easy
    uint8_t bytesB[2];
    uint16_t word16B;
} dataB;

union { //C++ code, makes combining several bytes into 16bit or 32bit data formats
    uint8_t bytes[4];
    uint32_t word32;
}

```

```

}data;

/*****
 * Initializing all required hardware and variables
 *****/
void setup(){
  pinMode(DATA, OUTPUT);
  pinMode(ERASE, OUTPUT);
  pinMode(LATCH, OUTPUT);
  pinMode(CLOCK, OUTPUT);
  pinMode(A3, OUTPUT);
  pinMode(10, OUTPUT);
  pinMode(11, OUTPUT);
  pinMode(pin, OUTPUT);
  digitalWrite(A3, HIGH);

  //initialize serial comms. @ 9600 bauds
  Serial.begin(9600);

  Wire.begin();
  SPI.begin();

  sendData(SRdata);
  delay(100);
  sendData(SRdata);

  delay(100);
  initialize_ADS1220(); // Initialize the thermocouple ADC
  delay(100);

  ads1.begin();
  ads1.setGain(GAIN_ONE); // 1 gain +/- 4.029V 1 bit = 0.125mV (default)

  //initialize all timers except for 0, to save time keeping functions
  InitTimersSafe();

  //sets the frequency for the specified pin
  SetPinFrequencySafe(OMF, OMFfrequency);
  SetPinFrequencySafe(PEF, PEFfrequency);

  PEFfactor = ((1/(PEFfrequency/2))/12)*1000000; //factor to delay PEF single shot sampling
  OMFfactor = ((1/OMFfrequency)*2)/24)*1000; //factor to delay OMF single shot sampling

  //Serial.print(F("OMF factor = "));
  //Serial.println(OMFfactor);

  digitalWrite(pin, HIGH); //LOW for on and HIGH for off, OMF system
  PEFoff(); // have PEF off initially

  RTC.begin();
  if (! RTC.isrunning()) {
    Serial.println(F("RTC is NOT running!"));
    // following line sets the RTC to the date & time this sketch was compiled
    RTC.adjust(DateTime(__DATE__, __TIME__));
  }

  Serial.println(F("Hi! begin program by inputing command into serial"));
  while(Serial.available() == 0){Serial.println(F("Type in 'start' to begin")); delay(1000);}
  Serial.println(F("The program was started!"));

  bitWrite(SRdata, 5, 1); // ensures ADG704 channel is set on SD card
  bitWrite(SRdata, 4, 0);

  sendData(SRdata);
  delay(10);

```

```

sendData(SRdata);

// initialize the SD card
Serial.print(F("Initializing SD card..."));

delay(1000);

if(!sd.begin(SS, SD_SCK_MHZ(50))) {
  Serial.println(F("Card failed, or not present"));
  // don't do anything more:
  return;
}
Serial.println(F("card initialized.));
delay(1000);

while (sd.exists(fileName1)) {
  if (fileName1[5] != '9') {
    fileName1[5]++;
  } else if (fileName1[4] != '9') {
    fileName1[5] = '0';
    fileName1[4]++;
  } else {
    Serial.println(F("Can't create General data file name"));
  }
}

while (sd.exists(fileName2)) {
  if (fileName2[5] != '9') {
    fileName2[5]++;
  } else if (fileName2[4] != '9') {
    fileName2[5] = '0';
    fileName2[4]++;
  } else {
    Serial.println(F("Can't create PEF file name"));
  }
}

while (sd.exists(fileName3)) {
  if (fileName3[5] != '9') {
    fileName3[5]++;
  } else if (fileName3[4] != '9') {
    fileName3[5] = '0';
    fileName3[4]++;
  } else {
    Serial.println(F("Can't create OMF file name"));
  }
}

Serial.print(F("Logging to: "));
Serial.print(fileName1);
Serial.print(F(", "));
Serial.print(fileName2);
Serial.print(F(", "));
Serial.println(fileName3);

if (!myFile.open(fileName1, O_CREAT | O_WRITE | O_EXCL)) {
  Serial.println(F("file.open"));
}

myFile.println(F("datetime,SampleTemp,OMFvoltage,PEFvoltage,"));
myFile.close();
SPI.end();

delay(1000);
}

```

```

/*****
 * Main Program. All timing and control of OMF and PEF application is taken
 * care of in here
 *****/
void loop(){
  unsigned long currentMinute = millis();
  Temp = ADS1220(); // Take thermocouple measurement
  if(Temp <= CriticalTemp){ // if thermocouple measurement below critical temp, turn on PEF
    if(mode == 0){
      mode = 1;
      //previousMinute = currentMinute;
      PEFon();
      Serial.println(F("Critical temperature reached! PEF turned on."));
      pwmWrite(PEF, PEFduty0);
      PEFprint = "PEF phase 0";
      PEFstate = 1;
    }
  }
  if(mode == 0){
    if(OMFstate == 0){
      if(((currentMinute - previousMinute2)/1000) >= OMFOffduration){
        previousMinute2 = currentMinute;
        OMFprint = "OMF off";
        digitalWrite(pin, HIGH);
        OMFstate = 1;
      }
    }
    if(OMFstate == 1){
      if(((currentMinute - previousMinute2)/1000) >= OMFduration){
        previousMinute2 = currentMinute;
        OMFprint = "OMF on";
        digitalWrite(pin, LOW);
        pwmWrite(OMF, OMFduty);
        OMFstate = 0;
      }
    }
  }
  // After critical temperature is reached turn on PEF and keep OMF on
  if(mode == 1){
    if(PEFstate == 0){
      if(((currentMinute - previousMinute)/1000) >= PEFphase2){
        previousMinute = currentMinute;
        PEFprint = "PEF phase 0";
        OMFprint = "OMF off";
        digitalWrite(pin, HIGH);
        pwmWrite(PEF, PEFduty0);
        PEFstate = 1;
      }
    }
    if(PEFstate == 1){
      if(((currentMinute - previousMinute)/1000) >= PEFphase0){
        previousMinute = currentMinute;
        PEFprint = "PEF phase 1";
        OMFprint = "OMF off";
        digitalWrite(pin, HIGH);
        pwmWrite(PEF, PEFduty1);
        PEFstate = 2;
      }
    }
    if(PEFstate == 2){
      if(((currentMinute - previousMinute)/1000) >= PEFphase1){
        previousMinute = currentMinute;

```

```

        PEFprint = "PEF phase 2";
        OMFprint = "OMF on";
        pwmWrite(PEF, PEFduty2);
        digitalWrite(pin, LOW);
        pwmWrite(OMF, OMFduty);
        PEFstate = 0;
    }
}
}
if(((currentMinute - previousMinute3)/1000) >= MeasurementFreq){ // Log data
    previousMinute3 = currentMinute;

    Serial.print(F("Sample Temperature = "));
    Serial.println(Temp);

    getTime();
    VoltageMeasrements();
    PEFcurrent();
    OMFcurrent();
    logData();
}
if(((currentMinute - previousMinute4)/1000) >= SerialUpdate){ // Update status of CU
    previousMinute4 = currentMinute;
    Serial.print(F("Current state: "));
    Serial.print(OMFprint);
    Serial.print(F(", "));
    Serial.println(PEFprint);
}
}

/*****
 * Function called to measure the T-type thermocouples in Sample.
 *****/
float ADS1220(void){
    bitWrite(SRdata, 5, 0); // ensures ADG704 channel is set on ADS1220
    bitWrite(SRdata, 4, 0);

    sendData(SRdata);
    delay(10);
    sendData(SRdata);

    uint32_t RefTemp = ADS1220_RefTemperature();
    uint32_t rawvoltage = ADSVoltage();

    //Serial.print(F("Raw = "));
    //Serial.println(RefTemp);

    if (rawvoltage & 0x800000) { // Sign extend negative numbers- conversion is a two's complement
        Value = 0xFF800000 | ((rawvoltage) & 0x7FFFFF); // write signed 24 bit value into 32 bit
    }
    else {
        Value = rawvoltage; // not negative number (MSb or bit 24 != 1)
    }

    RefTemp1 = RefTemp; // conversion of 2comp

    //Serial.print(F("converted = "));
    //Serial.println(RefTemp1);

    Value1 = Value*0.0015087; //LSB = ((2*Vref/gain)/2^24)*unit_factor, Vref = 1.62V, gain = 128,
        //unit_factor = 1000000 for uV and 1000 for mV
    RefTemp1 = RefTemp1*0.01207; //LSB = ((2*Vref/gain)/2^24)*unit_factor, Vref = 1.62V, gain = 16,
        //unit_factor = 1000000 for uV and 1000 for mV

    Value1 = Value1 + 1.6025; // Filter and Multiplexer offset correction in uV

```

```

RefTemp1 = (RefTemp1*0.000001)/0.0005;

if ((RefTemp1 < 139) && (RefTemp > 86)){ // RTD valid temp range is -35C to 100C
    RefTemp1 = 2.5831*RefTemp1 - 258.22; // linear eqn to convert RTD resistance to temperature.
    if(RefTemp1 > 10){
        RefTemp1 = (RefTemp1-((0.00000009297*RefTemp1*RefTemp1*RefTemp1*RefTemp1)-
            (0.00001272*RefTemp1*RefTemp1*RefTemp1)+(0.00004923*RefTemp1*RefTemp1)+
            (0.03601*RefTemp1)-0.4246)); // 4th order polynomial eqn for RTD correction for-20
            // to 85 ambient RTD. Below 10degC error is low.
    }
}
else{
    Serial.println(F("ERROR: RTD resistance out of range"));
}

//Serial.print(F("Board Temp = "));
//Serial.println(RefTemp1);

if ((RefTemp1 < 85) && (RefTemp1 > -40)) //Conversion of RTD temp to T-type thermocouple emf
{
    RefTemp1 = (0.00004*RefTemp1*RefTemp1) + (0.0386*RefTemp1) - 0.0004; //2nd order polynomial
    RefTemp1 = RefTemp1 * 1000; //convert mV into uV
}
else
{
    Serial.println(F("ERROR: BOARD REF TEMP OUT OF RANGE!!!"));
}

Value1 = Value1 + RefTemp1; // CJC!!!

if ((Value1 < 1630) && (Value1 > -1500)) //the number values here are emf in uV
{
    Value1 = Value1/1000; //convert uV into mV
    float cal = 0.005781*Value1 - 0.002619; //Linear model calibration equation
    Value1 = Value1 + cal;
    Value1 = -0.7385*Value1*Value1 + 25.95*Value1 + 0.007606;
}
else
{
    Serial.println("THERMOCOUPLE TEMP OUT OF RANGE!!!");
}
return Value1;
}

/*****
 * Function to initialize the ADS1220
 *****/
void initialize_ADS1220(){
    bitWrite(SRdata, 5, 0); // ensures ADG704 channel is set on ADS1220
    bitWrite(SRdata, 4, 0);

    sendData(SRdata);
    delay(10);
    sendData(SRdata);

    SPI.setBitOrder(MSBFIRST);
    SPI.setDataMode(SPI_MODE1);

    delay(100);
    SPI_Reset();
    delay(100);

    digitalWrite(10,LOW);

    writeRegister( CONFIG_REG0_ADDRESS, 0x78); // PGA on, 16 gain setting, AIN3 & AIN2

```

```

writeRegister( CONFIG_REG1_ADDRESS, 0x00); // internal temp sensor off, 20SPS data rate, single
// shot mode, 256kHz operating clock, burnout
// current off.
writeRegister( CONFIG_REG2_ADDRESS, 0x55); // External voltage reference at REP0 and REFN0, FIR
// filter on, IDAC current 500uA, Low-side pwr
// switch off.
writeRegister( CONFIG_REG3_ADDRESS, 0x80); // IDAC1 routed to AIN3, IDAC2 off, data ready
// default pin default.

delay(100);

digitalWrite(10, HIGH);

SPI_Start();
delay(100);
}

/*****
 * Calls ADS1220 and gets converted data
 *****/
uint32_t ADSVoltage(void){
    digitalWrite(10, LOW);
    SPI.beginTransaction(SPI_Settings(4000000, MSBFIRST, SPI_MODE1)); // slower than 150 ns minimum
// SPI clock period; MSBFIRST;
// only SPI_MODE 1 supported

    SPI_Junk_Received = SPI.transfer(0x41); // WREG one byte to register 01(binary)
    SPI_Junk_Received = SPI.transfer(0x0E); // Channel AIN1 and AIN0 selected, gain 128
    SPI_Junk_Received = SPI.transfer(0x08); // Start/Sync
    delay(100); // worst case scenario conversion should be available within 50 ms at 20 samples

    data.bytes[2] = SPI.transfer(0x00);
    data.bytes[1] = SPI.transfer(0x00);
    data.bytes[0] = SPI.transfer(0x00);
    SPI.endTransaction();
    digitalWrite(10, HIGH);

    data.bytes[3] = 0x00; // most significant byte of 4-byte word is empty for 24 bit conversion

    uint32_t bit32 = 0;
    bit32 = data.word32;

    return bit32;
}

/*****
 * reads RTD connected to ADS1220
 *****/
uint32_t ADS1220_RefTemperature(void) {
    digitalWrite(10, LOW);
    SPI.beginTransaction(SPI_Settings(4000000, MSBFIRST, SPI_MODE1)); // slower than 150 ns minimum
SPI clock period; MSBFIRST; only SPI_MODE 1 supported
    SPI_Junk_Received = SPI.transfer(0x41); // WREG one byte to register 00(binary)
    SPI_Junk_Received = SPI.transfer(0x78); // Channel AIN3 and AIN2 selected, gain 16
    SPI_Junk_Received = SPI.transfer(0x08); // Start/Sync command
    delay(100); // worst case scenario conversion should be available within 50 ms at 20 samples

    data.bytes[2] = SPI.transfer(0x00);
    data.bytes[1] = SPI.transfer(0x00);
    data.bytes[0] = SPI.transfer(0x00);
    SPI.endTransaction();
    digitalWrite(10, LOW);

    data.bytes[3] = 0x00; // most significant byte of 4-byte word is empty for 24 bit conversion
    int32_t value; // signed 16 bit integer

    value = data.word32;
}

```

```

    return value;
}

/*****
 * function to write to ADS1220 registers
 *****/
void writeRegister(uint8_t address, uint8_t value)
{
    digitalWrite(10, LOW);
    delay(5);
    SPI.transfer(WREG|(address<<2));
    SPI.transfer(value);
    delay(5);
    digitalWrite(10, HIGH);
}

/*****
 * function to read ADS1220 registers
 *****/
uint8_t readRegister(uint8_t address)
{
    uint8_t data;

    digitalWrite(10, LOW);
    delay(5);
    SPI.transfer(RREG|(address<<2));
    data = SPI.transfer(SPI_MASTER_DUMMY);
    delay(5);
    digitalWrite(10, HIGH);

    return data;
}

/*****
 * function to tell ADS1220 to do stuff based upon commands
 *****/
void SPI_Command(unsigned char data_in)
{
    digitalWrite(10, LOW);
    delay(2);
    digitalWrite(10, HIGH);
    delay(2);
    digitalWrite(10, LOW);
    delay(2);
    SPI.transfer(data_in);
    delay(2);
    digitalWrite(10, HIGH);
}

/*****
 * resets the ADS1220 to default values
 *****/
void SPI_Reset()
{
    SPI_Command(RESET);
}

/*****
 * initiates conversion on the ADS1220
 *****/
void SPI_Start()
{
    SPI_Command(START);
}

```

```

/*****
 * Measure current associated with PEF based upon frequency selected by user
 *****/
void PEFcurrent(void){
  int16_t value;
  bitWrite(SRdata, 5, 0); // ensures ADG704 channel is set on ADC122
  bitWrite(SRdata, 4, 1);
  sendData(SRdata);
  delay(10);
  sendData(SRdata);
  if(PEFfrequency == 20000){
    ADC122();
    for(int i = 0; i < 12; i++){
      dataB.bytesB[1] = RawconversionArray[i*4+2];
      dataB.bytesB[0] = RawconversionArray[i*4+3];
      value = NegativeCheck(dataB.word16B);
      PEFconversionArrayB[i] = value;
    }
  }
  else{
    for(int i = 0; i < 12; i++){
      ADC122_else();
      value = NegativeCheck(dataB.word16B);
      PEFconversionArrayB[i] = value;
      delayMicroseconds(PEFfactor);
    }
  }
}

/*****
 * Function used in PEFcurrent when PEF frequency is set below 20kHz
 *****/
void ADC122_else(){ // single shot sampling for PEF freqs lower than 20kHz
  digitalWrite(10,LOW);
  SPI.beginTransaction(SPISettings(6400000, MSBFIRST, SPI_MODE1));

  dataA.bytesA[1] = SPI.transfer(0x00); // two separate unions are used to capture the 32 bit
                                        // data string sent out
                                        // by ADC112, breaks them up into two separate 16bit
                                        // unsigned values.
                                        // data format of the 16bit unsigned value is
                                        // "0000xxxxxxxxxxxx" where 'x'
                                        // denotes the 12 bit conversion data of the ADC, this is
                                        // always followed by
                                        // four leading zeroes.

  dataA.bytesA[0] = SPI.transfer(0x00);
  dataB.bytesB[1] = SPI.transfer(0x00);
  dataB.bytesB[0] = SPI.transfer(0x00);

  SPI.endTransaction();
  digitalWrite(10,HIGH);
}

/*****
 * Function used within PEFcurrent() when PEF frequency is set at 20kHz
 *****/
void ADC122(void){ // SPI communication with ADC122 via SPI
                  // as the SPI communication speed. Max of ADC122 is 6.4MHz
                  // Arduino maximum is 4MHz which yields a 120KSps data rate.

  digitalWrite(10,LOW);
  SPI.beginTransaction(SPISettings(6400000, MSBFIRST, SPI_MODE1));

  for(int i = 0; i < 48; i++){
    RawconversionArray[i] = SPI.transfer(0x00); // two separate unions are used to capture the 32

```

```

// bit data string sent out
// by ADC112, breaks them up into two separate
// 16bit unsigned values.
// data format of the 16bit unsigned value is
// "0000xxxxxxxxxxxx" where 'x'
// denotes the 12-bit conversion data of the ADC,
// this is always followed by
// four leading zeroes.
}
SPI.endTransaction();
digitalWrite(10,HIGH);
}

/*****
* Checks if 2's compliment number is negative, and if it is converts it to
* readable format for Arduino.
*****/
int16_t NegativeCheck(uint16_t x){ // data sent out by ADC122 is set of two conversions in 32 bit
// format. After splitting 32bit data
// string into two 16 bit data strings check to see if the 12
// bit data contained within the 16 bit
// data string is of negative value (two's compliment
// format). If it is, convert the 12 bit negative
// number into 16 bit two's compliment negative number format.

int16_t y;
if( x & 0x800 ){ // two's complement 12 bit data within 16 bit bin number, check to see if
// number is negative
y = 0xf800 | (x & 0x7FF); // write 12 bit data as 16bit two's compliment
}
else{
y = x;
}
return y;
}

/*****
* Measured OMF current from ADS1115
*****/
void OMFcurrent(void){
int16_t adc0;
for(int i = 0; i < 24; i++){
adc0 = adsl.readADC_Differential_0_1(); // reads differential signal between AIN2 and AIN3
// for LT1999's ADS1115.

OMFconversionArrayB[i] = adc0;
delay(OMFfactor);
}
}

/*****
* Function to data log PEF and OMF voltage measurements, 10 measurement average
*****/
void VoltageMeasrements(void){
int OMFvoltageRAW = 0;
int PEFvoltageRAW = 0;
for(int i = 0; i < 10; i++){
OMFvoltageRAW = OMFvoltageRAW + analogRead(A1);
PEFvoltageRAW = PEFvoltageRAW + analogRead(A0);
}
OMFvoltageRAW = OMFvoltageRAW/10;
PEFvoltageRAW = PEFvoltageRAW/10;

OMFvoltage = OMFvoltageRAW*0.004883*14.7; // this formalua derived from votlage divider network
// on CU board.
PEFvoltage = PEFvoltageRAW*0.004883*2.15;
}

```

```

/*****
 * Back in Function used to control shift register outputs. Outputs of
 * shift registers control various IC packages on CU.
 *****/
void sendData(uint16_t mydataOut){
    PORTD &=~_BV(PD4); //clear everything out and prepare.
    PORTD &=~_BV(PD7); //enable output of shift register.
    PORTB |=_BV(PB0);
    PORTB &=~_BV(PB0); //prime the register clock.
    PORTD |=_BV(PD6);
    PORTD &=~_BV(PD6); //prime the data clock.
    for (int i = 0; i < 16; i++){
        PORTD &=~_BV(PD6); //begin clock cycle.
        //set pin to either 1 or 0 at bit i.
        if (bitRead(mydataOut,i)==1){
            PORTD |=_BV(PD4);
        }
        else{
            PORTD &=~_BV(PD4);
        }
        PORTD |=_BV(PD6); //shift register.
        PORTD &=~_BV(PD4); //zero the data pin to prevent bleed through.
    }
    PORTD &=~_BV(PD6); //stop shifting.
}

/*****
 * Turn PEF off
 *****/
void PEFoff(void){
    bitWrite(SRdata, 12, 0);
    bitWrite(SRdata, 13, 0);
    sendData(SRdata); // turn off PEF
}

/*****
 * Turn PEF on
 *****/
void PEFon(void){
    bitWrite(SRdata, 12, 1);
    bitWrite(SRdata, 13, 1);
    sendData(SRdata); // turn on PEF
}

/*****
 * Gets time from RTC and converts to character string
 *****/
void getTime(void){
    DateTime now;
    now = RTC.now();
    HOUR = now.hour();
    MINUTE = now.minute();
    MONTH = now.month();
    DAY = now.day();
    YEAR = now.year();

    sprintf(Str0,"%02d:%02d %02d/%02d/%04d",HOUR,MINUTE,MONTH,DAY,YEAR);
}

/*****
 * Function to log data
 *****/
void logData(void){
    bitWrite(SRdata, 5, 1); // ensures ADG704 channel is set on SD card
    bitWrite(SRdata, 4, 0);
}

```

```

sendData(SRdata);
delay(10);
sendData(SRdata);
sd.begin(SS, SD_SCK_MHZ(50));
myFile.open(fileName1, FILE_WRITE);

myFile.print(Str0);
myFile.print(F(", "));
myFile.print(Temp);
myFile.print(F(", "));
myFile.print(OMFvoltage);
myFile.print(F(", "));
myFile.println(PEFvoltage);
myFile.close();

myFile.open(fileName2, FILE_WRITE);
for(int i=0;i<12;i++){
  myFile.print(PEFconversionArrayB[i]);
  myFile.print(",");
}
myFile.println();
myFile.close();

myFile.open(fileName3, FILE_WRITE);
for(int i=0;i<24;i++){
  myFile.print(OMFconversionArrayB[i]);
  myFile.print(",");
}
myFile.println();
myFile.close();

SPI.end();
}

```

```

/*****
* NOTE: The following code is included to demonstrate UI functionality.
* The code is a snippet from the primary CU program, not included here.
*****/

```

```

#include "globals.h"

//Event handler for the LCD display
void myGenieEventHandler (void)
{
  genieFrame Event;
  genie.DequeueEvent(&Event);

  int temp = 0;

  if(Event.reportObject.cmd == GENIE_REPORT_EVENT)
  {
    if (Event.reportObject.object == GENIE_OBJ_FORM)
    {
      if (Event.reportObject.index == 1)
      {
        formtracker = 1;
        genie.WriteStr(6,Str0);
      }
      if (Event.reportObject.index == 5)
      {
        formtracker = 5;
        genie.WriteStr(7,Str0);
        infoUpdate();
      }
    }
  }
}

```

```

}
if (Event.reportObject.index == 6)
{
    formtracker = 6;
    genie.WriteStr(8,Str0);
    temp = ((intervals - 10000)/5000);
    genie.WriteObject(GENIE_OBJ_ROTARYSW, 0x00, temp);
    if(logtrue == HIGH)
    {
        genie.WriteStr(9,filenames);
    }
    else
    {
        genie.WriteStr(9,F("DATA LOGGING OFF!"));
    }
}
}
if (Event.reportObject.object == GENIE_OBJ_ROTARYSW)
{
    if (Event.reportObject.index == 0)
    {
        temp = genie.GetEventData(&Event);
        intervals = temp*5000+10000; // rotary has 5 settings ranging from 0~5, this equation
                                    // sets intervals with 5 second difference between each
                                    // interval.
    }
}
if (Event.reportObject.object == GENIE_OBJ_WINBUTTON)
{
    if (Event.reportObject.index == 31)
    {
        logtrue = LOW;
        genie.WriteStr(9,F("DATA LOGGING OFF!"));
    }
    if (Event.reportObject.index == 30)
    {
        logtrue = HIGH;
        genie.WriteStr(9,filenames);
    }
    if (Event.reportObject.index == 0)
    {
        if (OMFon == HIGH)
        {
            digitalWrite(DEACT, LOW); // turn on OMF
            OMFstart = millis();
        }
        if (PEFon == HIGH)
        {
            digitalWrite(SRdata, 12, 1);
            digitalWrite(SRdata, 13, 1);
            sendData(SRdata); // turn on PEF
            PEFstart = millis();
        }
        beginloop = HIGH;
        logtrue = HIGH;
        genie.WriteObject(GENIE_OBJ_FORM,6,0);
    }
}
if (Event.reportObject.index == 33)
{
    genie.WriteObject(GENIE_OBJ_FORM,8,0);
    USBcomm == 1;
    digitalWrite(SRdata, 7, 1); // USB data switch changed to usb comms mode.
    sendData(SRdata);
    beginloop = HIGH;
}
}

```

```

if (Event.reportObject.index == 32)
{
    genie.WriteObject(GENIE_OBJ_FORM,2,0);
    genie.WriteObject(GENIE_OBJ_WINBUTTON,5,1);
    genie.WriteStr(11,PEFfreq);
    genie.WriteStr(15,PEFphase1);
    genie.WriteStr(16,PEFphase2);
    genie.WriteStr(17,PEFphase3);
    genie.WriteStr(18,PEFduty1);
    genie.WriteStr(20,PEFduty2);
    genie.WriteStr(21,PEFduty3);
}
if (Event.reportObject.index == 5)
{
    State = HIGH; // numpad inputs for form 2 set for PEF
    genie.WriteStr(10,F("PEF inputs"));
    resetKeyValye();
    genie.WriteStr(11,PEFfreq);
    genie.WriteStr(15,PEFphase1);
    genie.WriteStr(16,PEFphase2);
    genie.WriteStr(17,PEFphase3);
    genie.WriteStr(18,PEFduty1);
    genie.WriteStr(20,PEFduty2);
    genie.WriteStr(21,PEFduty3);
}
if (Event.reportObject.index == 6)
{
    State = LOW; // numpad inputs on form 2 set for OMF
    genie.WriteStr(10,F("OMF inputs"));
    resetKeyValye();
    genie.WriteStr(11,OMFfreq);
    genie.WriteStr(15,OMFphase1);
    genie.WriteStr(16,OMFphase2);
    genie.WriteStr(17,OMFphase3);
    genie.WriteStr(18,OMFduty1);
    genie.WriteStr(20,OMFduty2);
    genie.WriteStr(21,OMFduty3);
}
if (Event.reportObject.index == 43)
{
    if (State == HIGH)
    {
        genie.WriteStr(10,F("PEF Freq 35-20000Hz, enter 0 to turn off"));
        resetKeyValye();
        buttontracker = 7;
    }
    else if (State == LOW)
    {
        genie.WriteStr(10,F("OMF freq 1-12Hz, enter 0 to turn off"));
        resetKeyValye();
        buttontracker = 14;
    }
}
if (Event.reportObject.index == 40)
{
    genie.WriteStr(10,F("Phase 1-100mins"));
    resetKeyValye();
    buttontracker = 1;
}
if (Event.reportObject.index == 41)
{
    genie.WriteStr(10,F("Phase 1-100mins"));
    resetKeyValye();
    buttontracker = 2;
}
if (Event.reportObject.index == 42)

```

```

    {
        genie.WriteStr(10,F("Phase 1-100mins"));
        resetKeyValye();
        buttontracker = 3;
    }
    if (Event.reportObject.index == 34)
    {
        genie.WriteStr(10,F("Duty 0-100%"));
        resetKeyValye();
        buttontracker = 4;
    }
    if (Event.reportObject.index == 35)
    {
        genie.WriteStr(10,F("Duty 0-100%"));
        resetKeyValye();
        buttontracker = 5;
    }
    if (Event.reportObject.index == 39)
    {
        genie.WriteStr(10,F("Duty 0-100%"));
        resetKeyValye();
        buttontracker = 6;
    }
}
if (Event.reportObject.object == GENIE_OBJ_KEYBOARD)
{
    if (Event.reportObject.index == 0)
    {
        temp = genie.GetEventData(&Event);
        if(temp >= 48 && temp <= 57 && counter <= 4)
        {
            keyvalue[counter] = temp;
            buttontrack(buttontracker); //update string after every entry
            counter = counter + 1;
        }
        else if(temp == 100)
        {
            counter--;
            keyvalue[counter] = 0;
            buttontrack(buttontracker); //update string after every entry
        }
        else if(temp == 8)
        {
            temp = atoi(keyvalue); //temp here is used to store keyvalue and to check if it is
            //within acceptable range
            finalwrite(buttontracker, temp);
            resetKeyValye();
        }
    }
}
}
}

/*****
 * Gets time from RTC and converts to character string
 *****/
void getTime(void){

    DateTime now;
    now = RTC.now();
    HOUR = now.hour();
    MINUTE = now.minute();
    MONTH = now.month();
    DAY = now.day();
    YEAR = now.year();
}

```

```

    sprintf(Str0,"%02d:%02d %02d/%02d/%04d",HOUR,MINUTE,DAY,MONTH,YEAR);
}

//keep time on each form up-to-date
void formTime(uint8_t form){
    getTime();
    genie.WriteString((form+2),Str0);
}

//function to take input from num pand and print to proper string
void buttontrack(uint8_t button){
    button = button % 7;
    switch(button)
    {
        case(1):
            genie.WriteString(15, keyvalue);
            break;
        case(2):
            genie.WriteString(16, keyvalue);
            break;
        case(3):
            genie.WriteString(17, keyvalue);
            break;
        case(4):
            genie.WriteString(18, keyvalue);
            break;
        case(5):
            genie.WriteString(20, keyvalue);
            break;
        case(6):
            genie.WriteString(21, keyvalue);
            break;
        case(0):
            genie.WriteString(11, keyvalue);
            break;
    }
}

//function to take input from num pad and print to proper string
void finalwrite(uint8_t button, int temp){
    button = button % 7;
    switch(button)
    {
        case(0):
            if(State == HIGH)
            {
                if(temp >= 35 && temp <= 20000)
                {
                    PEFfreq = temp; //remember this value input is going to be cut in half
                    SetPinFrequencySafe(PEF_PWM, PEFfreq);
                    genie.WriteString(10, F("Entered PEF freq"));
                    PEFon = HIGH;
                }
            }
            else if (temp == 0)
            {
                PEFon = LOW;
            }
            else
            {
                genie.WriteString(10, F("out of range"));
            }
        }
        else if (State == LOW)
        {
            if(temp >=1 && temp <= 12)
            {

```

```

    OMFfreq = temp;
    SetPinFrequencySafe(OMF_PWM, OMFfreq);
    genie.WriteStr(10, F("Entered OMF freq"));
    OMFon = HIGH;
}
else if (temp == 0)
{
    OMFon = LOW;
}
else
{
    genie.WriteStr(10, F("out of range"));
}
}
break;
case(1):
if(temp >=1 && temp <= 100)
{
    if(State == HIGH){ PEFphase1 = temp;}
    else if(State == LOW){OMFphase1 = temp;}
    genie.WriteStr(10, F("Entered Phase 1"));
}
else
{
    genie.WriteStr(10, F("out of range"));
}
}
break;
case(2):
if(temp >=1 && temp <= 100)
{
    if(State == HIGH){ PEFphase2 = temp;}
    else if(State == LOW){OMFphase2 = temp;}
    genie.WriteStr(10, F("Entered Phase 2"));
}
else
{
    genie.WriteStr(10, F("out of range"));
}
}
break;
case(3):
if(temp >=1 && temp <= 100)
{
    if(State == HIGH){ PEFphase3 = temp;}
    else if(State == LOW){OMFphase3 = temp;}
    genie.WriteStr(10, F("Entered Phase 3"));
}
else
{
    genie.WriteStr(10, F("out of range"));
}
}
break;
case(4):
if(temp >=0 && temp <= 100)
{
    if(State == HIGH){ PEFduty1 = temp;}
    else if(State == LOW){OMFduty1 = temp;}
    genie.WriteStr(10, F("Entered Duty 1"));
}
else
{
    genie.WriteStr(10, F("out of range"));
}
}
break;
case(5):
if(temp >=0 && temp <= 100)
{

```

```

        if(State == HIGH){ PEFduty2 = temp;}
        else if(State == LOW){OMFduty2 = temp;}
        genie.WriteStr(10, F("Entered Duty 2"));
    }
else
    {
        genie.WriteStr(10, F("out of range"));
    }
break;
case(6):
if(temp >=0 && temp <= 100)
    {
        if(State == HIGH){ PEFduty3 = temp;}
        else if(State == LOW){OMFduty3 = temp;}
        genie.WriteStr(10, F("Entered Duty 3"));
    }
else
    {
        genie.WriteStr(10, F("out of range"));
    }
break;
}
}

//Function to update display of either form 4 or 5, the forms which display system operation
parameters
void infoUpdate(void)
{
    if(formtracker == 5)
    {
        genie.WriteObject(GENIE_OBJ_LED_DIGITS, 1, OMFvolts);
        genie.WriteObject(GENIE_OBJ_LED_DIGITS, 3, OMFamps);
        genie.WriteObject(GENIE_OBJ_LED_DIGITS, 0, PEFvolts);
        genie.WriteObject(GENIE_OBJ_LED_DIGITS, 2, PEFamps);
        if ((OMFon == HIGH) && (PEFon == HIGH))
        {
            genie.WriteStr(14,F("OMF and PEF on"));
        }
        if ((OMFon == LOW) && (PEFon == LOW))
        {
            genie.WriteStr(14,F("OMF and PEF off"));
        }
        if ((OMFon == LOW) && (PEFon == HIGH))
        {
            genie.WriteStr(14,F("OMF off, PEF on"));
        }
        if ((OMFon == HIGH) && (PEFon == LOW))
        {
            genie.WriteStr(14,F("OMF on, PEF off"));
        }
    }
    if(formtracker == 1)
    {
        genie.WriteObject(GENIE_OBJ_SCOPE,0,tempReadings[0]);
        genie.WriteObject(GENIE_OBJ_SCOPE,0,tempReadings[1]);
        genie.WriteObject(GENIE_OBJ_SCOPE,0,tempReadings[2]);
        genie.WriteObject(GENIE_OBJ_SCOPE,0,tempReadings[3]);

        for(int i = 0; i < 4; i++){
            sprintf(temps,"T%d = %dC",i+1,tempReadings[i]);
            genie.WriteStr(i+2, temps);
        }
    }
}

void resetKeyValye(void){

```

```
for(int x = 0; x <= 5; x++)  
{  
    keyvalue[x] = 0;  
}  
}
```

## Appendix B. MatLab Code

```
%%%%%%%%%%%%%%%%%%%%%%%%%%%%%%%%%%%%%%%%%%%%%%%%%%%%%%%%%%%%%%%%%%%%%%%%
%Function used to calculate RMS current of OMF system%
%%%%%%%%%%%%%%%%%%%%%%%%%%%%%%%%%%%%%%%%%%%%%%%%%%%%%%%%%%%%%%%%%%%%%%%%
function [Irms] = currentcalc4(data)
[A, B] = size(data);
MM = zeros(A,B);
data1 = data.*0.000125; %LSB of ADS1115
data2 = data1.*0.05; %Gain correction from LT1999

for i = 1:1:A
    for j = 1:1:B
        MM(i,j) = data2(i,j)^2;
    end
end

MM1 = sum(MM,2);
MM2 = MM1./23;
MM3 = arrayfun(@(x) sqrt(x), MM2);
Vrms = MM3;
Irms = Vrms/0.03; %divide by the shunt resistor ohms to get Irms.

%%%%%%%%%%%%%%%%%%%%%%%%%%%%%%%%%%%%%%%%%%%%%%%%%%%%%%%%%%%%%%%%%%%%%%%%
%Function used to calculate RMS current of PEF system%
%%%%%%%%%%%%%%%%%%%%%%%%%%%%%%%%%%%%%%%%%%%%%%%%%%%%%%%%%%%%%%%%%%%%%%%%
function [Irms] = currentcalc2(data)

data = data';
[A B] = size(data);
x = zeros(A, B);

%-----
% Preform density based clustering algorithm
%-----
for c = 1:1:B
    x(:,c) = DBSCAN(data(:,c), 70, 2); %matrix x is the labels related to data
end

%-----
% Sort out the data array based upon labels as given by cluster array
%-----
for j = 1:1:B %for every column of grouping data
    xx = max(x(:,j)); %find the max grouping in that column
    group = zeros(12,xx);
    for i = 1:1:A %for every row of grouping data, in column j
        for t = 1:1:xx %for all possible grouping in column j
            if x(i,j) == t %check that data cell to see what grouping t is
                group(i,t) = data(i,j);
            end
        end
    end
    end
    group(group ==0) = NaN; %set all zeros to NaN
    groupmean = nanmean(group); %get the means of all columns
    meanmax = max(groupmean); %find the max of the means
    meanmin = min(groupmean); %find the min of the means

    if meanmin > 0 %just in case not enough negative groupings aren't found
        meanmin = -meanmax;
    end

    if meanmax < 100 %just in case not enough positive groupings aren't found
        meanmax = abs(meanmin);
    end

    MT(1,j) = (meanmax + abs(meanmin))/2; %average out the abs of the max and min, this is your
pk voltage measured
end

%-----
% Convert measured ADC code to final current measurement
```

```

%-----
Vpk = MT.*0.001221; %LSB of ADC1220, LSB is in Volts
Vrms = Vpk*sqrt(0.5); %get rms of sqr wave
Vtruerms = Vrms*0.05; %divide by gain of the LT1999 & ADC1220
Irms = Vtruerms/1.2; %divide by the shunt resistor ohms to get Irms
Irms = Irms';

end

%%%%%%%%%%%%%%%%%%%%%%%%%%%%%%%%%%%%%%%%%%%%%%%%%%%%%%%%%%%%%%%%%%%%%%%%
%MatLab script used to convert RGB values from JPEG image to LAB%
%%%%%%%%%%%%%%%%%%%%%%%%%%%%%%%%%%%%%%%%%%%%%%%%%%%%%%%%%%%%%%%%%%%%%%%%
beef = imread('SC 3 Day 7.JPG'); %image file name, change here
imshow(beef);
beefselection = getrect; %user selects rectangular area for analysis
beefcrop = imcrop(beef,beefselection);
imshow(beefcrop);

beeflab = rgb2lab(beefcrop,'WhitePoint','c'); %run RFG to LAB conversion

L = beeflab(:,:,1); %pull out the L value from beeflab 3D array
a = beeflab(:,:,2); %pull out the a value from beeflab 3D array
b = beeflab(:,:,3); %pull out the b value from beeflab 3D array
disp( [L(:), a(:), b(:)] );

%calculate the mean of L,a,b values from image
mean_L = mean(L(:));
mean_a = mean(a(:));
mean_b = mean(b(:));

%calculate the standard deviation of L,a,b values from image
std_L = std(L(:));
std_a = std(a(:));
std_b = std(b(:));

```

## Appendix C. Bill of Material, Electronic Components

Item	Quantity	Designator	Description
1	20	R1,R7,R10,R20,R21,R25, R30,R38,R39,R40,R41,R42 R43,R44,R72,R73,R74,R75, R76,R77	RES SMD 10K OHM 1% 1/16W 0402 (General Purpose)
2	5	R3,R11,R33,R45,R62	RES SMD 10K OHM 1% 1/10W 0603 (General Purpose)
3	1	R36	RES SMD 10K OHM 1% 1/8W 0805 (General Purpose)
4	1	R53	RES SMD 10K OHM 0.1% 1/10W 0603 (Current sense)
5	2	R47,R49	RES SMD 10K OHM 0.1% 1/8W 0805 (Voltage sense)
6	1	R18	RES 10K OHM 3W 5% AXIAL (OMF Voltage Bias)
7	3	R8,R9,R22	RES SMD 1K OHM 1% 1/16W 0402 (General Purpose)
8	3	R22,R50,R51	RES SMD 1K OHM 0.1% 1/16W 0402 (Voltage sense)
9	1	R15	RES 1K OHM 3W 5% AXIAL (OMF Voltage Bias)
10	4	R26,R28,R31,R32	RES SMD 100K OHM 1% 1/10W 0603 (General Purpose)
11	1	RN4	RES ARRAY 4 RES 1K OHM 1206 (LED resistors)
12	3	R2,R27,R29	RES SMD 47 OHM 5% 1/16W 0402 (Thermocouple)
13	1	R4	RES SMD 1.5K OHM 0.1% 1/10W 0603 (PEF voltage bias)
14	1	R5	RES SMD 1.6 OHM 1% 1/4W 1206 (PEF current sense)
15	1	R19	RES SMD 1.2 OHM 1% 1/4W 1206 (PEF current sense, alt)
16	2	R6,R60	RES SMD 20K OHM 1% 1/10W 0603 (General Purpose)
17	1	R12	RES SMD 88.7K OHM 1% 1/10W 0603
18	4	R13,R14,R64,R65	RES SMD 5.1 OHM 0.1% 1/16W 0603 (Filer resistor)
19	1	R16	RES 10.0 OHM 3W 5% AXIAL (OMF voltage bias)
20	1	R17	RES SMD 1M OHM 1% 1/16W 0402 (General Purpose)
21	3	R23,R66,R67	18.7k Ohm ±1% 1W Chip Resistor 2512
22	1	R24	RES SMD 64.9K OHM 1% 1/2W 1210 (Over voltage protection)
23	4	R54, R55,R34, R35	RES SMD 499 OHM 1% 1/16W 0402 (Filter resistors)
24	1	R37	RES SMD 75 OHM 2% 11W 1206 (OMF voltage bias)
25	1	R46	137k Ohm ±0.1% 0.125W, 1/8W Chip Resistor 0805 (2012 Metric)
26	1	R48	RES SMD 11.5K OHM 0.1% 1/8W 0805 (Voltage sense)
27	1	R52	RES SMD 56K OHM 0.5% 1/10W 0603 (Current sense, latch)
28	2	R56,R57	RES SMD 2M OHM 1% 1/16W 0402 (Filter resistors)
29	1	R58	RES SMD 3.24K OHM 0.1% 1/4W 1206
30	2	R59, R61	RES SMD 10 OHM 1% 1/10W 0603
31	1	R63	RES SMD 330 OHM 1% 1/16W 0402
32	3	R68,R70,R71	RES SMD 3K OHM 5% 1/2W 0805
33	1	R69	RES SMD 6.04K OHM 1% 1/2W 1206
34	1	R78	RES SMD 0.0 OHM JUMPER 1W 2512

35	1	R79	RES SMD 0.0 OHM JUMPER 1/8W 0805
36	1	R80	RES SMD 2K OHM 1% 1/10W 0603
37	1	RN1	RES ARRAY 4 RES 100K OHM 1206
38	1	U\$17	RES SMD 0.03 OHM 0.5% 1W 2412
39	1	U\$41	RES SMD 0.05 OHM 0.5% 1W 2412
40	1	U\$17,U41	RES SMD 0.0 OHM JUMPER 1W 2512
41	1	n/a	POT 10K OHM 25W WIREWOUND LINEAR
42	1	n/a	POT 10K OHM 1/2W CARBON LINEAR
43	1	U\$11	RES SMD 100 OHM 5% 10W 2010
44	4	C1,C5,C6,C49	CAP TANT 10UF 10V 10% 1411
45	2	C2,C11	CAP CER 10000PF 50V X7R 0603
46	1	C3	CAP TANT 10UF 10V 10% 1206
47	2	C9,C12	CAP CER 1UF 6.3V X5R 0402
48	3	C63,C64,C54	CAP CER 1UF 50V X7R 0603
49	2	C60,C29	CAP CER 1UF 10V X5R 0402
50	2	C58,C51	CAP CER 1UF 10V X7R 0603
51	23	C4,C8,C10,C15,C17, C19,C21,C22,C25,C26, C27,C28,C31,C32,C36, C39,C40,C43,C44, C48,C50,C62,C66	CAP CER 0.1UF 100V X5R 0402
52	4	C52,C53,C55,C56	CAP CER 0.1UF 50V X7R 0402
53	2	C38,C47	CAP CER 0.1UF 16V X7R 0603
54	1	C37	CAP CER 0.1UF 50V X7R 0805
55	2	C41,C42	CAP CER 0.1UF 100V X7S 0603
56	5	C7,C13,C23,C24,C45	CAP CER 10UF 25V X5R 0603
57	2	C65,C67	CAP CER 10UF 10V X5R 0402
58	2	C14,C18	CAP CER 0.33UF 50V X5R 0603
59	2	C16,C30	CAP CER 0.22UF 6.3V X5R 0402
60	1	C20	CAP CER 0.33UF 35V X5R 0402
61	2	C33,C34	CAP CER 0.27UF 6.3V X5R 0402
62	1	C35	CAP CER 4.7UF 6.3V X5R 0603
63	3	C59, C57, C61	CAP CER 2.2UF 10V X7R 0603
64	1	U\$7	CAP ALUM 3.3UF 20% 200V RADIAL
65	1	U\$6	CAP ALUM 10UF 20% 200V RADIAL
66	2	PC1,PC2	CAP ALUM 47UF 20% 25V SMD
67	2	3V3ON,5VON1	LED GREEN CLEAR 0805 SMD
68	2	5VON,5VON2	LED BLUE CLEAR 0805 SMD
69	1	L	LED YELLOW CLEAR 0805 SMD
70	1	LED2	LED RED CLEAR 0603 SMD
71	1	BAT1	HOLDER BATTERY COIN 12MM DIA THM

72	1	CN1	CONN RECEPT MINIUSB R/A 5POS SMD
73	1	JP2	CONN MICRO SD CARD PUSH-PUSH R/A
74	2	S1,S2	SWITCH TACTILE SPST-NO 0.05A 12V
75	1	U\$21	TERM BLOCK HDR 4POS 90DEG 2.5MM
76	1	N/A	TERM BLOCK PLUG 4POS STR 2.5MM
77	4	U\$23,U\$24,U\$1,U\$25	TERM BLOCK HDR 3POS 90DEG 2.5MM
78	4	N/A	TERM BLOCK PLUG 3POS STR 2.5MM
79	1	U\$13	TERM BLOCK 10POS SIDE ENT 2.54MM
80	7	U\$42,U\$43,U\$44, U\$45,U\$46,U\$47,U\$48	TEST POINT PC MINI .040"D BLACK
81	2	U\$49,U\$50	TEST POINT PC MINI .040"D YELLOW
82	9	U\$20,U\$55,U\$56,U\$57, U\$58,U\$59,U\$60,U\$61, U\$62	TEST POINT PC MINI .040"D RED
83	1	U\$28	TERM BLOCK PCB 2POS 5.0MM GREEN
84	3	U\$38,U\$39,U\$40	CONN FEMALE 3POS .1" SMD GOLD
85	1	U\$7	CONN FEMALE 2POS .1" SMD TIN
86	6	D1,D6,D7,D8,D9,D10	DIODE ZENER 10V 200MW SMINI2
87	2	D2,D11	DIODE ZENER 27V 500MW SOD123
88	1	D3	DIODE GEN PURP 100V 150MA 1206
89	1	D4	DIODE SCHOTTKY 30V 1A MICROSMP
90	2	DC/DC1,DC/DC3	CONV DC/DC +/-15V +/-50MA DIP
91	1	FB3	FERRITE BEAD 47 OHM 0805 1LN
92	1	L6	FERRITE BEAD 30 OHM 0805 1LN
93	1	IC1	IC JK TYPE POS TRG DUAL 16SOIC
94	1	IC2	IC GATE NAND 4CH 2-INP 14-SOIC
95	1	IC3	IC HEX INVERTER 14SOIC
96	1	IC7	IC GATE NOR 4CH 2-INP 14-SO
97	1	IC4	IC REG BUCK ADJ 1A TSOT23-6
98	1	IC5	IC OPAMP GP 1MHZ RRO 8VSSOP
99	1	IC6	IC MCU 8BIT 32KB FLASH 32TQFP
100	1	IC8	IC REG LDO 3.3V 1A SOT223
101	1	IC9	IC ADC 24-BIT 2KSPS 16-TSSOP
102	1	IC10	IC REG LDO ADJ 0.8A DPAK
103	1	IC11	IC MULTIPLEXER 4X1 10USOIC
104	1	IC14	IC MULTIPLEXER DUAL 8X1 28TSSOP
105	1	IC17	IC USB SWITCH DUAL 1X2 10-QFN
106	2	IC18,IC19	IC SHIFT REGISTER 8-BIT 16-TSSOP
107	1	IGBT2	IC PWR HYBRID 600V 20A SIP2
108	1	U3	IC USB FS SERIAL UART 28-SSOP

109	1	L4	FIXED IND 10UH 1.3A 120 MOHM SMD
110	2	Q1,Q2	MOSFET P-CH 250V 6A TO-220F
111	1	Q3	CRYSTAL 32.7680KHZ 12.5PF SMD
112	7	Q4,Q7,Q8,Q9,Q11,Q12,Q13	MOSFET N-CH 50V 220MA SOT-23
113	1	Q5	TRANS PNP 100V 1A TO-220
114	1	Q6	TRANS NPN 500V 12A TO-220
115	1	Q10	MOSFET P-CH 150V 0.53A SOT-23
116	1	T1	MOSFET P-CH 20V 2A SSOT3
117	1	U\$2	IC MONITOR PWR/CUR BIDIR 8VSSOP
118	5	U\$3,U\$4,U\$9,U\$10, U\$19,U\$51	DIODE GEN PURP 100V 150MA SOD123
119	1	U\$5	IC REG LDO ADJ 0.7A DDPK
120	1	U\$8	IC REG LDO 5V 1A SOT223
121	1	U\$12	IC MOTOR DRIVER PAR 12WSON
122	1	U\$14	IC REG LDO 5V 0.5A SOT223
123	1	U\$15	IC CURRENT MONITOR 3.5% 8VSSOP
124	2	U\$16,U\$18	IC OP AMP CUR SENSE 2MHZ 8MSOP
125	1	U\$22	IC REG LDO 15V 1A DPAK
126	1	U\$26	IC ADC 16BIT 860SPS LP 10MSOP
127	1	U\$27	IC REG LDO 12V 1A DPAK
128	1	U\$29	IC REG LDO 3.3V 0.15A SC70-5
129	2	U\$30,U\$31	DIODE ARRAY GP 70V 215MA SOT23
130	4	U\$32,U\$33,U\$34,U\$35	TVS DIODE 13VWM 21.5VC SOD128
131	1	U\$36	IC VREF SERIES 2.048V 8SOIC
132	1	U\$52	MOSFET P-CH 250V 0.197A SOT-23-6
133	2	U\$53,U\$54	MOSFET P-CH 150V 13A POWER33
134	1	U\$63	IC ADC 2CH 12BIT 200KSPS 10MSOP
135	1	U\$64	IC VREF SHUNT 2.5V SOT23-3
136	1	U1	IC VOLT-LEVEL TRANSLATOR 14-SOIC
137	1	U2	IC RTC CLK/CALENDAR I2C 8-SOIC
138	1	XTAL1	CER RES 16.0000MHZ 15PF SMD
139	1	J3	CONN HEADER FEMALE 6POS .1" GOLD

**Total Components 283**

Mfctr. Part Number	Distributor	Dstbr. Part #	Cost Each	Total parts cost
RC0402FR-0710KL	Digikey	311-10.0KLRCT-ND	\$0.00	\$0.07
RC0603FR-0710KL	Digikey	311-10.0KHRCT-ND	\$0.00	\$0.02
RC0805FR-0710KL	Digikey	311-10.0KCRCT-ND	\$0.01	\$0.01
RR0816P-103-D	Digikey	RR08P10.0KDCT-ND	\$0.04	\$0.04
ERA-6AEB103V	Digikey	P10KDACT-ND	\$0.29	\$0.58
RSMF3JT10K0	Digikey	RSMF3JT10K0CT-ND	\$0.19	\$0.19
311-1.00KLRCT-ND	Digikey	RC0402FR-071KL	\$0.00	\$0.01
ERA-2AEB102X	Digikey	P1.0KDCCT-ND	\$0.31	\$0.92
RSMF3JT1K00	Digikey	RSMF3JT1K00CT-ND	\$0.19	\$0.19
RC0603FR-07100KL	Digikey	311-100KHRCT-ND	\$0.00	\$0.02
CAY16-1001F4LF	Digikey	CAY16-1001F4LFCT-ND	\$0.06	\$0.06
CRCW040247R0JNED	Digikey	541-47JCT-ND	\$0.01	\$0.02
ERA-3AEB152V	Digikey	P1.5KDBCT-ND	\$0.21	\$0.21
CRCW12061R60FKEA	Digikey	541-1.60FFCT-ND	\$0.03	\$0.03
RC1206FR-071R2L	Digikey	311-1.20FRCT-ND	\$0.01	\$0.01
RC0603FR-0720KL	Digikey	311-20.0KHRCT-ND	\$0.00	\$0.01
RC0603FR-0788K7L	Digikey	311-88.7KHRCT-ND	\$0.00	\$0.00
CPF0603B5R1E1	Digikey	A103115CT-ND	\$0.28	\$1.13
ROX3SJ10R	Digikey	A106021CT-ND	\$0.17	\$0.17
RC0402FR-071ML	Digikey	311-1.00MLRCT-ND	\$0.00	\$0.00
CRCW251218K7FKEG	Digikey	541-18.7KAFCT-ND	\$0.30	\$0.91
CRCW121064K9FKEA	Digikey	541-64.9KAACT-ND	\$0.11	\$0.11
CRCW0402499RFKED	Digikey	541-499LCT-ND	\$0.01	\$0.04
RCP1206W75R0GEB	Digikey	541-2660-1-ND	\$1.81	\$1.81
ERA-6AEB1373V	Digikey	P137KDACT-ND	\$0.39	\$0.39
RT0805BRD0711K5L	Digikey	YAG1768CT-ND	\$0.30	\$0.30
RT0603DRE0756KL	Digikey	311-2622-1-ND	\$0.10	\$0.10
CRCW04022M00FKED	Digikey	541-2.00MLCT-ND	\$0.01	\$0.02
ERA-8ARB3241V	Digikey	P18647CT-ND	\$1.21	\$1.21
CRCW060310R0FKEA	Digikey	541-10.0HCT-ND	\$0.01	\$0.02
RC0402FR-07330RL	Digikey	311-330LRCT-ND	\$0.00	\$0.00
ERJ-P06J302V	Digikey	P3.0KADCT-ND	\$0.05	\$0.16
RNCP1206FTD6K04	Digikey	RNCP1206FTD6K04CT-ND	\$0.02	\$0.02
RC2512JK-070RL	Digikey	YAG1232CT-ND	\$0.05	\$0.05
RC0805JR-070RL	Digikey	311-0.0ARCT-ND	\$0.01	\$0.01
ERJ-3EKF2001V	Digikey	P2.00KHCT-ND	\$0.01	\$0.01

CAY16-1003F4LF	Digikey	CAY16-1003F4LFCT-ND	\$0.22	\$0.22
LVK24R030DER	Digikey	LVK24R030DERCT-ND	\$1.53	\$1.53
LVK24R050DER	Digikey	LVK24R050DERCT-ND	\$1.53	\$1.53
RC2512JK-070RL	Digikey	YAG1232CT-ND	\$0.16	\$0.16
RHS10KE	Digikey	RHS10KE-ND	\$54.35	\$54.35
450T328F103A1C1	Digikey	CT3057-ND	\$5.25	\$5.25
CHF2010CNP101RX	Digikey	CHF2010CNP101RX-ND	\$5.41	\$5.41
T491B106K010AT	Digikey	399-3705-1-ND	\$0.24	\$0.97
C0603C103J5RACTU	Digikey	399-1092-1-ND	\$0.02	\$0.03
T491A106K010AT	Digikey	399-3684-1-ND	\$0.22	\$0.22
GRM155R60J105KE19D	Digikey	490-1320-1-ND	\$0.01	\$0.02
UMK107AB7105KA-T	Digikey	587-3247-1-ND	\$0.10	\$0.31
GRM155R61A105KE15D	Digikey	490-3890-1-ND	\$0.01	\$0.02
GRM188R71A105KA61D	Digikey	490-3899-1-ND	\$0.08	\$0.16
GRM155R62A104KE14D	Digikey	490-10458-1-ND	\$0.01	\$0.19
C1005X7R1H104K050BB	Digikey	445-5932-1-ND	\$0.05	\$0.19
GRM188R71C104KA01D	Digikey	490-1532-1-ND	\$0.01	\$0.01
08055C104KAT2A	Digikey	478-1395-1-ND	\$0.01	\$0.01
CGA3E3X7S2A104K080AB	Digikey	445-6938-1-ND	\$0.06	\$0.13
ZRB18AR61E106ME01L	Digikey	490-10991-1-ND	\$0.36	\$1.78
CL05A106MP8NUB8	Digikey	1276-6830-1-ND	\$0.14	\$0.27
C1608X5R1H334K080AB	Digikey	445-7462-1-ND	\$0.12	\$0.25
GRM155R60J224KE01D	Digikey	490-5407-1-ND	\$0.03	\$0.05
C1005X5R1V334K050BC	Digikey	445-13862-1-ND	\$0.06	\$0.06
GRM155R60J274KE01D	Digikey	490-6291-1-ND	\$0.07	\$0.13
GRM188R60J475KE19D	Digikey	490-3297-1-ND	\$0.04	\$0.04
GRM188R71A225KE15D	Digikey	490-4520-1-ND	\$0.11	\$0.32
UVZ2D3R3MED	Digikey	493-1400-ND	\$0.15	\$0.15
UVK2D100MPD	Digikey	UVK2D100MPD-ND	\$0.25	\$0.25
EEE-1EA470WP	Digikey	PCE3908CT-ND	\$0.17	\$0.34
APT2012ZGC	Digikey	APT2012ZGC	\$0.46	\$0.93
APT2012VBC/D	Digikey	754-1794-1-ND	\$0.37	\$0.74
APT2012SYCK/J3-PRV	Digikey	754-1793-1-ND	\$0.33	\$0.33
LTST-C190EKT	Digikey	160-1182-1-ND	\$0.16	\$0.16
3001	Digikey	36-3001-ND	\$0.55	\$0.55
675031020	Digikey	WM5461CT-ND	\$0.99	\$0.99
101-00581-59	Digikey	101-00581-59-1-ND	\$1.67	\$1.67
TL3342F160QG/TR	Digikey	EG2531CT-ND	\$0.60	\$1.21
1778780	Digikey	277-2317-1-ND	\$1.08	\$1.08

1778858	Digikey	277-2324-ND	\$1.23	\$1.23
1778777	Digikey	277-2316-1-ND	\$0.80	\$3.22
1778845	Digikey	277-2323-ND	\$1.00	\$3.99
1-282834-0	Digikey	A98074-ND	\$6.12	\$6.12
5001	Digikey	36-5001-ND	\$0.23	\$1.61
5004	Digikey	36-5004-ND	\$0.23	\$0.46
5000	Digikey	36-5000-ND	\$0.23	\$2.07
1935161	Digikey	277-1667-ND	\$0.35	\$0.35
NPPC031KFXC-RC	Digikey	S5634-ND	\$0.73	\$2.19
NPTC021KFXC-RC	Digikey	S5594-ND	\$0.59	\$0.59
DZ2J100M0L	Digikey	DZ2J100M0LCT-ND	\$0.12	\$0.71
MMSZ5254B-TP	Digikey	MMSZ5254B-TPMSCT-ND	\$0.11	\$0.22
CD1206-S01575	Digikey	CD1206-S01575CT-ND	\$0.09	\$0.09
MSS1P3L-M3/89A	Digikey	MSS1P3L-M3/89AGICT-ND	\$0.27	\$0.27
PWR1317AC	Digikey	811-1819-5-ND	\$33.81	\$67.62
BK2125HS470-T	Digikey	587-1911-1-ND	\$0.04	\$0.04
MH2029-300Y	Digikey	MH2029-300YCT-ND	\$0.04	\$0.04
CD4027BM96	Digikey	296-31493-1-ND	\$0.36	\$0.36
CD4011BM96	Digikey	296-14474-1-ND	\$0.35	\$0.35
HEF4069UBT,653	Digikey	568-8083-1-ND	\$0.34	\$0.34
74HC02D,652	Digikey	568-3947-5-ND	\$0.35	\$0.35
LM2734YMK/NOPB	Digikey	LM2734YMK/NOPBCT-ND	\$2.33	\$2.33
LMV358IDGKR	Digikey	296-13455-1-ND	\$0.68	\$0.68
ATMEGA328PB-AU	Digikey	ATMEGA328PB-AU-ND	\$1.40	\$1.40
NCP1117ST33T3G	Digikey	NCP1117ST33T3GOSCT-ND	\$0.39	\$0.39
ADS1220IPWR	Digikey	296-39851-1-ND	\$8.71	\$8.71
MC33269DTG	Digikey	MC33269DTGOS-ND	\$0.77	\$0.77
ADG704BRMZ-REEL	Digikey	ADG704BRMZ-REELCT-ND	\$2.84	\$2.84
ADG707BRUZ	Digikey	ADG707BRUZ-ND	\$6.36	\$6.36
TS3USB221ERSER	Digikey	296-25222-1-ND	\$1.06	\$1.06
MM74HC595MTCX	Digikey	MM74HC595MTCXCT-ND	\$0.39	\$0.77
IRAMX20UP60A	Digikey	IRAMX20UP60A-ND	\$24.13	\$24.13
FT232RL-REEL	Digikey	768-1007-1-ND	\$4.50	\$4.50
SRR0604-100ML	Digikey	SRR0604-100MLCT-ND	\$0.64	\$0.64
FQPF9P25	Digikey	FQPF9P25FS-ND	\$1.40	\$2.79
ECS-.327-12.5-13FLX-C	Digikey	XC1911CT-ND	\$0.58	\$0.58
BSS138	Digikey	BSS138CT-ND	\$0.09	\$0.66
TIP30C	Digikey	TIP30C-ND	\$0.46	\$0.46
BUL743	Digikey	BUL743	\$1.53	\$1.53

SI2325DS-T1-GE3	Digikey	SI2325DS-T1-GE3CT-ND	\$0.88	\$0.88
FDN340P	Digikey	FDN340PCT-ND	\$0.32	\$0.32
INA225AIDGKT	Digikey	296-37540-1-ND	\$2.80	\$2.80
1N4148W-TP	Digikey	1N4148WTPMSCT-ND	\$0.11	\$0.57
TL783CKTTR	Digikey	296-20778-1-ND	\$2.18	\$2.18
NCP1117ST50T3G	Digikey	NCP1117ST50T3GOSCT-ND	\$0.39	\$0.39
DRV8839DSSR	Digikey	296-35701-1-ND	\$1.37	\$1.37
UA78M05CDCYR	Digikey	296-12290-1-ND	\$0.54	\$0.54
INA200AIDGKR	Digikey	296-21331-1-ND	\$2.60	\$2.60
LT1999HMS8-20F#PBF	Digikey	LT1999HMS8-20F#PBF-ND	\$5.35	\$10.70
MC7815BDTRKG	Digikey	MC7815BDTRKGOSCT-ND	\$0.57	\$0.57
ADS1115IDGSR	Digikey	296-38849-1-ND	\$5.65	\$5.65
MC7812BDTG	Digikey	MC7812BDTGOS-ND	\$0.55	\$0.55
TPS71733DCKR	Digikey	296-19675-1-ND	\$0.99	\$0.99
BAV199-TP	Digikey	BAV199-TPMSCT-ND	\$0.23	\$0.46
PTVS13VP1UP,115	Digikey	568-5313-1-ND	\$0.40	\$1.61
REF5020ID	Digikey	296-22202-5-ND	\$6.96	\$6.96
ZVP4525E6TA	Digikey	ZVP4525E6CT-ND	\$0.78	\$0.78
FDMC86259P	Digikey	FDMC86259PCT-ND	\$1.91	\$3.82
ADC122S625CIMM/NOPB	Digikey	ADC122S625CIMM/NOPBCT-ND	\$6.63	\$6.63
LM4040DIM3-2.5/NOPB	Digikey	LM4040DIM3-2.5/NOPBCT-ND	\$0.70	\$0.70
TXB0104DR	Digikey	296-21928-1-ND	\$1.39	\$1.39
DS1307Z+T&R	Digikey	DS1307Z+T&RCT-ND	\$3.27	\$3.27
CSTCE16M0V53-R0	Digikey	490-1198-1-ND	\$0.40	\$0.40
PPPC061LFBN-RC	Digikey	S7039-ND	\$0.55	\$0.55

<b>Total</b>	<b>\$300.32</b>
--------------	-----------------

## Appendix D. Costs of Goods Sold Analysis

BoM SCboard Ver5.4

Last Modified: 7/31/2017

<b>Item</b>	
Electronic Components	\$300.32
PCB	\$81.18
Wire assembly	\$80.00
Enclosure	\$120.00
External Power Supply	\$150.00
<b>Total BoM</b>	<b>\$731.50</b>
<hr/>	
<b>COGS</b>	
Transformation Cost	25%
Assembly Labor	\$182.88
Packaging	\$1.50
Software	\$5.00
User Manual	\$0.75
Shipping	\$20.00
	\$210.13
<b>Product COGS</b>	<b>\$941.63</b>
<hr/>	
Distributor/commission (25%)	\$235.41
<b>Sales COGS</b>	<b>\$1,177.03</b>
<b>Gross Margin</b>	<b>\$322.97</b>
<b>GM %</b>	<b>22%</b>
<b>ASP</b>	<b>\$1,500.00</b>

## Appendix E. Summary of Thermocouple emf Measurement System Calibration Data

Table 15. Pre-calibrated data, Temperature measurements summary. Bias error is the difference between Fluid bath temperatures and CU measured temperatures.

	Set Points, C	Fluid Bath, C	Fluid Bath std dev, C	CU temp average, C	CU temp Std dev, C	bias error avg, C	bias error std dev, C
Channel 1	-20	-20.27168333	0.015378945	-19.925767	0.016045	-0.345917	0.005569
	-10	-10.30156	0.008006977	-10.144367	0.010896	-0.157193	0.007669
	0	-0.297473333	0.007988361	-0.267133	0.009101	-0.068180	0.005334
	10	9.723086667	0.016539906	9.662267	0.017214	0.029587	0.005720
	20	19.69382	0.018404932	19.581167	0.018931	0.095770	0.006277
	30	29.64527333	0.017710838	29.512200	0.018530	0.122387	0.005288
	40	39.59674667	0.011426751	39.472333	0.012673	0.119623	0.005870
Channel 2	-20	-20.27441333	0.013682052	-19.924733	0.014611	-0.349680	0.005632
	-10	-10.29998	0.008010338	-10.136933	0.009246	-0.159147	0.005332
	0	-0.296513333	0.009822077	-0.260033	0.010344	-0.034613	0.005150
	10	9.720266667	0.012238937	9.662400	0.013127	0.059010	0.005429
	20	19.69528333	0.008853419	19.587800	0.019448	0.108317	0.005550
	30	29.64402667	0.017898859	29.514833	0.018233	0.130230	0.005532
	40	39.59671667	0.013276475	39.477200	0.014271	0.121337	0.005978
Channel 4	-20	-20.26611333	0.013234033	-19.928333	0.014229	-0.337780	0.005455
	-10	-10.29415333	0.007381147	-10.131000	0.008806	-0.164343	0.005444
	0	-0.295516667	0.007743275	-0.258633	0.009228	-0.036783	0.005095
	10	9.720136667	0.012055214	9.669033	0.012806	0.051097	0.005333
	20	19.69453667	0.022591973	19.587800	0.023003	0.107147	0.005883
	30	29.64456	0.017360198	29.522800	0.018297	0.125290	0.005603
	40	39.59560333	0.014616603	39.482600	0.014719	0.114257	0.005968
Channel 5	-20	-20.26559333	0.013267443	-19.928567	0.016179	-0.337027	0.008753
	-10	-10.29319667	0.008813287	-10.129033	0.010223	-0.163500	0.005321
	0	-0.295863333	0.007523459	-0.259100	0.009393	-0.036667	0.005267
	10	9.720053333	0.015750288	9.665367	0.016849	0.054060	0.005293
	20	19.69444667	0.018283675	19.587467	0.019047	0.107280	0.005521
	30	29.64868	0.01212182	29.524333	0.012752	0.120693	0.005064
	40	39.59784333	0.013324552	39.483200	0.013707	0.114417	0.005107
	Maximum error/std dev -->		0.022591973		0.023002954	0.345917	0.008753
	Average error/std dev -->		0.0143		0.0152	0.1354	0.0058

Table 16. Pre-calibrated data, emf measurement summary. Bias error is the difference between DAQ emf and CU measured emf.

	Set Points, C	Fluid Bath, C	Fluid Bath std dev, C	CU emf average, mV	CU emf Std dev, mV	DAQ emf average, mV	DAQ emf Std dev, mV	bias error avg, mV	bias error std dev, mV
Channel 1	-20	-20.271683	0.015379	-0.753657	0.000572	-0.760839	0.000638	-0.007182	0.000289
	-10	-10.301560	0.008007	-0.387856	0.000395	-0.392644	0.000435	-0.004789	0.000292
	0	-0.297473	0.007988	-0.010710	0.000330	-0.013415	0.000389	-0.002704	0.000275
	10	9.723087	0.016540	0.376302	0.000674	0.375960	0.000702	-0.000342	0.000290
	20	19.693820	0.018405	0.770777	0.000753	0.772654	0.000768	0.001877	0.000291
	30	29.645273	0.017711	1.173608	0.000744	1.177825	0.000771	0.004217	0.000272
	40	39.596747	0.011427	1.585551	0.000514	1.592162	0.000546	0.006611	0.000273
Channel 2	-20	-20.274413	0.013682	-0.753614	0.000530	-0.760818	0.000569	-0.007203	0.000280
	-10	-10.299980	0.008010	-0.387734	0.000338	-0.392519	0.000363	-0.004785	0.000268
	0	-0.296513	0.009822	-0.010508	0.000416	-0.013225	0.000453	-0.002717	0.000277
	10	9.720267	0.012239	0.376309	0.000512	0.375875	0.000536	-0.000435	0.000282
	20	19.695283	0.008853	0.771009	0.000685	0.772833	0.000706	0.001823	0.000268
	30	29.644027	0.017899	1.173721	0.000743	1.177928	0.000776	0.004207	0.000269
	40	39.596717	0.013276	1.585767	0.000569	1.592385	0.000607	0.006617	0.000286
Channel 4	-20	-20.266113	0.013234	-0.753755	0.000512	-0.760561	0.000520	-0.006805	0.000352
	-10	-10.294153	0.007381	-0.387350	0.000317	-0.392137	0.000360	-0.004787	0.000277
	0	-0.295517	0.007743	-0.010374	0.000341	-0.013061	0.000391	-0.002687	0.000296
	10	9.720137	0.012055	0.376546	0.000490	0.376014	0.000549	-0.000532	0.000299
	20	19.694537	0.022592	0.771040	0.000923	0.772844	0.000980	0.001803	0.000253
	30	29.644560	0.017360	1.174047	0.000744	1.178161	0.000764	0.004114	0.000300
	40	39.595603	0.014617	1.585978	0.000606	1.592543	0.000647	0.006565	0.000291
Channel 5	-20	-20.265593	0.013267	-0.753760	0.000585	-0.760579	0.000548	-0.006819	0.000358
	-10	-10.293197	0.008813	-0.387279	0.000362	-0.392081	0.000410	-0.004802	0.000288
	0	-0.295863	0.007523	-0.010403	0.000353	-0.013091	0.000382	-0.002688	0.000276
	10	9.720053	0.015750	0.376417	0.000650	0.375868	0.000680	-0.000549	0.000280
	20	19.694447	0.018284	0.771020	0.000744	0.772796	0.000789	0.001776	0.000269
	30	29.648680	0.012122	1.174117	0.000517	1.178182	0.000577	0.004066	0.000300
	40	39.597843	0.013325	1.586020	0.000559	1.592541	0.000616	0.006521	0.000280
	Maximum error/std dev -->		0.022592		0.000923		0.000980	0.007203237	0.000358
	Average error/std dev -->		0.0143		0.0005927		0.0006246	0.003929368	0.0002897

Table 17. Pre-calibrated data with calibration correction applied, temperature measurement summary.

	Set Points, C	Fluid Bath, C	Fluid Bath std dev, C	CU temp average, C	CU temp Std dev, C	bias error avg, C	bias error std dev, C
<b>Channel 1</b>	-20	-20.27168333	0.015378945	-20.113956	0.015585	-0.157728	0.004607
	-10	-10.30156	0.008006977	-10.254056	0.010535	-0.047504	0.007052
	0	-0.297473333	0.007988361	-0.297708	0.008624	0.000234	0.004326
	10	9.723086667	0.016539906	9.698183	0.017210	0.024903	0.004915
	20	19.69382	0.018404932	19.656535	0.018777	0.037285	0.005446
	30	29.64527333	0.017710838	29.585884	0.018121	0.059389	0.004397
	40	39.59674667	0.011426751	39.489078	0.012195	0.107669	0.004987
<b>Channel 2</b>	-20	-20.27441333	0.013682052	-20.112804	0.014426	-0.161609	0.004662
	-10	-10.29998	0.008010338	-10.250799	0.009006	-0.049181	0.004676
	0	-0.296513333	0.009822077	-0.292407	0.010867	-0.004107	0.004324
	10	9.720266667	0.012238937	9.698373	0.013086	0.021893	0.004606
	20	19.69528333	0.008853419	19.662326	0.017094	0.032958	0.004743
	30	29.64402667	0.017898859	29.588627	0.018098	0.055400	0.004547
	40	39.59671667	0.013276475	39.494211	0.013494	0.102505	0.005106
<b>Channel 4</b>	-20	-20.26611333	0.013234033	-20.116634	0.013943	-0.149479	0.004846
	-10	-10.29415333	0.007381147	-10.240561	0.008450	-0.053592	0.004639
	0	-0.295516667	0.007743275	-0.288923	0.008911	-0.006593	0.004276
	10	9.720136667	0.012055214	9.704420	0.012521	0.015717	0.004426
	20	19.69453667	0.022591973	19.663104	0.023021	0.031433	0.005044
	30	29.64456	0.017360198	29.596564	0.018109	0.047996	0.004955
	40	39.59560333	0.014616603	39.499217	0.014370	0.096386	0.004545
<b>Channel 5</b>	-20	-20.26559333	0.013267443	-20.116769	0.015930	-0.148824	0.007969
	-10	-10.29319667	0.008813287	-10.238668	0.009657	-0.054529	0.004506
	0	-0.295863333	0.007523459	-0.289677	0.009214	-0.006186	0.004275
	10	9.720053333	0.015750288	9.701135	0.016594	0.018919	0.004799
	20	19.69444667	0.018283675	19.662593	0.018560	0.031853	0.004726
	30	29.64868	0.01212182	29.598270	0.012585	0.050410	0.004387
	40	39.59784333	0.013324552	39.500211	0.013276	0.097633	0.004553
	Maximum error/std dev -->		0.022591973		0.023021053	0.161609	0.007969
	Average error/std dev -->		0.0149		0.0152	0.0604	0.0051

## Appendix F. Summary of Thermocouple system RTD CJC data

Table 18. Pre-calibrated data, DAQ measured data points

Set Points, C	Thermal Chamber, C	Thermal Chamber std dev, C	Ice Bath, C	Ice Bath std dev, C	DAQ board temp, C	DAQ board temp std dev, C	Screw Terminal, C	Screw Terminal std dev, C
-20	-23.842	0.052	0.137	0.002	-16.260	0.063	-16.073	0.049
-10	-9.854	0.025	0.130	0.001	-2.100	0.040	-1.563	0.043
0	-0.345	0.199	0.135	0.001	7.567	0.324	8.092	0.266
10	9.988	0.311	0.150	0.003	19.065	0.322	19.490	0.259
22	22.836	0.073	0.134	0.001	33.088	0.554	33.950	0.099
45	43.748	0.011	0.138	0.001	49.390	0.088	48.850	0.043
55	53.960	0.012	0.138	0.001	59.361	0.080	58.960	0.044
65	64.040	0.023	0.138	0.001	69.183	0.073	68.950	0.034
75	73.850	0.014	0.138	0.001	78.915	0.066	78.770	0.027
85	84.060	0.020	0.133	0.001	88.980	0.056	89.080	0.069
Maximum value/error/std dev -->		0.311	0.150	0.003		0.554		0.266
Average value/error/std dev -->		0.149	0.137	0.002		0.279		0.146

Table 19. Pre-Calibrated data, CU measured data points. Bias error is taken as the difference between CU measured temp and DAQ measured Ice bath temp.

Set Points, C	Thermal Chamber, C	Thermal Chamber std dev, C	Ice Bath, C	Ice Bath std dev, C	CU board temp, C	CU board temp std dev, C	CU measured temp, C	CU measured temp std dev, C	bias error, C	bias error std dev, C
-20	-23.842	0.052	0.137	0.002	-16.286	0.058	0.210	0.091	-0.073	0.092
-10	-9.854	0.025	0.130	0.001	-1.579	0.048	0.078	0.066	0.053	0.057
0	-0.345	0.199	0.135	0.001	8.271	0.319	0.282	0.252	-0.147	0.252
10	9.988	0.311	0.150	0.003	19.837	0.309	0.090	0.154	0.060	0.154
22	22.836	0.073	0.134	0.001	35.026	0.051	1.829	0.036	-1.695	0.035
45	43.748	0.011	0.138	0.001	49.956	0.025	1.704	0.019	-1.566	0.019
55	53.960	0.012	0.138	0.001	60.132	0.023	1.239	0.018	-1.101	0.018
65	64.040	0.023	0.138	0.001	70.199	0.027	1.195	0.016	-1.057	0.017
75	73.850	0.014	0.138	0.001	79.998	0.024	1.136	0.017	-0.998	0.017
85	84.060	0.020	0.133	0.001	89.015	0.050	1.074	0.034	-0.941	0.034
Maximum value/error/std dev -->		0.311	0.150	0.003		0.319	1.829	0.252	0.060	0.252
Average value/error/std dev -->		0.149	0.137	0.002		0.168	0.884	0.123	-0.747	0.123

Table 20. Post-Calibrated data, CU measured data points. Bias error is taken as the difference between CU measured temp and DAQ measured Ice bath temp.

Set Points, C	Thermal Chamber, C	Thermal Chamber std dev, C	Ice Bath, C	Ice Bath std dev, C	CU board temp, C	CU board temp std dev, C	CU measured temp, C	CU measured temp std dev, C	bias error, C	bias error std dev, C
-20	-23.842	0.052	0.137	0.002	-16.286	0.058	0.241	0.091	0.104	0.092
-10	-9.854	0.025	0.130	0.001	-1.579	0.048	0.175	0.066	0.045	0.057
0	-0.345	0.199	0.135	0.001	8.271	0.319	0.441	0.252	0.306	0.252
10	9.988	0.311	0.150	0.003	19.837	0.309	0.429	0.102	0.279	0.102
22	22.836	0.073	0.134	0.001	35.026	0.051	0.480	0.055	0.346	0.056
45	43.748	0.011	0.138	0.001	49.956	0.025	0.193	0.025	0.055	0.025
55	53.960	0.012	0.138	0.001	60.132	0.023	0.278	0.018	0.140	0.018
65	64.040	0.023	0.138	0.001	70.199	0.027	0.428	0.016	0.290	0.016
75	73.850	0.014	0.138	0.001	79.998	0.024	0.580	0.016	0.442	0.016
85	84.060	0.020	0.133	0.001	89.015	0.050	0.099	0.033	-0.034	0.033
Maximum value/error/std dev -->		0.311	0.150	0.003		0.319	0.580	0.252	0.442	0.252
Average value/error/std dev -->		0.149	0.137	0.002		0.000	0.334	0.096	0.197	0.096

## REFERENCES

- [1] Z. Qian and G. Wei, "Electric-Field-Induced Phase Transition of Confined Water Nanofilms between Two Graphene Sheets," *J. Phys. Chem. A*, vol. 118, no. 39, pp. 8922–8928, Oct. 2014.
- [2] S. Meng, E. G. Wang, and S. Gao, "The pressure induced phase transition of confined water from ab initio molecular dynamics simulation," *J. Phys. Condens. Matter*, vol. 16, no. 49, p. 8851, 2004.
- [3] A. E. Delgado, L. Zheng, and D.-W. Sun, "Influence of Ultrasound on Freezing Rate of Immersion-frozen Apples," *Food Bioprocess Technol.*, vol. 2, no. 3, pp. 263–270, Sep. 2009.
- [4] P. Wilson, "Supercooling of Water," 2012.
- [5] D. G. Fahrenheit, "Experimenta & Observationes De Congelatione Aquae in Vacuo Factae a D. G. Fahrenheit, R. S. S.," *Philos. Trans. 1683-1775*, vol. 33, pp. 78–84, 1724.
- [6] R. Becker, "Kinetics of the formation of nuclei and statistical theory of condensation," *Discuss. Faraday Soc.*, vol. 5, no. 0, pp. 55–61, Jan. 1949.
- [7] W. Band, "On The Nature of The Liquid State," *J. Chem. Phys.*, vol. 7, no. 12, pp. 1114–1114, Dec. 1939.
- [8] J. Frenkel, *Kinetic Theory of Liquids*, Reissue edition. Dover Publications, Inc., 1955.
- [9] L. Ickes, A. Welti, C. Hoose, and U. Lohmann, "Classical nucleation theory of homogeneous freezing of water: thermodynamic and kinetic parameters," *Phys. Chem. Chem. Phys.*, vol. 17, no. 8, pp. 5514–5537, Feb. 2015.
- [10] W. A. Cooper, "A Possible Mechanism for Contact Nucleation," *J. Atmospheric Sci.*, vol. 31, no. 7, pp. 1832–1837, Oct. 1974.
- [11] M. Dymarska, B. J. Murray, L. Sun, M. L. Eastwood, D. A. Knopf, and A. K. Bertram, "Deposition ice nucleation on soot at temperatures relevant for the lower troposphere," *J. Geophys. Res. Atmospheres*, vol. 111, no. D4, p. D04204, Feb. 2006.
- [12] K. Diehl, C. Quick, S. Matthias-Maser, S. K. Mitra, and R. Jaenicke, "The ice nucleating ability of pollen: Part I: Laboratory studies in deposition and condensation freezing modes," *Atmospheric Res.*, vol. 58, no. 2, pp. 75–87, Jul. 2001.
- [13] C. Marcolli, S. Gedamke, T. Peter, and B. Zobrist, "Efficiency of immersion mode ice nucleation on surrogates of mineral dust," *Atmos Chem Phys*, vol. 7, no. 19, pp. 5081–5091, Oct. 2007.
- [14] *Microphysics of Clouds and Precipitation | H.R. Pruppacher | Springer*. .
- [15] N. E. Dorsey, "The freezing of supercooled water," *Trans Am Philos Soc*, vol. 38, pp. 248–256, 1948.
- [16] A. F. Heneghan, P. W. Wilson, G. Wang, and A. D. J. Haymet, "Liquid-to-crystal nucleation: Automated lag-time apparatus to study supercooled liquids," *J. Chem. Phys.*, vol. 115, no. 16, pp. 7599–7608, Oct. 2001.
- [17] T. Inada, X. Zhang, A. Yabe, and Y. Kozawa, "Active control of phase change from supercooled water to ice by ultrasonic vibration 1. Control of freezing temperature," *Int. J. Heat Mass Transf.*, vol. 44, no. 23, pp. 4523–4531, Dec. 2001.
- [18] T. W. Barlow and A. D. J. Haymet, "ALTA: An automated lag-time apparatus for studying the nucleation of supercooled liquids," *Rev. Sci. Instrum.*, vol. 66, no. 4, pp. 2996–3007, Apr. 1995.
- [19] Owen R. Fennema, *Low-temperature preservation of foods and living matter*. New York: MDekker, 1973.
- [20] R. M. George, "Freezing processes used in the food industry," *Trends Food Sci. Technol.*, vol. 4, no. 5, pp. 134–138, 1993.
- [21] J. G. Grandison and A. S. Brennan, "Food Processing Handbook," in *Food Processing Handbook*, 2nd ed., John Wiley & Sons, Incorporated, 2012, pp. 150–151.
- [22] W. B. Van Arsdel, M. J. Copley, and R. L. Olson, *Quality and stability of frozen foods; time, temperature tolerance and its significance*. New York: Wiley-Interscience, 1969.

- [23] J. M. Pardo, F. Suess, and K. Niranjana, "An Investigation into the Relationship Between Freezing Rate and Mean Ice Crystal Size for Coffee Extracts," *Food Bioprod. Process.*, vol. 80, no. 3, pp. 176–182, Sep. 2002.
- [24] "United States \$72.98 Billion Frozen Food Market Analysis By Product (Fruits & Vegetables, Potatoes, Ready Meals, Meat, Fish/Seafood, Soup) And Segment Forecasts To 2024 - Research and Markets," *Business Wire*, 2016.
- [25] "Frozen Food Market Size And Share | Industry Report, 2024." [Online]. Available: <http://www.grandviewresearch.com/industry-analysis/frozen-food-market>. [Accessed: 11-May-2017].
- [26] V. P. M, S. Thomas, L. B. Iturriaga, and P. D. Ribotta, Eds., *Advances in Food Science and Technology, Volume 1*, 1 edition. Wiley-Scrivener, 2013.
- [27] "Frozen Food and Technology." John Wiley & Sons, Inc, 2013.
- [28] Paul B McNulty, "FROZEN FOOD TECHNOLOGY," 1986.
- [29] C. P. Mallett, *Frozen Food Technology*. Springer Science & Business Media, 1993.
- [30] R. Paul Singh author, *Introduction to food engineering*, Fifth edition.. Amsterdam: Elsevier, Academic Press, 2014.
- [31] P. J. Fellows, *Food Processing Technology: Principles and Practice*, 3 edition. oxford etc.; Boca Raton (Florida) [etc.: Woodhead Publishing, 2009.
- [32] C. James, G. Purnell, and S. J. James, "A Review of Novel and Innovative Food Freezing Technologies," *Food Bioprocess Technol.*, vol. 8, no. 8, pp. 1616–1634, Aug. 2015.
- [33] V. O. Salvadori and R. H. Mascheroni, "Analysis of impingement freezers performance," *J. Food Eng.*, vol. 54, no. 2, pp. 133–140, Sep. 2002.
- [34] S. Venketesh and C. Dayananda, "Properties, potentials, and prospects of antifreeze proteins," *Crit. Rev. Biotechnol.*, vol. 28, no. 1, pp. 57–82, 2008.
- [35] M. Hassas-Roudsari and H. D. Goff, "Ice structuring proteins from plants: Mechanism of action and food application," *Food Res. Int.*, vol. 46, no. 1, pp. 425–436, Apr. 2012.
- [36] J. Jaczynski, R. Tahergorabi, A. Hunt, and J. Park, "Safety and Quality of Frozen Aquatic Food Products," in *Handbook of Frozen Food Processing and Packaging, Second Edition*, 0 vols., CRC Press, 2011, pp. 343–386.
- [37] A. LeBail, D. Chevalier, D. M. Mussa, and M. Ghoul, "High pressure freezing and thawing of foods: a review," *Int. J. Refrig.*, vol. 25, no. 5, pp. 504–513, Aug. 2002.
- [38] L. Picart, E. Dumay, J.-P. Guiraud, and J. C. Cheftel, "Microbial inactivation by pressure-shift freezing: effects on smoked salmon mince inoculated with *Pseudomonas fluorescens*, *Micrococcus luteus* and *Listeria innocua*," *LWT - Food Sci. Technol.*, vol. 37, no. 2, pp. 227–238, Mar. 2004.
- [39] L. Cheng, D.-W. Sun, Z. Zhu, and Z. Zhang, "Emerging techniques for assisting and accelerating food freezing processes: A review of recent research progresses," *Crit. Rev. Food Sci. Nutr.*, vol. 57, no. 4, pp. 769–781, Mar. 2017.
- [40] A. E. Delgado and D.-W. Sun, "Ultrasound-Assisted Freezing," in *Ultrasound Technologies for Food and Bioprocessing*, H. Feng, G. Barbosa-Canovas, and J. Weiss, Eds. Springer New York, 2011, pp. 495–509.
- [41] H. Kiani, D.-W. Sun, and Z. Zhang, "The effect of ultrasound irradiation on the convective heat transfer rate during immersion cooling of a stationary sphere," *Ultrason. Sonochem.*, vol. 19, no. 6, pp. 1238–1245, Nov. 2012.
- [42] M. Anese, L. Manzocco, A. Panozzo, P. Beraldo, M. Foschia, and M. C. Nicoli, "Effect of radiofrequency assisted freezing on meat microstructure and quality," *Food Res. Int.*, vol. 46, no. 1, pp. 50–54, Apr. 2012.
- [43] E. Xanthakis, A. Le-Bail, and H. Ramaswamy, "Development of an innovative microwave assisted food freezing process," *Innov. Food Sci. Emerg. Technol.*, vol. 26, pp. 176–181, Dec. 2014.

- [44] N. Owada, "Highly-efficient freezing apparatus and highly-efficient freezing method," US7237400 B2, 03-Jul-2007.
- [45] M. Sato and K. Fujita, "Freezer, freezing method and frozen objects," US7418823 B2, 02-Sep-2008.
- [46] T. Suzuki *et al.*, "Experimental Investigation of Effectiveness of Magnetic Field on Food Freezing Process," *Trans. Jpn. Soc. Refrig. Air Cond. Eng.*, vol. 26, pp. 371–386, 2011.
- [47] International Institute of Refrigeration, Ed., *23rd IIR International Congress of Refrigeration: refrigeration for sustainable development = 23e Congrès International du Froid : le froid pour le développement durable : proceedings*. Paris: International Institute of Refrigeration, 2011.
- [48] C. James, B. Reitz, and S. J. James, "The Freezing Characteristics of Garlic Bulbs (*Allium sativum* L.) Frozen Conventionally or with the Assistance of an Oscillating Weak Magnetic Field," *Food Bioprocess Technol.*, vol. 8, no. 3, pp. 702–708, Mar. 2015.
- [49] "Experimental of the effects of static magnetic field on carp frozen process-- 《Journal of Shandong University(Engineering Science)》 2013年06期." [Online]. Available: [http://en.cnki.com.cn/Article\\_en/CJFDTOTAL-SDGY201306016.htm](http://en.cnki.com.cn/Article_en/CJFDTOTAL-SDGY201306016.htm). [Accessed: 29-Sep-2017].
- [50] E. Xanthakis, M. Havet, S. Chevallier, J. Abadie, and A. Le-Bail, "Effect of static electric field on ice crystal size reduction during freezing of pork meat," *Innov. Food Sci. Emerg. Technol.*, vol. 20, no. Supplement C, pp. 115–120, Oct. 2013.
- [51] N. k. Rastogi, M. n. Eshtiaghi, and D. Knorr, "Accelerated Mass Transfer During Osmotic Dehydration of High Intensity Electrical Field Pulse Pretreated Carrots," *J. Food Sci.*, vol. 64, no. 6, pp. 1020–1023, Nov. 1999.
- [52] M. Jalté, J.-L. Lanoisellé, N. I. Lebovka, and E. Vorobiev, "Freezing of potato tissue pre-treated by pulsed electric fields," *LWT - Food Sci. Technol.*, vol. 42, no. 2, pp. 576–580, Mar. 2009.
- [53] S. Shayanfar, O. Chauhan, S. Toepfl, and V. Heinz, "Pulsed electric field treatment prior to freezing carrot discs significantly maintains their initial quality parameters after thawing," *Int. J. Food Sci. Technol.*, vol. 49, no. 4, pp. 1224–1230, Apr. 2014.
- [54] J. H. Mok, J.-Y. Her, T. Kang, R. Hoptowit, and S. Jun, "Effects of pulsed electric field (PEF) and oscillating magnetic field (OMF) combination technology on the extension of supercooling for chicken breasts," *J. Food Eng.*, vol. 196, pp. 27–35, Mar. 2017.
- [55] S. Timothy, "COMBINATION PULSED ELECTRIC FIELD AND OSCILLATING MAGNETIC FIELD ASSISTED SUPERCOOLING OF BEEF AND FISH: A NOVEL PRESERVATION TECHNIQUE," University of Hawaii at Manoa, 2015.
- [56] M. Mok and J. H. Mok, "Emerging pulsed electric field (PEF) and static magnetic field (SMF) combination technology for food freezing," *Int. J. Refrig.*, vol. 50, pp. 137–145, 201502.
- [57] G. G. Stonehouse and J. A. Evans, "The use of supercooling for fresh foods: A review," *J. Food Eng.*, vol. 148, no. Supplement C, pp. 74–79, Mar. 2015.
- [58] M. P. Fuller and M. Wisniewski, "The use of infrared thermal imaging in the study of ice nucleation and freezing of plants<sup>11</sup>This communication was intended for inclusion in the Special Issue of J. Thermal Biology to commemorate the Life and Works of Professor Grainger (Volume 22, No. 6). Owing to circumstances beyond the control of both the authors and the Editorial Board this was unfortunately not realised.," *J. Therm. Biol.*, vol. 23, no. 2, pp. 81–89, Apr. 1998.
- [59] C. James, P. Hanser, and S. James, "Super-cooling phenomena in fruits, vegetables and seafoods," 2011.
- [60] C. James, V. Seignemartin, and S. J. James, "The freezing and supercooling of garlic (*Allium sativum* L.)," *Int. J. Refrig.*, vol. 32, no. 2, pp. 253–260, Mar. 2009.
- [61] M. Ando, S. Mizuochi, Y. Tsukamasa, and K. Kawasaki, "Suppression of fish meat softening by strict control of storage temperature," *Fish. Sci.*, vol. 73, no. 3, pp. 705–712, Jun. 2007.

- [62] T. W. Agustini, T. Suzuki, T. Hagiwara, S. Ishizaki, M. Tanaka, and R. Takai, "Change of K value and water state of yellowfin tuna *Thunnus albacares* meat stored in a wide temperature range (20°C to -84°C)," *Fish. Sci.*, vol. 67, no. 2, pp. 306–313, Apr. 2001.
- [63] Y. Fukuma, A. Yamane, T. Itoh, Y. Tsukamasa, and M. Ando, "Application of supercooling to long-term storage of fish meat," *Fish. Sci.*, vol. 78, no. 2, pp. 451–461, Mar. 2012.
- [64] L. E. Jeremiah and L. L. Gibson, "The influence of storage temperature and storage time on color stability, retail properties and case-life of retail-ready beef," *Food Res. Int.*, vol. 34, no. 9, pp. 815–826, Nov. 2001.
- [65] L. E. Jeremiah and L. L. Gibson, "The influence of storage and display conditions on the retail properties and case-life of display-ready pork loin roasts," *Meat Sci.*, vol. 47, no. 1–2, pp. 17–27, Sep. 1997.
- [66] S. A. Tassou, J. S. Lewis, Y. T. Ge, A. Hadawey, and I. Chaer, "A review of emerging technologies for food refrigeration applications," *Appl. Therm. Eng.*, vol. 30, no. 4, pp. 263–276, Mar. 2010.
- [67] S. Charoenrein and N. Preechathamwong, "Undercooling associated with slow freezing and its influence on the microstructure and properties of rice starch gels," *J. Food Eng.*, vol. 100, no. 2, pp. 310–314, Sep. 2010.
- [68] S. Wei, X. Xiaobin, Z. Hong, and X. Chuanxiang, "Effects of dipole polarization of water molecules on ice formation under an electrostatic field," *Cryobiology*, vol. 56, no. 1, pp. 93–99, Feb. 2008.
- [69] P. K. Jha *et al.*, "A review on effect of DC voltage on crystallization process in food systems," *Innov. Food Sci. Emerg. Technol.*, vol. 42, no. Supplement C, pp. 204–219, Aug. 2017.
- [70] G. Sutmann, "Structure formation and dynamics of water in strong external electric fields," *J. Electroanal. Chem.*, vol. 450, no. 2, pp. 289–302, Jun. 1998.
- [71] W. Sun, Z. Chen, and S. Huang, "Effect of an external electric field on liquid water using molecular dynamics simulation with a flexible potential," *J. Shanghai Univ. Engl. Ed.*, vol. 10, no. 3, pp. 268–273, Jun. 2006.
- [72] M. Otani, I. Hamada, O. Sugino, Y. Morikawa, Y. Okamoto, and T. Ikeshoji, "Electrode Dynamics from First Principles," *J. Phys. Soc. Jpn.*, vol. 77, no. 2, p. 024802, Feb. 2008.
- [73] L. J. Michot, F. Villiéras, M. François, I. Bihannic, M. Pelletier, and J.-M. Cases, "Water organisation at the solid–aqueous solution interface," *Comptes Rendus Geosci.*, vol. 334, no. 9, pp. 611–631, Jan. 2002.
- [74] T. Hozumi, A. Saito, S. Okawa, and Y. Eshita, "Effects of shapes of electrodes on freezing of supercooled water in electric freeze control," *Int. J. Refrig.*, vol. 28, no. 3, pp. 389–395, May 2005.
- [75] Y. Wang, B. Zhang, Z. Gong, K. Gao, Y. Ou, and J. Zhang, "The effect of a static magnetic field on the hydrogen bonding in water using frictional experiments," *J. Mol. Struct.*, vol. 1052, no. Supplement C, pp. 102–104, Nov. 2013.
- [76] K. X. Zhou, G. W. Lu, Q. C. Zhou, J. H. Song, S. T. Jiang, and H. R. Xia, "Monte Carlo simulation of liquid water in a magnetic field," *J. Appl. Phys.*, vol. 88, no. 4, pp. 1802–1805, Jul. 2000.
- [77] K.-T. Chang and C.-I. Weng, "The effect of an external magnetic field on the structure of liquid water using molecular dynamics simulation," *J. Appl. Phys.*, vol. 100, no. 4, p. 043917, Aug. 2006.
- [78] H. Inaba, T. Saitou, K. Tozaki, and H. Hayashi, "Effect of the magnetic field on the melting transition of H<sub>2</sub>O and D<sub>2</sub>O measured by a high resolution and supersensitive differential scanning calorimeter," *J. Appl. Phys.*, vol. 96, no. 11, pp. 6127–6132, Nov. 2004.
- [79] 周子鹏 · 赵红霞 · 韩吉田 and Z. Z. H. Jitian, "直流磁场作用下水的过冷和结晶现象, Supercooling and crystallization of water under DC magnetic fields," *化工学报*, vol. 63, no. 5, pp. 1405–1408, May 2012.
- [80] V. D. Aleksandrov, A. A. Barannikov, and N. V. Dobritsa, "Effect of magnetic field on the supercooling of water drops," *Inorg. Mater.*, vol. 36, no. 9, pp. 895–898, Sep. 2000.

- [81] H. Zhao, F. Zhang, H. Hu, S. Liu, and J. Han, "Experimental study on freezing of liquids under static magnetic field," *Chin. J. Chem. Eng.*, vol. 25, no. 9, pp. 1288–1293, Sep. 2017.
- [82] L. Otero, A. C. Rodríguez, and P. D. Sanz, "Effects of static magnetic fields on supercooling and freezing kinetics of pure water and 0.9% NaCl solutions," *J. Food Eng.*, vol. 217, no. Supplement C, pp. 34–42, Jan. 2018.
- [83] L. Otero, M. Pérez-Mateos, A. C. Rodríguez, and P. D. Sanz, "Electromagnetic freezing: Effects of weak oscillating magnetic fields on crab sticks," *J. Food Eng.*, vol. 200, no. Supplement C, pp. 87–94, May 2017.
- [84] "H-Bridges – the Basics | Modular Circuits." .
- [85] "MOSFET and Metal Oxide Semiconductor Tutorial," *Basic Electronics Tutorials*, 03-Sep-2013. .
- [86] "Bipolar Transistor Tutorial, The BJT Transistor," *Basic Electronics Tutorials*, 01-Sep-2013. .
- [87] "Semiconductor Basics & Semiconductor Physics Tutorial," *Basic Electronics Tutorials*, 12-Aug-2013.
- [88] "Design and Application Guide of Bootstrap Circuit for High-Voltage Gate-Drive IC." FairChild, 18-Dec-2014.
- [89] P. Meyer and J. Tucker, "Providing Continuous Gate Drive Using a Charge Pump." Texax Instruments, Feb-2011.
- [90] "HV Floating MOS-Gate Driver ICs." International Rectifier, 23-Mar-2007.
- [91] A. Sattar, "Insulated Gate Bipolar Transistor (IGBT) Basics." IXYS Corp.
- [92] "IGBTs Or MOSFETs: Which Is Better For Your Design?," *Electronic Design*, 04-Oct-1999. [Online]. Available: <http://www.electronicdesign.com/power/igbts-or-mosfets-which-better-your-design>. [Accessed: 13-Jul-2017].
- [93] B. Yarborough, "Components and Methods for Current Measurement." Vishay Dale, 31-Aug-2015.
- [94] S. Ziegler, R. C. Woodward, H. H. C. Lu, and L. J. Borle, "Current Sensing Techniques: A Review," *IEEE Sens. J.*, vol. 9, no. 4, pp. 354–376, Apr. 2009.
- [95] "INA20x High-Side Measurement Current-Shunt Monitor With Open-Drain Comparator and Reference." Texax Instruments, Oct-2015.
- [96] "INA225 36-V, Programmable-Gain, Voltage-Output, Bidirectional, Zero-Drift Series, Current-Shunt Monitor." Texax Instruments, Mar-2014.
- [97] "High Voltage, Bidirectional Current Sense Amplifier." Linear Technology, 2010.
- [98] "AC Inductance and Inductive Reactance in an AC Circuit," *Basic Electronics Tutorials*, 25-Jun-2013. .
- [99] "Series Resistor-Inductor Circuits | Reactance and Impedance -- Inductive | Electronics Textbook." [Online]. Available: <https://www.allaboutcircuits.com/textbook/alternating-current/chpt-3/series-resistor-inductor-circuits/>. [Accessed: 25-Jul-2017].
- [100] A. S. Nastase, "How to Derive the RMS Value of Pulse and Square Waveforms," *Mastering Electronics Design*. [Online]. Available: <https://masteringelectronicsdesign.com/how-to-derive-the-rms-value-of-pulse-and-square-waveforms/>. [Accessed: 25-Jul-2017].
- [101] B. Olshausen, "Aliasing." 10-Oct-2000.
- [102] A. W. Van Herwaarden and P. M. Sarro, "Thermal sensors based on the seebeck effect," *Sens. Actuators*, vol. 10, no. 3, pp. 321–346, Nov. 1986.
- [103] W. F. Roeser, "Thermoelectric Thermometry," *J. Appl. Phys.*, vol. 11, no. 6, pp. 388–407, Jun. 1940.
- [104] G. Recktenwald, "Conversion of Thermocouple Voltage to Temperature." 14-Jul-2010.
- [105] Committee E-20, Ed., *Manual on the Use of Thermocouples in Temperature Measurement*. 100 Barr Harbor Drive, PO Box C700, West Conshohocken, PA 19428-2959: ASTM International, 1981.
- [106] S. Iwanaga, E. S. Toberer, A. LaLonde, and G. J. Snyder, "A high temperature apparatus for measurement of the Seebeck coefficient," *Rev. Sci. Instrum.*, vol. 82, no. 6, p. 063905, Jun. 2011.

- [107] “Standard Specification and Temperature-Electromotive Force (emf) Tables for Standardized Thermocouples,” ASTM International, 2012.
- [108] “Thermocouples - Part 1: EMF specifications and tolerances,” IEC, International Standard, Aug. 2013.
- [109] “ITS-90 Thermocouple Database, Web Version 2.0.” [Online]. Available: <https://srdata.nist.gov/its90/main/>. [Accessed: 25-Jul-2017].
- [110] B. Baker, “Precision Temperature-Sensing With RTD Circuits.” Microchip, 02-Jan-2008.
- [111] “The RTD.” Omega.
- [112] “Standard Specification for Industrial Platinum Resistance Thermometers,” ASTM International, 2014.
- [113] “Industrial platinum resistance thermometers and platinum temperature sensors,” IEC 60751:2008, Jul. 2008.
- [114] T. Dust and P. Sekar, “PSoC® 3, PSoC 4, and PSoC 5LP – Temperature Measurement with an RTD.” Cypress.
- [115] “Callendar-Van Dusen equations for the calibration of platinum resistance thermometers.” Wika Alexander Wiegand SE & Co. KG, Aug-2014.
- [116] “Callendar-Van Dusen Equation and RTD Temperature Sensors.” ILX Lightwave.
- [117] “ADS1220 4-Channel, 2-kSPS, Low-Power, 24-Bit ADC with Integrated PGA and Reference.” Texas Instruments, Aug-2016.
- [118] “Thermocouple Analog Front End (AFE) Using RTD and Internal Temperature Sensor of ADS1220 for Cold Junction Compensation (CJC).” Texas Instruments, Oct-2014.
- [119] N. Aupetit, “How to filter the input of a high-side current sensing.” ST microelectronics, Oct-2013.
- [120] H. Zumbahlen, “CHAPTER 8 ANALOG FILTERS,” in *BASIC LINEAR DESIGN*, p. 8.1-8.143.
- [121] “PCB Design Guidelines For Reduced EMI.” Texas Instruments, Nov-1999.
- [122] S. Pithadia and S. More, “Grounding in mixed-signal systems demystified, Part 1.” Texas Instruments, 2013.
- [123] H. Ott, “Partitioning and Layout of a Mixed-Signal PCB.” Printed Circuit Design, Jun-2001.
- [124] “Design Considerations for Mixed-Signal PCB Layout.” e2v Semiconductors, Aug-2010.
- [125] A. D. I. Engineeri, *Linear Circuit Design Handbook*, 1 edition. Amsterdam ; Boston: Newnes, 2008.
- [126] “IEC 61010-1:2010,” International Standard, Jun. 2010.
- [127] “ATMEL 8-BIT MICROCONTROLLER WITH 4/8/16/32KBYTES IN-SYSTEM PROGRAMMABLE FLASH.” Atmel Corporation, Nov-2015.
- [128] “Platinum SMD Flat Chip Temperature Sensor.” Vishay Beyschlag, 08-Dec-2015.
- [129] “American National Standard for Expressing Uncertainty - U.S. Guide to the Expression of Uncertainty in Measurement,” ANSI/NCSL, Z540-2–1997, Oct. 1997.
- [130] “Guide to the Expression of Uncertainty in Measurement,” International Standards Organization, Geneva, Switzerland, 1993.
- [131] “Keysight 34970A Data Acquisition/Switch Unit Family 34970A 34972A Technical Overview.” Keysight Technologies, 02-Aug-2014.
- [132] K. Thyholt and T. Isaksson, “Differentiation of Frozen and Unfrozen Beef Using Near-Infrared Spectroscopy,” *J. Sci. Food Agric.*, vol. 73, no. 4, pp. 525–532, Apr. 1997.
- [133] K. O. Honikel, “Reference methods for the assessment of physical characteristics of meat,” *Meat Sci.*, vol. 49, no. 4, pp. 447–457, Aug. 1998.
- [134] “A simple digital imaging method for estimating black-soil organic matter under visible spectrum: Archives of Agronomy and Soil Science: Vol 63, No 10.” [Online]. Available: <http://www.tandfonline.com/doi/abs/10.1080/03650340.2017.1280728>. [Accessed: 27-Sep-2017].

- [135] D. Wu and D.-W. Sun, "Colour measurements by computer vision for food quality control – A review," *Trends Food Sci. Technol.*, vol. 29, no. 1, pp. 5–20, Jan. 2013.
- [136] H. Anger, "F. J. Francis Und F. M. Clydesdale: Food Colorimetry: Theory And Applications. 477 Seiten, 195 Abb., 40 Tab. Westport, Connecticut, The Avi Publishing Company, Inc., 1975. Preis: 36.00 \$," *Food Nahr.*, vol. 21, no. 1, pp. 90–91, Jan. 1977.
- [137] R. S. Bradley, "The electrical conductivity of ice," *Trans. Faraday Soc.*, vol. 53, no. 0, pp. 687–691, Jan. 1957.
- [138] S. D. Shackelford, T. L. Wheeler, and M. Koohmaraie, "Relationship between shear force and trained sensory panel tenderness ratings of 10 major muscles from *Bos indicus* and *Bos taurus* cattle," *J. Anim. Sci.*, vol. 73, no. 11, pp. 3333–3340, Nov. 1995.
- [139] D. F. Olivera, R. Bambicha, G. Laporte, F. C. Cárdenas, and N. Mestorino, "Kinetics of colour and texture changes of beef during storage," *J. Food Sci. Technol.*, vol. 50, no. 4, pp. 821–825, Aug. 2013.
- [140] D. L. Hopkins, E. N. Ponnampalam, R. J. van de Ven, and R. D. Warner, "The effect of pH decline rate on the meat and eating quality of beef carcasses," *Anim. Prod. Sci.*, vol. 54, no. 4, pp. 407–413, Apr. 2014.
- [141] D. Gunders, "Wasted: How America Is Losing Up to 40 Percent of Its Food from Farm to Fork to Landfill," *NRDC*. [Online]. Available: <https://www.nrdc.org/resources/wasted-how-america-losing-40-percent-its-food-farm-fork-landfill>. [Accessed: 31-Oct-2017].
- [142] D. Gunders, "Wasted: How America Is Losing Up to 40 Percent of Its Food from Farm to Fork to Landfill," *NRDC*. [Online]. Available: <https://www.nrdc.org/resources/wasted-how-america-losing-40-percent-its-food-farm-fork-landfill>. [Accessed: 31-Oct-2017].